

Quantum Information Science and Quantum Metrology: Novel Systems and Applications

A dissertation presented
by

Péter Kómár

to
The Department of Physics
in partial fulfillment of the requirements
for the degree of
Doctor of Philosophy
in the subject of

Physics

Harvard University
Cambridge, Massachusetts
December 2015

©2015 - Péter Kómár

All rights reserved.

Thesis advisor

Mikhail D. Lukin

Author

Péter Kómár

Quantum Information Science and Quantum Metrology: Novel Systems and Applications

Abstract

The current frontier of our understanding of the physical universe is dominated by quantum phenomena. Uncovering the prospects and limitations of acquiring and processing information using quantum effects is an outstanding challenge in physical science. This thesis presents an analysis of several new model systems and applications for quantum information processing and metrology.

First, we analyze quantum optomechanical systems exhibiting quantum phenomena in both optical and mechanical degrees of freedom. We investigate the strength of non-classical correlations in a model system of two optical and one mechanical mode. We propose and analyze experimental protocols that exploit these correlations for quantum computation.

We then turn our attention to atom-cavity systems involving strong coupling of atoms with optical photons, and investigate the possibility of using them to store information robustly and as relay nodes. We present a scheme for a robust two-qubit quantum gate with inherent error-detection capabilities. We consider several remote entanglement protocols employing this robust gate, and we use this system to study the performance of the gate in practical applications.

Abstract

Finally, we present a new protocol for running multiple, remote atomic clocks in quantum unison. We show that by creating a cascade of independent Greenberger-Horne-Zeilinger states distributed across the network, the scheme asymptotically reaches the Heisenberg limit, the fundamental limit of measurement accuracy. We propose an experimental realization of such a network consisting of neutral atom clocks, and analyze the practical performance of such a system.

Contents

Title Page	i
Abstract	iii
Table of Contents	v
List of Figures	xii
List of Tables	xiii
Citations to Previously Published Work	xiv
Acknowledgments	xv
Dedication	xvii
1 Introduction and Motivation	1
1.1 Overview and Structure	1
1.2 Optomechanical Systems	3
1.3 Atom-Cavity Systems	4
1.4 Quantum Repeaters	5
1.5 Atomic Clocks and Quantum Metrology	6
1.6 Rydberg Blockade	9
2 Single-photon nonlinearities in two-mode optomechanics	11
2.1 Introduction	11
2.2 Multimode optomechanics	14
2.3 Equal-time correlations	17
2.3.1 Average transmission and reflection	17
2.3.2 Intensity correlations	20
2.3.3 Absence of two-photon resonance at $\Delta = 0$	23
2.3.4 Finite temperature	25
2.4 Delayed coincidence and single phonon states	30
2.4.1 Driven mode	31
2.4.2 Heralded single phonon states	34
2.5 Reaching strong coupling	37
2.6 Conclusions	38

3 Optomechanical quantum information processing	40
3.1 Introduction	40
3.2 Model	42
3.3 Resonant strong-coupling optomechanics	43
3.4 An OM single-photon source	46
3.5 Single-phonon single-photon transistor	47
3.6 Phonon-phonon interactions	49
3.7 Conclusions	51
4 Heralded Quantum Gates with Integrated Error Detection	52
4.1 Introduction	52
4.2 Heralding gate	54
4.3 Performance	56
4.3.1 Model	56
4.3.2 Effective Hamiltonian	57
4.3.3 Success probability	58
4.3.4 Gate time	59
4.4 Additional errors	60
4.5 Possible implementation	62
4.6 Application	63
4.7 Conclusion	64
5 Remote entanglement distribution using individual atoms in cavities	65
5.1 Introduction	65
5.2 High-fidelity quantum repeater	68
5.2.1 Secret key rate	74
5.2.2 Repeater architecture	76
5.3 Other cavity based repeaters	78
5.3.1 Single-photon entanglement creation	78
5.3.2 Initial purification	80
5.3.3 CNOT gates	82
5.4 Numerical optimization	84
5.5 Conclusion	94
6 Heisenberg-Limited Atom Clocks Based on Entangled Qubits	97
6.1 Introduction	97
6.2 Feedback loop	103
6.3 Spectroscopic noises	104
6.3.1 Phase estimation with multiple GHZ groups	105
6.3.2 Optimization	106
6.4 Comparison with other schemes	107

7 A quantum network of clocks	111
7.1 Introduction	111
7.2 The concept of quantum clock network	113
7.3 Preparation of network-wide entangled states	116
7.4 Interrogation	118
7.5 Feedback	120
7.6 Stability analysis	121
7.7 Security	125
7.8 Outlook	126
8 Quantum network of neutral atom clocks	130
8.1 Introduction	130
8.2 Description of the protocol	132
8.2.1 Collective excitations	133
8.2.2 Non-local connection	133
8.2.3 Local connection	135
8.2.4 Local GHZ growing	136
8.3 Implementation	138
8.4 Clock network optimization	140
8.5 Conclusion	143
A Appendices for Chapter 2	144
A.1 Derivation of reflected mode operator	144
A.2 Analytic model	145
B Appendices for Chapter 3	148
B.1 Phonon nonlinearities	148
B.1.1 Model	148
B.1.2 Displaced frame	149
B.1.3 Hybridized modes	150
B.1.4 Adiabatic elimination of the cavity mode	152
B.1.5 Simple perturbation theory	153
B.1.6 Corrections	154
B.1.7 Numerical simulation	155
B.2 Phonon-phonon interactions	157
C Appendices for Chapter 4	160
C.1 Perturbation theory	160
C.1.1 Success probability and fidelity	165
C.1.2 N -qubit Toffoli gate	165
C.1.3 CZ-gate	167
C.1.4 Two-photon driving	169

C.2	Gate time	172
C.3	Numerical simulation	174
C.4	Additional errors	177
D	Appendices for Chapter 5	181
D.1	Error analysis of the single-photon scheme	181
D.2	Error analysis of the two-photon scheme	183
D.3	Deterministic CNOT gate	184
D.4	Rate analysis	186
D.4.1	Deterministic gates	189
D.4.2	Probabilistic gates	192
E	Appendices for Chapter 6	196
E.1	Figure of merit: Allan-variance	196
E.2	Single-step Uncorrelated ensemble	198
E.2.1	Sub-ensembles and projection noise	198
E.2.2	Effects of laser fluctuations: Phase slip errors	199
E.2.3	Optimal Ramsey time	200
E.3	Cascaded interrogation using GHZ states	202
E.3.1	Parity measurement	203
E.3.2	Failure of the maximally entangled GHZ	204
E.3.3	Cascaded GHZ scheme	205
E.3.4	Rounding errors: finding the optimal n_0	207
E.3.5	Phase slip errors: limitations to the Ramsey time T from laser noise	210
E.3.6	Extending the Ramsey time beyond the laser noise limit	211
E.3.7	Individual qubit noise and final result	214
E.4	Analytic solution of $x^n = A \exp[-1/x]$	215
E.5	Upper bound on the tail of the distribution of the estimated phase	217
E.5.1	Upper bound on the tail of the binomial distribution	218
E.5.2	Upper bound on the distribution of the estimated phase	219
E.6	Threshold fidelity	221
F	Appendices for Chapter 7	223
F.1	GHZ cascade in a network of K clocks	223
F.1.1	Parity measurement	224
F.1.2	Cascaded GHZ scheme	225
F.1.3	Rounding errors	228
F.1.4	Phase slip errors	230
F.1.5	Pre-narrowing the linewidth	233
F.1.6	Individual qubit dephasing noise	234
F.2	Security countermeasures	235

F.2.1	Sabotage	235
F.2.2	Eavesdropping	236
F.2.3	Rotating center role	237
F.3	Network operation	237
F.3.1	Different degree of feedback	237
F.3.2	Timing	238
F.3.3	Dick effect	239
F.3.4	More general architectures	239
F.3.5	Accuracy	241
F.3.6	Efficient use of qubits	242
F.3.7	Required EPR generation rate	242
F.3.8	Threshold fidelity	243
G	Appendices for Chapter 8	245
G.1	Local entangling errors	245
G.1.1	Imperfect blockade	245
G.1.2	Decaying Rydberg states	248
G.1.3	Rydberg interaction induced broadening	248
G.2	Non-local entangling errors	252
G.2.1	Imperfect blockade	252
G.2.2	Rydberg state decay	253
G.2.3	Photon propagation and detection errors	253
G.2.4	Memory loss	254
G.2.5	Imperfect branching ratios	254
G.3	Implementation with Yb	255
G.3.1	Rydberg lifetimes	255
G.3.2	Self-blockade, Δ_{11}	256
G.3.3	Cross-blockade, Δ_{12}	256
G.3.4	Decay rates of lower levels	257
G.3.5	Photon channels	257
G.4	Optimization	257
G.4.1	Optimal parameters	258
G.4.2	Comparison of error sources	259
G.5	Clock precision	262
G.5.1	Imperfect initialization	262
G.5.2	Measurement	263
G.5.3	Fisher information	264
G.5.4	Cramér-Rao bound	265
G.5.5	Allan-deviation	266
G.5.6	Comparison to non-entangled interrogation	267
G.5.7	Optimal clock network size	267
G.6	Multiple local ensembles	269

Contents

G.7 Calculating $\text{Var}(\phi_{j,k})$	270
G.7.1 Calculating $\langle \phi_{j,k} \rangle$	270
G.7.2 Calculating $\langle \phi_{j,k}^2 \rangle$	272
G.7.3 Result for $\text{Var}(\phi_{j,k})$	273
G.8 Calculating $\text{Var}(\psi_j)$	273
G.8.1 Calculating $\langle \psi_j \rangle$	274
G.8.2 Calculating $\langle \psi_j^2 \rangle$	274
G.8.3 Result for $\text{Var}(\psi_j)$	275
G.9 Calculating $\text{Var}(\Delta_j)$	276
G.9.1 Calculating $\langle \Delta_j \rangle$	276
G.9.2 Calculating $\langle \Delta_j^2 \rangle$	277
G.9.3 Result for $\text{Var}(\Delta_j)$	278
Bibliography	280

List of Figures

2.1	Two-mode optomechanical system	14
2.2	Lower level diagram of 2+1 optomechanical system	16
2.3	Photon statistics in anti-symmetric mode, a	18
2.4	Photon statistics in symmetric mode, s	19
2.5	Photon statistics in reflected mode, R	19
2.6	Illustration of dominant processes	22
2.7	Aggregate photon statistics	25
2.8	Temperature dependence of the relevant levels	26
2.9	Effect of non-zero temperature on photon statistics of mode a	26
2.10	Effect of non-zero temperature on photon statistics of mode s	27
2.11	Autocorrelation of mode a	33
2.12	Autocorrelation of mode s	35
2.13	Diagram of the metastable subspace	36
3.1	Model of two resonators	42
3.2	Behavior of the coupled system	44
3.3	A single-phonon single-photon transistor	47
3.4	Controlled phase gate	49
4.1	Level structures of qubit and control atoms	56
4.2	Success probability	60
4.3	Level structure of auxiliary atom	61
5.1	The general architecture of a quantum repeater	69
5.2	Entanglement generation	70
5.3	Schematics of the heralded CZ gate	72
5.4	Secret key fraction	75
5.5	Number of swap levels	77
5.6	Purification	81
5.7	CNOT gate structure	82
5.8	CNOT gates comparison	86

List of Figures

5.9	Example of repeater architecture	87
5.10	Optimal secret key rate I	89
5.11	Optimal secret key rate II	90
6.1	GHZ cascade	101
6.2	Comparison of clock protocols	108
7.1	The concept of world-wide quantum clock network	115
7.2	Entangled state preparation between distant nodes	117
7.3	Performance of different operation schemes	122
7.4	Schematics of security countermeasures	127
8.1	Steps to generate of pairwise entanglement	134
8.2	Connecting links into non-local GHZ state	136
8.3	Local GHZ creation	137
8.4	Implementation with Yb levels	139
B.1	Comparison of effective and exact description	156
C.1	Level structure of qubit an auxiliary atoms	162
C.2	Error and success probability vs cooperativity	168
C.3	Level structure of auxiliary atom	169
C.4	Gate time and success probability vs driving strength	176
C.5	Conditional fidelity	177
C.6	Gate time and success probability vs detuning	178
F.1	GHZ cascade protocol for K clocks	226
G.1	Coupling through doubly excited states	250
G.2	Optimal parameter values	259
G.3	Minimal error per atom	262
G.4	Average Fisher information	265
G.5	Optimal network size	268
G.6	Maximal gain over classical schemes	269
G.7	Arc length in a circular cloud	272

List of Tables

5.1	Characteristics of the three gates	84
5.2	Parameters in the numerical optimization	85
8.1	Error budget	141
C.1	Comparison of CZ and Toffoli gates	161
C.2	Perturbation validity criteria	173
G.1	Error budget of 2D setup	260
G.2	Error budget of 3D setup	261

Citations to Previously Published Work

Most of the chapters of this thesis have appeared in print elsewhere. By chapter number, they are:

- Chapter 2: “Single-photon nonlinearities in two-mode optomechanics,” P. Kómár, S. D. Bennett, K. Stannigel, S. J. M. Habraken, P. Rabl, P. Zoller, and M. D. Lukin, *Phys. Rev. A* **87**, 013839 (2013).
- Chapter 3: “Optomechanical Quantum Information Processing with Photons and Phonons,” K. Stannigel, P. Kómár, S. J. M. Habraken, S. D. Bennett, M. D. Lukin, P. Zoller, and P. Rabl, *Phys. Rev. Lett.* **109**, 013603 (2012).
- Chapter 4: “Heralded Quantum Gates with Integrated Error Detection in Optical Cavities,” J. Borregaard, P. Kómár, E. M. Kessler, A. S. Sørensen, and M. D. Lukin, *Phys. Rev. Lett.* **114**, 110502 (2015).
- Chapter 5: “Long-distance entanglement distribution using individual atoms in optical cavities,” J. Borregaard, P. Kómár, E. M. Kessler, A. S. Sørensen, and M. D. Lukin, *Phys. Rev. A* **92**, 012307 (2015).
- Chapter 6: “Heisenberg-Limited Atom Clocks Based on Entangled Qubits,” E. M. Kessler, P. Kómár, M. Bishof, L. Jiang, A. S. Sørensen, J. Ye, and M. D. Lukin, *Phys. Rev. Lett.* **112**, 190403 (2014).
- Chapter 7: “A quantum network of clocks,” P. Kómár, E. M. Kessler, M. Bishof, L. Jiang, A. S. Sørensen, J. Ye, and M. D. Lukin, *Nature Physics* **10**, 582587 (2014).
- Chapter 8: “Quantum network of netural atom clocks,” P. Kómár, T. Topcu, E. M. Kessler, A. Derevianko, J. Ye, V. Vuletić, and M. D. Lukin, *arXiv: ...*, (2015).

Acknowledgments

First of all, I would like to thank my research advisor, Prof. Mikhail Lukin, for his scientific insights and ideas, and especially for his attention and patience in guiding my work and education.

I would like to thank other members of my thesis committee, Prof. John Doyle and Prof. Subir Sachdev, with whom I was fortunate to work as a teaching fellow. Their knowledge and thoroughness inspired both my teaching and research.

I am grateful to Prof. Andrei Derevianko at University of Nevada, Prof. Pierre Meystre at University of Arizona, Prof. Peter Rabl in Vienna, Till Rosenband at Harvard, Prof. Anders Sørensen in Copenhagen, Prof. Vladan Vuletić at MIT, Prof. Jun Ye at JILA, and Prof. Peter Zoller in Innsbruck for the enlightening discussions and their invaluable contributions to my research in the past five years.

I would like to thank all colleagues with whom I worked namely, Michael Bishof, Soonwon Choi, Manuel Endres, Ruffin Evans, Michael Goldman, Michael Gullans, Steven Habraken, Márton Kanász-Nagy, Shimon Kolkowitz, Ronen Kroese, Peter Maurer, Travis Nicholson, János Perczel, Thibault Peyronel, Arthur Safira, Alp Sipahigil, Kai Stannigel, Alex Sushkov, Jeff Thompson, Turker Topcu, Dominik Wild, Norman Yao, Leo Zhou. I am especially grateful to Steven Bennett, Johannes Borregaard, and Eric Kessler; besides many years of fruitful collaboration, they helped me as mentors and friends.

I would also like to thank David Morin, Jacob Barandes, Nick Schade and people from the Bok Center, John Girash, Colleen Noonan, and Matthew Sussman, for their efforts in guiding me to become a better teacher.

I am thankful for my friends in Cambridge and Boston: Travis and John Woolcott,

Acknowledgments

who gave me tremendous help during my first year, and continued to keep an eye on me; Bence Béky and Margit Szabari for teaching me the tricks and traditions of living in the US; and Kartiek Agarwal, Debanjan Chowdhury and Ilya Feige for our endless discussions about life.

The Physics Department staff has been an invaluable resource. I would like to thank Monika Bankowski, Jennifer Bastin, Lisa Cacciabuado, Karl Coleman, Carol Davis, Sheila Ferguson, Joan Hamilton, Dayle Maynard, Clare Ploucha, Janet Ragusa and Sarah Roberts, for helping me at countless occasions.

I am grateful to the Harvard International Office, and especially to Darryl Zeigler, for all the help making me feel myself at home at Harvard.

I am thankful to the Office of Career Services, and especially Laura Stark and Heather Law, for helping me transition to the next stage of my career.

Finally, I would like to thank my family, Erzsébet Kómár, Antal Kómár, Anna Kómár and Szilvia Kiriakov, for their immense support and understanding towards my education and work. I cannot thank you enough. This thesis is dedicated to you.

*Dedicated to my parents Erzsébet and Antal,
my sister Anna,
and my fiancée Szilvia.*

Chapter 1

Introduction and Motivation

1.1 Overview and Structure

The field of quantum science aims to answer conceptual and practical questions about the fundamental behavior, controllability and applicability of systems governed by quantum physics. Such systems arise whenever a few degrees of freedom of a physical system become isolated from their environment.

Realizing and maintaining the required isolation is a formidable task. The interaction within the isolated components needs to be much stronger than the collective coupling to modes of the environment. Once achieved, the system starts to explore an expanded set of states: Its dynamics are not constrained to a countable number of pointer (or “classical”) states anymore, originally selected by the environment, rather it moves around smoothly in the entire Hilbert space, with its motion governed by a Hamilton operator. Internal components of such a system are said to be “strongly coupled”, and their dynamics to be “coherent”.

The variety of (“quantum”) states in the Hilbert space gives rise to counter-intuitive phenomena such as superposition, tunneling and entanglement. Besides being academically exciting, these phenomena hold the promise that future devices and protocols relying on them will perform better than any conceivable scheme based solely on classical dynamics.

The discovery of efficient quantum algorithms for problems that are conjectured to not be efficiently computable fueled the field of Quantum Computing. In Chapters 2 and 3, we analyze the capabilities of nano-scale optomechanical systems to perform coherent logical operations, the elemental steps of quantum computation.

Protocols that rely on entanglement to distribute secret keys between distant parties are the main focus of Quantum Communication. Their security is based on fundamental physical limitations, rather than practical one due to computational complexity. In Chapters 4 and 5, we describe how a system consisting of a few atoms isolated in an optical cavity can be used to realize a quantum gate with integrated error detection, and we analyze its usefulness in a quantum communication setup.

The idea of preparing a detector in a quantum superposition in order to focus its sensitivity to the quantity of interest is the central topic of Quantum Metrology. In Chapters 6, 7 and 8, we present a protocol for operating a network of atomic clocks, which combines local and remote entanglement to surpass the accuracy of classical protocols and asymptotically reach the fundamental quantum limit of precision, the Heisenberg limit.

1.2 Optomechanical Systems

The current fabrication technology allows the creation of integrated devices with nanometer-scale features such as waveguides [148], photonic band-gap materials [88], non-linear inductive elements [139], antenna arrays [241], optical cavities [165], and mechanical resonators of various shapes and sizes [10].

Coupling components with different physical properties can give rise to devices which incorporate the best characteristics of each component. Optical components are fast ($\sim 100 - 1000$ THz) and fairly isolated, however, making them strongly interact with each other is challenging [45]. Mechanical components, on the other hand, are much slower ($\sim 0.01 - 10$ GHz), but are usually much more sensitive to changes in their surroundings [10]. One successful application is using mechanical elements as transducers between two optical degrees of freedom allows for efficient filtering and frequency conversion [79] when driven by classical light.

The interaction between the light field and a mechanical surface originates mainly from the light-pressure displacing the mechanics, and gives rise to a non-linear parametric coupling between light intensity and mechanical motion [150]. In Chapter 2, we analyze a quantum model of two optical cavities and a mechanical oscillator interacting through this coupling. We find that if the system is driven by a weak laser pulse (accurately described by a Poisson-process of photon arrivals), the output light exhibits super- and sub-Poissonian characteristics. We find that if the system is properly tuned, and is sufficiently cooled down, then it can be used for coherent quantum operations. If the energy difference between the two optical modes is bridged by the mechanical mode, then we can use the photons leaving the output port to herald the

creation of a single mechanical excitation.

Using oscillators as quantum registers in a future quantum computer requires them to be anharmonic [138]. This is because consecutive levels of an anharmonic oscillator are separated by unequal frequency intervals, which makes it possible to address transitions independently. The inherent non-linearity of the optomechanical coupling holds the promise of rendering the coupled oscillator system sufficiently anharmonic for computational tasks. In Chapter 3, we propose a quantum logic architecture based on coupled optomechanical components. We find that, under sufficiently strong cooling, the system exhibits non-classical behavior and is able to store information and perform logic gates on the qubits.

1.3 Atom-Cavity Systems

Coupling individual atoms to optical cavities is one of the most effective ways to realize a well-controllable and manifestly quantum system [137, 231]. The first model, named after E. Jaynes and F. Cummings [111, 204], describes the coherent dynamics of a single transition between two levels of an atom and a single, confined optical mode. This model is exactly solvable and serves as a great source of intuition.

As the physical size of an optical cavity is decreased, the zero-point electric field corresponding to the ground state of its modes increases. As a result, individual atoms placed inside such a cavity, coupled through their electric dipole moment, start to interact strongly with the optical modes. Once this interaction becomes much stronger than the coupling of the atoms to the radiation environment outside of the cavity, the system becomes strongly coupled, and their states hybridize. From

a spectroscopic point of view, this results in a resolvable splitting of the optical resonances.

Optical cavities built on photonic crystal waveguides [220] have high zero-point electric fields, and produce couplings to atoms larger than their spontaneous emission rate. Their observed lifetime is then considerably decreased [81]; an effect called Purcell-enhancement.

Once such strong interaction is demonstrated, the prospect of using these systems for coherent quantum logic operations becomes realistic. In Chapter 4, we consider a model of three atoms placed inside and coupled by a single optical cavity. We show that with tailored driving pulses and a proper choice of atomic levels this system can perform a controlled-NOT operation on two of the atoms and can be made tolerant to the dominating error, caused by the loss of a photon, by post-selecting on the state of the third atom.

1.4 Quantum Repeaters

Creating quantum entanglement between systems separated by large distances is the most important prerequisite of quantum communication protocols. Experimental realizations rely on exchanging weak light pulses via carefully monitored optical fibers [167]. The reliability of direct transmission of photon pulses is limited by the fiber attenuation length, the maximum of which ($\sim 20\text{ km}$) is achieved at telecom wavelength ($\sim 1\mu\text{m}$).

Classical communication solves the attenuation problem by incorporating fiber segments which amplify the signal. Conceptually, this classical amplification relies on

detecting some of the signal photons and emitting more in synchrony. Unfortunately, such a process fails for quantum channels using single-photon pulses, because the detection event can measure the photon only once, therefore it necessarily discards essential information about its quantum state.

Overcoming the attenuation problem in quantum channels requires using more resources. The scheme of quantum repeaters consists of repeater stations placed between the sender and the receiver [17, 18, 70]. These stations, instead of relaying the information forward, create pairwise entanglement with their neighbors using direct photon transmission via fibers, which are much shorter than the total length. Once all entangled pairs are heralded, each station performs a local quantum logic operation between the two pairs that they have access to. This is called entanglement connection, resulting in entanglement between the two outermost parties. An alternative solution encodes the information in states of a many-photon pulse, and applies periodic quantum error-correction along its way [155].

The transmission rate and reliability of such a quantum repeater protocol depends strongly on the fidelity of the entanglement connection step. In Chapter 5, we show that the atom-cavity system described in Chapter 4 would serve as a great quantum entanglement connection gate, and achieve outstanding quantum repeater performance for total distances of $\sim 100 - 1000$ km.

1.5 Atomic Clocks and Quantum Metrology

Currently, atomic clocks are the best time-keeping devices. They are used to create and broadcast a precise time and frequency standard. The workings of atomic

clocks rely on two main components: the reference oscillator, realized by an isolated, narrow-linewidth electromagnetic transition of an atomic species, [60] and the slaved oscillator, the microwave or optical source of a strong, coherent field. The clock keeps time by periodically interrogating the atoms with the field of the slaved oscillator (laser), and measuring the deviation of their frequencies. The measurement result is then used to correct the frequency of the laser. This closes the feedback loop, and results in an actively stabilized laser field, which serves as the clock signal [62].

The accuracy of an atomic clock, characterized by the average fractional frequency deviation, the Allan-deviation [4, 186], is determined by several factors. Employing higher atomic reference frequency, longer interrogation cycles, longer averaging time and more atoms improve the overall accuracy. Consequently, there are many independent ways to improve the accuracy: Choosing an atomic transition with optical frequency, instead of microwave, boosts the performance of the clock by five orders of magnitude. The central frequencies of the current record-holder atomic clocks are all in the optical domain [131]. The optimal length of the interrogation cycle usually falls slightly above the coherence time of the laser, and in any case, increasing it fails to help beyond the atomic coherence time even in schemes that eliminate the limiting effect of the laser [27, 183]. The maximal total averaging time is usually determined by the refresh rate of the clock signal required by the application, or by other noises such as frequency flicker noise [13].

The dependence of the precision on the number of atoms is a true quantum phenomenon. It is due to the fundamental limit on the maximal information a single measurement can obtain about the atoms. When N atoms are measured indepen-

dently, the Allen-deviation scales as $\propto N^{-1/2}$, and is limited by projection noise. This limit is called the “Standard Quantum Limit”. It originates from the inherent uncertainty of a single two-level system prepared in superposition [194].

The Standard Quantum Limit describes the limit of precision if all atoms are prepared and measured independently, or as an uncorrelated ensemble. Although it is accurate in most cases, it is higher than the fundamental quantum limit, due to Heisenberg uncertainty. The latter predicts $\propto N^{-1}$ scaling of the precision with atom number N [102]. The gap between the two limits, and proposals trying to close it, is the main focus of Quantum Metrology [95, 82].

By preparing the collection of atoms in an entangled state, the subsequent measurement will have lower uncertainty and will provide more information about the detuning of the laser frequency from the atomic reference. States such as squeezed states [6, 28], Greenberger-Horne-Zeilinger (GHZ) states [237, 24], and optimally entangled states [38, 21], all promise a significant improvement, and some even reach the Heisenberg limit for large N . In Chapter 6, we calculate a limit on the best achievable performance using a cascade of GHZ states, and compare it with the other algorithms. We find that for total averaging times shorter than the atomic coherence time, the precision of our scheme surpasses the precision of the best classical protocol.

Once we establish that entangling the available atoms is beneficial, finding the optimal protocol for a network of atomic clocks becomes an important problem. In Chapter 7, we assume that a large number of identical atomic clocks are joined together in a quantum network using a quantum communication scheme. We show that this network can be operated in a way that every clock atom is entangled with all

atoms in the network, forming a global, multi-party GHZ state. We characterize the enhancement of the overall precision and compare it with precisions of schemes using only local or no entanglement.

1.6 Rydberg Blockade

In most cases, interactions between atoms in cold ensembles are accurately modeled by short-range or contact interactions [51]. They can be neglected if the gas is not too dense, and the duration of the phenomena under investigation is short compared to the inverse of average collision rate. This breaks down when a few atoms acquire significant magnetic or electric dipole moments and, as a result, start interacting via dipole-dipole interaction, whose strength scales as $\propto R^{-3}$ with separation R .

One way to induce a strong electric dipole moment in an atom is to optically excite the outermost electron to a level with high principle quantum number ($n > 30$), a Rydberg level. Rydberg levels have small energy spacing ($\propto n^{-3}$), long spontaneous lifetimes ($\propto n^3$), and strong transition dipole moments ($\propto n^2$) [190]. These properties make Rydberg atoms a promising tool to realize fast and reliable quantum logic operations [135].

Blockade between Rydberg atoms is an especially strong and promising phenomenon. When one atom gets excited into a Rydberg state, the long-range interaction originating from its (transition) electric dipole moment shifts the Rydberg levels of all other atoms out of resonance, and prevents them from being excited [226]. This effect creates an exceptionally strong non-linearity: it limits the number of Rydberg excitations in the cloud to zero and one, allowing the cloud to be used

as a qubit. In Chapter 8, we present and analyze a quantum protocol that relies on strong Rydberg blockade to perform fast, high-fidelity operations between different quantum registers. We propose to use different delocalized spin-waves of the atomic cloud to store information, and employing the Rydberg blockade to mediate interactions between them. We show that even after taking the physical imperfections into account, our scheme provides a feasible way to prepare the network-wide global GHZ state required by the quantum clock network of Chapter 7.

Chapter 2

Single-photon nonlinearities in two-mode optomechanics

2.1 Introduction

Optomechanical systems (OMSs) involve the interaction between optical and mechanical modes arising from radiation pressure force, canonically in an optical cavity with a movable mirror [118, 142, 11, 90, 84]. Recent progress in optomechanical (OM) cooling techniques has been rapid [149, 92, 9, 119, 56, 198, 219, 235], and experiments have now demonstrated cooling to the mechanical ground state [162, 217, 42], OM induced transparency [234, 187], and coherent photon-phonon conversion [86, 230, 106]. These developments have attracted significant interest, and motivated proposals for applications exploiting OM interactions at the quantum level, ranging from quantum transducers [212, 188, 175, 215] and mechanical storage of light [242, 2, 44] to single-photon sources [171] and OM quantum information processing [211, 199]. Significant

advantages of OM platforms for these applications are the possibility for mass production and on-chip integration using nanofabrication technologies, wide tuneability and the versatility of mechanical oscillators to couple to a wide variety of quantum systems [200].

The force exerted by a single photon on a macroscopic object is typically weak; consequently, experiments have so far focused on the regime of strong optical driving, where the OM interaction is strongly enhanced but effectively linear [99, 216]. However, recent progress in the design of nanoscale OMSs [42, 79, 40, 63] and OM experiments in cold atomic systems [101, 32] suggests that the regime of single-photon strong coupling, where the OM coupling strength g exceeds the optical cavity decay rate κ , is within reach of the next generation of OM experiments. In this regime, the inherently nonlinear OM interaction is significant at the level of single photons and phonons [143, 132, 171, 161]. For example, the presence of a single photon can—via the mechanical mode—strongly influence or even block the transmission of a second photon, leading to photon blockade. This single-photon nonlinearity was recently analyzed for canonical OMSs consisting of a single optical mode coupled to a mechanical mode [171, 122, 129]. However, with a single optical mode, the OM coupling is highly off-resonant, leading to a suppression of effective photon-photon interactions by the large mechanical frequency $\omega_m \gg g$ [171].

In this chapter we develop a quantum theory of a weakly driven *two-mode* OMS [151, 211, 133, 14] in which two optical modes are coupled to a mechanical mode. The key advantage of this approach is that photons in the two optical modes can be resonantly exchanged by absorbing or emitting a phonon via three-mode mixing. We

extend our earlier results [211], where we discussed possible applications of resonant optomechanics such as single-photon sources and quantum gates, by exploring one-time and two-time photon correlations of both optical modes. Specifically, we find that the photon-photon correlation function of the undriven optical mode exhibits delayed bunching for long delay times, arising from a heralded single mechanical excitation after detection of a photon in the undriven mode. Finally, we compare the two-mode OMS to the canonical atomic cavity QED system with a similar low-energy level spectrum [39, 31]. Despite several similarities we find that, in stark contrast to the atom-cavity system, the OMS studied here does *not* exhibit nonclassical correlations unless the strict strong coupling condition $g > \kappa$ is met. Our results serve as a guideline for OM experiments nearing the regime of single-photon nonlinearity, and for potential quantum information processing applications with photons and phonons.

The remainder of this chapter is organized as follows. In Sec. 2.2, we introduce the system and details of the model. In Sec. 2.3, we calculate the equal-time intensity correlation functions of both transmitted and reflected photons, and discuss signatures of nonclassical photon statistics. In Sec. 2.4, we investigate two-time correlation functions of the transmitted photons, and discuss delayed coincidence correlations that indicate the heralded preparation of a single phonon state. Finally, we provide a brief outlook on the feasibility of strong OM coupling in Sec. 2.5, and conclude in Sec. 2.6 with a summary of our results. Appendix A.2 contains details of our analytic model used to derive several results discussed in this chapter.

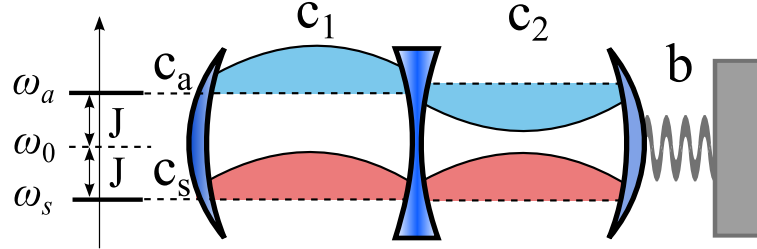


Figure 2.1: Optomechanical system consisting of two tunnel-coupled optical cavity modes c_1 and c_2 , and a mechanical oscillator b coupled to one of the cavity modes by radiation pressure. The coupled optical modes are diagonalized in terms of symmetric and antisymmetric modes, c_s and c_a .

2.2 Multimode optomechanics

We consider the setup shown schematically in Fig. 2.1, consisting of two optical cavities separated by a semitransparent mirror. The cavity modes are coupled by photons tunneling through the fixed mirror in the middle, and the mode on the right couples to the motion of a vibrating endmirror oscillator through radiation pressure. The Hamiltonian describing the system is ($\hbar = 1$)

$$H_0 = \omega_0(c_1^\dagger c_1 + c_2^\dagger c_2) - J(c_1^\dagger c_2 + c_1 c_2) + \omega_m b^\dagger b - g(b^\dagger + b)c_2^\dagger c_2 + H_{\text{dr}}(t), \quad (2.1)$$

where $c_{1,2}$ are annihilation operators for the two cavity modes, which we assume to be degenerate with frequency ω_0 , and J is the photon tunneling amplitude through the central mirror. The motion of the endmirror on the right is described by a single mechanical mode with annihilation operator b and frequency ω_m , and the parametric coupling strength g corresponds to the shift of the cavity frequency due to a single mechanical phonon. Finally, $H_{\text{dr}}(t) = \sum_{i=1,2} (\Omega_i c_i e^{i\omega_L t} + \text{h.c.})$ describes two coherent driving fields of amplitudes Ω_i and frequency ω_L , which are applied to the left and right cavities.

We are interested in a three-mode resonant interaction in which the two optical modes exchange a photon by absorbing or emitting a phonon in the mechanical mode. We begin by diagonalizing the optical part of H_0 in the first line of Eq. 2.1 in terms of the symmetric and antisymmetric combinations of the optical modes, $c_s = \frac{1}{\sqrt{2}}(c_1 + c_2)$ and $c_a = \frac{1}{\sqrt{2}}(c_1 - c_2)$, with eigenfrequencies $\omega_{a,s} = \omega_0 \pm J$. In the frame rotating at the laser frequency ω_L we obtain

$$\begin{aligned} H' = & -\Delta c_a^\dagger c_a - (\Delta + 2J)c_s^\dagger c_s + \omega_m b^\dagger b \\ & + \frac{g}{2} (c_a^\dagger c_s + c_s^\dagger c_a) (b + b^\dagger) + \sum_{\eta=s,a} \Omega_\eta (c_\eta^\dagger + c_\eta), \end{aligned} \quad (2.2)$$

where $\Delta = \omega_L - \omega_a$ is the laser detuning from the c_a mode, and $\Omega_{s,a} = (\Omega_1 \pm \Omega_2)/\sqrt{2}$.

Next, we focus on the case of three-mode resonance, $\omega_m = 2J$, and assume $\omega_m \gg g, |\Delta|, \Omega_i$. The third inequality here corresponds to a weak optical drive, the relevant limit for studying single-photon nonlinear effects in this work. This allows us to make a rotating wave approximation with respect to the remaining large frequency scale ω_m , and in the frame defined by the transformation $U = \exp[-i\omega_m t(b^\dagger b - c_s^\dagger c_s)]$, the Hamiltonian H' simplifies to

$$H = -\Delta(c_a^\dagger c_a + c_s^\dagger c_s) + \frac{g}{2}(c_a^\dagger c_s b + b^\dagger c_s^\dagger c_a) + \Omega_a(c_a^\dagger + c_a). \quad (2.3)$$

This is the starting point for our analysis discussed below. Note that the assumptions made in deriving Eq. (2.3) are fulfilled in most experimental systems of interest [100, 243], and H represents a generic description for resonant two-mode optomechanics [151, 65, 47, 133].

The nonlinear terms proportional to g in Eq. (2.3) describe coherent photon exchange between the two optical modes mediated by absorption or emission of a

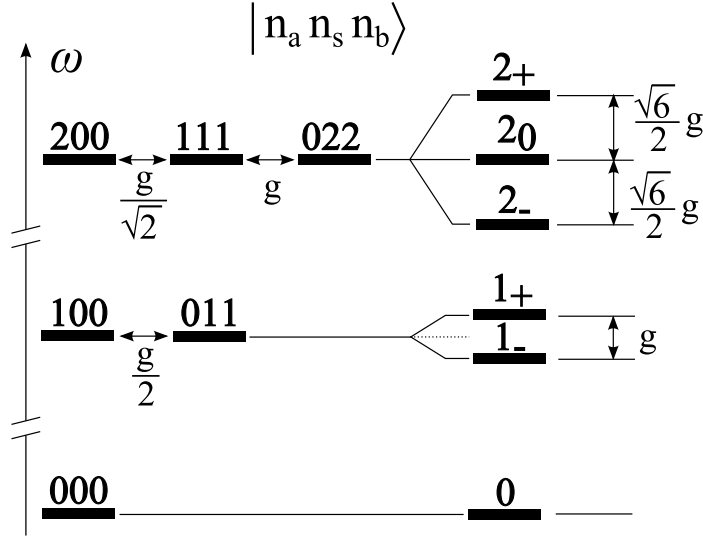


Figure 2.2: Level diagram showing the relevant zero-, one- and two-photon states at zero temperature and under the three-mode resonance condition $\omega_s - \omega_a = \omega_m$. States are labeled by $|n_a n_s n_b\rangle$ denoting the number n_a (n_s) of antisymmetric (symmetric) photons and the number of phonons n_b . The optomechanical coupling g splits the degeneracy of states $|n_a n_s n_b\rangle$ and $|n_a - 1, n_s + 1, n_b + 1\rangle$.

phonon. The resulting low energy level diagram is shown in Fig. 2.2, where $|n_a n_s n_b\rangle$ represents a state with n_a and n_s photons in the c_a and c_s modes, and n_b phonons in the mechanical mode. In the absence of a drive we diagonalize H in this few-photon subspace, yielding the eigenstates

$$|0\rangle = |000\rangle, \quad (2.4)$$

$$|1_{\pm}\rangle = \frac{1}{\sqrt{2}} (|100\rangle \pm |011\rangle), \quad (2.5)$$

$$|2_{\pm}\rangle = \frac{1}{\sqrt{6}} \left(|200\rangle \pm \sqrt{3} |111\rangle + \sqrt{2} |022\rangle \right), \quad (2.6)$$

$$|2_0\rangle = \frac{1}{\sqrt{3}} \left(\sqrt{2} |200\rangle - |022\rangle \right). \quad (2.7)$$

Note that in the diagonal basis the weak driving field couples all states with photon number differing by one. In the following sections we use this low energy Hilbert space to understand photon correlations in the system.

In addition to the coherent evolution modeled by the Hamiltonian H , we describe optical and mechanical dissipation using a master equation for the system density operator ρ ,

$$\dot{\rho} = -i[H, \rho] + \kappa\mathcal{D}[c_a]\rho + \kappa\mathcal{D}[c_s]\rho \quad (2.8)$$

$$+ \frac{\gamma}{2}(N_{\text{th}} + 1)\mathcal{D}[b]\rho + \frac{\gamma}{2}N_{\text{th}}\mathcal{D}[b^\dagger]\rho, \quad (2.9)$$

where H is given by Eq. 2.3, 2κ and γ are energy decay rates for the optical and mechanical modes, respectively, N_{th} is the thermal phonon population and $\mathcal{D}[\hat{o}]\rho = 2\hat{o}\rho\hat{o}^\dagger - \hat{o}^\dagger\hat{o}\rho - \rho\hat{o}^\dagger\hat{o}$. Below we study nonlinear effects at the level of single photons, both numerically and analytically, by solving Eq. 2.8 approximately in the limit of weak optical driving, $\Omega \equiv \Omega_a \ll \kappa$.

2.3 Equal-time correlations

2.3.1 Average transmission and reflection

Before focusing on photon-photon correlations, we first study the average transmission through the cavity, which is proportional to the mean intracavity photon number. In Fig. 2.3 and 2.4 we show the intracavity photon number of the two optical modes,

$$\bar{n}_i = \langle c_i^\dagger c_i \rangle, \quad (2.10)$$

where $i = a, s$, and angle brackets denote the steady state average. At $\Delta/g = \pm\frac{1}{2}$, both transmission curves exhibit a maximum, indicating that the driving field is in resonance with an eigenmode of the system. The position of these peaks can

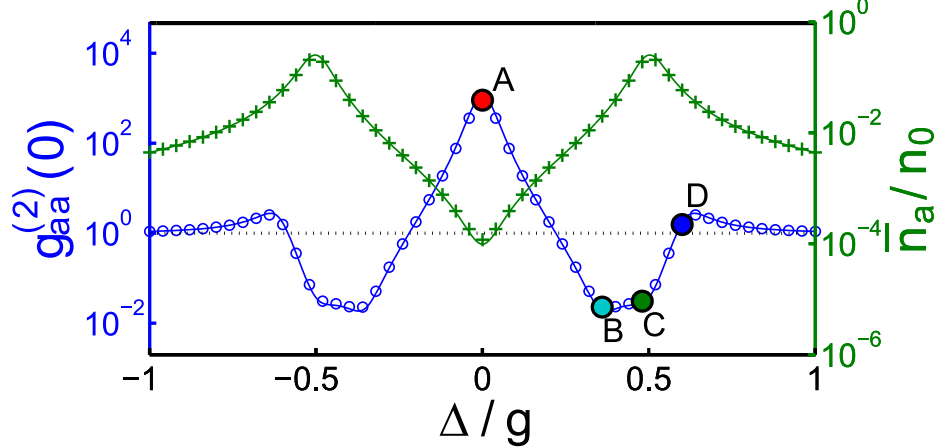


Figure 2.3: Normalized average photon number (green “+”) and photon-photon correlation function (blue “o”) for driven mode c_a as a function of laser detuning at zero temperature. Solid lines are calculated from analytic model (see Eqs. (2.19-2.24)) and points show full numerical calculation. The average photon number is normalized by $n_0 = (\Omega/\kappa)^2$. ($g/\kappa = 20$ and $\gamma/\kappa = 0.2$)

be understood from the level diagram shown in Fig. 2.2, which at finite g shows a splitting of the lowest photonic states into a doublet, $|1_{\pm}\rangle = (|100\rangle \pm |011\rangle)/\sqrt{2}$.

In addition to the transmission, we plot the mean reflected photon number in Fig. 2.5. As discussed below, the reflected photon statistics can also exhibit signatures of nonlinearity. We calculate properties of the reflected light using the annihilation operator $c_R = c_a + i\frac{\Omega}{\kappa}$, obtained from standard input-output relations for a symmetric two-sided cavity (see Appendix A.1). The mean reflected photon number $\bar{n}_R = \langle c_R^\dagger c_R \rangle$ is plotted in Fig. 2.5. At $\Delta/g = \pm\frac{1}{2}$, the average reflection has a minimum where the average transmission has a maximum. Note that in contrast to a single cavity, even on resonance the transmission probability is less than unity and the reflection probability remains finite.

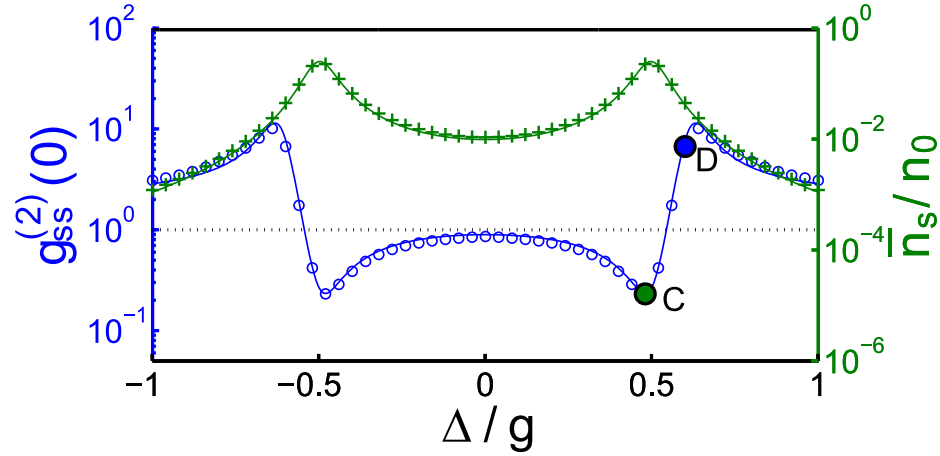


Figure 2.4: Normalized average photon number (green “+”) and photon-photon correlation function (blue “o”) for the undriven mode c_s as a function of laser detuning at zero temperature. Solid lines are calculated from analytic model (see Eqs. (2.19-2.24)) and points show full numerical calculation. The average photon number is normalized by $n_0 = (\Omega/\kappa)^2$. ($g/\kappa = 20$ and $\gamma/\kappa = 0.2$)

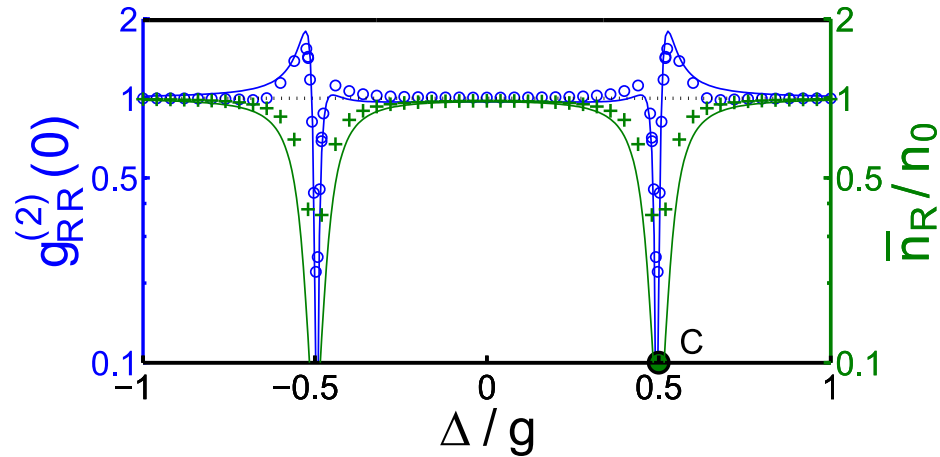


Figure 2.5: Normalized average photon number (green “+”) and photon-photon correlation function (blue “o”) for the reflected field c_R , as a function of laser detuning at zero temperature. Solid lines are calculated from analytic model (see Eqs. (2.19-2.24)) and points show full numerical calculation. The average photon number is normalized by $n_0 = (\Omega/\kappa)^2$. The small discrepancy between the analytic and numerical results is due to the approximation $g/\kappa \gg 1$ to simplify the expressions in Eqs. (2.19-2.24) ($g/\kappa = 20$ and $\gamma/\kappa = 0.2$)

2.3.2 Intensity correlations

To characterize nonclassical photon statistics in the light transmitted through the OMS, we study the equal-time photon-photon correlation functions,

$$g_{ii}^{(2)}(0) = \frac{\langle c_i^\dagger c_i^\dagger c_i c_i \rangle}{\langle c_i^\dagger c_i \rangle^2}, \quad (2.11)$$

where all operators are evaluated at the same time and $i = a, s, R$. A normalized correlation of $g_{ii}^{(2)}(0) < 1$ indicates photon anti-bunching, and the limit $g_{ii}^{(2)}(0) \rightarrow 0$ corresponds to the complete photon blockade regime in which two photons never occupy the cavity at the same time. The solid curves show $g_{aa}^{(2)}(0)$ in Fig. 2.3, $g_{ss}^{(2)}(0)$ in Fig. 2.4 and $g_{RR}^{(2)}(0)$ in Fig. 2.5 as a function of the laser detuning and in the limit of weak driving $\Omega/\kappa \ll 1$. The most pronounced features of these correlation functions occur at $|\Delta|/g = 0, \frac{1}{\sqrt{8}}, \frac{1}{2}$ and $\frac{\sqrt{6}}{4}$, as marked by dots A, B, C and D, respectively. As we explain in detail in the following analysis, we find that the photon bunching at A and anti-bunching at B are the result of destructive quantum interference, while the features at points C and D arise from one- and two-photon resonances.

To gain insight into the two photon correlation functions shown in Fig. 2.3, 2.4 and 2.5, we develop an approximate analytic model for the system by considering only the six levels shown in Fig. 2.2. Assuming that the system is initially prepared in $|000\rangle$, these are the only levels significantly populated by weakly driving the c_a mode. We make the ansatz [39]

$$\begin{aligned} |\psi\rangle = & A_{000}|000\rangle + A_{100}|100\rangle + A_{011}|011\rangle \\ & + A_{200}|200\rangle + A_{111}|111\rangle + A_{022}|022\rangle, \end{aligned} \quad (2.12)$$

and describe the dynamics by evolving $|\psi\rangle$ under the action of the non-Hermitian

Hamiltonian, $\tilde{H} = H - i [\kappa c_a^\dagger c_a + \kappa c_s^\dagger c_s + \frac{\gamma}{2} b^\dagger b]$. This approach allows us to evaluate intensities up to order Ω^2 and two-point correlation up to order Ω^4 , since the neglected quantum jumps lead to higher order corrections. By neglecting the typically small mechanical decay rate $\gamma \ll \kappa$, the amplitudes in Eq. 2.12 then satisfy

$$\dot{A}_{000} = 0, \quad (2.13)$$

$$\dot{A}_{100} = -i\frac{g}{2}A_{011} - i\Omega A_{000} - \tilde{\kappa}A_{100}, \quad (2.14)$$

$$\dot{A}_{011} = -i\frac{g}{2}A_{100} - \tilde{\kappa}A_{011}, \quad (2.15)$$

$$\dot{A}_{200} = -i\frac{g}{\sqrt{2}}A_{111} - i\sqrt{2}\Omega A_{100} - 2\tilde{\kappa}A_{200}, \quad (2.16)$$

$$\dot{A}_{111} = -i\frac{g}{\sqrt{2}}A_{200} - igA_{022} - i\Omega A_{011} - 2\tilde{\kappa}A_{111}, \quad (2.17)$$

$$\dot{A}_{022} = -igA_{111} - 2\tilde{\kappa}A_{022}, \quad (2.18)$$

where $\tilde{\kappa} = \kappa - i\Delta$. It is straightforward to solve Eqs. (2.13–2.18) for the steady state amplitudes (see Appendix A.2). To lowest order in Ω/κ the mean occupation numbers are $\bar{n}_a = |\bar{A}_{100}|^2$, $\bar{n}_s = |\bar{A}_{011}|^2$ and $\bar{n}_R = |\bar{A}_{100} + i\Omega/\kappa|^2$, where \bar{A} denote steady state amplitudes. We obtain

$$\frac{\bar{n}_a}{n_0} = \frac{\kappa^2 [R_\kappa(0)]^{1/2}}{R_\kappa(\frac{g}{2})}, \quad (2.19)$$

$$\frac{\bar{n}_s}{n_0} = \frac{g^2 \kappa^2}{4R_\kappa(\frac{g}{2})}, \quad (2.20)$$

$$\frac{\bar{n}_R}{n_0} \approx \frac{[R_{\kappa/2}(\frac{g}{2})]^2}{[R_\kappa(\frac{g}{2})]^2}, \quad (2.21)$$

where $R_K(\omega) = [K^2 + (\Delta - \omega)^2][K^2 + (\Delta + \omega)^2]$ and $n_0 = (\Omega/\kappa)^2$. From the factors $R_K(\omega)$ in the denominators (numerators) in these expressions, we obtain the positions of the resonances (antiresonances) in the average intracavity photon numbers, in

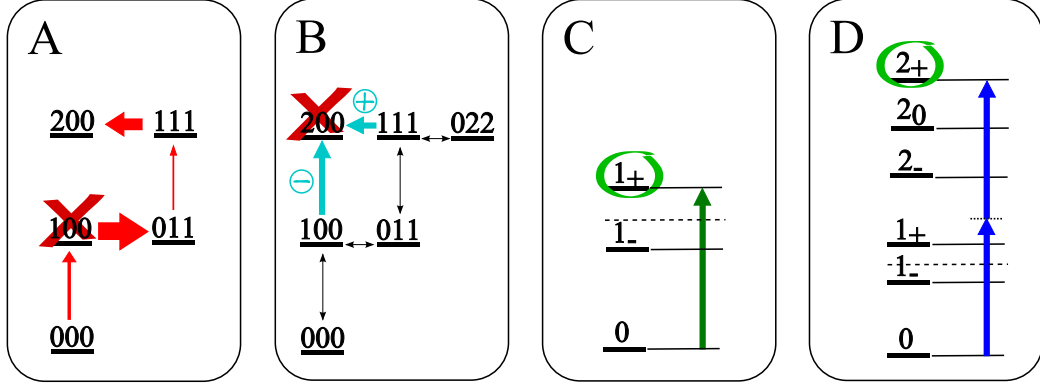


Figure 2.6: Illustration of the origin of the features marked with A,B,C and D on Fig. 2.3, 2.4 and 2.5 as explained in the text. Suppression (enhancement) of the steady state population of a specific level is indicated by a red X (green circle).

excellent agreement with the numerical results shown in Fig. 2.3, 2.4 and 2.5. Our six-level model also provides the equal-time correlations (see Appendix A.2),

$$g_{aa}^{(2)}(0) = \frac{R_\kappa\left(\frac{g}{\sqrt{8}}\right) R_\kappa\left(\frac{g}{2}\right)}{R_\kappa(0) R_\kappa\left(\frac{\sqrt{6}}{4}g\right)}, \quad (2.22)$$

$$g_{ss}^{(2)}(0) = \frac{2R_\kappa\left(\frac{g}{2}\right)}{R_\kappa\left(\frac{\sqrt{6}}{4}g\right)}, \quad (2.23)$$

$$g_{RR}^{(2)}(0) \approx \frac{R_\kappa\left(\frac{g}{2}\right) R_{16\kappa^3/g^2}\left(\frac{g}{2} - \frac{2\kappa^2}{g}\right)}{\left[R_{\kappa/2}\left(\frac{g}{2}\right)\right]^2}. \quad (2.24)$$

Again, these expressions are in agreement with the features seen in the numerical results in Fig. 2.3, 2.4 and 2.5. The positions of maxima and minima are seen directly by the arguments of the factors $R_K(\omega)$. Note that we assumed $g/\kappa \gg 1$ to obtain the simplified expressions in Eqs. (2.22-2.24), but we retained the shift of order $g(\kappa/g)^2$ in the argument in Eq. 2.24 because this shift is larger than the width of the antiresonance.

We now discuss each feature in Fig. 2.3, 2.4 and 2.5 in terms of our six-level model together with the diagonal basis in Eqs. (2.4-2.7). First, at detuning $\Delta = 0$ (point

A in Fig. 2.3) we see $g_{aa}^{(2)}(0) > 1$, indicating bunching. This is due to destructive interference that suppresses the population in $|100\rangle$ (panel A in Fig. 2.6), and can be understood as the system being driven into a dark state, $|d\rangle \propto g|000\rangle - \Omega|011\rangle$, similar to electromagnetically induced transparency (EIT) [134, 234]. In the dark state, $|011\rangle$ remains populated, allowing transitions to $|111\rangle$ which in turn is strongly coupled to $|200\rangle$. The net result is a relative suppression of the probability to have one photon compared to two photons in the driven mode, leading to bunching at $\Delta = 0$. Second, at detuning $\Delta = g/\sqrt{8}$ (point B), mode c_a shows anti-bunching due to a suppressed two-photon probability. Again, this is due to destructive interference, or the presence of a dark state in which $|200\rangle$ remains unpopulated (panel B). Third, at detuning $\Delta = \frac{g}{2}$ (point C), all modes show anti-bunching. This is due to a one-photon resonant transition $|0\rangle \rightarrow |1_+\rangle$ (panel C). Finally, at detuning $\Delta = \frac{\sqrt{6}}{4}g$ (point D), both c_a and c_s show bunching due to a two-photon resonant transition $|0\rangle \rightarrow |2_+\rangle$ (panel D).

2.3.3 Absence of two-photon resonance at $\Delta = 0$

At first glance, the level diagram in Fig. 2.2 together with bunching in Fig. 2.3 suggest a two-photon resonance at zero detuning $\Delta = 0$, where the energy of the eigenstate $|2_0\rangle$ is equal to the energy of two drive photons. However, as discussed above, the bunching at $\Delta = 0$ arises entirely from the suppression of a one-photon population; further, we find that the expected two-photon resonance is cancelled by interference. This can be seen from a second order perturbative calculation of the two-photon Rabi frequency $\Omega_{0,2_0}^{(2)}$ for the transition $|0\rangle \rightarrow |2_0\rangle$. The two-photon state

$|2_0\rangle$ can be populated by the drive $H_{\text{dr}} = \Omega(c_a^\dagger + c_a)$ from state $|0\rangle$ via two intermediate one-photon eigenstates, $|1_\pm\rangle$ given by Eq. 2.5, with energies $\omega_{1\pm} = -\Delta \pm \frac{g}{2}$ in the rotating frame. The resulting Rabi frequency is

$$\Omega_{0,20}^{(2)} = \sum_{n=1_-,1_+} \frac{\langle 2_0 | H_{\text{dr}} | n \rangle \langle n | H_{\text{dr}} | 0 \rangle}{\omega_n}, \quad (2.25)$$

which vanishes at $\Delta = 0$ as a consequence of destructive interference between the two amplitudes. The exact cancellation is lifted by including finite dissipation and the full spectrum; nonetheless this simple argument shows that the expected two-photon resonance at $\Delta = 0$ is strongly suppressed.

Further evidence of the absence of a two-photon resonance at $\Delta = 0$ is the lack of bunching in the undriven mode in Fig. 2.4. If there were a two-photon resonance, one would expect that bunching should also occur in the undriven mode, since the state $|2_0\rangle$ involves both c_a and c_s modes. This is indeed the case at detuning $\Delta = \frac{\sqrt{6}}{4}g$ (see point D in Fig. 2.4), where both modes show bunching as a result of two-photon resonance. In contrast, we see no bunching in the undriven mode at $\Delta = 0$. This supports our conclusion that the observed bunching at $\Delta = 0$ arises from suppression of population in $|100\rangle$ due to interference, as discussed in Section 2.3.2, and not from two-photon resonance. As discussed above, this interference does not suppress population in $|011\rangle$, so we do not expect bunching in the c_s mode from this effect.

Finally, to confirm our intuitive picture we plot the intensity correlation function, $g_{\text{tot}}^{(2)}(0) = \langle n_{\text{tot}}(n_{\text{tot}} - 1) \rangle / \langle n_{\text{tot}} \rangle^2$, of the total photon number, $n_{\text{tot}} = n_a + n_s$, in the coupled OM system in Fig. 2.7. The probability to find one photon in the combined cavity is maximal at $\Delta/g = \pm \frac{1}{2}$ due to one-photon resonance. Similarly, we observe antibunching at point C and bunching at point D, due to interference and two-photon

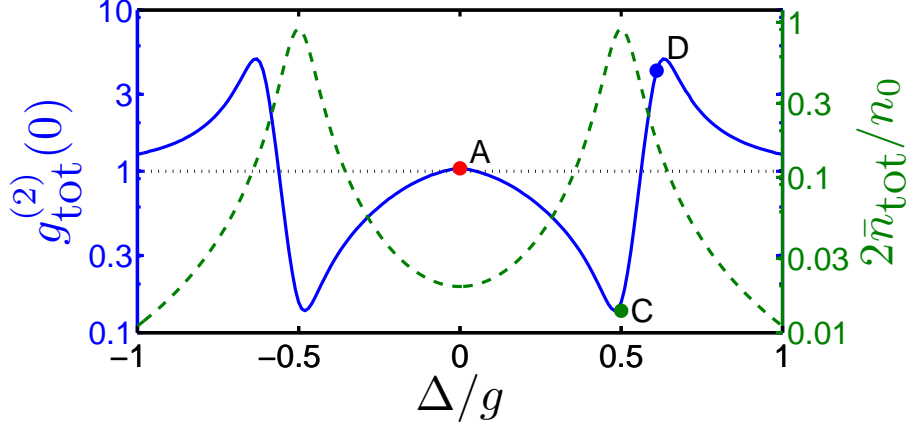


Figure 2.7: Average number (green dashed) and intensity correlation (blue solid) of total photon number in the coupled OM system. Parameters are the same as in Fig. 2.3, and dots mark the same detunings. One- and two-photon resonances are seen at C and D, but we see no bunching in the total photon number at $\Delta = 0$ (point A). This reflects the lack of two-photon resonance due to destructive interference (see Eq. 2.25).

resonance respectively, as discussed in Section 2.3.2. However, we find neither bunching nor antibunching at $\Delta = 0$, demonstrating the absence of a two-photon resonance despite the fact that $|2_0\rangle$ lies at twice the drive frequency.

2.3.4 Finite temperature

So far in our analysis we have focused on the case where the mechanical system is prepared in its vibrational ground state, $|0_m\rangle$. This condition can be achieved using high frequency resonators operated at cryogenic temperatures [162], and in the limit of weak driving $\Omega/\kappa \ll 1$ such that optical heating of the mechanical mode can be neglected. The mechanical ground state could also be prepared using OM cooling [149, 92, 9, 119, 56, 198, 219, 235, 162, 217, 42], using an optical mode far-detuned from the ones we consider here for nonlinear interactions [211]. Nonetheless, in the

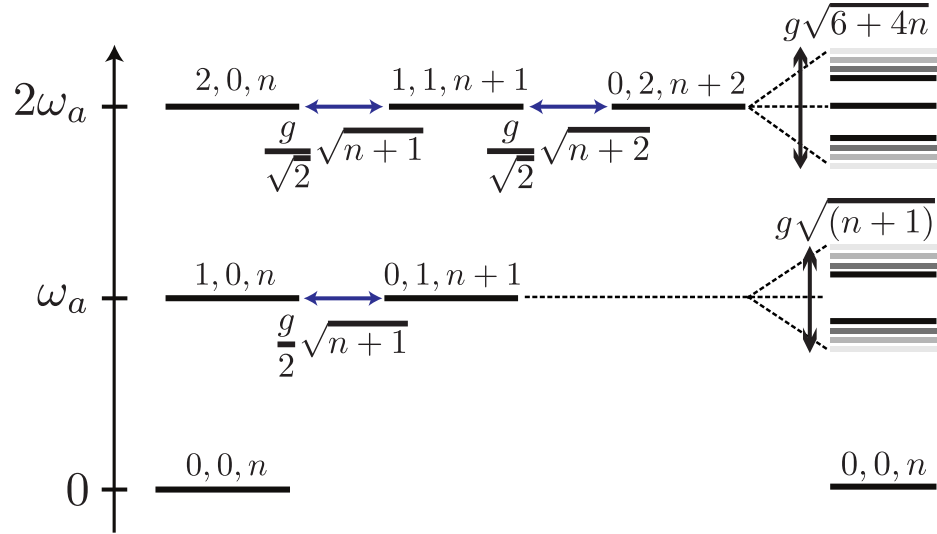


Figure 2.8: Level diagram showing the six states populated by the drive from level $|0,0,n\rangle$ (left), and the associated eigenmodes (right) with n -dependent splittings.

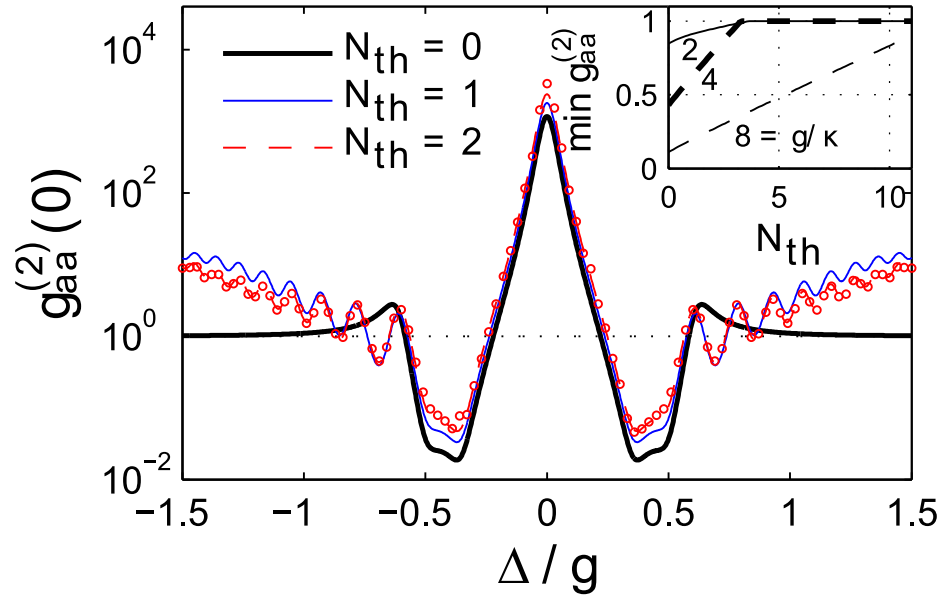


Figure 2.9: Driven mode correlation function $g_{aa}^{(2)}(0)$ for thermal mechanical occupation $N_{th} = 0, 1, 2$. Solid lines show the analytic calculation with $\gamma \rightarrow 0$, and dots show the full numerical results for $N_{th} = 2$ only. The inset shows the minimal $g_{aa}^{(2)}(0)$ as a function of N_{th} for several coupling strengths. Parameters are $g/\kappa = 20$, and (for numerics) $\gamma/\kappa = 10^{-3}$.

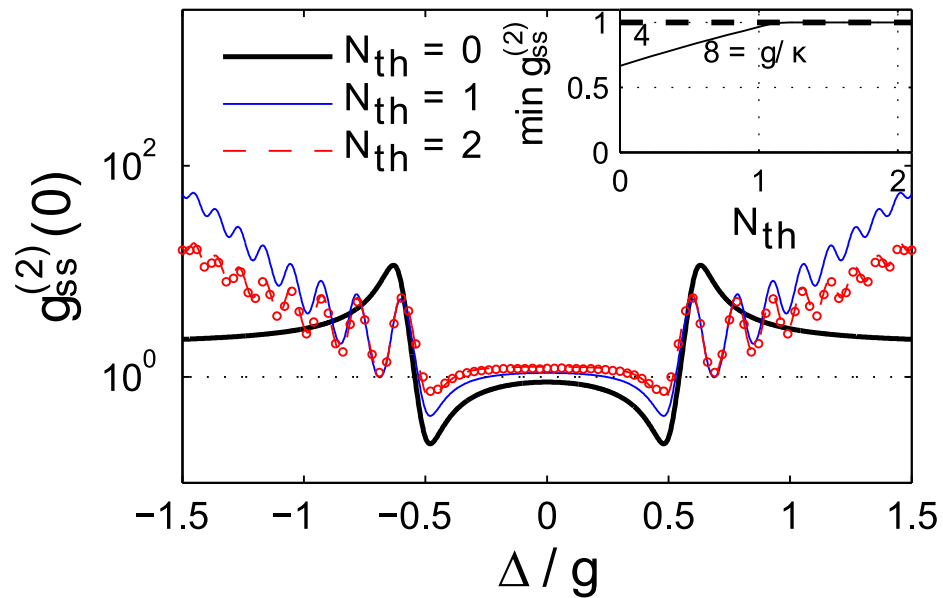


Figure 2.10: Undriven mode correlation function $g_{ss}^{(2)}(0)$ for thermal mechanical occupation $N_{th} = 0, 1, 2$. Solid lines show the analytic calculation with $\gamma \rightarrow 0$, and dots show the full numerical results for $N_{th} = 2$ only. The inset shows the minimal $g_{ss}^{(2)}(0)$ as a function of N_{th} for several coupling strengths. Parameters are $g/\kappa = 20$, and (for numerics) $\gamma/\kappa = 10^{-3}$.

following we extend our analytic treatment to the case of finite temperature, and show that many of the nonclassical features are robust even in the presence of small but finite thermal occupation of the mechanical mode.

To generalize our previous results we now consider a finite equilibrium occupation number $N_{\text{th}} > 0$ of the mechanical mode, but still assume that $\gamma(N_{\text{th}} + 1) \ll \kappa, g$. Within this approximation we proceed as above, and make a similar six-level ansatz as in Eq. (2.12) for each phonon number n ,

$$\begin{aligned} |\psi_n\rangle = & A_{0,0,n}|0,0,n\rangle + A_{1,0,n}|1,0,n\rangle \\ & + A_{0,1,n+1}|0,1,n+1\rangle + A_{2,0,n}|2,0,n\rangle \\ & + A_{1,1,n+1}|1,1,n+1\rangle + A_{0,2,n+2}|0,2,n+2\rangle, \end{aligned} \quad (2.26)$$

where $|\psi_n\rangle$ includes states up to two photons that are connected by the weak drive and coupling g , starting from the state $|00n\rangle$. As shown in Fig. 2.8 the coupling between the states within each six-level subspace depends explicitly on the phonon number n . Following the same approach as above, the amplitudes in Eq. (2.26) evolve according to

$$\dot{A}_{0,0,n} = 0, \quad (2.27)$$

$$\dot{A}_{1,0,n} = -i\frac{g}{2}\sqrt{n+1}A_{0,1,n+1} - i\Omega A_{0,0,n} - \tilde{\kappa}A_{1,0,n}, \quad (2.28)$$

$$\dot{A}_{0,1,n+1} = -i\frac{g}{2}\sqrt{n+1}A_{1,0,n} - \tilde{\kappa}A_{0,1,n+1}, \quad (2.29)$$

$$\dot{A}_{2,0,0} = -ig\sqrt{\frac{n+1}{2}}A_{1,1,n+1} - i\sqrt{2}\Omega A_{1,0,n} - 2\tilde{\kappa}A_{2,0,n}, \quad (2.30)$$

$$\dot{A}_{1,1,n+1} = -ig\sqrt{\frac{n+1}{2}}A_{2,0,n} - ig\sqrt{\frac{n+2}{2}}A_{0,2,n+2} - i\Omega A_{0,1,n+1} - 2\tilde{\kappa}A_{1,1,n+1}, \quad (2.31)$$

$$\dot{A}_{0,2,n+2} = -ig\sqrt{\frac{n+2}{2}}A_{1,1,n+1} - 2\tilde{\kappa}A_{0,2,n+2}. \quad (2.32)$$

We solve for the steady state amplitudes within each subspace n and average the result over the initial thermal phonon distribution, assuming no coupling between subspaces due to the small phonon relaxation rate. We obtain the average photon numbers

$$\bar{n}_a = \sum_n \zeta_n |\bar{A}_{1,0,n}|^2, \quad \bar{n}_s = \sum_n \zeta_n |\bar{A}_{0,1,n+1}|^2, \quad (2.33)$$

where $\zeta_n = e^{-\beta \hbar \omega_m n} (1 - e^{-\beta \hbar \omega_m})$ and $\beta^{-1} = k_B T$. Similarly, the $g_{ii}^{(2)}(0)$ functions are given by

$$g_{aa}^{(2)}(0) = 2 \sum_n \zeta_n |\bar{A}_{2,0,n}|^2 / \bar{n}_a^2, \quad (2.34)$$

$$g_{ss}^{(2)}(0) = 2 \sum_n \zeta_n |\bar{A}_{0,2,n+2}|^2 / \bar{n}_s^2. \quad (2.35)$$

We provide the expressions for the steady state amplitudes $\bar{A}_{2,0,n}$ and $\bar{A}_{0,2,n+2}$ in the Appendix A.2.

We plot the correlation functions, $g_{aa}^{(2)}(0)$ in Fig. 2.9 and $g_{ss}^{(2)}(0)$ in Fig. 2.10 for different thermal phonon numbers, N_{th} . Solid lines were calculated from the above analytic approach with $\gamma \rightarrow 0$, and we find excellent agreement with the full numerical results including small but finite γ (dots, shown only for thermal occupation $N_{\text{th}} = 2$). We see that the zero temperature features such as antibunching survive at finite temperature for sufficiently strong coupling [211]. In the insets we plot the minimum antibunching as a function of thermal occupation number for several ratios g/κ . Antibunching remains visible up to a critical thermal phonon number, set by g/κ , beyond which the contributions from different phonon numbers smear out the effect and antibunching vanishes. In addition, for detunings $|\Delta| > g/2$, a series of

new resonances appear in the correlation functions, and for small but finite occupation numbers we find new antibunching features that are absent for $N_{\text{th}} = 0$. These new features can be understood from the n -dependent splitting of the one- and two-photon manifolds as indicated in Fig. 2.8. For higher temperatures the individual resonances start to overlap, and we observe an overall increase over a broad region of large positive and negative detunings due to the cumulative effect of different phonon numbers.

2.4 Delayed coincidence and single phonon states

In addition to the equal-time correlations discussed above, quantum signatures can also be manifested in photon intensity correlations with a finite time delay. We now turn to a discussion of delayed coincidence characterized by the two-time intensity correlations functions,

$$g_{ii}^{(2)}(\tau) = \frac{\langle c_i^\dagger(0)c_i^\dagger(\tau)c_i(\tau)c_i(0) \rangle}{\langle c_i^\dagger c_i \rangle^2}, \quad (2.36)$$

for both driven and undriven modes, $i = a, s$. Expressing this correlation in terms of a classical light intensity I , $g^{(2)}(\tau) = \langle I(\tau)I(0) \rangle / \langle I \rangle^2$, and using the Schwarz inequality, we obtain the inequalities [39, 31],

$$g^{(2)}(\tau) \leq g^{(2)}(0), \quad (2.37)$$

$$|g^{(2)}(\tau) - 1| \leq |g^{(2)}(0) - 1|. \quad (2.38)$$

Similar to the classical inequality $g^{(2)}(0) > 1$ at zero delay, violation of either of these inequalities at finite delay is a signature of quantum light. We calculate the delayed

coincidence correlation functions for both the driven and undriven modes.

2.4.1 Driven mode

The correlation function $g_{aa}^{(2)}(\tau)$ is shown in Fig. 2.11(a) for two values of the detuning Δ . The most striking feature is the apparent vanishing of $g_{aa}^{(2)}(\tau)$ at several values of τ when the detuning is $\Delta = 0$ (curve A in Fig. 2.11(a)). These are due to Rabi oscillations at frequency $g/2$ following the detection of a photon. This vanishing of the finite delay correlation function is reminiscent of wavefunction collapse that occurs in a cavity containing an atomic ensemble [39], and while its origins are similar, there are important differences as we now discuss.

We can understand the finite delay intensity correlations in terms of the simple six-level model discussed in the previous section. We extend this model to describe finite delay correlations by considering the effect of photodetection on the steady state of the system. Detection of a photon in the driven mode projects the system onto the conditional state [89],

$$|\psi^a\rangle = \frac{c_a|\psi\rangle}{\|c_a|\psi\rangle\|}, \quad (2.39)$$

where $|\psi\rangle$ is given by Eq. 2.12 with steady state amplitudes and $\|\cdot\|$ denotes normalization after the jump. The conditional state $|\psi^a\rangle$ has an *increased* amplitude A_{100} after the jump (see jump at $\tau = 0$ in Fig. 2.11 (b)). Following this initial photodetection, the amplitude A_{100} subsequently undergoes Rabi oscillations with frequency $g/2$, and decays back to its steady state at rate 2κ . For sufficiently large bunching at zero delay and strong coupling $g > \kappa$, the Rabi oscillations of the amplitude $A_{100}(\tau)$ can cause it to cross zero several times before it decays back to steady state. As the

probability to detect a second photon is dominated by A_{100} , its zeros are responsible for the zeros in the correlation function $g_{aa}^{(2)}(\tau)$ zero at these delay times.

The zeros in $g^{(2)}(\tau)$ appear similar to those exhibited in a cavity strongly coupled to an atomic ensemble [39, 179, 31] or a single atom [45]. However, in stark contrast to the atomic case, the zeros in Fig. 2.11(a) are the result of Rabi oscillations following the initial quantum jump. This is qualitatively different from the atomic case, where the change in sign of the relevant amplitude (the analogy of A_{100}) occurs *immediately* after the jump itself, and the amplitude is damped back to steady state at the atomic decay rate Γ , without Rabi oscillation. As a consequence, the vanishing correlation function in the atomic case occurs at a delay set by $\tau_0 \sim \gamma^{-1} \ln C$, requiring only strong cooperativity $C = g^2/\kappa\gamma > 1$ to be visible. On the other hand, the zeros in Fig. 2.11(a) occur at delay times set by $\tau \sim 1/g$, requiring strictly strong coupling $g > \kappa$.

Before moving on to correlations of the undriven mode, we briefly discuss the correlations of the driven mode at the other value of detuning shown in Fig. 2.11(a). At detuning $\Delta = \frac{g}{\sqrt{2}}$ (curve E), which shows bunching at zero time, $g_{aa}^{(2)}(0) \gtrsim 1$, increases above its initial value at finite delay. This is a violation of the classical inequality in Eq. 2.37, and is an example of “delayed bunching,” or an increased probability to detect a second photon at a finite delay time. A similar effect was recently studied in a single mode OMS [122]. However, like the Rabi oscillations, the increased correlation function decays back to its steady state value of 1 on the timescale of κ^{-1} .

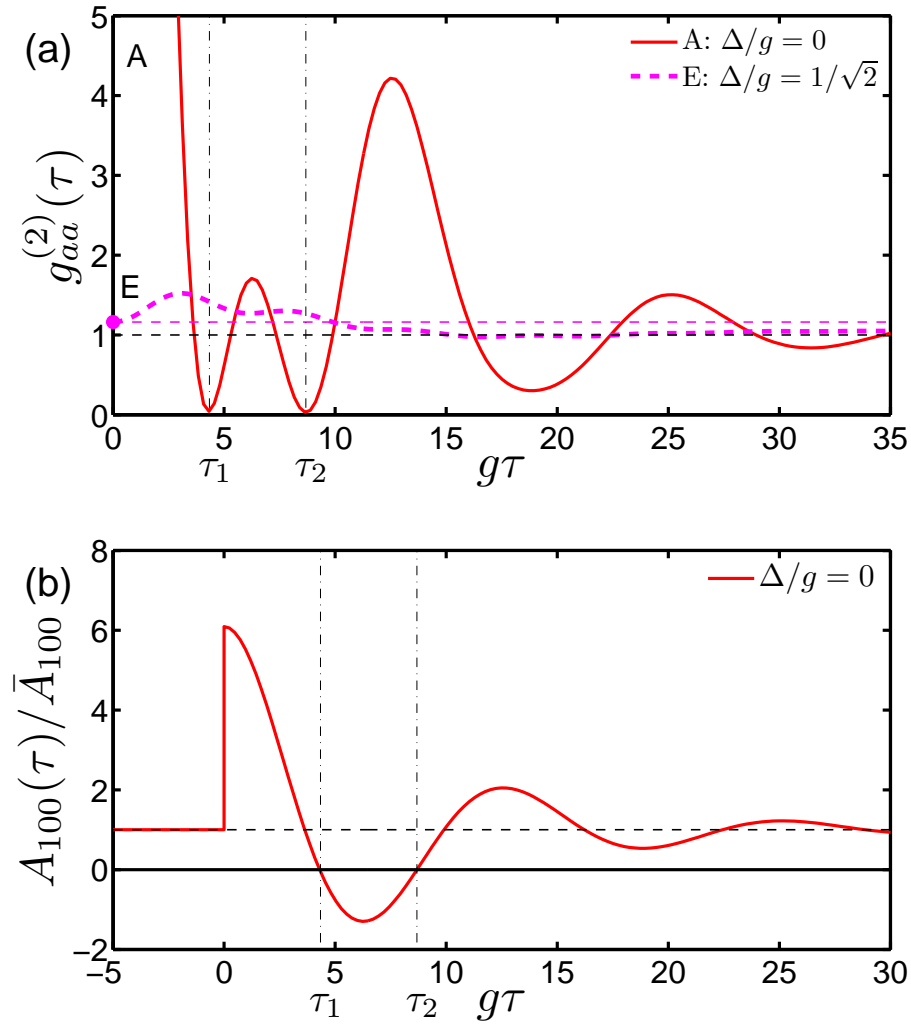


Figure 2.11: (a) Finite time delay intensity correlation function $g_{aa}^{(2)}(\tau)$ for detunings $\Delta/g = 0$ (A) and $\frac{1}{\sqrt{2}}$ (E). Detuning for curve A is the same as marked in Fig. 2.3, while E shows a new effect not seen at equal times. Thin dashed line indicates the classical bound (see Eq. 2.37) for curve E. (b) Evolution of amplitude A_{100} (normalized by its steady state value) at detuning A, $\Delta/g = 0$, after detecting a driven c_a photon at $\tau = 0$. Vertical dash-dotted lines mark delay times (τ_1, τ_2) where this amplitude vanishes resulting in the vanishing of $g_{aa}^{(2)}(\tau)$ in (a). Parameters are $g/\kappa = 8$ and $\gamma/\kappa = 0.02$.

2.4.2 Heralded single phonon states

We now turn to a discussion of the delayed coincidence correlations of the undriven mode c_s . We note that correlations of the driven and undriven modes can be measured separately provided sufficient frequency resolution, smaller than the mechanical frequency. The correlation function $g_{ss}^{(2)}(\tau)$ of the undriven mode is shown in Fig. 2.12 for several values of detuning. Similar to the driven mode, the correlation function of the undriven mode exhibits Rabi oscillations that decay on the short optical timescale $1/\kappa$. For detuning $\Delta = 0$ and $\Delta/g = \frac{\sqrt{6}}{4}$ (curves A and D in Fig. 2.12), the correlation $g_{ss}^{(2)}(\tau)$ is described by our previous six-level model of Eqs. (2.13–2.18). However, at detuning $\Delta = \frac{g}{\sqrt{2}}$ (curve E), we see that $g_{ss}^{(2)}(\tau)$ has a long tail that decays on the much longer mechanical timescale $1/\gamma$. This is due to the heralded preparation of a single phonon by detection of a photon in the undriven mode, as we now discuss.

The increase in delayed coincidence can be understood by extending the above analytic six-level model to account for the conditional state of the system after detection of a photon in the undriven mode. To do this, we simply add three additional states to the six-level ansatz in Eq. 2.12,

$$|\psi\rangle = \dots + A_{001}|001\rangle + A_{101}|101\rangle + A_{012}|012\rangle, \quad (2.40)$$

since these are the states populated by detection of a c_s photon from the original six states (see Fig. 2.13). Using the same approach as before, we obtain the following

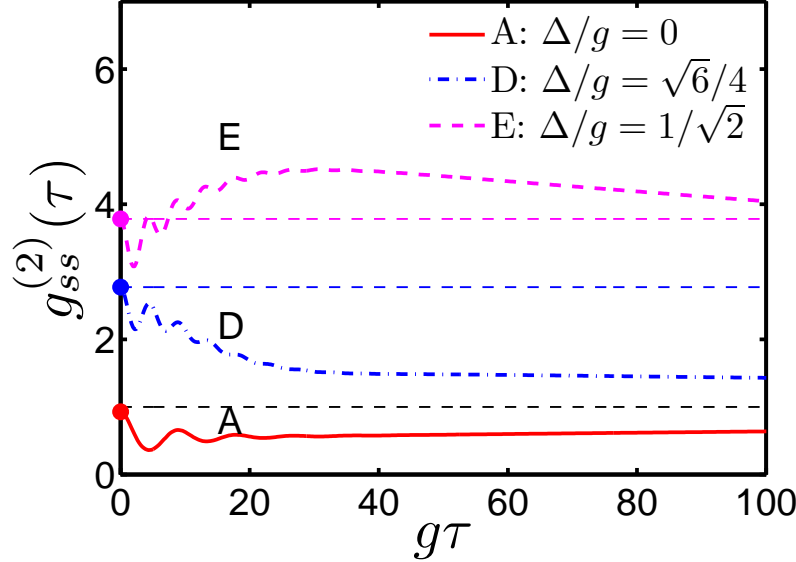


Figure 2.12: Finite time delay intensity correlation function $g_{ss}^{(2)}(\tau)$ for detunings $\Delta/g = 0$ (A), $\sqrt{6}/4$ (D) and $1/\sqrt{2}$ (E). Thin dashed lines indicate the classical bounds (see Eq. 2.37). Labels A, D, E correspond to the same detunings marked in Fig. 2.3 and Fig. 2.11. Parameters are $g/\kappa = 8$, and $\gamma/\kappa = 0.02$.

equations for the amplitudes,

$$\dot{A}_{001} \approx -\frac{\gamma}{2}A_{001}, \quad (2.41)$$

$$\dot{A}_{101} = -i\frac{g}{\sqrt{2}}A_{012} - i\Omega A_{001} - \tilde{\kappa}A_{101}, \quad (2.42)$$

$$\dot{A}_{012} = -i\frac{g}{\sqrt{2}}A_{101} - \tilde{\kappa}A_{012}, \quad (2.43)$$

where we used $\gamma \ll \kappa$ and kept the leading term in Eq. 2.41. We obtain $g_{ss}^{(2)}(\tau)$ by solving these equations for initial conditions determined by the conditional state $|\psi^s\rangle$ after a quantum jump,

$$|\psi^s\rangle = \frac{c_s|\psi\rangle}{||c_s|\psi\rangle||}, \quad (2.44)$$

which is a superposition of states $|001\rangle, |101\rangle, |012\rangle$ (see Appendix A.2 for details),

but in the limit of weak driving consist mainly of $|001\rangle$.

Detection of a photon in the undriven mode implies that the three-wave mixing interaction converted a photon from the driven mode into the undriven mode by simultaneously adding a phonon. The relevant three-level subspace after the jump (see Fig. 2.13) has a similar structure as in the steady state, but the presence of an extra phonon modifies the splitting of the one-photon states $|1'_{\pm}\rangle = (|101\rangle \pm |012\rangle)/\sqrt{2}$ to $\frac{g}{\sqrt{2}}$ (instead of $g/2$ without a phonon). This changes the one-photon resonance

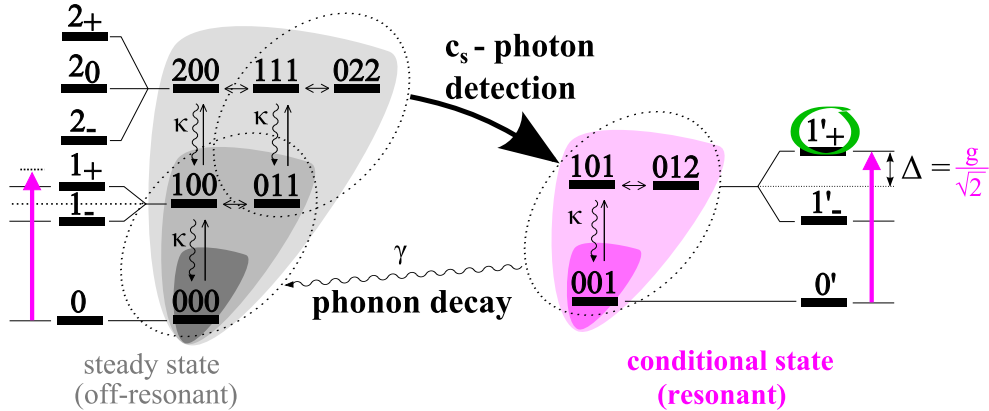


Figure 2.13: Effect of detection of a c_s photon at detuning $\Delta/g = \frac{1}{\sqrt{2}}$. In steady state (gray region on left), the drive is far off-resonant. However, after detection of a c_s photon the system jumps into the conditional subspace (pink region on right). Due to the presence of an extra phonon in this subspace, the drive is resonant and the probability to detect a second photon is much higher than in steady state. This increased probability persists as long as the extra phonon, which decays slowly at rate γ .

condition for the drive to $\Delta = \frac{g}{\sqrt{2}}$. Therefore, at this value of the detuning, the process of exciting the system and emitting a single c_s photon is off-resonant; while after the detection of a first c_s photon the system is prepared in $|001\rangle$, bringing it into resonance with the drive. This *enhances* the probability for subsequent excitation and emission of a second c_s photon, increasing the correlation function at finite delay.

The maximum delayed coincidence occurs after a delay of $\tau \sim 1/\kappa$, when the photons have reached the metastable steady state in the conditional subspace with one extra phonon. Eventually, the delayed coincidence returns to its true steady state value of one on the timescale $\tau \sim 1/\gamma$, which is the mechanical decay time of the state $|001\rangle$. The long tails observed for other values of detuning (curves A and D) are also due to the presence of an extra phonon, but in these cases the system remains off-resonant after the initial c_s photon and the effect is less pronounced. Note that the probability to detect a photon from the *driven* mode also increases in the conditional state, so a similar effect is seen in the delayed cross-correlation function $g_{as}^{(2)}(\tau)$, where the photon in the undriven mode is detected first.

2.5 Reaching strong coupling

The nonclassical correlations predicted in this chapter require strong optomechanical coupling, $g > \kappa$, as well as sideband resolution, $\omega_m \gg \kappa, \gamma$. While the combination of these conditions has not yet been demonstrated, several experimental efforts are currently directed at reaching this regime. By using micro- and nano-fabricated OMSs such as microtoroids or photonic crystal beams, high frequency mechanical systems with $\omega_m \approx 50$ MHz - 5 GHz can be combined with low loss optical modes, such that the condition $\omega_m \gg \kappa \gg \gamma$ is satisfied [188, 198, 79]. At the same time the mechanical system can already be prepared close to the quantum ground state by working at cryogenic temperatures. In micro-fabricated OMSs, single-photon couplings of about $g/\kappa \approx 0.001$ have been demonstrated [79, 63, 230] The largest value to date of $g/\kappa \approx 0.007$ has been reached in photonic crystal beam resonators [43],

where colocalized optical and vibrational resonances are highly confined to maximize coupling while the surrounding structure is engineered to minimize loss. Conversely, in cold atomic experiments the effective strong OM coupling regime has been reached [170], while sideband resolution remains a challenge [210].

There are several existing proposals for how to meet the challenge of $g/\kappa > 1$ in the photonic crystal beam setup. First, the single-photon optomechanical coupling can be increased by making use of nanoslots in the structure [182, 58] to further localize the electric field at the position of the mechanical mode. This could improve g by a factor of 10 [133]. Second, numerical studies suggest that κ can be further decreased by fine tuning the size and position of the slots in the photonic crystals [160, 213]. Finally, new materials are currently being tested for an overall improvement of the OM properties of nano-fabricated devices [239]. Thus by using these ultrahigh Q photonic crystals or similar designs, an increase of g/κ by a factor of ~ 100 is realistic. Note that once the strong coupling condition has been achieved, the implementation of two or multimode OMSs with adjustable tunneling $2J \sim \omega_m$ can be realized via evanescent field coupling, as has already been demonstrated in the weak coupling regime [188, 79, 100].

2.6 Conclusions

We have studied nonclassical intensity correlations in a driven, near-resonant optomechanical system with one mechanical and two optical modes. In the regime of strong coupling $g > \kappa$, this system allows for nonlinear quantum optics through a resonant three-mode interaction in which the exchange of two photons is mediated by

a phonon. We have identified several different processes that can lead to nonclassical antibunching and delayed bunching, and we have derived a simple analytic model that allows us to describe and interpret photon-photon correlations in this system both at zero and at finite temperature. Our findings will be important as experiments approach the regime of strong OM coupling, and for potential applications of OMSs for quantum information processing. In particular, the long-lived correlation found for the undriven mode raises the intriguing possibility to exploit such a setup as a quantum memory. The generation of heralded single phonons on detection of a photon from the undriven mode may have implications for building OM quantum repeaters and quantum communication devices.

Chapter 3

Optomechanical quantum information processing

3.1 Introduction

Optomechanics describes the radiation pressure interaction between an optical cavity mode and the motion of a macroscopic mechanical object, as it appears, for example, in a Fabry-Pérot cavity with a moveable mirror [118, 142, 11]. First demonstrations of optomechanical (OM) laser cooling [149, 92, 9, 119, 56, 219, 198, 235] have recently attracted significant interest and led to tremendous progress in the development of new fabrication methods and experimental techniques for controlling OM interactions at the quantum level. Apart from ground-state cooling [217, 42], this includes the demonstration of slow light [234, 187], and the coherent interconversion of optical and mechanical excitations [86, 230]. These achievements pave the way for a new type of quantum light-matter interface and give rise to interesting perspec-

tives for novel OM-based quantum technologies. As a solid-state approach, such an all-OM platform would benefit directly from advanced nanofabrication and scalable integrated photonic circuit techniques. At the same time, long mechanical lifetimes comparable to those of atomic systems allow us to combine optical nonlinearities with a stationary quantum memory for light.

In this work we study strong OM coupling effects in *multimode* OM systems (OMSs) and describe how resonant or near-resonant interactions in this setting allow us to exploit the intrinsic nonlinearity of radiation pressure in an optimal way. Our approach is based on the resonant exchange of photons between two optical modes mediated by a single phonon. This resonance induces much stronger nonlinearities than achievable in single-mode OMSs, where nonlinear effects are suppressed by a large mechanical frequency [143, 132, 171, 161]. Consequently, multimode OMSs provide a promising route for accessing the single-photon strong-coupling regime, where the coupling g_0 as well as the mechanical frequency ω_m exceeds the cavity decay rate κ [171]. This regime is within reach of state-of-the-art nanoscale OM devices [42, 79, 40, 63] or analogous cold atom OMSs [101, 32], and here we discuss how strong OM interactions in a multimode setup can be used to generate single photons and to perform controlled gate operations between photonic or mechanical qubits. Combined with very recently developed photon-phonon interfaces and quantum memories based on linearized OM couplings [86, 230, 188], our results provide a basis for efficient OM classical and quantum information processing with applications ranging from photon transistors to quantum repeaters and networks.

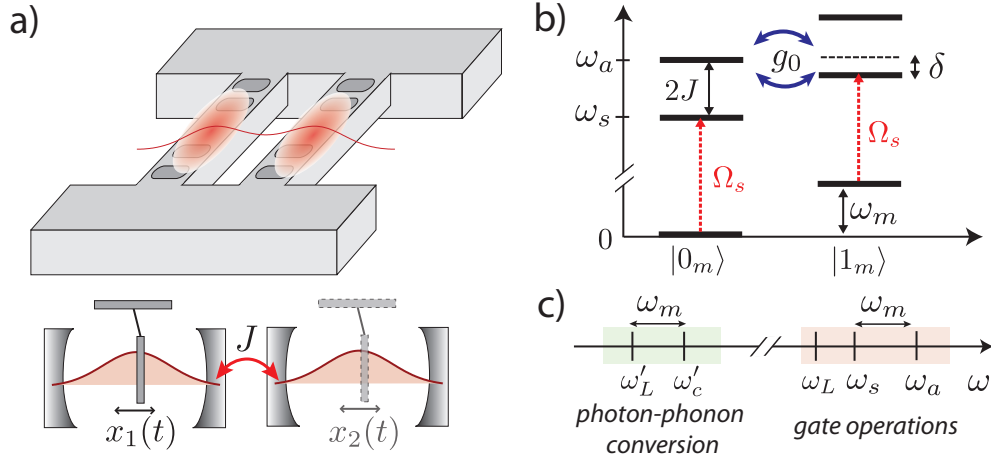


Figure 3.1: a) Setup of two tunnel-coupled OM crystal cavities (see Ref. [79, 42] for more details). b) Level diagram showing the lowest mechanical and optical excitations in a two mode OMS. Resonant coupling ($\delta = 0$) occurs when the tunnel splitting $2J$ between the optical modes is comparable to the mechanical frequency ω_m . c) Different sets of strongly and weakly coupled optical modes and control laser fields can be used for nonlinear interactions ($\omega_s, \omega_a, \omega_L$) and purely linear photon storage and retrieval operations (ω'_c, ω'_L).

3.2 Model

We consider a setup of two tunnel-coupled OMSs [151, 100, 65, 188, 47] as schematically shown in Fig. 3.1, focusing on the OM crystal design [79, 42] as a specific example. Each OMS $i = 1, 2$ is represented by an optical mode of frequency ω_c and a bosonic operator c_i , which is coupled via optical gradient forces to the motion of an isolated mechanical mode b_i with vibrational frequency ω_m^i . The Hamiltonian for this system is ($\hbar = 1$)

$$H = \sum_{i=1,2} \omega_m^i b_i^\dagger b_i + \omega_c c_i^\dagger c_i + g_0 c_i^\dagger c_i (b_i + b_i^\dagger) - J(c_1^\dagger c_2 + c_1 c_2^\dagger) + \sum_{i=1,2} \Omega_i (c_i e^{i\omega_L t} + \text{H.c.}), \quad (3.1)$$

where J is the tunneling amplitude between the optical modes and g_0 denotes the single-photon OM coupling; Ω_i are the local amplitudes of external control laser fields of frequency ω_L . Below we also consider an additional set of cavity modes and driving fields with frequencies ω'_c and ω'_L , respectively. As indicated in Fig. 3.1(c), we assume these modes to be separated in frequency and used for cooling the mechanical modes [236, 141], and linear photon storage and retrieval operations [86, 230, 242, 2] only.

Apart from the coherent dynamics described by Eq. (3.1), we include dissipation through cavity decay and mechanical damping and model the evolution of the system density operator ρ by a master equation (ME)

$$\dot{\rho} = -i[H, \rho] + \sum_i \kappa \mathcal{D}[c_i]\rho + \mathcal{L}_\gamma\rho, \quad (3.2)$$

where $\mathcal{D}[c]\rho = 2c\rho c^\dagger - \{c^\dagger c, \rho\}_+$, and $\mathcal{L}_\gamma = \sum_i \frac{\gamma}{2}(N_{\text{th}} + 1)\mathcal{D}[b_i] + \frac{\gamma}{2}N_{\text{th}}\mathcal{D}[b_i^\dagger]$. Here, κ is the optical field decay rate, $\gamma = \omega_m/Q$ the mechanical damping rate for a quality factor Q and $N_{\text{th}} = (e^{\hbar\omega_m/k_B T} - 1)^{-1}$ the mechanical equilibrium occupation number for temperature T . Below we identify $\Gamma_m = \frac{\gamma}{2}(3N_{\text{th}} + \frac{1}{2})$ as the characteristic decoherence rate for mechanical qubit states¹.

3.3 Resonant strong-coupling optomechanics

We focus on the strong coupling regime $\omega_m, g_0 \gg \kappa, \Gamma_m$, and our main goal is to show how the multimode OMS described by Eq. (3.1) can be used for implementing controlled interactions between qubits encoded in photonic or phononic de-

¹ Γ_m corresponds to the initial decoherence rate of a phonon superposition $(|0_m\rangle + |1_m\rangle)/\sqrt{2}$.

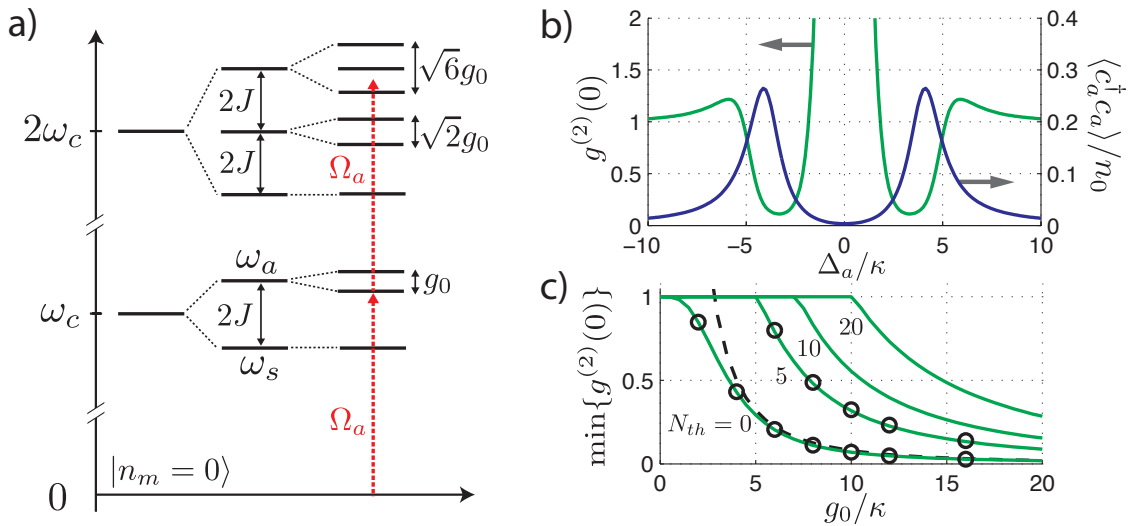


Figure 3.2: a) Energy level diagram of a resonantly coupled OMS, $\delta = 2J - \omega_m = 0$, and for a single mechanical mode in the ground state. b) Excitation spectrum and $g^{(2)}(0)$ for a weak coherent field exciting the c_a mode, where $g_0/\kappa = 8$ and $n_0 = \Omega_a^2/\kappa^2$. c) Minimal value of $g^{(2)}(0)$ as a function of the OM coupling strength g_0 and for different values of N_{th} . The analytical results (solid lines) given in the text are in good agreement with exact numerics (circles). The dashed line shows the asymptotic scaling $\sim 8\kappa^2/g_0^2$ at zero temperature.

grees of freedom. To illustrate this we first consider a single mechanical resonator, $b \equiv b_1$, $\omega_m \equiv \omega_m^1$. We introduce symmetric and antisymmetric optical modes $c_{s,a} = (c_1 \pm c_2) / \sqrt{2}$ with eigenfrequencies $\omega_{s,a}$ split by $2J$. Further, we assume that $\omega_m \sim 2J \gg g_0, \kappa, |\delta|$, where $\delta = 2J - \omega_m$ (see Fig. 3.1(b)). This condition can be achieved in nanoscale OMSs where $\omega_m \sim \text{GHz}$ [79, 42, 40, 63] and a matching tunnel splitting can be designed by appropriately adjusting the spacing between the cavities [79, 100]. In this regime we can make a rotating wave approximation with respect to the large frequency scale $\omega_m \sim 2J$ and after changing into a frame rotating with ω_L we obtain [100]

$$H = -\Delta_s c_s^\dagger c_s - \Delta_a c_a^\dagger c_a + \omega_m b^\dagger b + \frac{g_0}{2} (c_a c_s^\dagger b^\dagger + c_a^\dagger c_s b) + H_\Omega(t). \quad (3.3)$$

Here $\Delta_{s,a} = \omega_L - \omega_{s,a}$ are the detunings of the driving field from the c_s and c_a mode, respectively, and $H_\Omega(t) = \sum_{\eta=s,a} (\Omega_\eta(t) c_\eta + \text{H.c.})$ accounts for the external driving fields with slowly varying amplitudes $\Omega_{s,a}(t) = (\Omega_1(t) \pm \Omega_2(t)) / \sqrt{2}$.

The two-mode OM coupling in Eq. (3.3) describes photon transitions between the energetically higher mode c_a to the lower mode c_s , while simultaneously absorbing or emitting a phonon. For $(\Delta_s - \Delta_a - \omega_m) = \delta = 0$, this leads to a resonant interaction between states $|n_a, n_s, n_m\rangle$ and $|n_a - 1, n_s + 1, n_m + 1\rangle$, where n_a , n_s and n_m label the occupation numbers of the two optical modes and the mechanical mode, respectively. In analogy to atomic cavity quantum electrodynamics (QED) [172], the nonlinear scaling of the corresponding transition amplitudes $\frac{g_0}{2} \sqrt{n_a(n_s + 1)(n_m + 1)}$ results in an anharmonic level diagram as shown in Fig. 3.2(a). If g_0 exceeds the cavity linewidth κ , one and two photon transitions can be spectrally resolved, indicating the onset of strong single-photon nonlinearities.

3.4 An OM single-photon source

As a potential first application of the nonlinear OM interaction we discuss the use of the OMS as a single-photon source, which is characterized by a vanishing equal time two-photon correlation function $g^{(2)}(0)$. In Fig. 3.2(b) we plot the excitation spectrum $\langle c_a^\dagger c_a \rangle$ and $g^{(2)}(0) = \langle c_a^\dagger c_a^\dagger c_a c_a \rangle / \langle c_a^\dagger c_a \rangle^2$, for the case where only the c_a mode is weakly driven. Around the single-photon resonances $\Delta_a = \pm g_0/2$ we observe strong anti-bunching $g^{(2)}(0) < 1$ as a clear signature of non-classical photon statistics. To quantify this effect we assume that $\Gamma_m \ll \kappa$, which allows us to treat subspaces connected to different $|n_m\rangle$ separately. For weak driving fields $\Omega_a \ll \kappa$, the system dynamics can then be restricted to the six states $|0_a, 0_s, n_m\rangle, |1_a, 0_s, n_m\rangle, |0_a, 1_s, n_m + 1\rangle, |2_a, 0_s, n_m\rangle, |1_a, 1_s, n_m + 1\rangle, |0_a, 2_s, n_m + 2\rangle$ and we calculate the relevant occupation probabilities $p_{1,0,n_m}$ and $p_{2,0,n_m}$ to leading order in Ω_a [39]. We obtain

$$p_{1,0,n} = \left| \frac{4\Omega_a d}{X_n} \right|^2, \quad p_{2,0,n} = 8 \left| \frac{\Omega_a^2 (8d^2 - g_0^2)}{(X_n (2X_n - g_0^2))} \right|^2, \quad (3.4)$$

where $d = \Delta_a - i\kappa$ and $X_n = d^2 - g_0^2(n + 1)$. By taking the appropriate thermal averages, $\langle n_a \rangle = \sum_n \zeta_n p_{1,0,n}$ and $g^{(2)}(0) = 2 \sum_n \zeta_n p_{2,0,n} / \langle n_a \rangle^2$, where $\zeta_n = (1 - e^{-\beta \hbar \omega_m}) e^{-\beta \hbar \omega_m n}$ and $\beta^{-1} = k_B T$, the two photon correlation function can be evaluated for arbitrary temperatures T .

In Fig. 3.2(c) we plot the minimal value of $g^{(2)}(0)$ as a function of the coupling strength g_0 and for different N_{th} . As the OM coupling increases we find that for $T = 0$ the minimum of the correlation function scales as $\min_{\Delta_a} \{g^{(2)}(0)\} \simeq 8\kappa^2/g_0^2$. This demonstrates an improved scaling over off-resonant photon blockade effects in single-mode OMSs, where for large ω_m only a small reduction $g^{(2)}(0) \simeq 1 - g_0^2/(\kappa\omega_m)$ can be

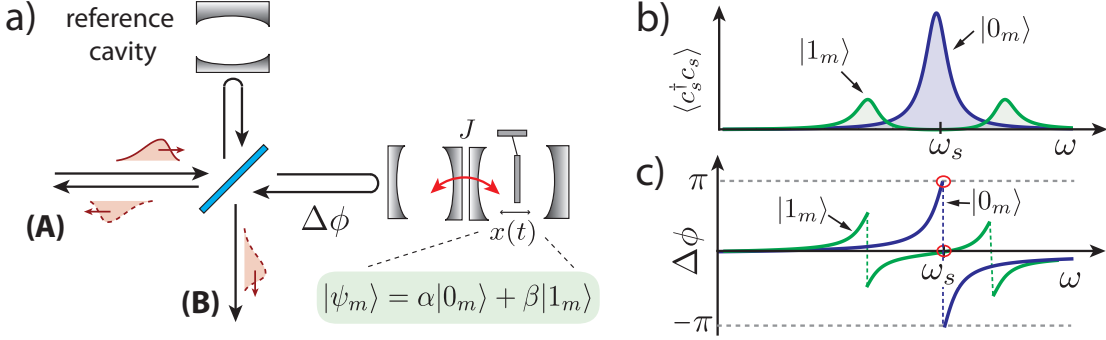


Figure 3.3: a) An incoming photon in port (A) passes through the interferometric setup and leaves through port (A) or (B), depending on the phase shift $\Delta\phi$ acquired upon reflection from the two-mode OMS. b), c) For a mechanical system in state $|0_m\rangle$, the OMS exhibits a single resonance at ω_s ($\Delta\phi = \pi$), while for state $|1_m\rangle$ the resonance splits by $g_0 \gg \kappa$ and the photon does not enter the cavity ($\Delta\phi = 0$).

obtained [171]. Since the positions of the single and two-photon resonances depend explicitly on the mechanical state $|n_m\rangle$, finite temperature degrades the quality of the single-photon source. Nevertheless, with increasing coupling strength the anti-bunching effect becomes surprisingly robust and when combined with cooling cycles to achieve $\langle n_m \rangle \sim 1$ [42], allows the operation of OM single-photon sources even at environmental temperatures of a few Kelvin.

3.5 Single-phonon single-photon transistor

Given the ability to generate single photons, Fig. 3.3 illustrates a basic scheme for using the same resonant OMS to implement a two-qubit gate [69]. First, we assume that the state of a control photon is mapped onto a mechanical superposition state $\alpha|0_m\rangle + \beta|1_m\rangle$. This can be achieved with conventional cooling followed by photon-phonon conversion techniques using linearized OM interactions with an aux-

iliary mode ω'_c (see Fig. 3.1(c)). Next, a single target photon of central frequency $\sim \omega_s$ is sent through the interferometric setup as described in Fig. 3.3. If the mechanical mode is in the state $|0_m\rangle$, the incoming photon couples to a single resonant state $|0_a, 1_s, 0_m\rangle$ (see Fig. 3.1(b)), such that it enters the cavity and picks up a phase before being reflected. Instead, if the mechanical resonator is in the state $|1_m\rangle$, the resonant coupling between $|0_a, 1_s, 1_m\rangle$ and $|1_a, 0_s, 0_m\rangle$ splits the cavity resonance, and for $g_0 > \kappa$ the photon is reflected without a phase shift. Under ideal conditions, the final result is an entangled state

$$|\psi\rangle = \alpha|0_m, 1_A, 0_B\rangle + \beta|1_m, 0_A, 1_B\rangle, \quad (3.5)$$

where A and B are the two ports of the interferometer. This state can be converted back into an entangled state between the initial control and target photon.

Assuming that the storage and retrieval of the control photon can be achieved with high fidelity, the error for producing the entangled state (3.5) with $\alpha = \beta = 1/\sqrt{2}$ is approximately given by

$$\epsilon \approx \frac{4\kappa^2}{g_0^2} + \frac{1}{(\tau_p \kappa)^2} + \tau_p \Gamma_m, \quad (3.6)$$

where τ_p is the duration of the single-photon pulse. The individual contributions in Eq. (3.6) arise from an imperfect photon reflection, the finite spectral width of the photon pulse, and mechanical decoherence, respectively. A minimal error is achieved for $\tau_p^{-1} \approx \sqrt[3]{\kappa^2 \Gamma_m}$ where we obtain $\epsilon \approx \max\{4\kappa^2/g_0^2, \sqrt[3]{\Gamma_m^2/\kappa^2}\}$. Assuming an OM crystal device with $\omega_m/(2\pi) = 4$ GHz and $Q = 10^5$ as discussed in Ref. [42], but with an improved OM coupling $g_0/(2\pi) = 50$ MHz and a lower decay rate $\kappa/(2\pi) = 5$ MHz, we obtain gate errors $\epsilon \approx 0.1$ for environmental temperatures around $T \approx 100$ mK.

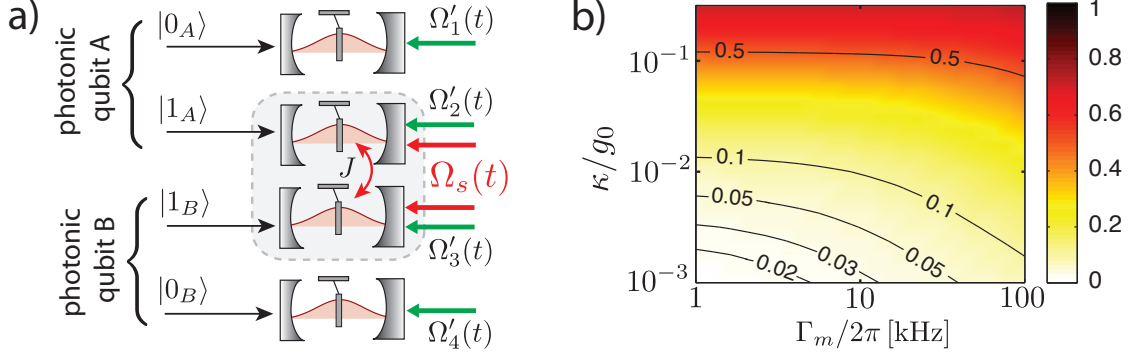


Figure 3.4: a) OM quantum memory, where ‘path-encoded’ photonic qubits are stored in long-lived mechanical states using tunable linearized OM interactions $\sim \Omega'_i(t)$. Deterministic gate operation between stationary qubits are implemented by a controlled phonon-phonon interaction $\sim \Omega_s(t)$ as described in the text. b) The total error ϵ_g for implementing a controlled phase gate between two phononic qubits is minimized with respect to Δ_s and plotted as a function of κ and Γ_m (see text). The parameters for this plot are $g_0/(2\pi) = 50$ MHz, $\gamma/(2\pi) = 4$ kHz, $\alpha = 1$ and $g_0/\delta = 1/3$.

3.6 Phonon-phonon interactions

Finally, we consider the possibility to perform a controlled gate operation between two qubits stored in long-lived mechanical modes. Our approach is depicted in Fig. 3.4(a), and combines the long coherence times of an OM quantum memory [86, 230, 242, 2] with the practical utility of exploiting interactions between stationary phononic qubits. We focus on the limit $\Gamma_m \ll \kappa$, and assume that optical (e.g. ‘path encoded’) qubits are first mapped onto long-lived states $|0_m\rangle$ and $|1_m\rangle$ of two or more mechanical modes. The OM coupling is then employed to generate nonlinear interactions between the phonons only.

We consider nonlinear interactions between two mechanical modes b_1 and b_2 described by Eq. (3.1), detuned from resonance such that $g_0 < |(2J - \omega_m^i)|$ and direct transitions between photons and phonons are suppressed. To obtain the effective

phonon-phonon interactions, we first diagonalize H to second order in $\xi_i = g_0/(2J - \omega_m^i)$ with the transformation $H \rightarrow e^{iS}He^{-iS}$, where $S = \frac{i}{2}(c_s^\dagger c_a(\xi_1 b_1^\dagger - \xi_2 b_2^\dagger) - \text{H.c.})$. This yields $H = H_0 + H_g + H_\Omega(t)$, where $H_0 = -\Delta_s c_s^\dagger c_s - \Delta_a c_a^\dagger c_a + \sum_i \omega_m^i b_i^\dagger b_i$,

$$H_g = \frac{g_0}{4} [(c_s^\dagger c_s + 1)c_a^\dagger c_a(\xi_1 + \xi_2) + (c_a^\dagger c_a - c_s^\dagger c_s)\mathcal{N}_b], \quad (3.7)$$

and we have neglected small corrections to the driving Hamiltonian $H_\Omega(t)$. The phonon operator in Eq. (3.7) is given by $\mathcal{N}_b = \xi_1 b_1^\dagger b_1 + \xi_2 b_2^\dagger b_2 - (\xi_1 + \xi_2)(b_1^\dagger b_2 + b_2^\dagger b_1)/2$. For simplicity we focus on symmetric detuning, $\omega_m^{1,2} = 2J \mp \delta$, where $\mathcal{N}_b = \frac{g_0}{\delta}(b_1^\dagger b_1 - b_2^\dagger b_2)$. The transformation also modifies the dissipative terms in the Eq. (3.2); most importantly, we find an optically-induced decay channel for the mechanical modes, $\mathcal{L}_\gamma \rightarrow \mathcal{L}_\gamma + \kappa g_0^2/(4\delta^2)\mathcal{D}[c_s(b_1 + b_2)]$.

We assume that only the c_s mode is weakly driven by a slowly-varying control field $\Omega_s(t)$. In this case the c_a mode remains unpopulated and we neglect it. Next, we shift the driven mode, $c_s \rightarrow \alpha + c_s$, by the classical amplitude α , yielding an effective ME for c_s , b_1 and b_2 . Finally, we adiabatically eliminate the c_s mode, valid in the limit $|\alpha| \sim \mathcal{O}(1)$ and $(g_0^2|\alpha|/4\delta) \ll |\Delta_s + i\kappa|$, to obtain an effective ME for the mechanical modes (see Appendix B for more details),

$$\begin{aligned} \dot{\rho}_m = & -i[H_m + \Lambda(b_1^\dagger b_1 - b_2^\dagger b_2)^2, \rho_m] + \mathcal{L}_\gamma \rho_m \\ & + \Gamma_\phi \mathcal{D}[(b_1^\dagger b_1 - b_2^\dagger b_2)]\rho_m + \frac{\gamma'}{2} \sum_i \mathcal{D}[b_i]\rho_m. \end{aligned} \quad (3.8)$$

Here, $\gamma' = \kappa|\alpha|^2 g_0^2/(2\delta^2)$, and the phonon-phonon interaction and the phonon dephasing rate are given by

$$\Lambda = \frac{g_0^4 |\alpha|^2 \Delta_s}{16\delta^2(\Delta_s^2 + \kappa^2)}, \quad \Gamma_\phi = \frac{g_0^4 |\alpha|^2 \kappa}{16\delta^2(\Delta_s^2 + \kappa^2)}. \quad (3.9)$$

The effective Hamiltonian in Eq. (3.8) describes a phonon nonlinearity with a tunable strength $\Lambda(t) \sim |\alpha(t)|^2$. The relevant cross-coupling is given by

$$H_{\text{int}} \simeq 2\Lambda b_1^\dagger b_1 b_2^\dagger b_2, \quad (3.10)$$

and when acting for a time $t_g = \pi/(2\Lambda)$, this Hamiltonian implements a controlled-phase gate between two qubits encoded in states $|0_m\rangle$ and $|1_m\rangle$. During this time, phonons experience intrinsic and optically-induced decoherence as seen in Eq. (3.8). In Fig. 3.4, we plot the resulting gate error $\epsilon_g = 1 - \langle \psi_0 | \rho_m(t_g) | \psi_0 \rangle$ for an initial state $|\psi_0\rangle = \frac{1}{2}(|0_m\rangle + |1_m\rangle)^{\otimes 2}$ optimized with respect to Δ_s . Using the total decoherence rate of this state, $\Gamma_{\text{decoh}} = 2\Gamma_m + \Gamma_\phi + \gamma'/2$, we find that $\epsilon_g \propto \Gamma_{\text{decoh}}/\Lambda$ is minimized for $|\Delta_s| \simeq g_0/2$, where $\epsilon_g \propto 4(\kappa/g_0)$. While this scaling with g_0 is weaker than for a gate based on photon reflection (see Eq. (3.6)), the ability to perform a gate between stationary qubits represents an important advantage of this approach.

3.7 Conclusions

We have described single-photon and single-phonon nonlinear effects in strongly coupled multimode OMSs. We have shown how induced nonlinearities on or near resonance can be used for controlled quantum gate operations between flying optical or stationary phononic qubits. Our results provide a realistic route towards the quantum nonlinear regime of OMSs, and a framework for future OM information processing applications.

Chapter 4

Heralded Quantum Gates with Integrated Error Detection

4.1 Introduction

Exploiting quantum systems for information processing offers many potential advantages over classical information processing like highly secure quantum networks [54, 117, 70] and powerful quantum computers [124, 203, 85]. One of the main challenges for the realization of functional quantum computers is to perform gates with sufficiently high quality so that the remaining errors can be suppressed by error correction codes, which makes the computation fault tolerant [120]. At the same time, applications to long distance quantum communication can be enabled by quantum repeaters, which combine probabilistic entanglement generation over short distances with subsequent entanglement connection steps [70]. For these protocols, the probabilistic nature of the entanglement generation is acceptable, but it is essential

that high fidelity entanglement is achieved conditioned on a heralding measurement. Experimentally, such high fidelity entanglement is often much easier to implement and may be realized in situations where it is impossible to perform any quantum operations deterministically. Here we introduce a similar concept for gate operations and develop the concept of heralded quantum gates with integrated error detection. In the resulting gate, the infidelity, which would be present for a deterministic gate is converted into a failure probability, which is heralded by an auxiliary atom. Once successful, the resulting gate can have an arbitrarily small error. Such heralded gates could facilitate fault tolerant quantum computation since detectable errors may be easier to correct than undetectable errors [98, 173, 229]. Alternatively it can be directly incorporated into quantum repeater architectures for long distance quantum communication.

Optical cavities are ideal for conversion between the stationary gate qubits and flying qubits (photons), which is fundamental for quantum networks [181, 121, 169]. Quantum gates can, in principle, also be directly implemented in optical cavities [168], but the experimental requirements for this are very challenging due to spontaneous emission and cavity loss. The essential parameter quantifying this is the cooperativity of the atom-cavity system, C . It has been argued that directly implementing gates in optical cavities leads to a poor error scaling $1 - F \propto 1/\sqrt{C}$, where F is the fidelity of the gate [115, 208]. However, as a result of the integrated error detection, the heralded gates that we propose exhibit high fidelities when successful. This enables efficient entanglement swapping and removes the necessity of intermediate entanglement purification in quantum repeaters thus increasing the distribution rate

significantly. Compared to using other deterministic, cavity based gates, an increase in the rate of up to two orders of magnitude can be achieved for modest cooperativities (< 100) and a distance of 1000 km [25].

4.2 Heralding gate

The basic idea is to use a heralding auxiliary atom in addition to qubit atoms in the same cavity. One of the atomic qubit states, e.g., state $|1\rangle$ couples to the cavity mode while $|0\rangle$ is completely uncoupled (see Fig. 4.1(a)). Such a system has previously been considered for two-qubit gates [71, 69, 209, 208, 177], multi-qubit gates [71, 245] and photon routing [220]. If any of the qubit atoms is in state $|1\rangle$ the cavity resonance is shifted compared to the bare cavity mode, which can be exploited to make a gate between two or more qubits by reflecting single photons off the cavity [71]. The efficiency of such schemes, however, is limited by photon losses, inefficient detectors and non-ideal single photon sources [220, 177]. We circumvent these problems by introducing an auxiliary atom in the cavity to serve as both an intra-cavity photon source and a detector. As opposed to previous heralded gates in optical cavities, which relied on the null detection of photons leaving the cavity [164, 15, 93], the final heralding measurement on the atom can then be performed very efficiently.

In our approach, the auxiliary atom has two metastable states $|g\rangle, |f\rangle$ which can be coupled through an excited state $|E\rangle$ (see Fig. 4.1(a)). We assume the $|E\rangle \leftrightarrow |f\rangle$ transition to be energetically close to the cavity frequency and to be a nearly closed transition, so that we need to drive the $|g\rangle \rightarrow |E\rangle$ transition, e.g with a two-

photon process, (see below). The gate can be understood through the phase evolution imposed on the atoms. We consider adiabatic excitation of the auxiliary control atom via Stimulated Raman Adiabatic Passage [196, 123], driven by an external driving pulse with Rabi frequency $\Omega(t)$ and a coupling to the cavity photon g_f . In the case when all the qubit atoms are in the non-coupled states $|00..0\rangle$, an adiabatic excitation will result in a dark state $\sim g_f|0,g\rangle - \Omega|1,f\rangle$ with zero energy and vanishing phase. Here the number refers to the number of cavity photons. However, the qubit states Ψ with at least one of the qubit atoms in the coupled state, results in a cavity-induced shift of the state $|1,f,\Psi\rangle$, which in turn, causes an AC Stark shift and dynamical phase to be imprinted into the $|g,\Psi\rangle$ state after the driving pulse is turned off. All states but the completely uncoupled qubit state $|00...0\rangle$ will thus acquire a phase, the magnitude of which depends on the length of the driving pulse. With an appropriate pulse length and simple single qubit rotations, we can use this to realize a general N -qubit Toffoli gate or a control-phase (CZ) gate.

Naively, the gates will be limited by errors originating from cavity decay and spontaneous emission from the atoms, which carry away information about the qubit state. These errors are, however, detectable since the auxiliary atom will be trapped in state $|f\rangle$ if either a cavity excitation or an atomic excitation is lost. Conditioning on detecting the auxiliary atom in state $|g\rangle$ at the end of the gate thus rules out the possibility of any dissipative quantum jumps having occurred during the gate. As a result, the conditional fidelity of the gate is greatly enhanced at the modest cost of a finite but potentially low failure probability.

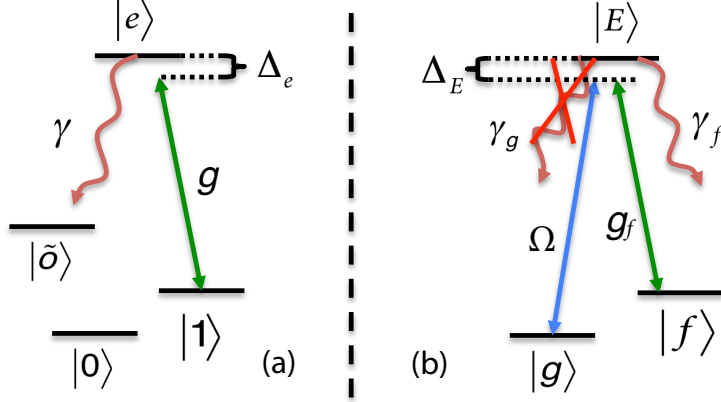


Figure 4.1: (a) Level structure of the qubit atoms. Only state $|1\rangle$ couples to the cavity and we assume that the excited level decays to some level $|\tilde{o}\rangle$, possibly identical to $|f\rangle$ or $|0\rangle$. (b) Level structure of the auxiliary atom and the transitions driven by the weak laser (Ω) and the cavity (g_f). We assume that $|E\rangle \leftrightarrow |f\rangle$ is a closed transition, i.e. $\gamma_g = 0$.

4.3 Performance

4.3.1 Model

We now analyze the performance of the gates and derive the success probabilities, gate times and gate errors (see Tab. C.1 in Appendix C.1) The Hamiltonian in a proper rotating frame is (see Fig. 4.1)

$$\begin{aligned} \hat{H} = & \Delta_E |E\rangle\langle E| + g_f (\hat{a}|E\rangle\langle f| + H.c) + \hat{V} + \hat{V}^\dagger \\ & + \sum_k \Delta_e |e\rangle_k\langle e| + g (\hat{a}|e\rangle_k\langle 1| + H.c), \end{aligned} \quad (4.1)$$

where k labels the qubit atoms ($\hbar = 1$), $2\hat{V} = \Omega|E\rangle\langle g|$ and we have assumed that all couplings (g, Ω) are real. We have defined $\Delta_E = \omega_E - \omega_g - \omega_L$, and $\Delta_e = \omega_e - \omega_g - \omega_L + \omega_f - \omega_1$, where ω_L is the laser frequency and otherwise ω_x is the frequency associated with level x . We describe the cavity decay and atomic spontaneous emission with Lindblad operators so that $\hat{L}_0 = \sqrt{\kappa}\hat{a}$ corresponds to the

cavity decay, $\hat{L}_f = \sqrt{\gamma_f}|f\rangle\langle E|$ to the decay of the excited state of the auxiliary atom and $\hat{L}_k = \sqrt{\gamma}|\tilde{o}\rangle_k\langle e|$ describes the decay of the excited qubit states to some arbitrary ground state $|\tilde{o}\rangle$. The nature of $|\tilde{o}\rangle$ is not important for the dynamics of the gates and it may or may not coincide with $|0\rangle$ or $|1\rangle$.

4.3.2 Effective Hamiltonian

We assume a weak driving pulse justifying for a perturbative treatment of \hat{V} using the formalism of Ref. [178]. In the perturbative description we adiabatically eliminate the coupled excited states of the atoms and the cavity (assuming $\Omega^2/\Delta_E \ll \Delta_E$ and $\Omega \ll g$), which leads to an energy shift of the ground states but otherwise conserves them since the Hamiltonian cannot connect different unexcited states without decay. The dynamics are therefore described by an effective Hamiltonian, $\hat{H}_{\text{eff}} = |g\rangle\langle g| \sum_n \Delta_n \hat{P}_n$ where

$$\Delta_n = \text{Re} \left\{ \frac{-\frac{\Omega^2}{4\gamma}((\frac{\Delta_e}{\gamma}-i/2)i+2nC)}{(2\frac{\Delta_e}{\gamma}-i)((2\frac{\Delta_E}{\gamma}-i)i/4+C)+(2\frac{\Delta_E}{\gamma}-i)nC} \right\} \quad (4.2)$$

and \hat{P}_n projects on the states with n qubits in state $|1\rangle$. For simplicity, we have assumed that the auxiliary atom is identical to the qubit atoms such that $g_f = g$ and $\gamma_f = \gamma$ (see Appendix C.1 for a more general treatment) and we have defined the cooperativity $C = g^2/\gamma\kappa$. We consider the limit $C \gg 1$ and from Eq. (4.2) we find that the energy shift, in the case when all qubit atoms are in $|0\rangle$, becomes very small $\Delta_0 \sim \Delta_E \Omega^2 / (16\gamma^2 C^2) \rightarrow 0$, i.e., we drive into a zero energy dark state as mentioned in the description above. On the contrary, for $n > 0$, the C in the nominator of Δ_n reflects that the coupling of the qubit atoms shifts the cavity resonance and as a result an AC stark shift of $\sim \Omega^2/\Delta_E$ is introduced. Furthermore, we find that in the

effective evolution, errors caused by spontaneous emission or cavity decay ($\hat{L}_0, \hat{L}_f, \hat{L}_k$) project the system out of the effective space into orthogonal subspaces, which allows for an efficient error detection by measuring the ancilla atom.

4.3.3 Success probability

The dynamics described by \hat{H}_{eff} can be used to implement a Toffoli gate. Assuming the qubit atoms to be on resonance ($\Delta_e = 0$) and having $\Delta_E \sim \gamma\sqrt{C}$ gives energy shifts $\Delta_{n>0} \sim \Omega^2/(4\gamma\sqrt{C})$ while $\Delta_0 \sim \mathcal{O}(\Omega^2/C^{3/2})$. Hence, $|00\dots0\rangle$ is the only state, which remains unshifted and we can choose a gate time of $t_{\text{T}} \sim 4\pi\sqrt{C}\gamma/\Omega^2$ to make a Toffoli gate. By conditioning on measuring the auxiliary atom in state $|g\rangle$ at the end of the gate, the detectable errors from cavity decay and spontaneous emission only reduce the success probability instead of reducing the fidelity. Consequently, the fidelity becomes limited by more subtle, undetectable errors (see Appendix C.1). The dominant error originates from the qubit dependent decay rate, Γ_n , of $|g\rangle \rightarrow |f\rangle$. As we demonstrate in Appendix C.1), this leads to a fidelity lower bounded by $1 - F \lesssim 0.3/C$, with a success probability of $P_s \sim 1 - 3/\sqrt{C}$. Thus is a substantial improvement over the leading error in the case of deterministic cavity-assisted gates. For generic states, the fidelity can even be markedly higher, and improving with increasing particle number N , see Appendix C.1.

In the special case of only two qubits, the Toffoli gate is referred to as a CZ-gate, and in this case, we can even improve the gate to have an arbitrarily small error by combining it with single qubit rotations. For the general Toffoli gate discussed above, we needed $\Delta_e = 0$ to ensure the correct phase evolution, but making the single

qubit transformations $|0\rangle \rightarrow e^{-i\Delta_0 t/2}|0\rangle$ and $|1\rangle \rightarrow e^{-i(\Delta_1 - \Delta_0)t/2}|0\rangle$, at the end of a driving pulse of length $t_{\text{CZ}} = |\pi/(\Delta_2 - 2\Delta_1 + \Delta_0)|$, ensures the right phase evolution of the CZ-gate without any constraints on Δ_e . Hence, it is possible to tune Δ_e to eliminate the detrimental effect of having a qubit dependent decay rate. Choosing $\Delta_E = \frac{\gamma}{2}\sqrt{4C+1}$ and $\Delta_e = \frac{1}{2}C\gamma^2/\Delta_E$ ensures $\Gamma_0 = \Gamma_1 = \Gamma_2$, and thus removes all dissipative errors from the heralded gate. The conditional error is then limited only by non-adiabatic effects, that can in principle be made arbitrarily small by reducing the driving strength. The success probability is $1 - P_s \sim 6/\sqrt{C}$ in the limit $C \gg 1$ (see Fig. 4.2). We thus have a heralded two qubit gate with arbitrarily small error with a success probability that can approach 1 (it is possible to decrease the scaling factor of the probability from ~ 6 to ~ 3.4 at the expense of an error scaling as $1/C$ by tuning Δ_E, Δ_e).

4.3.4 Gate time

We now consider the gate time. The gate time of the Toffoli gate is $t_T \sim 4\pi\sqrt{C}\gamma/\Omega^2$ and for the CZ-gate we have $t_{\text{CZ}} \sim 15\pi\sqrt{C}\gamma/(2\Omega^2)$ for $C \gg 1$. Since $t_{\text{CZ}} > t_T$ we focus on t_{CZ} . The gate time is set by the strength (Ω) of the driving pulse, which is limited by non-adiabatic errors. This is investigated and we also verify our analytical results numerically in Appendix C.3. Assuming realistic parameters of $\kappa = 100\gamma$ [218, 220], we find that a driving of $\Omega = \sqrt{C}\gamma/4$ keeps the non-adiabatic error of the gate below 4×10^{-5} for $C \leq 1000$. The gate times decreases as $1/\sqrt{C}$ as shown in Fig. 4.2. For a cooperativity of 100 the gate time is $\approx 1 \mu\text{s}$ for typical atomic decay rates.

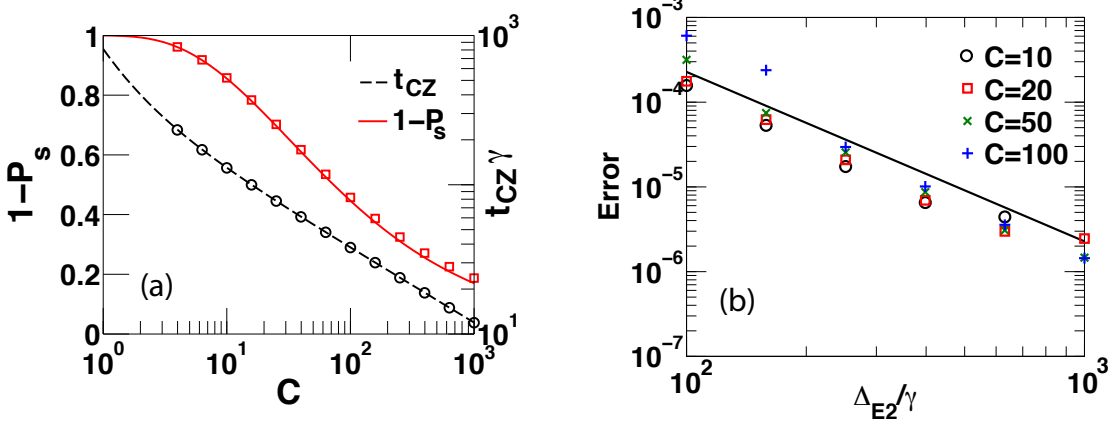


Figure 4.2: (a) Failure probability ($1 - P_s$ - left axis) and gate time (t_{CZ} - right axis) as a function of the cooperativity (C) for the CZ gate. The gate time is in units of the inverse linewidth $1/\gamma$ of the qubit atoms. We have assumed a driving of $\Omega = \sqrt{C}\gamma/4$. (b) Gate error as a function of the detuning Δ_{E2} in the two-photon-driven CZ-gate for $C = 10, 20, 50$, and 100 . We have assumed that $\Omega_{MW} = 4\gamma C^{1/4}$ and that $\gamma_g = \gamma$. The gate error decreases as γ^2/Δ_{E2}^2 and is independent of C . We have assumed $\Omega \sim \Delta_{E2}/8$ resulting in a gate time $\sim 400/\gamma$. Solid/dashed lines are analytical results and symbols are numerical simulations (see Appendix C). For both plots, we have assumed $\kappa = 100\gamma$.

4.4 Additional errors

So far, we have assumed a model where there is no decay from $|E\rangle \rightarrow |g\rangle$. In real atoms, there will, however, always be some decay $|E\rangle \rightarrow |g\rangle$ with a decay rate $\gamma_g > 0$. The result of such an undetectable decay is that both the CZ-gate and the Toffoli gate will have an error $\sim \gamma_g/(\gamma\sqrt{C})$. To make this error small, it is thus essential to suppress the branching ratio γ_g/γ . Below, we show how to suppress γ_g by driving the $|g\rangle \rightarrow |E\rangle$ transition with a two photon process. As a result, we realize a CZ gate with an error arbitrary close to zero and a Toffoli gate with an error scaling as $1/C$ even for a realistic atomic system.

Specifically, we think of a level structure for the auxiliary atom, shown in Fig. 4.3,

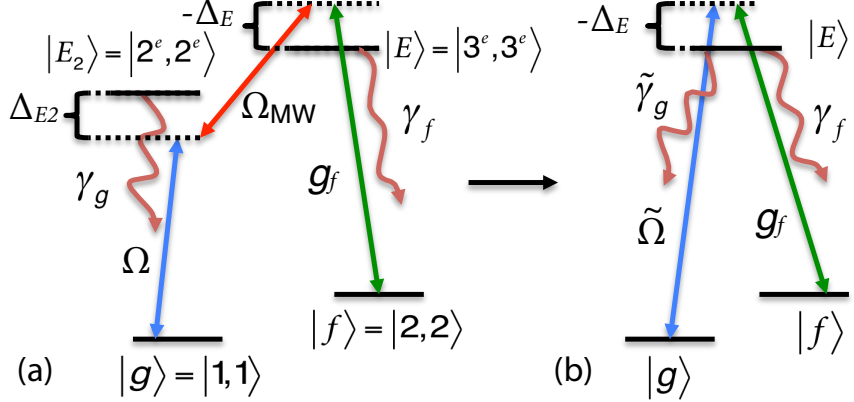


Figure 4.3: (a) Level structure of the auxiliary atom and the transitions driven by a weak laser (Ω), a microwave field (Ω_{MW}) and the cavity (g_f). We assume that $|E\rangle \leftrightarrow |f\rangle$ is a closed transition and, for simplicity, we also assume that $|E_2\rangle \leftrightarrow |g\rangle$ is a closed transition but this is not a necessity. Here $|r^{(e)}, r^{(e)}\rangle$ with $r = 1, 2, 3$ refers to how the atom may be realized in the $(5^2P_{3/2})$ states $|F^{(e)} = r, m^{(e)} = r\rangle$ $5^2S_{1/2}$ of Rb⁸⁷. (b) Effective three-level atom realized by mapping the two-photon drive to give an effective decay rate $\tilde{\gamma}_g$ and an effective drive $\tilde{\Omega}$.

where we still assume $|E\rangle \leftrightarrow |f\rangle$ to be a closed transition. For simplicity, we have also assumed $|E_2\rangle \leftrightarrow |g\rangle$ to be a closed transition. Such a level structure could, e.g. be realized in ⁸⁷Rb as shown in Fig. 4.3. We assume that a microwave field couples the two excited states such that we can have a two photon transition from $|g\rangle \rightarrow |E\rangle$ and that Ω is small, allowing for a perturbative treatment of the coupling. Thus we can map the system to a simple three-level atom with levels $|g\rangle$, $|E\rangle$ and $|f\rangle$ and a decay rate $\tilde{\gamma}_g$ and drive $\tilde{\Omega}$ between $|g\rangle$ and $|E\rangle$, determined by the two photon driving process as shown in Fig. 4.3. The dynamics are thus similar to what we have already described for the simple three level atom except that we have the extra decay $\tilde{\gamma}_g$ that introduces an error in the gates $\sim (\tilde{\gamma}_g/\gamma)/\sqrt{C}$, as previously described. In the limit $C \gg 1$, we find $\tilde{\gamma}_g/\gamma \sim \frac{\gamma_g \Omega_{MW}^2}{4\gamma \Delta_{E2}^2}$. Thus by increasing Δ_{E2} , we can in principle make these errors arbitrarily small. The error of the CZ-gate for different Δ_{E2} is shown in

Fig. 4.2, assuming an initial state of $(|0\rangle + |1\rangle)^{\otimes 2}$. Note that in order to prevent an increasing scattering probability of level $|E2\rangle$, we need to have $\Omega_{MW} \propto C^{1/4}$ resulting in a gate error that is independent of the cooperativity, see Appendix C. The success probability and time of the gates are the same as before with $\Omega \rightarrow \tilde{\Omega} \sim \frac{\Omega_{MW}\Omega}{2\Delta_{E2}}$. With similar considerations about the validity of our perturbation as before, we find that for realistic parameters, we can use $\Omega = \Delta_{E2}/8$, $\Omega_{MW} \sim 4\gamma C^{1/4}$ resulting in a gate time of $\sim 10 \mu s$ for typical atomic decay rates and $C \lesssim 1000$, see Appendix C.

4.5 Possible implementation

As an example implementation, we consider ultra-cold ^{87}Rb atoms coupled to nanophotonic cavities [218, 220]. There are some additional errors originating from the extra states in the ^{87}Rb atoms in this case. In Appendix C.4, we treat these errors and find that with a detuning of $\Delta_{E2} = 100\gamma$ and a cooperativity of $C \approx 100$, a heralded CZ gate with $\sim 67\%$ success probability and a heralded error of $\approx 10^{-3}$ can be realized in $\approx 10 \mu s$ time. This justifies neglecting atomic decoherence which is typically much slower. Alternatively the gate can be implemented with atom-like solid-state qubits such as NV and SiV centers in diamond [49]. These systems can exhibit closed transitions and long-lived electronic spin states which are the essential requirement for the gate [221], while high cooperativities are possible in diamond nanocavities [37]. A particular advantage of such system is the long-lived nuclear spin degrees of freedom, which allows each of the color centers to act as a multi-qubit quantum network node [145]. By entangling electronic spins via the heralded gate, a high-fidelity, fully deterministic gate can subsequently be performed on qubits stored

in nuclear spins [208].

4.6 Application

As a particular application, we consider a quantum repeater where entanglement is first created in small segments (links), which are subsequently connected using entanglement swapping [33]. By organizing the repeater in a tree structure, the probabilistic nature of the gate can be efficiently circumvented. The success rate of distributing entanglement across the total distance L , scales as $\sim (L/L_0)^{1-\log_2(3/p)}$, where $p < 1$ is the success probability of the swap, L is the total distribution distance and L_0 is the length between the links [25] (note that in the limit $p \rightarrow 1$, the above expression underestimates the rate, e.g., for $p = 1$ the actual rate is ~ 3 times faster for 128 links). This is a substantial improvement over direct transmission where the success rate scales exponentially with L . For a realization with nuclear spin memories where the swap can be performed deterministically the rate can scale even better as $\sim \log_2(L/L_0)^{-1}$. In order to maintain the favorable scaling without resorting to time consuming purification, the total number of links, N_{\max} should be kept below $N_{\max} \sim -\ln(F_{\text{final}})/(\epsilon_0 + \epsilon_g)$, where F_{final} is the required fidelity of the final distributed pair and $\epsilon_0, \epsilon_g \ll 1$ are the errors of the initial entanglement generation and the entanglement swapping respectively. Thus, it is essential that the errors are kept small, which can be obtained with the heralded gate.

4.7 Conclusion

In conclusion, we have introduced a heralded two-qubit quantum gate with a conditional fidelity arbitrarily close to unity and an N -qubit Toffoli gate with an error scaling as $1/C$. The gates have a built-in error detection process, which removes the necessity of extracting the error by the more complicated process of entanglement purification or quantum error correction. Our gate is designed for the specific case of optical cavities, and allows exploiting realistic systems for quantum communication, even though the error rate would inhibit this with deterministic gates. Similar advantages can be realized in other systems such as those based on circuit QED, where certain errors could be heralded and thus alleviate the daunting requirements of fault tolerant computation.

Chapter 5

Remote entanglement distribution using individual atoms in cavities

5.1 Introduction

Distribution of entanglement is an essential task in quantum communication [117, 54, 169]. Entanglement can be used to make highly secure communication channels due to the sensitivity of entangled quantum systems to external influences [195]. While this sensitivity makes it possible to detect any attack from an eavesdropper, it also makes it hard to distribute entanglement over large distances since any noise from the environment quickly destroys the entanglement. Direct transmission of a quantum signal suffers from loss and decoherence from the transmission channel, which results in an exponential decrease of the rate with distance [33]. To overcome this problem, it has been proposed to use quantum repeaters, where entanglement is first created over short distances by direct transmission and then stored in quantum

memories until it can be swapped to larger distances [33, 70] (See Fig. 5.1). Much effort has been devoted to the construction of quantum repeaters based on atomic ensembles, where the large number of atoms, in principle, enables highly efficient quantum memories [192, 29]. Nonetheless, the limited efficiencies demonstrated in current experiments with atomic ensembles [192, 103] prevents the construction of a practical quantum repeater based on currently existing setups.

Single emitter systems such as color centers and trapped ions have also been considered for quantum repeaters [48, 191]. The long coherence times demonstrated with, e.g. trapped ions make them desirable as quantum memories. Nonetheless, entanglement needs to be created non-locally between two memories in the initial step of a repeater. This requires efficient transfer of information from the quantum memories onto light in the form of single photons. To this end, it is an advantage to place the emitter inside a cavity, which can greatly enhance the light-emitter coupling [169, 181]. Entanglement swapping can then be performed with a cavity mediated CNOT gate [168, 66] but in this case, the detrimental effect of cavity loss and spontaneous emission from the emitters may prevent obtaining efficient entanglement swapping. The parameter characterizing the effect of dissipation in the emitter-cavity system is the cooperativity, C . It has been argued that a direct implementation of gates in a cavity will make the gate fidelity, F , have a poor scaling of $1 - F \sim 1/\sqrt{C}$ [115, 208]. To overcome this problem for current cavities with limited C , it has been suggested to employ entanglement purification after each swap operation to boost the entanglement but this either requires a large number of resources or a time consuming sequential generation of purification pairs [18, 61, 72, 166].

Here we analyze and compare a number of cavity-based quantum repeaters which combines various proposals for entanglement generation and cavity-assisted CNOT gates. We find that the best scheme is where high-fidelity entanglement is generated using a two-photon detection scheme similar to Ref. [68] and swapped to large distances using the heralded CZ-gate proposed in Ref. [26]. The heralded gate enables nearly perfect entanglement swapping when successful allowing for many swaps without the need of entanglement purification. As a result, high-rate entanglement distribution is achieved even for low cooperativities.

Compared to the other cavity-based repeaters, this high-fidelity repeater achieves up to two orders of magnitude higher secret key rate (see below) for realistic parameters and large distances (1000 km). Specifically, we have compared to repeaters where entanglement is generated using a single-photon detection scheme similar to Ref. [35], which allows for a better rate at the expense of fidelity. Furthermore, we have considered schemes where entanglement swapping is achieved using the deterministic CNOT gate suggested in Ref. [208], combining it with the local entanglement generation scheme of Ref. [209]. The advantage of this gate is that the fidelity scales as $1 - F \sim 1/C$, which is a significant improvement from the $1/\sqrt{C}$ scaling, characterizing the performance of a direct implementation of gates in a cavity. As a result, long-distance entanglement distribution can also be achieved with this gate but it requires cooperativities above 100, which might be challenging to achieve experimentally. Furthermore, we include the possibility of initial purification in repeaters based on the single-photon detection scheme in order to allow for the higher rate of this scheme to compensate for the lower fidelity compared to the two-photon detection

scheme.

To reflect a realistic near-term approach to quantum repeaters, we only consider scenarios with 2 or 4 qubits per repeater station. For the same reason, we also do not consider the possibility of intermediate entanglement purification. Here, initial purification refers to purification in the elementary links (see Fig. 5.1) while intermediate purification refers to purification in the subsequent stages of a repeater. We have numerically optimized all the considered repeater schemes for a range of cooperativities and distances to find the highest achievable secret key rate (see below). Note that a similar optimization of repeater schemes based on dynamical programming was described in Ref. [112]. In that work, both initial and intermediate entanglement purification was considered assuming high-fidelity operations. Our optimization is less detailed since we do not consider intermediate purification. On the other hand, we include how the errors of the operations depend on the physical parameters such as the cooperativity and investigate concrete physical implementations. Finally, we compare the high-fidelity repeater considered here to both an ion-trap repeater and one of the best repeaters based on atomic ensembles [192]. For a distance of 1000 km, the high-fidelity repeater outperforms both of these schemes for $C \gtrsim 30$.

5.2 High-fidelity quantum repeater

We will first describe the details of the high-fidelity quantum repeater, which we find to have the best performance and later discuss and compare with the various other schemes. The first step in any quantum repeater is to create non-local entanglement in the elementary links (see Fig. 5.1). To this end, a two-photon detection scheme,

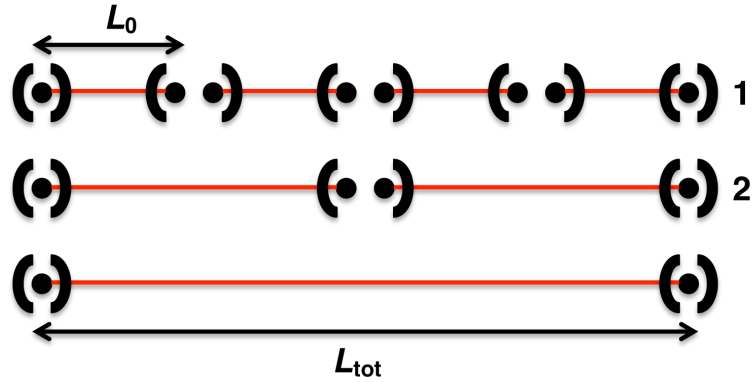


Figure 5.1: The general architecture of a quantum repeater. The total distance, over which entanglement should be distributed, is divided into elementary links of length L_0 connected by repeater stations pictured as cavities containing single emitters. After creating entanglement in the elementary links, the entanglement is swapped to larger distances by combining the elementary links. The numbers to the right in the figure refers to the swap level of the repeater. In the first swap level, the four elementary links are connected pairwise to make two longer links. In the second swap levels these two links are connected to create entanglement over the total distance. The total number of swap levels is thus 2 for this depicted setup.

as proposed in Ref. [68], is considered. The basic setup is shown in Fig. 5.2(a). Both emitters are initially prepared in the excited state $|e\rangle$ by a strong excitation pulse and the cavity is assumed to couple both the $|e\rangle \rightarrow |1\rangle$ and $|e\rangle \rightarrow |0\rangle$ transitions with equal coupling strength $g/\sqrt{2}$ (see Fig. 5.2(b)). The two transitions are, however, assumed to produce photons with different polarizations such that the emission of a cavity photon creates an entangled state between the photon and the emitter of the form $\frac{1}{\sqrt{2}}(|0\rangle|1_1\rangle_L + |1\rangle|1_2\rangle_L)$ where $|1_1\rangle_L$ ($|1_2\rangle_L$) is the single photon state with polarization 1 (2). The probability of one of the emitters to emit a photon of either polarization through the cavity, into an optical fiber transmitting it to the detection stage during a time interval $[0; T]$ is

$$P_{\text{phot}} = \frac{4C}{1+4C} (1 - e^{-\gamma(1+4C)T}), \quad (5.1)$$

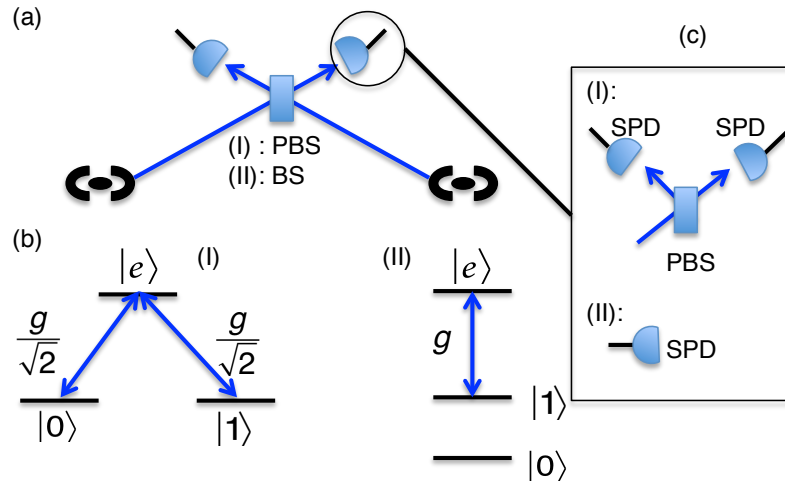


Figure 5.2: Entanglement generation in the elementary links where emission from two cavities are combined on a beam splitter. (a) shows the basic setup, (b) shows the level structure of the emitters and (c) shows the detection setup. (I) refers to the two-photon detection scheme and (II) refers to the single-photon detection scheme. Both schemes use a central station with either (I) three polarizing beam splitters (PBS) and four single-photon detectors or (II) a single balanced beam splitter (BS) and two single-photon detectors. g denotes the cavity coupling. For the two-photon scheme the levels $|0\rangle$ and $|1\rangle$ are assumed to have equal coupling of $g/\sqrt{2}$ to the excited state $|e\rangle$.

assuming perfect outcoupling to the fiber and that the decay rate of the cavity, κ , is much larger than the cavity coupling, g . We have here introduced the cooperativity $C = g^2/\kappa\gamma$, where γ is the spontaneous emission rate of the emitters into modes other than the cavity. This is the key parameter characterizing the performance of the cavity-based repeaters. The photons are sent from the cavities to a central polarizing beam splitter (PBS). If two photons of the same polarizations are incident on the PBS, they leave in different output ports, while photons of different polarization leave in the same output port. The outputs are then sent to a second set of polarizing beam splitters and all four outputs of these are finally measured with single photon detectors (SPD). A click in a detector in each arm heralds the creation of the Bell state $|\Phi^+\rangle = (|00\rangle + |11\rangle)/\sqrt{2}$ between the emitters up to a local qubit rotation. Neglecting dark counts of the detectors, the heralded fidelity is unity (see App. D.2) while the success probability of the scheme is $P_{\text{2click}} = \frac{1}{2}\eta^2 P_{\text{phot}}^2$ with η being the total detection efficiency including inefficient outcoupling of the cavity light, losses in the transmission fibers and imperfect detectors. Compared to schemes based on single-photon detection (see below) the rate of this two-photon detection scheme decreases rapidly with decreasing η . On the other hand, it has a high fidelity, which is desirable for the subsequent stages of entanglement swapping, as we will show below.

For entanglement swapping, we find that the best performance is achieved using the heralded CZ-gate described in Ref. [26]. The gate was described in detail for ^{87}Rb atoms in Ref. [26] but it can be easily generalized to any set of emitters, which have the appropriate level structure (see Fig. 5.3). Note that the gate operation relies on only qubit state $|1\rangle$ coupling to the cavity while the states $|0\rangle$ and $|1\rangle$

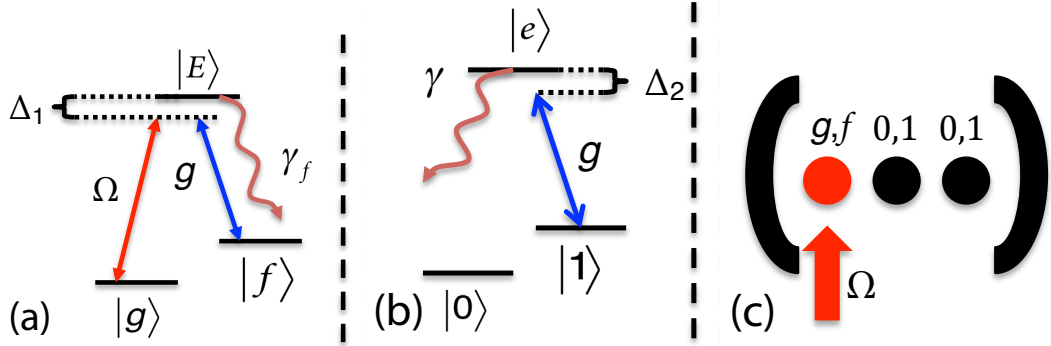


Figure 5.3: Schematics of the heralded CZ gate [26]. (a) is the level structure of the auxiliary atom, (b) is the level structure of the qubit atoms and (c) shows the cavity containing the auxiliary atom and the two qubit atoms. Assuming that $|E\rangle$ only decays to $|f\rangle$ by e.g. driving the transition $|g\rangle \rightarrow |E\rangle$ with a two photon process, any spontaneous emission or cavity decay will change the state of the auxiliary atom from the initial state $|g\rangle$ to $|f\rangle$. The gate is thus conditioned on measuring the auxiliary atom in state $|g\rangle$ at the end of the gate.

had equal cavity couplings in the entanglement generation scheme. To achieve this change in couplings, the state $|0\rangle$ should be mapped to another level in between the entanglement generation and the gate operation. For a realization with alkali atoms where the qubit states would be realized in the hyperfine ground states, this could be achieved by applying a magnetic field to resolve the hyperfine states and applying a microwave pulse resonant with only the $|0\rangle$ state.

In the heralded gate, the cavity is assumed to contain two qubit atoms and one auxiliary atom to facilitate the gate. The auxiliary atom is initialized in a state $|g\rangle$ that does not couple to the cavity and it would therefore not interfere with the entanglement generation scheme. By addressing the auxiliary atom with a weak laser pulse, an AC Stark shift is introduced, which gives a phase that depends on the state of the qubit atoms. Together with single qubit rotations, this enables a CZ-gate between the two qubit atoms. Furthermore, the auxiliary atom can function as an

error detector in the sense that any cavity decay or spontaneous emission changes the state of the atom. Performing a heralding measurement of the state of the auxiliary atom at the end of the driving pulse removes all dissipative errors. As a consequence, the gate gets limited only by non-adiabatic effects. As shown in Ref. [26], a heralded error below 4×10^{-5} is possible with a gate time of $\sim 377/(\gamma\sqrt{C})$, where γ is the atomic linewidth. The failure probability of the gate scales as $1/\sqrt{C}$ and the high fidelity thus comes at the cost of a finite but possibly low failure probability. A CZ gate combined with single qubit rotations is sufficient to perform direct entanglement swapping. For simplicity, we assume perfect single qubit rotations and 100% efficient measurement of atomic states for all schemes considered. Relaxing this assumption will in general decrease the rate of all the considered repeater schemes but schemes with a high number of swap levels, such as the high-fidelity repeater, will be influenced more on the rate than schemes with a low number of swap levels.

The advantage of the high-fidelity repeater can be understood by considering the requirement for reaching a certain threshold fidelity, F_{final} of the distributed pair. In this case, the maximum number of swap levels is $N_{\text{max}} \sim -\log_2(F_{\text{final}}/(\epsilon_0 + \epsilon_g))$, where $\epsilon_0, \epsilon_g \ll 1$ are the errors of the initial entanglement generation and the entanglement swapping respectively. The combination of the high-fidelity two-photon detection scheme and the heralded gate thus makes it possible to have a repeater with many elementary links while maintaining a high fidelity of the final distributed pair even for low cooperativities since the error of the heralded gate is still high in this regime.

5.2.1 Secret key rate

We imagine that the distributed entanglement is used to generate a secret key between two parties referred to as Alice and Bob. There exist various quantum key distribution schemes [195, 17, 80, 36], however, the general idea is that Alice and Bob can exclude that an eavesdropper has any information about the key by measuring their qubits and comparing results. We will assume that a six-state version of the BB84 protocol described in Ref. [36] is used to generate the secret key. This protocol consists of three main steps. First Alice and Bob picks a basis according to some probability distribution and measure the state of their qubits thereby producing two bit strings referred to as the *raw key*. Afterwards they compare their choice of basis and only keep the bits where they chose the same measurement basis thereby producing a *sifted key*. Finally, Alice and Bob estimate the information that some eavesdropper could possibly have obtained about their key and perform privacy amplification [195]. If the errors are not too big, they can obtain a shorter but completely secure key. For the six-state protocol, the secret key rate, r_{secret} can be defined as

$$r_{\text{secret}} = r_{\text{dist}} p_{\text{sift}} f_{\text{secret}}, \quad (5.2)$$

where r_{dist} is the distribution rate of the entangled pairs, p_{sift} is the probability that Alice and Bob choose the same measurement basis and f_{secret} is the secret key fraction, which depends on the fidelity of the distributed pairs. We assume a worst case scenario where the distributed pairs are Werner states of the form

$$\rho = F|\Phi^+\rangle\langle\Phi^+| + \frac{1-F}{3}\left(|\Phi^-\rangle\langle\Phi^-| + |\Psi^+\rangle\langle\Psi^+| + |\Psi^-\rangle\langle\Psi^-|\right). \quad (5.3)$$

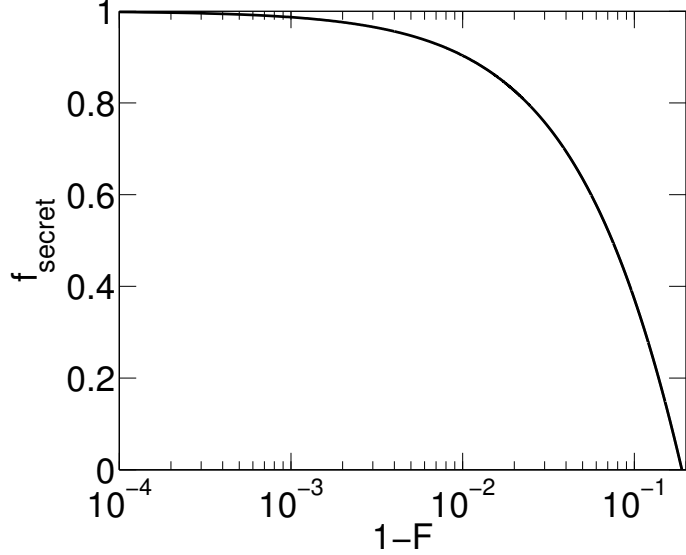


Figure 5.4: Secret key fraction (f_{secret}) as a function of the infidelity, $1 - F$, of the final entangled pair. For $1 - F \gtrsim 19\%$ it is no longer possible to extract a secret key from the raw keys.

For such states, it is shown in Ref. [195] that the secret key fraction in the six-state protocol can be estimated in the limit of infinitely long raw keys to be

$$f_{\text{secret}} = 1 - h(\epsilon) - \epsilon + (1 - \epsilon)h\left(\frac{1 - 3\epsilon/2}{1 - \epsilon}\right), \quad (5.4)$$

where $\epsilon = 2(1 - F)/3$ and $h(p) = -p\log_2(p) - (1 - p)\log_2(1 - p)$ is the binary entropy.

Eq. (5.4) is valid in the limit of perfect sifting and privacy amplification, which we assume to be the case. Furthermore, we assume an asymmetric version of the six state protocol, where one basis is used almost all the time such that $p_{\text{sift}} \approx 1$ [195].

Fig. 5.4 shows how the secret key fraction depends on the fidelity of the distributed pairs. As shown in the figure, high-fidelity pairs are required in order to have a non-vanishing secret key fraction. Again, this points to the high-fidelity two-photon detection scheme and the nearly error-free heralded entanglement swapping as the best choice for the repeater.

5.2.2 Repeater architecture

The main goal of the quantum repeater is to overcome the effect of fiber losses. We model the fiber losses with a transmission efficiency $\eta_f = e^{-L_0/2L_{\text{att}}}$, where L_0 is the length of the elementary links of the repeater and L_{att} is the fiber attenuation length. η_f enters in the total detection efficiency η as described above. For a given resource of $2^n + 1$ repeater stations, one can either use all stations in a single repeater with n swap levels or one can construct a number of parallel, independently operated chains of repeaters with less swap levels. Increasing the number of swap levels, decreases the fiber losses in the elementary links and thus increases the rate of entanglement generation. If, however, the length of the elementary links is already small, e.g. imperfect SPD dominates the rate, then increasing the number of swap levels does not lead to any improvement. In this case it is advantageous to use the extra repeater stations to make another repeater with less swap levels, which runs in parallel with the already existing one. To make a proper assessment of the performance of repeater one should therefore include that adding swap levels costs resources in the form of additional repeater stations. In our comparison, we therefore consider a normalized secret key rate, $\tilde{r}_{\text{secret}} = r_{\text{secret}} / (\# \text{ of stations})$, which is the secret key rate divided by the total number of repeater station instead of the bare secret key rate. To evaluate the performance of the repeater we calculate the achievable rate $\tilde{r}_{\text{secret}}$ as described in Appendix D.4 with the assumptions summarized in Tab. 5.2 about fiber losses etc.. The resulting rate for various swap level used in the repeater is shown in Fig. 5.5 as a function of distance. As seen in the figure, the optimal number of swap level changes with distance while considering the normalized secret key rate. The rate was

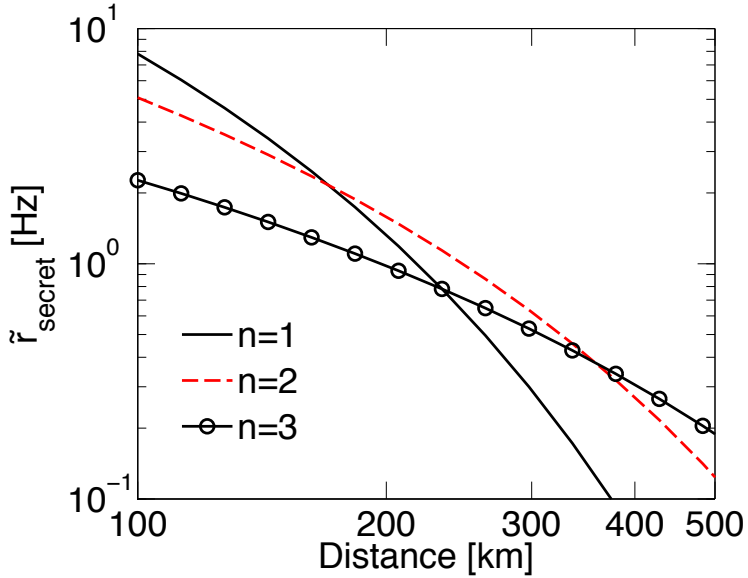


Figure 5.5: Normalized secret key rate per station ($\tilde{r}_{\text{secret}}$) as a function of the distribution distance for a high-fidelity repeater consisting of the two-photon entanglement generation scheme and the heralded gate for entanglement swapping. We have considered $n = 2, 3$ and 4 swap levels and have assumed a cooperativity of $C = 100$ and two qubits per repeater station. The secret key rate was calculated as described in App. D.4 with the assumptions summarized in Tab. 5.2.

calculated as described in App. D.4 for a cooperativity of 100 with the assumptions summarized in Tab. 5.2 about fiber losses, detection efficiencies etc. For distances $\lesssim 150$ km, only a single swap level is needed since the fiber losses are relatively small while more swap levels are needed as the distance increases.

In most repeater schemes, the qubits in each repeater station are assumed to be operated simultaneously with half of the qubits being used to generate entanglement with the neighboring station to each side such that entanglement attempts in all the elementary links are done simultaneously. We will refer to this as a *parallel* repeater. We will, however, also consider another sequential way of operating the qubits, where all qubits in a station are first used to make entanglement in one elementary link.

After this has been obtained, all but one qubit are then used to make entanglement over the neighboring link in the opposite direction. This is referred to as a *sequential* repeater. The advantage of the sequential repeater is that the rate of the lowest level in the repeater, the entanglement generation, is increased. This comes at the cost of a waiting time between entanglement attempts in neighboring links. As the number of qubits per repeater station increases the sequential repeater will start to outperform the parallel repeater. We find that this happens with 4 qubits per repeater station (see Sec. 5.4).

5.3 Other cavity based repeaters

We have found that the high-fidelity repeater that we have described above outperforms a number of other cavity-based repeater schemes, which can be constructed with different schemes of entanglement generation and CNOT gates. Below, we describe the constituents of these other schemes and compare them to those of the high-fidelity repeater

5.3.1 Single-photon entanglement creation

It has also been suggested to use single-photon detection schemes similar to Ref. [35] to generate entanglement in the elementary links. The setup of a single-photon detection scheme is also shown in Fig. 5.2. We assume that the two emitters are initially prepared in a state

$$(1 - \epsilon^2)|00\rangle + \epsilon^2|ee\rangle + \epsilon\sqrt{1 - \epsilon^2}(|0e\rangle + |e0\rangle) \quad (5.5)$$

by a weak excitation pulse such that the excitation probability is ϵ^2 . An emitter can then go from state $|e\rangle$ to state $|1\rangle$ by emitting a cavity photon. The emitted photons are collected from the cavities and combined on a balanced beam splitter (BS) on a central station between the two cavities. Neglecting losses, the detection of a single photon after the BS will project the state of the emitters into the Bell state $|\Psi^+\rangle = \frac{1}{\sqrt{2}}(|01\rangle + |10\rangle)$, up to a single qubit rotation, in the limit $\epsilon^2 \ll 1$, where we can neglect the possibility of double excitations. The probability of an emitter to go from $|e\rangle$ to $|1\rangle$, by emission of a cavity photon during a time interval $[0; T]$, is P_{phot} (see Eq. (5.1)) under similar assumptions as in the two-photon scheme described above. Neglecting dark counts but including losses, the total probability of a single click at the central station is $P_{\text{1click}} = 2\eta P_{\text{phot}}\epsilon^2(1-\epsilon^2) + (2\eta-\eta^2)P_{\text{phot}}^2\epsilon^4$ with η being the total detection efficiency as for the two-photon scheme. The first term is the probability to emit and detect a single photon while the second term is the probability of emitting two cavity photons but only getting a single click (we assume that we do not have access to number-resolving detectors). The probability, to have a single click and have created the state $|\Psi^+\rangle$, is $P_{\text{correct}} = 2\eta P_{\text{phot}}\epsilon^2(1 - \epsilon^2)$. The average heralded fidelity conditioned on a single click is thus $F_1 = P_{\text{correct}}/P_{\text{1click}}$. To lowest order in ϵ , $F_1 \sim 1 - (1 - \eta/2)P_{\text{phot}}\epsilon^2$ while the success probability is $P_{\text{1click}} \sim 2\eta P_{\text{phot}}\epsilon^2$. There is thus a tradeoff set by ϵ^2 between the success probability and the fidelity for the single-photon detection scheme. This is in contrast to the two-photon detection scheme where $F = 1$ regardless of success probability.

The success probability of the single-photon detection scheme is not as sensitive to the detection efficiency η as the two-photon detection scheme as shown in

Fig. 5.6. If the detection efficiency η is large, the two-photon scheme is desirable since it will have both a high success probability and a high fidelity. However, if η is small, the single-photon scheme will be advantageous since it has a relatively high success probability. Due to the possible high success probability but limited fidelity of the single-photon scheme, it might be desirable to combine it with entanglement purification to increase the final fidelity. In this way, the higher success probability of the single-photon scheme may compensate the lower fidelity. We have therefore considered the possibility of initial entanglement purification in repeaters based on the single-photon detection scheme as described below.

5.3.2 Initial purification

Based on a detailed analysis of the various errors that limit the fidelity for the single-photon scheme including dark counts of the detectors (see App. D.1 for details), we find that the purification protocol of Ref. [18] effectively corrects for the errors in the single-photon scheme and we assume that this is used for the initial purification. However, as pointed out in Ref. [158] an improved fidelity, at the expense of a factor of ~ 2 in the success probability, can be obtained by only accepting outcomes where the two heralding qubits are found in state $|1\rangle|1\rangle$ instead of also accepting $|0\rangle|0\rangle$ outcomes. We will also consider this modification to the purification protocol of Ref. [18]. The protocol relies on a CNOT operation, which we assume to be made with the same gate used to perform the subsequent entanglement swapping (see below). To reflect the most realistic near-term quantum repeaters we consider at most 4 qubits per repeater stations. We therefore assume that the purification is performed in a

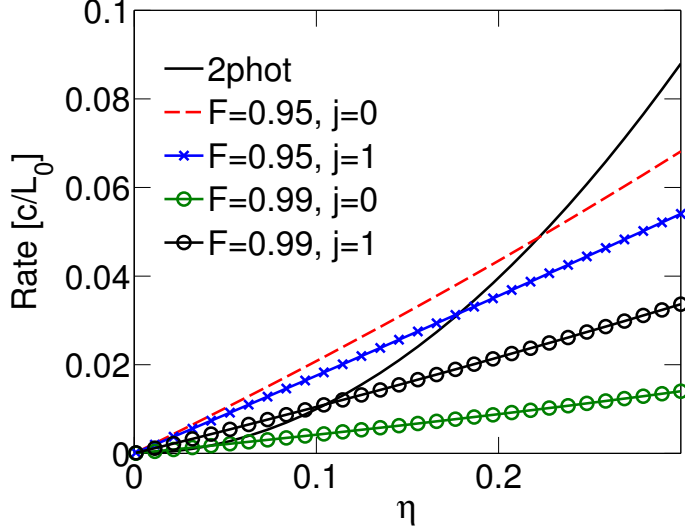


Figure 5.6: Rate of entanglement generation for the two-photon scheme and the single-photon scheme with target fidelity $F \geq 0.95$ and $F \geq 0.99$ both without purification ($j = 0$) and with one round of purification ($j = 1$). The rate is shown as a function of the total detection efficiency η . We have neglected dark counts and assumed that the CNOT gate is deterministic and have perfect fidelity. The rate has been calculated as described in App. D.4. Furthermore, we have assumed that each repeater station contains 4 qubits, which are either used for purification or to increase the rate of the entanglement generation.

pumping scheme [75], where the fidelity of a single pair is pumped by combining it with pairs of lower fidelity since this requires the lowest number of qubits per station.

The effect of combining the single-photon scheme with initial purification is shown in Fig. 5.6 where, for simplicity, the purification is assumed to be performed with a deterministic gate with perfect fidelity and without the modification of Ref. [158]. If high fidelity pairs are desired for, e.g., a repeater with many swap levels, entanglement purification can increase the rate of the entanglement generation. For high collection efficiencies it is, however, desirable to use the two photon scheme since this has a higher rate. In particular, the two photon scheme becomes desirable if high fidelity pairs are required.

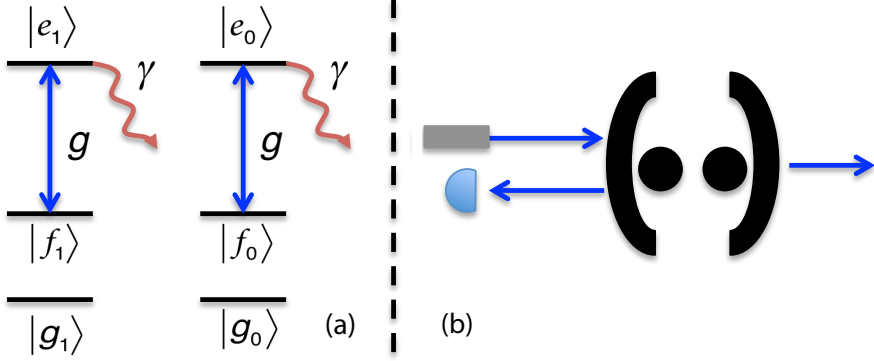


Figure 5.7: Deterministic gate based on reflection and teleportation based CNOT operation [209, 208](a) Level structure of the qubit atoms. The levels $|r_0\rangle$ and $|r_1\rangle$ where $r = g, f$ or e are assumed to be degenerate such that the quantum information is encoded in the horizontal degrees of freedom. (b) The setup to create entanglement between the level states $|g\rangle, |f\rangle$ of the atoms. Weak coherent light is sent onto the cavity and any reflected light is measured with a SPD.

5.3.3 CNOT gates

In our analysis, both the initial purification and the subsequent entanglement swapping involves a cavity-based CNOT gate. Besides the heralded CNOT gate used in the high-fidelity repeater, which we will refer to as *gate 1*, a deterministic cavity-based gate proposed in Ref. [208] could be used. Combining the gate scheme of Ref. [208] with the local entanglement generation scheme of Ref. [209] results in a deterministic CNOT gate with an error scaling as $1/C$. We will refer to this gate as *gate 2*. This gate does not require an auxiliary atom as gate 1 but rather two auxiliary levels in the qubit atoms as shown in Fig. 5.7(a). In this scheme, the quantum information is stored in the horizontal/qubit degree of freedom (subscripts 0 and 1) and the vertical/level degree of freedom (denoted g and f) is used to make an entanglement assisted CNOT gate between the atoms. Separating the qubit degree of freedom from the level degree of freedom, the gate works by ideally making the

transformation

$$|q1\rangle|q2\rangle \otimes |gg\rangle \rightarrow |q1\rangle|q2\rangle \otimes \frac{1}{\sqrt{2}}(|gf\rangle + |fg\rangle), \quad (5.6)$$

where $|g\rangle, |f\rangle$ denote the vertical states and $|q1\rangle$ ($|q2\rangle$) is the qubit state of the first (second) qubit, which could be entangled with atoms at neighboring repeater stations. The entanglement between the levels $|g\rangle$ and $|f\rangle$ can be used to make a CNOT gate, if the levels of the atoms can be measured non-destructively, i.e. without revealing any information about the qubit state as described in Ref. [208]. Both the transformation shown in Eq. (5.6) and the non-destructive measurements can be obtained by sending a weak coherent pulse onto a two-sided cavity and detecting any reflected light (see Fig. 5.7(b) and App. D.3). If the light is resonant with the empty cavity mode, atoms in $|f\rangle$ will shift the cavity resonance. Consequently, photons will be reflected and constitutes a QND measurement of the presence of atoms in $|f\rangle$. Spontaneous emission from the atoms will limit the fidelity of the gate to $F \sim 1 - 1.2/(\eta_d C)$, where η_d is the detection efficiency and $C = g^2/\kappa\gamma$ is the cooperativity. The gate time is limited by the time of the single qubit rotations and the coherent pulses. We assume that this gives a gate time on the order of $10 \mu s$.

As a benchmark, we also consider a naive approach where a direct gate between two qubits is made in a cavity without the use of an auxiliary atom or auxiliary atomic states. To characterize such a gate, we consider a situation where the setup of gate 1 is used to make a deterministic gate by simply ignoring the heralding condition. We will refer to this gate as *gate 3*. For such a gate, we find that the gate fidelity will scale as $1 - F \sim 3/\sqrt{C}$ and the time of the gate will be limited by the time of the single qubit rotations which we assume to be $\sim 10 \mu s$.

Gate	Fidelity	Probability	Gate time
1	$F = 4 \cdot 10^{-5}$	$P_g \sim 1 - 6/\sqrt{C}$	$377/(\gamma\sqrt{C}) + 10 \mu\text{s}$
2	$F \sim 1 - 1.2/(\eta_d C)$	$P_g = 1$	$10 \mu\text{s}$
3	$F \sim 1 - 3.6/\sqrt{C}$	$P_g = 1$	$10 \mu\text{s}$

Table 5.1: Characteristics of the three gates considered for the cavity-based repeaters. C is the cooperativity of the atom-cavity system and η_d is the single photon detection efficiency in gate 2. The time of the single qubit rotations is assumed to be $10 \mu\text{s}$.

The characteristics of the three gates we consider are summarized in Tab. 5.1 and illustrated in Fig. 5.8. It is clear, that a repeater based on gate 3 will never be advantageous but we consider it as a reference since the physical requirements for implementing this gate are less than for gate 1 and 2, which requires either an auxiliary atom or auxiliary atomic levels.

5.4 Numerical optimization

We have numerically optimized the secret key rate per repeater station for both the high-fidelity repeater and all other cavity-based repeaters consisting of the elements considered in Sec. 5.3. The secret key rate is calculated as described in Sec. 5.2.1 and App. D.4. It depends on experimental parameters such as the efficiency of single photon detectors, dark count rates. The values of these parameters are assumed fixed and are thus not part of the optimization. All the experimental parameters are summarized in Tab. 5.2 together with the values assumed in the optimizations. We have assumed fiber transmission losses for telecom wavelengths, which may require wavelength conversion techniques [3]. The free parameters in the optimizations are

Parameter	Value	Description
γ	$2\pi \cdot 6$ MHz	Spontaneous emission rate of atoms. This enters in the probability of emitting a photon in the entanglement generation schemes (see Eq. (5.1)) and in the gate time of gate 1 and 2.
η_d	50%	Combined efficiency of SPD detectors and outcoupling of light from the cavities. This enters in the total detection efficiency η in the entanglement generation schemes since $\eta = \eta_d \eta_f$. It also enters the fidelity of gate 2.
L_{att}	22 km	Attenuation length of the fibers. The total transmission probability over a length L is assumed to be $\eta_f = e^{-L/L_{att}}$. The value assumed corresponds to telecom wavelengths.
τ_{local}	10 μ s	Time of local qubit operations
r_{dark}	25 Hz	Dark count rate of SPD detectors. We include dark counts in the entanglement generation step but not in the gate operations since the gate operations are assumed to be fast.
c	$2 \cdot 10^5$ km/s	Reduced speed of light in the transmission fibers [192].

Table 5.2: Experimental parameters which influence the rate and fidelity of the repeaters. The second column gives the values used in all optimizations.

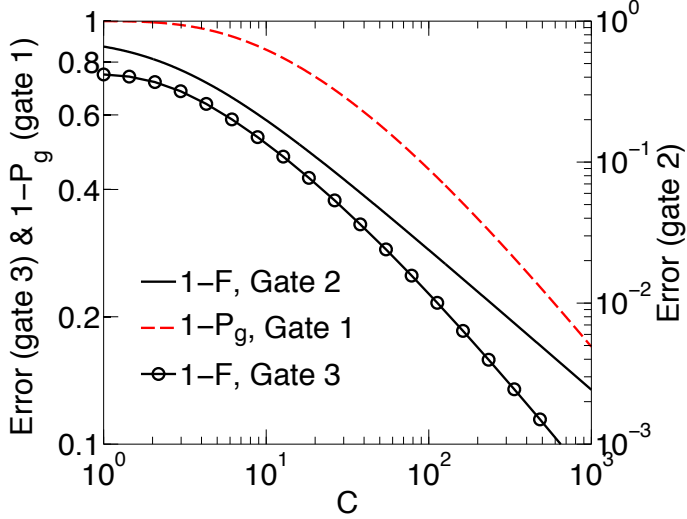


Figure 5.8: Characteristics of the three gates described in the text. The errors of gate 2 (black/solid line, right axis) and gate 3 (black/circled line, left axis) are shown as a function of the cooperativity. The error is defined as $1 - F$ where F is the fidelity of the gate. We have assumed $\eta_d = 0.5$ for the error of gate 2. Gate 1 has conditional fidelity ~ 1 but a finite failure probability $1 - P_g$ which is also shown as a function of cooperativity (red/dashed line, left axis).

the number of swap levels, the number of purifications with/without the modification of Ref. [158] and whether a parallel or sequential repeater protocol is used. In the optimizations, we calculate the secret key rate on a grid of all these parameters and pick the combination giving the highest rate. Fig. 5.9 shows a specific example where the combination of the single-photon scheme with gate 2 is investigated for a parallel repeater and a cooperativity of 100. The number of swap levels and purifications, giving the highest rate for a specific distance, can be directly read off from the figure. The same calculations are then done for a sequential repeater protocol and compared to the parallel repeater protocol with/without the modified purification in order to find the highest rate for this specific combination of entanglement generation scheme and CNOT gate. This is done for all combinations of entanglement generation schemes

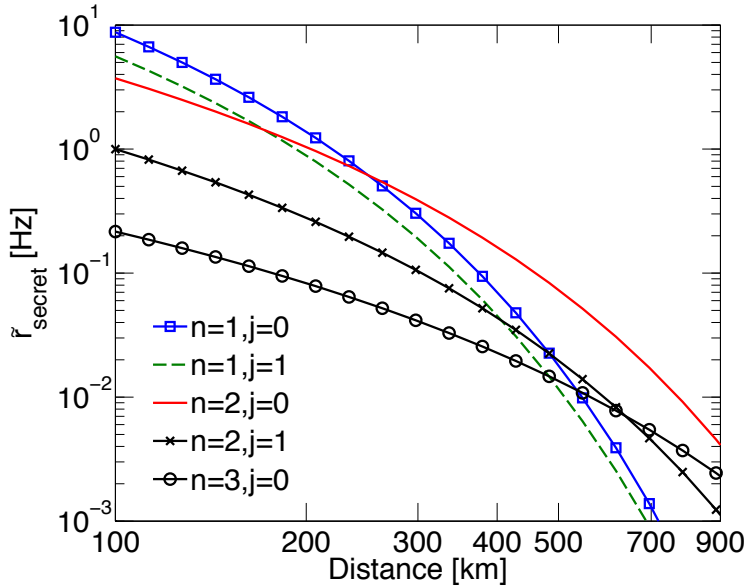


Figure 5.9: Normalized secret key rate per station ($\tilde{r}_{\text{secret}}$) as a function of the distribution distance (Distance) for a parallel repeater based on the single photon generation scheme and gate 2. The cooperativity was assumed to be 100 and we assumed 4 qubits per repeater station. The optimal number of swap levels (n) and purification rounds (j) for a given distance can be directly read off from the plot as the combination giving the highest rate. Note that because the gate fidelity is limited, curves with $j = 2$ and $n = 3, j = 1$ are not shown since they result in a much lower secret key rate. The purification schemes was considered to be without the modification of Ref. [158].

and CNOT gates. The optimal evolution time, T , and excitation probability, ϵ , in the entanglement generation schemes are found for each grid point using a built-in numerical optimization in the program MATLAB. The key parameter, determining the performance of the CNOT gates, is the cooperativity (see Tab. 5.1). We therefore optimize for cooperativities $C \in [10; 1000]$ and distances between 100 km and 1000 km. Finally, the optimizations are performed for both 2 qubits per repeater station and 4 qubits per repeater station. Note that the auxiliary atom used in gate 1 is not counted as a qubit and schemes based on this gate thus in principle contain an additional atom per repeater station.

We model the effect of the non-perfect gates, as depolarizing channels such that the output of a gate operation described by a unitary U_S working on a set \mathcal{S} of two qubits is

$$\tilde{\rho} = F' U_S \rho U_S^\dagger + \frac{1 - F'}{4} (\text{Tr}\{\rho\}_{\mathcal{S}} \otimes \mathbb{1}_S), \quad (5.7)$$

where $F = F' + (1 - F')/4$ is the fidelity of the gate, $\mathbb{1}_S$ is the identity matrix of the set, $\text{Tr}\{\dots\}_{\mathcal{S}}$ is the trace over the set and ρ is the initial density matrix describing the system before the gate operation. We use Eq. (5.7) to propagate the density matrix from the entanglement generation (see App. D.1-D.2) through the steps of initial purification and entanglement swapping and calculate the average fidelity of the distributed pairs. To calculate the secret key fraction, we treat the distributed pairs as Werner states as described in section 5.2.1.

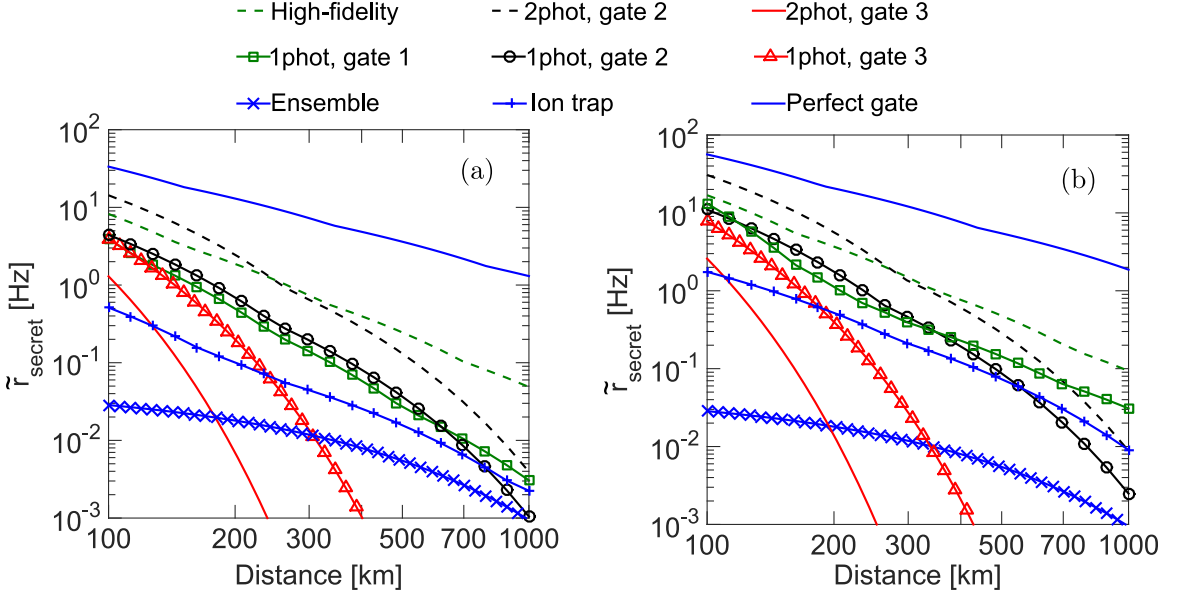


Figure 5.10: Normalized secret key rate per station ($\tilde{r}_{\text{secret}}$) as a function of the distribution distance (Distance) for the high-fidelity repeater and other cavity-based repeaters assuming a cooperativity of $C = 100$. (a) is for 2 qubits per repeater station while (b) is for 4 qubits per repeater station. The other cavity-based repeaters are labelled as, e.g., “1phot, gate 2”, which indicates that it is a repeater based on the single-photon detection scheme and gate 2. The rate of an ensemble-based repeater (“Ensemble”) is also shown [193]. For simplicity, we have assumed a fixed number of four swap levels in the ensemble-based repeater even though a smaller number of swap levels might increase the rate for small distances ($\lesssim 400$ km). Finally, we have plotted the rate of an ion trap repeater scheme (“Ion trap”) with a collection efficiency of 10% and gate fidelity of 99.3% and the ultimate rate obtainable with perfect deterministic gates and perfect entanglement generation with the two-photon scheme (“Perfect gate”) for comparison. For the ion trap repeater we have plotted the highest rate obtainable with either the one-photon or two-photon scheme.

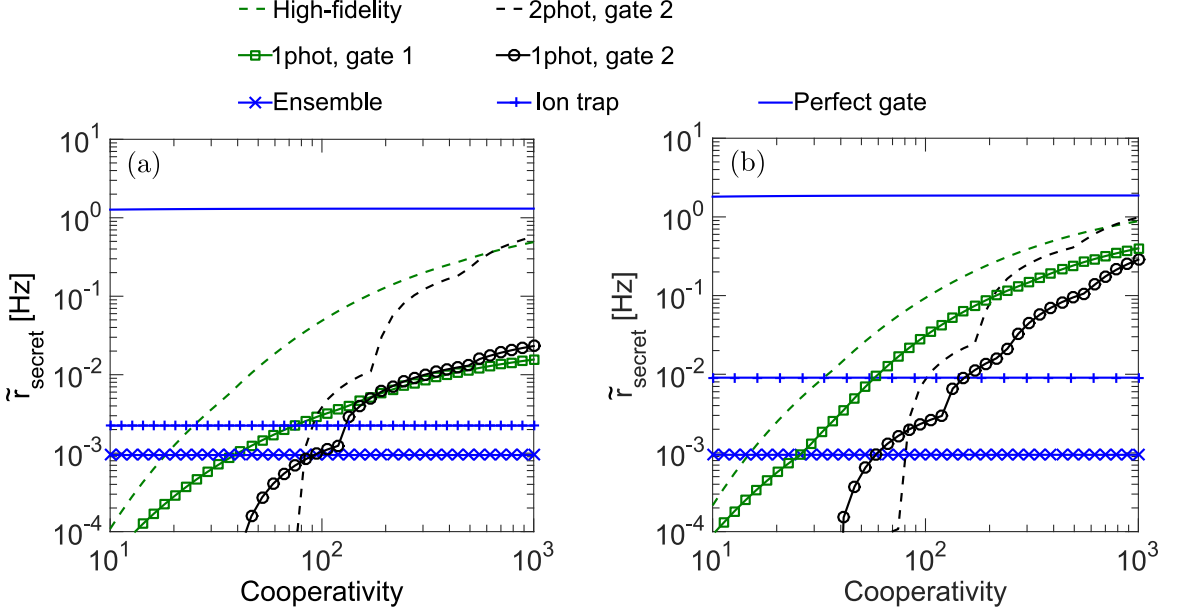


Figure 5.11: Normalized secret key rate per station ($\tilde{r}_{\text{secret}}$) as a function of the cooperativity (C) for the high-fidelity repeater and other repeaters assuming a distribution distance of 1000 km. (a) is for 2 qubits per repeater station while (b) is for 4 qubits per repeater station.

The secret key rates per repeater station of the high-fidelity repeater and the other cavity-based repeaters are shown in Fig. 5.10 for distances $[100; 1000]$ km and a cooperativity of 100 and in Fig. 5.11 for a distance of 1000 km and cooperativities in the interval $[10; 1000]$. As shown in Fig. 5.10, the repeaters based on gate 3 are simply not able to distribute entanglement over large distances for realistic cooperativities. As a consequence, repeaters based on gate 3 do not appear on Fig. 5.11 since their secret key rate is simply too low.

In general, the high-fidelity repeater (2-photon, gate 1) achieves the highest secret key rate for a broad range of cooperativities and long distances $\gtrsim 300$ km. This reflects both that this protocol allows for a higher number of swap levels and that the secret key rate favors the distribution of high-fidelity pairs since these gives the

highest secret fraction (see Fig. 5.4). It is also apparent from Fig. 5.11 that while repeaters based on gate 2 need cooperativities above 100 for a distance of 1000 km, repeaters based on gate 1 are able to function with much lower cooperativities around $30 - 40$. This is because the heralded gate has nearly unit fidelity, independent of the cooperativity. For high cooperativities or low distances, a repeater based on the two-photon detection scheme and gate 2 can give a slightly higher secret key rate than the high-fidelity repeater. This improvement is, however, less than a factor of 2 in the secret key rate. The steps in the rates of the schemes based on gate 2 in Fig. 5.11 originate from the fact that as the cooperativity increases, the fidelity of gate 2 increases and at some point the fidelity is high enough to allow for another swap level, which makes the rate increase abruptly. From the optimizations, we find that the sequential repeater architecture achieves slightly higher rates (less than a factor 2) than the parallel repeater architecture for 4 qubits per repeater station, while the opposite is the case for 2 qubits per repeater station.

In general, repeaters based on the two-photon detection schemes outperform repeaters based on the single-photon detection scheme except for repeaters based on gate 3. This reflects that repeaters based on gate 3 cannot perform many swap levels since the fidelity simply decreases too rapidly with the number of swap levels. The result of the optimization was that no swap levels were actually preferred for repeaters based on gate 3 for $C \leq 1000$. As a result, the elementary links in these repeaters are long and fiber losses therefore significantly decrease the total detection probability η in the entanglement generation schemes. In the limit of very low η , the one-photon scheme is advantageous since the success probability only depends

linearly on η . For the optimizations, we have assumed that the combined efficiency of the SPD detectors and outcoupling of light from the cavities is $\eta_d = 50\%$. If this efficiency is smaller, repeaters based on single-photon detection may be desirable. We also find that the purification protocol, in general, performs better with than without the modification of Ref. [158]. The improvement is, however, limited to a factor of $\lesssim 2$ for the parameters considered in Figs. 5.10-5.11.

It is important to stress that the rates plotted in Figs. 5.10-5.11 are the secret key rates divided by the total number of repeater stations. The actual distribution rate can thus be obtained by multiplying with the number of repeater stations. For the high-fidelity repeater, we find a secret key rate of ~ 16 Hz over 1000 km for 33 repeater stations and a cooperativity of 1000 assuming 2 qubits per repeater station. For a more modest cooperativity of 100, a secret key rate of ~ 1.5 Hz over 1000 km can be obtained.

We can compare the rate found here to the rate obtainable with repeaters based on atomic ensembles. In Ref. [193] an efficient repeater based on atomic ensembles is described, which achieves one of the highest distribution rates for repeaters based on atomic ensembles [192]. The fidelity of the distributed pair and the distribution rate are derived in Ref. [193] for a repeater with four swap levels corresponding to 17 repeater stations. Based on this, we have calculated the secret key rate assuming an optimistic, basic repetition rate of the ensembles of 100 MHz and memory and SPD efficiencies of 90%. The rate of the ensemble-based repeater is also shown in Figs. 5.10-5.11 for similar assumptions about fiber losses etc. as for the cavity-based repeaters. We have assumed that the repeater uses four swap levels for all distances

even though a smaller number of swap levels may be desirable for smaller distances ($\lesssim 400$ km) [193]. For a distance of 1000 km, we find a rate of ~ 0.03 Hz for 33 repeater stations. This shows that repeaters based on individual atoms in cavities may be very promising candidates for realizing efficient quantum repeaters with rates exceeding those obtainable with atomic ensembles. The main reason for this is that very efficient entanglement swapping can be realized in the cavity-based repeaters which greatly enhances the distribution rates for long distances. On the contrary, repeaters based on atomic ensembles and linear optics have an upper limit on the swapping efficiency of 50%.

For comparison we have also considered a repeater based on ion traps where there is no cavity to collect the light. Non-local entanglement can still be created by collecting the emitted light with a lens as demonstrated in Ref. [109] where a collection efficiency of 10% was reported. The entanglement swapping can be realized using a gate, which has been demonstrated experimentally with a fidelity of 99.3% and a gate time of $50\ \mu\text{s}$ [16]. Note that this fidelity was measured for the generation of a single state in Ref. [16] but we will assume it to be the fidelity of the entanglement swap. The rate of such a ion-trap repeater is shown in Figs. 5.10-5.11 with assumptions about fiber losses etc. summarized in Tab. 5.2. We have assumed a collection efficiency of 10% and as a result, the one photon scheme with modified purification performs better than the two-photon scheme for 4 qubits per repeater station. However for two qubits, where purification is not possible, the two-photon scheme is in general advantageous except for small distances (< 200 km). We have assumed a gate fidelity of 99.3% and have plotted the highest rate obtainable with either the one-photon or

two-photon scheme.

It is seen that the high-fidelity repeater outperforms the ion-trap repeater for $C \gtrsim 30$, which is mainly due to the low collection efficiency in the entanglement generation. The ultimate rate, obtainable with a repeater with perfect deterministic entanglement swapping and entanglement generation based on the two-photon detection scheme with a collection efficiency set by $4C/(1 + 4C)$, is also shown in Figs. 5.10-5.11. A similar repeater was considered in Ref. [191] to demonstrate the feasibility of repeaters based on trapped ions. For $C = 1000$, the high-fidelity repeater achieves only a factor of ~ 2 slower rate than this ultimate limit for a distance of 1000 km.

5.5 Conclusion

In conclusion, we have performed a detailed analysis of quantum repeaters based on individual emitters in optical cavities. We have found that a high-fidelity repeater based on the heralded gate described in Ref. [26] combined with a two-photon detection scheme is the best option over a large parameter regime and enables high secret key rates over large distances even for limited cooperativities < 100 . Compared with a number of other cavity based repeaters it achieves rates that are up to two orders of magnitude faster for long distances (1000 km) and cooperativities < 100 . For small distances or higher cooperativities, a repeater based on the deterministic CNOT gate described in Ref. [208] combined with a two-photon detection scheme can achieve rates which are slightly higher than the high-fidelity repeater but the improvement is less than a factor of 2.

We have also compared the high-fidelity repeater to the repeater in Ref. [193],

which is based on atomic ensembles. For a distance of 1000 km and $C \gtrsim 20$ the high-fidelity repeater begins to outperform the ensemble-based repeater and an improvement of more than two orders of magnitude in the secret key rate is possible for $C \gtrsim 100$. The main reason for the advantage of the high-fidelity repeater is that entanglement can be swapped very efficiently using the heralded CNOT gate described in Ref. [26]. Consequently, the number of swap levels in the repeater can be increased without the need of intermediate purification, which greatly enhances the rate for large distances. A similar advantage could in principle be achieved by resorting to a trapped ion system, where efficient gates can be implemented. For current systems, the collection efficiencies are, however, so low that a trapped ion system could be outperformed by a cavity system with a limited finesse of $C \gtrsim 30$. If the collection efficiency could be overcome, e.g. by placing the ions in a cavity with a high cooperativity, the rate can be substantially improved, but with $C > 1000$ the high fidelity repeater investigated here is within a factor of two of this ideal repeater. It should, however, be noted that we have compared schemes with strong physical differences in our analysis. The high-fidelity repeater requires an extra auxiliary atom while auxiliary atomic levels are required to decrease the error of the deterministic cavity-based CNOT gates. The ensemble-based and ion-trap repeaters are also very different physical systems compared to the cavity-based repeaters with individual atoms. The different experimental difficulties in realizing the physical requirements for the various repeater schemes should be included in a more advanced assessment.

Finally, we note that while we have investigated a number of different possible repeater protocols there may be even more advantageous procedures. Hence the

results that we have derived here should be seen as lower limits to the achievable communication rates. A particular interesting possibility could be to investigate proposals along the lines of Ref. [228, 227], which also rely on heralding measurements to detect errors during entanglement generation and two qubit operations. Possibly some of the ideas from these schemes could be used to improve the communication beyond what we have found here.

Chapter 6

Heisenberg-Limited Atom Clocks Based on Entangled Qubits

6.1 Introduction

Currently, atomic clocks based on optical transitions achieve the most precise [156, 23, 126] and accurate [52, 23] frequency references. Additionally, the development of optical frequency combs [78, 176, 114, 240] – establishing a coherent link between the optical and radio frequencies – enabled the application of optical frequency standards to a wide range of scientific and technological fields including astronomy, molecular spectroscopy and global positioning systems.

The improvement of frequency standards using quantum resources, such as entanglement [38, 6, 130, 184, 28], has been actively explored in recent years. While clock protocols based on uncorrelated atoms at best achieve a stability scaling $\propto 1/\sqrt{N}$, where N is the number of atoms – a scaling commonly known as the standard quan-

tum limit (SQL) [41] – the use of entangled resources, in principle, allows one to surpass this limit. However, a characterization of the improvement obtainable by using entanglement requires a detailed investigation of the decoherence present in the system. Previous studies have focused on two kind of noise sources: i) single particle decoherence resulting from the interaction of the atoms with the environment and ii) frequency fluctuations in the laser used to excite the clock transition [in the following also referred to as local oscillator (LO)]. It is well known that fully entangled states (e.g., Greenberger-Horne-Zeilinger (GHZ) states) allow for improved spectroscopic sensitivity, but in the same way that these states benefit from their increased sensitivity in the laser interrogation, they are generally prone to various types of noise sources canceling any quantum gain. It has therefore been long believed that such states fail to increase clock stability regardless of the noise model being used [24, 237, 184, 110]. On the other hand, it has been shown that for clocks with local oscillator noise limited stability, the use of moderately squeezed atomic states can yield a modest improvement over the SQL [6, 130]. A recent study demonstrated further that, in principle, highly squeezed states could achieve Heisenberg-limited stability (i.e., a $1/N$ scaling with the available resources representing the ultimate limit allowed by the laws of quantum mechanics [95]) using a complex adaptive measurement scheme [28]. At the same time, it has been shown that the single particle decoherence-limited regime can be reached for long averaging time at a logarithmic cost in N by interrogating uncorrelated atomic ensembles for suitably chosen times [183, 27].

In this chapter, we introduce a protocol involving groups of sequentially larger

GHZ states to estimate local oscillator deviations from the atomic reference in a manner reminiscent of the phase estimation algorithm [159]. Furthermore, we unify previous treatments of decoherence for atomic clocks and incorporate previous proposals involving uncorrelated atoms to effectively narrow the LO linewidth [183, 27] and thereby identify ultimate limits to the stability of atomic clocks based on entangled atoms. We find that for LO-noise limited clocks, the proposed quantum protocol is found to be nearly optimal, realizing the Heisenberg limit of clock stability up to a logarithmic correction in the particle number. Importantly, it reaches the fundamental noise floor resulting from individual dephasing of the clock qubits N times faster than the best known classical schemes, where N is the total number of particles employed.

The central idea of our approach can be understood as follows. In modern atomic clocks, the frequency of a LO is locked to an ultra-narrow transition of the clock atoms serving as the frequency reference. The long-term stability of such a clock after a given total averaging time τ is directly related to the precision by which the accumulated laser phase relative to the atoms can be determined. To this end, the phase is repeatedly measured in a standard Ramsey protocol [174]: Using the LO, the clock qubits are prepared in a superposition of $|1\rangle$ and $|0\rangle$, denoting the levels of the clock transition. After the qubits evolve freely for a time T (Ramsey interrogation time), they are subsequently measured in an orthogonal basis ($|\pm\rangle \equiv |1\rangle \pm |0\rangle$), which yields an estimate of the accumulated phase difference between the LO and the atomic frequency reference. It is known, that since each of these Ramsey sequences introduces measurement noise, it is optimal to extend the Ramsey time T to its maximum value

$T \rightarrow \tau$ [30].

A single GHZ state consisting of N entangled atoms – whose state after the interrogation is $|\text{GHZ}\rangle_T \propto |0\rangle^{\otimes N} + \exp(-iN\Phi_{\text{LO}})|1\rangle^{\otimes N}$ – accumulates the laser phase (denoted by Φ_{LO}) N times faster than an uncorrelated state, allowing a more precise phase measurement [95]. However, fluctuations in the laser frequency renders the laser phase a random variable with a probability distribution that grows in width as we increase the Ramsey time T . Whenever the laser phase realized in a particular Ramsey cycle induces a full phase wrap on the state [i.e., the atomic phase $N\Phi_{\text{LO}} \notin [-\pi, \pi]$], a subsequent measurement yields a 2π error in the estimation. For a single GHZ state, this accounts for a strict limitation on the maximally allowed Ramsey time in order to limit the initial variance of Φ_{LO} , and the resulting laser stability is found to yield no improvement over classical protocols [237].

To address this problem, we use a protocol involving an incoherent version of the *phase estimation algorithm* [159], similar to the one outlined in [94] but adapted to be applicable also when the frequency fluctuates and phases exceed 2π . The phase estimation algorithm has recently been successfully applied experimentally for global interferometric phase estimation [105, 152], and its use in clock synchronization protocols has been discussed [59]. Here, we demonstrate how the same techniques can be applied to guarantee optimal laser stability by allowing the Ramsey interrogation time to be extended to its maximum value.

Let us assume, for the moment, that the accumulated laser phase after the interrogation time T lies in the interval $\Phi_{\text{LO}} \in [-\pi, \pi]$, and has an exact binary representation $(\Phi_{\text{LO}} + \pi)/2\pi = \sum_{j=1}^M Z_j/2^j$, with digits $Z_j \in \{0, 1\}$ (both conditions will be

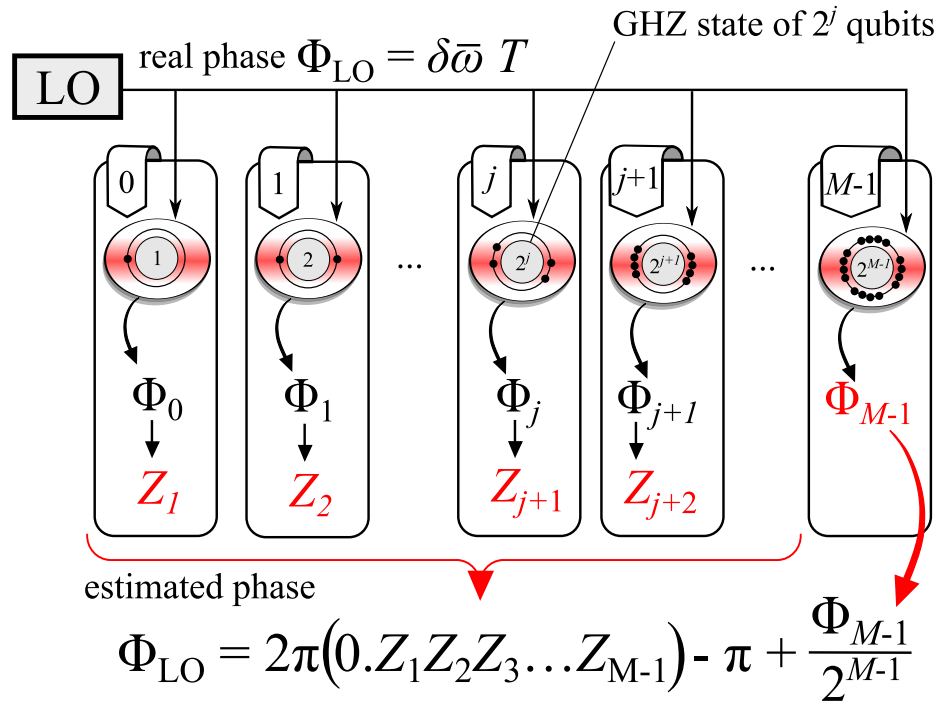


Figure 6.1: The proposed clock operation scheme employs M different groups of clock atoms prepared in correlated states of varying size to interrogate the relative phase Φ_{LO} of the LO field. A single group j contains n_0 independent instances of GHZ-like states, each entangling 2^j qubits, and therefore accumulating a phase $\Phi_j = 2^j \Phi_{\text{LO}} \bmod [-\pi, \pi]$ during a single cycle. Each group is then used to measure this phase, which gives a direct estimate on the digit Z_{j+1} in a binary representation of the LO phase $(\Phi_{\text{LO}} + \pi)/2\pi = (0.Z_1Z_2Z_3\dots)$, subsequently used to feedback the LO frequency.

relaxed below). One can then readily show that a GHZ state consisting of 2^{M-1} atoms picks up the phase $\Phi_{M-1} = 2^{M-1}\Phi_{\text{LO}} \bmod [-\pi, \pi] = \pi(Z_M - 1)$. Thus, by measuring if the phase is 0 or π , the last digit of the laser phase can be determined. However, without the remaining digits this information is useless. In our protocol, these digits are found by an additional, simultaneous interrogation with successively smaller GHZ states of $2^{M-2}, 2^{M-3}, \dots$ entangled atoms (see Fig. 6.1). Each of these states picks up a phase proportional to its size, $\Phi_j = 2^j\Phi_{\text{LO}} \bmod [-\pi, \pi]$, and this phase gets a contribution of $\pi(Z_j - 1)$. By distinguishing whether the phase is shifted by π or not, we can determine the value of the bit Z_j . The combined information provides an estimate with an accuracy given by the largest GHZ state, while the cascade increases the total number of atoms employed only by a factor of two: $\sum_{j=0}^{M-1} 2^j \approx 2^M = 2 \times 2^{M-1}$.

However, in the limit of large averaging times, the assumption $\Phi_{\text{LO}} \in [-\pi, \pi]$ is not justified anymore. Here, the optimal Ramsey time $T \sim \tau$ can attain values that induce phase wraps of the laser itself, causing the binary representation of the laser phase to contain digits $Z_j \neq 0$ for $j \leq 0$, which are inaccessible to the technique discussed above. To overcome this, we extend the cascade to the classical domain, and employ additional groups of *uncorrelated* atoms that interrogate the laser with successively decreasing interrogation times, or alternatively, using dynamical decoupling techniques [183, 27, 225]. Each of these ensembles acquires a phase that is reduced by multiples of two from the laser phase, and thus, following the arguments from above, allows one to gain information on the digits Z_j with $j \leq 0$. The information of all digits combined provides the total number of phase wraps, which in turn yields a Heisenberg-limited estimate of the laser phase. By this, the protocol effectively

eliminates all limitations arising from the LO noise, and allows the Ramsey time to extend to its optimal value.

6.2 Feedback loop

In the following, we provide a derivation of the above results combined with feedback analysis that allows us to characterize the achievable stability of a clock using our protocol. Modern clocks periodically measure the fluctuating LO frequency $\omega(t)$ against the frequency standard ω_0 of the clock atoms to obtain an error signal. After each Ramsey cycle of duration T [i.e., at times $t_k = kT$ ($k = 1, 2 \dots$)], the measurement data yield an estimate of the relative phase, $\Phi_{\text{LO}}(t_k) = \int_{t_k-T}^{t_k} dt [\omega(t) - \omega_0]$, accumulated by the LO. This estimate in turn is used to readjust the frequency of the LO: $\omega(t_k) \rightarrow \omega(t_k) - \alpha \Phi_{\text{LO}}^{\text{est}}(t_k)/T$, where $\Phi_{\text{LO}}^{\text{est}}(t_k)$ represents a suited estimator of the phase $\Phi_{\text{LO}}(t_k)$ ¹, and $\alpha < 1$ is a suitably chosen gain.

The stability of the actively stabilized LO, after a total averaging time τ , is characterized by the Allan deviation (ADEV) which is directly proportional to the measurement uncertainty $\Delta\Phi_{\text{LO}}(t_k)$ after each Ramsey cycle (see Appendix E.1),

$$\sigma_y(\tau) \equiv \frac{1}{\omega_0 \tau} \sqrt{\sum_{k=1}^{\tau/T} \sum_{l=1}^{\tau/T} T^2 \langle \delta\bar{\omega}_k \delta\bar{\omega}_l \rangle} \approx \frac{1}{\omega_0 \sqrt{\tau T}} \Delta\Phi_{\text{LO}}(T). \quad (6.1)$$

Here, $\delta\bar{\omega}_k = \Phi_{\text{LO}}(t_k)/T$ is the average detuning of the (stabilized) LO during the k th cycle. To obtain Eq. 6.1, we use the fact that after the frequency feedback the detuning averages become approximately uncorrelated for realistic laser spectra, $\langle \delta\bar{\omega}_k \delta\bar{\omega}_l \rangle \approx \langle \delta\bar{\omega}^2 \rangle \delta_{kl}$ [27, 7, 23]. Other noise sources (such as the bias of the linear

¹Alternatively, it is also possible to perform direct phase feedback.

estimator, the Dick effect, or a sub-optimal gain α [194]) are not fundamental, and neglected in the following.

6.3 Spectroscopic noises

For small values of the accumulated Ramsey phase, the ultimate precision by which this phase can be estimated is determined by the Cramér-Rao bound [57, 95] which links the estimation error to the quantum Fisher information (QFI) $\Delta\Phi_{\text{LO}} \sim 1/\sqrt{\mathcal{F}}$ (for a review, see [95]). The QFI, \mathcal{F} , is maximized, e.g., by the use of GHZ states for which $\mathcal{F} \sim N^2$. In clock stabilization, however, the LO frequency fluctuations account for the fact that the accumulated Ramsey phase is a random variable which can obtain large values, inherently violating the small phase assumption of the Cramér-Rao bound. In particular for a single GHZ states, phase wraps of the atomic phase, $\Phi(t_k) = N\Phi_{\text{LO}}(t_k) \notin [-\pi, \pi]$, cannot be detected. Consequently, the cycle time T has to be chosen such that the prior distribution of $\Phi(t_k)$ is well localized within $[-\pi, \pi]$. This limits the maximally allowed Ramsey time to a value $T_{\max} \sim \gamma_{\text{LO}}^{-1}/N^2$ (see Appendix E.3), where we assumed a white frequency noise spectrum of the LO, $S_\omega(f) = \gamma_{\text{LO}}$ (for $1/f$ -noise one finds the less stringent condition $T_{\max} \sim \gamma_{\text{LO}}^{-1}/N$). In most cases, this value lies below the optimal (i.e., maximal) value implied by Eq. 6.1 $T \sim \tau$, resulting in a laser stability for GHZ states which shows no improvement over the stability achieved with uncorrelated atoms [237, 184].

However, unlike the individual particle noise resulting in the finite atom linewidth γ_{ind} , the LO frequency fluctuations affect all clock atoms alike, and this *collective noise* does not represent a fundamental metrological limitation. We can use a cascade of

GHZ states of varying size to measure the Φ_{LO} in a binary representation, as discussed above. In general, the phase does not have an exact binary representation ending at the digit Z_M . We therefore employ n_0 duplicates at each level of the cascade (as opposed to sequential procedure suggested in [94]) ($n_0 = N / \sum_{j=0}^{M-1} 2^j \approx N/2^M$) to improve the precision. In the case where all digits Z_j ($j = 1 \dots, M-1$) are determined correctly according to the relation

$$Z_j = [2(\Phi_{j-1} + \pi) - (\Phi_j + \pi)]/2\pi, \quad (6.2)$$

the last group ($j = M-1$) then yields a Heisenberg-limited estimate of the LO phase with accuracy $(\Delta\Phi_{\text{LO}})_{\text{pr}} = 1/(2^{M-1}\sqrt{n_0}) = 2\sqrt{n_0}/N$.

6.3.1 Phase estimation with multiple GHZ groups

However, in general the estimation of the binary digits Z_j is not perfect. A rounding error occurs whenever $|\Phi_{j-1}^{\text{est}} - \Phi_{j-1}| > \pi/2$ (where Φ_j^{est} represents a suitable estimator derived from the n_0 measurement outcomes), leading to the wrong Z_j , and a variance contribution of $(2\pi 2^{-j})^2$ for Φ_{LO} . We can approximate their total variance contribution with the sum $(\Delta\Phi_{\text{LO}})^2_{\text{re}} = P_{\text{re}} \sum_{j=1}^{M-1} (2\pi 2^{-j})^2$, where $P_{\text{re}} = 2 \int_{\pi/2}^{\infty} d\phi \rho(\phi)$, and $\rho(\phi)$ is the Gaussian probability distribution of the error $\Phi_j^{\text{est}} - \Phi_j$ with a width proportional to $1/\sqrt{n_0}$ (see Appendix E.3). Consequently, rounding errors can be exponentially suppressed by choosing a sufficiently large value for n_0 . The total measurement uncertainty of this estimation scheme is thus $(\Delta\Phi_{\text{LO}})^2 = (\Delta\Phi_{\text{LO}})^2_{\text{pr}} + (\Delta\Phi_{\text{LO}})^2_{\text{re}}$. In Appendix E.3, we show that the optimal allocation of resources is achieved for the choice $n_0^{\text{opt}} \sim \frac{16}{\pi^2} \log(N)$, for which rounding errors are negligible,

yielding the total measurement accuracy

$$\Delta\Phi_{\text{LO}} \approx (\Delta\Phi_{\text{LO}})_{\text{pr}} = \frac{8}{\pi} \sqrt{\log(N)}/N. \quad (6.3)$$

This measurement precision obtains the Heisenberg limit (up to a logarithmic correction resulting from the cost to suppress rounding errors) despite it being applicable to a general (typically large) phase.

So far we have assumed that $\Phi_{\text{LO}} \in [-\pi, \pi]$ in each cycle. However, for realistic laser noise spectra there is always a finite probability that the LO phase Φ_{LO} lies outside the interval $[-\pi, \pi]$ after the interrogation time. Such phase wraps of the laser phase itself add to the final measurement uncertainty in Eq. 6.3 by the amount $(\Delta\Phi_{\text{LO}})_{\text{slip}}^2 = (2\pi)^2 P_{\text{slip}}$, where $P_{\text{slip}} = 2 \int_{\pi}^{\infty} d\phi \rho_{\text{LO}}(\phi)$, and ρ_{LO} is the Gaussian prior distribution of Φ_{LO} . Its width grows with $\gamma_{\text{LO}} T$, which puts a constraint on the maximally allowed Ramsey time $T \leq \frac{\pi^2}{4} \gamma_{\text{LO}}^{-1} [\log(\gamma_{\text{LO}} \tau N)]^{-1}$, and thus the achievable ADEV σ_y ($\propto 1/\sqrt{T}$) as we demonstrate in Appendix E.3.

This, however, does not represent a fundamental limitation as we can extend the scheme by adding additional classical measurements with a shorter Ramsey periods to assess the number of phase slips of the laser phase itself $\dots Z_{-3} Z_{-2} Z_{-1} Z_0$. As demonstrated in Appendix E.3, this allows extending the Ramsey time by a factor k adding only a negligible number of atoms $N^* \approx \frac{8}{\pi^2} \log(kN^2) \log_2(k) \ll N$.

6.3.2 Optimization

With all phase wraps counted correctly, the Ramsey time is only limited by individual noise processes. The finite linewidth of the atomic clock transition γ_{ind} gives rise to the fundamental constraint $T \leq \gamma_{\text{ind}}^{-1}/2^{M-1}$. For averaging times $\tau \leq \gamma_{\text{ind}}^{-1}/2^{M-1}$,

we can choose $T \approx \tau$, and using the optimized value for n_0 found above the resulting clock stability is obtained from Eq. 6.1

$$\sigma_y(\tau)^{(1)} \approx \frac{2}{\omega_0 \tau} \frac{\sqrt{n_0^{\text{opt}}}}{N} \approx \frac{8}{\pi \omega_0 \tau} \frac{\sqrt{\log(N)}}{N}. \quad (6.4)$$

It scales linearly with the averaging time τ , and realizes the Heisenberg bound of laser stability up to a logarithmic correction. In contrast, in the regime $\tau \geq \gamma_{\text{ind}}^{-1}/2^{M-1}$, T is limited by the presence of individual particle noise to a value $T \approx \gamma_{\text{ind}}^{-1}/2^{M-1} = 2\gamma_{\text{ind}}^{-1}n_0/N$, and we find

$$\sigma_y(\tau)^{(2)} \approx \frac{1}{\omega_0} \sqrt{\frac{\gamma_{\text{ind}}}{\tau N}}. \quad (6.5)$$

Eq. 6.5 represents the fundamental noise floor for laser stability resulting from quantum metrological bounds in the presence of individual particle noise [82]. As we have seen, the proposed protocol reaches this optimal value rapidly after the averaging time $\tau_0 \sim \gamma_{\text{ind}}^{-1}\log(N)/N$ (cf. Fig. 6.2), $N/\log(N)$ times faster than any classical scheme. In Appendix E.6 we derive the necessary threshold fidelities in the GHZ state preparation our scheme can tolerate without compromising the stability in Eqs. (6.4) & (6.5).

6.4 Comparison with other schemes

In the following, we benchmark the stability of our protocol against different approaches by comparing the lowest achievable ADEV as a function of averaging time τ (cf. Fig. 6.2). First, we consider the standard procedure in which all atoms are interrogated in an uncorrelated fashion. The scheme is identical to N independent measurements of Φ_{LO} , and therefore the ADEV is limited by the standard quantum

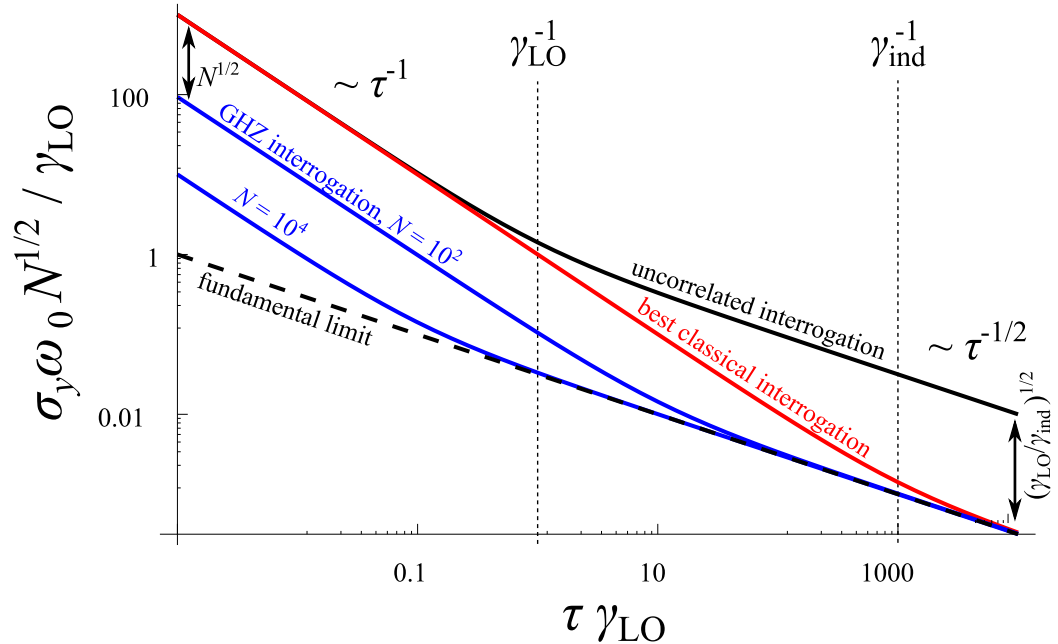


Figure 6.2: Allan deviation σ_y for different protocols as a function of averaging time τ , normalized to the standard quantum limit, for $\gamma_{LO}/\gamma_{ind} = 10^3$. The solid black line corresponds to the standard scheme using a single uncorrelated ensemble. It fails to reach the fundamental noise floor set by the atomic transition linewidth (cf. Eq. 6.5, broken line). A more sophisticated classical scheme which uses exponentially increasing Ramsey times in each cycle [183, 27] allows to extend the regime of linear scaling with $1/\tau$ up to the point where the bound (6.5) is met. In comparison, the proposed cascaded GHZ protocol (blue solid curves) enables an $\sim N$ times faster convergence. For short averaging times the stability is enhanced by a factor \sqrt{N} as compared to classical protocols.

limit: $\sigma_y \sim \frac{1}{\omega_0 \tau \sqrt{N}}$ for $\tau < \gamma_{\text{LO}}^{-1}$. Since the Ramsey time is limited, by the LO noise, to $T < \gamma_{\text{LO}}^{-1}$ due to uncorrected phase wraps, this fails to achieve the fundamental bound, Eq. 6.5, giving suboptimal ADEV, $\sigma_y(\tau) \sim \frac{1}{\omega_0} \sqrt{\frac{\gamma_{\text{LO}}}{\tau N}}$, in the long time limit $\tau > \gamma_{\text{LO}}^{-1}$. Second, we discuss the recently published classical protocol which interrogates the LO with uncorrelated atoms for exponentially increasing Ramsey times in each cycle [27, 183]. This protocol can be understood as the classical part ($j \leq 0$) of the cascaded interrogation proposed here. It eliminates the constraint of the LO linewidth, and allows to extend the interrogation time T to its maximum value, enabling a linear scaling with τ up to the point where the fundamental bound (6.5) is reached. However, using an uncorrelated interrogation, the scheme displays a standard-quantum-limited scaling (i.e. $\propto 1/\sqrt{N}$), for short averaging times.

The above analysis illustrates the quantum gain of the proposed clock operation protocol using cascaded GHZ states. As compared to the best known classical scheme, our scheme provides a $\sqrt{N/\log(N)}$ enhancement for short averaging times. As a result it reaches the fundamental noise floor for laser stability in the presence of single particle decoherence [Eq. 6.5] $\sim N/\log(N)$ times faster. This results identifies the possible advantage of using entanglement previously debated in the literature [237, 110, 130, 184, 28, 6, 38, 147]: While the long term limitation is set by atomic decoherence, entangled atoms reaches this limit faster thus improving the bandwidth of the stable oscillator. Our results motivate the development of quantum enhanced atomic clocks based on entangled ions and neutral atoms. Furthermore, it lays the foundations for the recently proposed network of quantum clocks [121] which achieves the optimal use of resources in a global network through network-wide entangled

states.

Chapter 7

A quantum network of clocks

7.1 Introduction

The development of precise atomic clocks plays an increasingly important role in modern society. Shared timing information constitutes a key resource for navigation with a direct correspondence between timing accuracy and precision in applications such as the Global Positioning System (GPS). By combining precision metrology and quantum networks, we propose a quantum, cooperative protocol for operating a network of geographically remote optical atomic clocks. Using non-local entangled states, we demonstrate an optimal utilization of global resources, and show that such a network can be operated near the fundamental precision limit set by quantum theory. Furthermore, the internal structure of the network, combined with quantum communication techniques, guarantees security both from internal and external threats. Realization of such a global quantum network of clocks may allow construction of a real-time single international time scale (world clock) with unprecedented stability

and accuracy.

With the advances of highly phase coherent lasers, optical atomic clocks containing multiple atoms have demonstrated stability that reaches the standard quantum limit (SQL) set by the available atom number and interrogation time [23, 107, 156]. Reaching beyond the SQL, we stand to gain a significant improvement of clock performance by preparing atoms in quantum correlated states (e.g., spin squeezed states [127, 38]). Here we describe a new approach to maximize the performance of a network composed of multiple clocks allowing one to gain the advantage of all resources available at each node. Several recent advances in precision metrology and quantum science, along with future improvements in quantum control, may put this approach within reach. On the one hand, phase coherent optical links spanning the entire visible spectrum have been demonstrated, with the capability of delivering the most stable optical oscillator from one color or location to another [240, 67]. On the other hand, quantum communication and entanglement techniques are enabling distant quantum objects to be connected in a quantum network [54, 117, 169]. Combining these two technological frontiers, we show here that a distributed network composed of quantum-limited clocks separated by large distances – as appropriate, e.g., for satellite-based clocks possibly operated by different nations – can be operated as an ultimate “world clock”, where all members combine their individual resources in a quantum coherent way to achieve greater clock stability and distribute this international time scale in real time for all.

The distributed architecture allows each participant of the network to profit from a stability of the local clock signal that is enhanced by a factor proportional to the total

number of parties (as compared to an independent operation of the individual clocks) without losing sovereignty or compromising security. This cooperative gain strongly incentivizes joining the collaborative network while retaining robustness against disruptions of communication channels. On the one hand, the local clocks can be used to identify and correct systematic errors originating from the phase links. On the other hand, the nodes can fall back to relying on the locally stabilized clocks if the phase links fail. We demonstrate that by preparing quantum-correlated states of remote clocks, the network can yield the best possible clock signal allowed by quantum theory for the combined resources. Furthermore, enabled through the use of quantum communication techniques, such a network can be made secure, such that only parties contributing to its operation may enjoy the benefit of an ultra-precise clock signal. Besides serving as a real-time clock for the international time scale, the proposed quantum network also represents a large-scale quantum sensor that can be used to probe the fundamental laws of physics, including relativity and connections between space-time and quantum physics.

7.2 The concept of quantum clock network

Fig. 7.1 illustrates the basic concept for the proposed quantum clock network. We consider a set of K atomic clocks (constituting the nodes of the network), each based on a large number of atoms (clock qubits) serving as the frequency reference ω_0 at different geographical locations. In our approach, each clock has its own independently operated local oscillator (LO), $\mathcal{E}_j(t) \propto e^{i\nu_j t}$, with detuning $\delta_j = \nu_j - \omega_0$, ($j = 1, 2 \dots K$). It keeps the time by interrogating its qubits periodically, and uses

the measurement data to stabilize the LO frequency at the reference frequency of the atomic transition. However, as opposed to the conventional approach, we consider the situation in which each network node allocates some of its qubits to form entangled states stretching across all nodes. When interrogated within a properly designed measurement scheme, such entangled network states provide ultra-precise information about the deviation of the center-of-mass (COM) frequency $\nu_{\text{COM}} = \sum_j \nu_j / K$ of all local oscillators from the atomic resonance.

Each clock cycle consists of three stages: preparation of the clock atom state (initialization), interrogation by the LOs (measurement) and correction of the laser frequency according to the measurement outcome (feedback). In the further analysis, we assume, for convenience, that in each interrogation cycle one of the nodes plays the role of the center, which initiates each Ramsey cycle and collects the measurement data from the other nodes via classical channels [Fig. 7.1 b)], as well as LO signals via optical links, to feedback the COM signal. (The role of the center can alternate to provide extra security, see Appendix F.2). This information, in turn, can be utilized in a feedback cycle to yield a Heisenberg-limited stability of the COM clock signal generated by the network, which is subsequently distributed to the individual nodes in a secure fashion. As a result, after a few cycles, the LOs corresponding to each individual node achieve an accuracy and stability effectively resulting from interrogating atoms in the entire network.

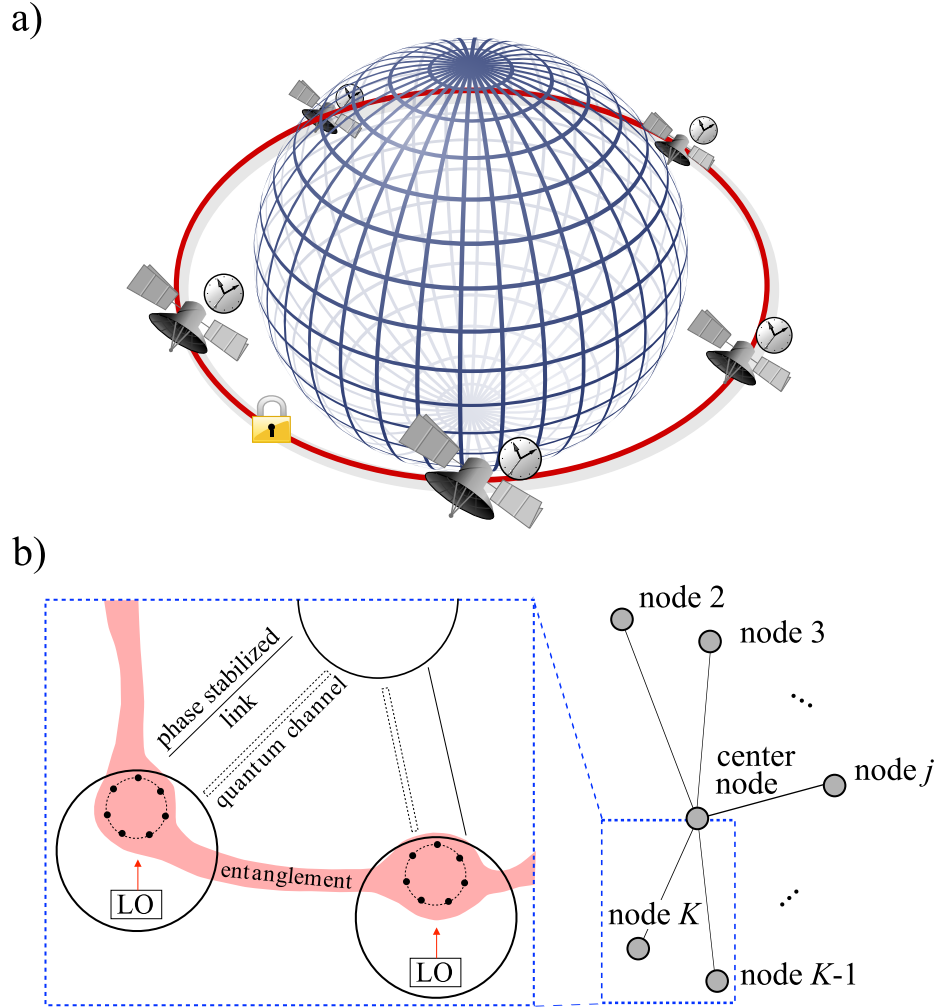


Figure 7.1: The concept of world-wide quantum clock network. a) Illustration of a cooperative clock operation protocol in which individual parties (e.g., satellite based atomic clocks from different countries) jointly allocate their respective resources in a global network involving entangled quantum states. This guarantees an optimal use of the global resources, achieving an ultra-precise clock signal limited only by the fundamental bounds of quantum metrology and, in addition, guaranteeing secure distribution of the clock signal. b) In addition to locally operating the individual clocks, the different nodes (i.e., satellites) employ network-wide entangled states to interrogate their respective local oscillators (LOs). The acquired information is sent to a particular node serving as a center where it is used to stabilize a center of mass mode of the different LOs. This yields an ultra-precise clock signal accessible to all network members.

7.3 Preparation of network-wide entangled states

In the initialization stage of each clock cycle, entangled states spanning across the nodes at different geographical positions of the network are prepared. In the following, we describe exemplarily how a single network-wide GHZ state can be prepared. The entangled states employed in the proposed quantum network protocol – which is described in the following section – consist of products of GHZ states of different sizes. They can be prepared by repetition of the protocol that we now describe.

For simplicity, we assume that each node j ($j = 1, \dots, K$) contains an identical number n of clock qubits which we label as $1_j, 2_j, \dots, n_j$ (in Appendix F.3, we discuss the case where the nodes contain different amounts of clock qubits). Further, we assume, for convenience, that the center node ($j = 1$) has access to additional $2(K - 1)$ ancilla qubits $a_2, \dots, a_K, b_2, \dots, b_K$ besides the n clock atoms (a slightly more complicated procedure allows to refrain from the use of ancilla qubits, see Appendix F.3). The entangling procedure starts at the center with the creation of a fully entangled state of one half of the ancilla qubits $\{b_j\}$, and its first clock qubit 1_1 . This can be realized, e.g. with a single qubit $\pi/2$ -rotation (on qubit 1_1) and a collective entangling operation, which is equivalent to a series of CNOT gates [159] (between 1_1 and each b_j). The result is a GHZ state, $[|00\dots0\rangle_{1_1,b_2,b_3,\dots,b_K} + i|11\dots1\rangle_{1_1,b_2,b_3,\dots,b_K}] / \sqrt{2}$. In parallel, the center uses the other half of the ancillas $\{a_j\}$ to create single EPR pairs with each node $j \neq 1$, either by directly sending flying qubits and converting them to stationary qubits, or by using quantum repeater techniques to prepare high-fidelity entanglement [70]. As a result of this procedure, one part of the pair is stored at the center node (qubit a_j), while the other one is stored at the j th node (qubit

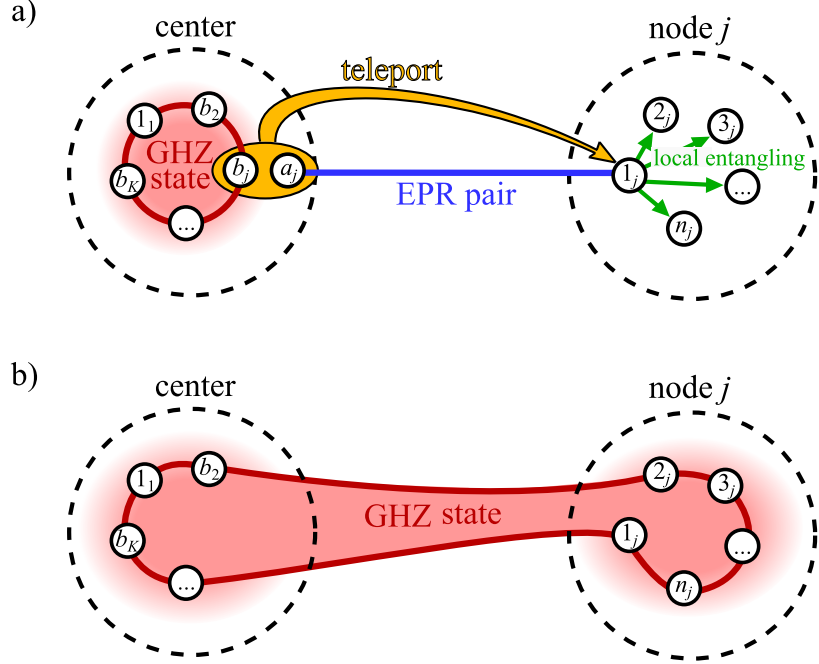


Figure 7.2: Entangled state preparation between distant nodes. a) The center node ($j = 1$) initiates the initialization sequence by preparing a local GHZ state across the qubits $\{b_j\}_{j=2}^K$ and 1_1 , as well as $(K - 1)$ EPR pairs on the qubit pairs $\{(a_j, 1_j)\}_{j=2}^K$. Quantum teleportation expands this GHZ state to the first qubit within each of the individual nodes. b) Originating from the teleported qubits, the nodes grow the GHZ state to involve all the desired local qubits by employing local entangling operations. The procedure results in a common GHZ states over all atoms of the nodes.

1_j), forming the states $[|00\rangle_{a_j,1_j} + |11\rangle_{a_j,1_j}]/\sqrt{2}$ for every j (see Fig. 7.2).

Next, the center performs $K - 1$ separate Bell measurements on its ancilla qubit pairs $\{(b_j, a_j)\}$. This teleports the state of qubit b_j to qubit 1_j ($j = 2, \dots, K$), up to a local single-qubit rotation, which is performed after the measurement outcomes are sent to the node via classical channels. The result of the teleportations is a collective GHZ state $\frac{1}{\sqrt{2}}|00\dots 0\rangle_{1_1,1_2,\dots 1_K} + i|11\dots 1\rangle_{1_1,1_2,\dots 1_K}$, stretching across the first qubits of all K nodes.

In the final step of entangling, all nodes (including the center) extend the entanglement to all of their remaining clock qubits. To do this, each node j per-

forms the collective entangling operation mentioned before based on 1_j and targeting qubits $2_j, 3_j, \dots, n_j$. At the end of the protocol the different nodes share a common GHZ state $[(\mathbf{0}) + i|\mathbf{1}\rangle]/\sqrt{2}$, where $|\mathbf{0}\rangle$ and $|\mathbf{1}\rangle$ are product states of all qubits $\{i_j : i = 1, 2, \dots, n, j = 1, 2, \dots, K\}$ being in $|0\rangle$ or $|1\rangle$, respectively. As discussed below, in practice the entanglement distribution can be done either via polarization- or frequency-entangled photons with frequency difference in the microwave domain, in which case the ancillary qubits involved in the entanglement distribution will be different from the clock qubits. Typically, as part of the preparation process, time delays arise between the initialization of different clock qubits. Its detrimental effects can be entirely avoided by proper local timing or prior preparation of entanglement, as discussed in Appendix F.3.

7.4 Interrogation

The use of entangled resources during the interrogation phase enables an optimal use of the available resources via the following procedure. Assume we have a total of \tilde{N} qubits at our disposal which are equally distributed between the K nodes (indexed $j = 1, \dots, K$) and prepared in a non-local GHZ state $[(\mathbf{0}) + i|\mathbf{1}\rangle]/\sqrt{2}$, where $|\mathbf{0(1)}\rangle \equiv |0(1)\rangle^{\otimes \tilde{N}}$. During the interrogation time T , a clock qubit at node j picks up a relative phase $\phi_j = \delta_j T$. Due to the non-local character of the state, these phases accumulate in the total state of the atoms $[(\mathbf{0}) + ie^{i\Phi}|\mathbf{1}\rangle]/\sqrt{2}$, where the collective phase after the interrogation time T is given as

$$\Phi = \sum_{j=1}^K \frac{\tilde{N}}{K} \phi_j = \tilde{N} \delta_{\text{COM}} T, \quad (7.1)$$

where $\delta_{\text{COM}} = \nu_{\text{COM}} - \omega_0$. To extract the phase information picked up by the different GHZ states, the individual nodes j measure their respective qubits in the x -basis, and evaluate the parity of all measurement outcomes $p_j = \pm 1$. Subsequently, the nodes send this information to the center node via a classical channel, where the total parity $p = \prod_j p_j$ is evaluated, and the phase information is extracted [24, 125]. Note, that only the full set $\{p_j | j = 1 \dots K\}$ contains information.

The proportionality with \tilde{N} in Eq. 7.1 represents the quantum enhancement in the estimation of δ_{COM} . However, for realistic laser noise spectra, this suggested enhancement is corrupted by the increase of uncontrolled phase slips for a single GHZ state [237]: Whenever, after the Ramsey time T , the phase Φ – which due to the laser frequency fluctuations constitutes a random variable itself – falls out of the interval $[-\pi, \pi]$ the estimation fails. This limitation restricts the maximal Ramsey time to values $T < (\tilde{N}\gamma_{\text{LO}})^{-1}$, preventing any quantum gain in the estimation.

To circumvent this problem, we use entangled states consisting of products of successively larger GHZ ensembles, see Appendix F.1 and [116]. In this approach, atoms are split into several independent, shared groups. We write the number of the first group of atoms as $\tilde{N} = 2^{M-1}K$, for some natural number M . Furthermore, the network shares additional groups of atoms, each containing $2^j K$ ($j = 0, \dots M-2$) equally distributed between the nodes and prepared in GHZ states. Additionally, each node has a small number of uncorrelated atoms interrogated by the LOs. Using a protocol reminiscent of the phase estimation algorithm [116, 159, 91], measurement results from each level j allow to directly assess the bits $Z_j \in \{0, 1\}$ of the binary fraction representation of the laser phase $\Phi_{\text{LO}} = \delta_{\text{COM}}T = 2\pi[(Z_1 - 1)2^{-1} + Z_22^{-2} +$

$Z_3 2^{-3} \dots$. (See Appendix F.1 for details.) This yields an estimate of Φ_{LO} with Heisenberg-limited accuracy, up to a logarithmic correction, see Appendix F.1:

$$\Delta\Phi_{\text{LO}} = \frac{8}{\pi} \log(N)/N, \quad (7.2)$$

even for Ramsey times beyond the limits of the laser frequency fluctuations [$T > (\tilde{N}\gamma_{\text{LO}}^{-1})$], where N represent the total number of clock atoms employed in the scheme. The logarithmic correction arises due to the number of particles required to realize this (incoherent) version of the phase estimation algorithm.

7.5 Feedback

The measured value of the phase Φ_{LO} , gives an estimate on the COM detuning $\tilde{\delta}_{\text{COM}}$ after each Ramsey cycle, which is subsequently used by the center node to stabilize the COM laser signal. To this end, the center generates the COM of the frequencies. Every node sends its local oscillator field \mathcal{E}_i to the center via phase-stable optical links, and the center synthesizes the COM frequency ν_{COM} by averaging the ν_j frequencies with equal weights. This can be implemented via heterodyne beat of the local oscillator in the center against each incoming laser signal, resulting in K beat frequencies. Synthesizing these beat frequencies allows the local oscillator of the central node to phase track ν_{COM} . The center distributes the stabilized clock signal to different members of the network by sending individual error signals $\tilde{\delta}_j = \tilde{\delta}_{\text{COM}} + (\nu_j - \nu_{\text{COM}})$ to all nodes j , respectively, and corrects its own LO as well, accordingly. Alternatively, the center can be operated to provide restricted feedback information to the nodes, see Appendix F.2.

7.6 Stability analysis

In this section, we demonstrate that the proposed quantum clock network achieves the best clock signal, allowed by quantum theory for the available resources, i.e. the total atom number. To quantify this cooperative gain, we compare networks of different types (classical or quantum mechanical interrogation of the respective LOs) and degrees of cooperation (no cooperation, classical, or quantum cooperation).

First, we analyze the stability of the proposed quantum clock network, corresponding to the case of quantum interrogation and cooperation (curve a in Fig. 7.3). In this case, the analysis resulting in Eq. 7.2 suggests that near Heisenberg-limited scaling with a total atom number can be achieved for the entangled clock network. In particular, for a given total particle number N and for averaging times shorter than the timescale set by individual qubit noise $\tau < 1/(\gamma_i N)$ (where γ_i is the atomic linewidth, the factor N results from the enhanced decoherence of the entangled interrogation state [110]), the network operation achieves a Heisenberg-limited Allan deviation (ADEV) of the COM laser mode

$$\sigma_y(\tau) \sim \frac{\sqrt{\log(N)}}{\omega_0 N} \frac{1}{\tau}, \quad (7.3)$$

up to small numerical corrections (see Appendix F.1). The $1/\tau$ scaling results from the effective cancellation of the low frequency part of the laser noise spectrum, achieved by the cascaded protocol described above, possibly in combination with additional stages of uncorrelated interrogations using varying Ramsey times [183, 27], see [116]. This allows the cycle time T (which is assumed to be equal to the interrogation time) to be extended to the total available measurement time τ .

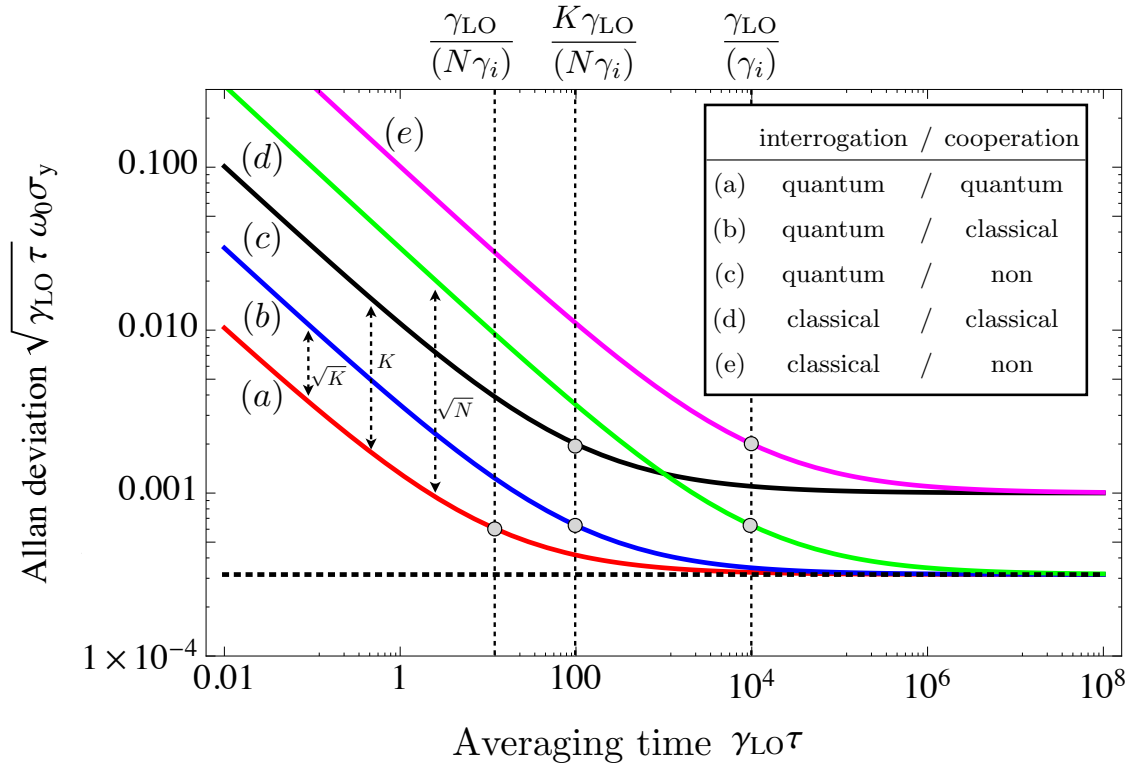


Figure 7.3: Performance of different operation schemes. Comparison of the achievable (rescaled) Allan deviation $\sqrt{\gamma_{\text{LO}}\tau}\omega_0\sigma_y$ using clock networks of different types and degrees of cooperation. (a) the proposed protocol realizing quantum interrogation and cooperation, (b) quantum interrogation and classical cooperation, (c) quantum interrogation and no cooperation, (d) classical interrogation and classical cooperation, (e) classical interrogation and no cooperation (cf. text). The dotted base line represents the fundamental bound arising from the finite width of the clock atoms transition [compare Eq. 7.4]. This optimal stability can be attained only via cooperation between the nodes. The quantum clock network (a) represents the optimal form of cooperation, and reaches this boundary faster than any other operational mode. Parameters are $N = 1000$, $K = 10$, $\gamma_i = 10^{-4}\gamma_{\text{LO}}$.

Eventually, for large averaging times $\tau > 1/(\gamma_i N)$ the Ramsey time becomes fundamentally limited by individual noise processes that determine the atomic linewidth $T \leq 1/(\gamma_i N)$. As a result, the $1/N$ scaling breaks down, and the ADEV returns to the square root scaling with both the employed particle number and averaging time,

$$\sigma_y(\tau) \sim \frac{1}{\omega_0 \sqrt{N}} \sqrt{\frac{\gamma_i}{\tau}}, \quad (7.4)$$

up to constant numerical factors. Eq. 7.4 results from fundamental quantum metrological bounds [82] (In the case of dominating trap losses, the loss rate simply replaces γ_i in the above formula.), and represents the best conceivable clock stability in the presence of individual particle decoherence which, in a network, can only be achieved via cooperation. Independently operating a clock, in contrast, can only achieve a stability scaling with the local number of atoms, i.e. $\sigma_y(\tau) \propto \sqrt{K/N}$.

Fig. 7.3 illustrates the comparison of entangled clock network with other approaches. A network in which the K nodes cooperate classically (curve b in Fig. 7.3), by locally measuring the individual phase deviation ϕ_j , and combining the outcomes via classical channels, outperforms individually operated clocks (curve c) by a factor of \sqrt{K} (for both cases, assuming optimal quantum interrogation for individual nodes [116, 28]). The quantum network protocol (curve a) increases this cooperative advantage by an additional factor of \sqrt{K} for short averaging times, reaching Heisenberg-limit. Furthermore the ADEV converges to the fundamental bound [Eq. 7.4] K times faster compared to the case of classical cooperation (curve b). Although an optimal, classical, local protocol (e.g. [183, 27]), combined with classical cooperation (curve d), eventually reaches the same bound [Eq. 7.4], this approach is atom-shot noise limited, and hence its stability is reduced by a factor of \sqrt{N} for short averaging times

[compare Eq. 7.3] compared to the quantum network protocol. Hence, the optimal stability [Eq. 7.4] is reached at averaging times that are N times longer than for the proposed quantum network. Naturally, all of the above approaches are superior to a classical scheme without cooperation (curve e).

As a specific example, we first consider ion clocks that can currently achieve a stability of 2.8×10^{-15} after 1 s of averaging time [52]. The entangled states of up to 14 ions has already been demonstrated [153] as was the entanglement of remote ions [144]. We consider a network of ten clocks, each containing ten ions. Using Al^+ ($\omega_0 = 2\pi \times 1121 \text{ THz}$, $\gamma_i = 2\pi \times 8 \text{ mHz}$), we find that the quantum cooperative protocol can reach 4×10^{-17} fractional frequency uncertainty after 1 s. Larger improvements could potentially be achieved using e.g. Yb^+ ions, due to the long coherence time (2.2×10^4 s) of its octupole clock transition.

The quantum gain could be even more pronounced for neutral atomic clocks. For a network consisting of ten clocks similar to the one operated in JILA [23], each containing 1000 neutral atoms with central frequency $\omega_0 = 2\pi \times 429 \text{ THz}$ and linewidth $\gamma_i = 2\pi \times 1 \text{ mHz}$, the quantum cooperative scheme can achieve a stability of $\sim 2 \times 10^{-18}$ after 1s averaging, and is an order of magnitude better than the best classical cooperative scheme. Future advances, employing clock transitions with linewidths of a few tens of μHz (such as erbium), could possibly allow for further improvement, achieving fractional frequency uncertainty beyond 10^{-20} after $\tau \sim 100$ s. This level of stability is in the same order of magnitude as the required sensitivity to successfully use the network as a gravitational interferometer [197].

So far we have assumed perfect operation and infinitely fast entanglement distribu-

tion rates. In Appendix F.3, we analyze these assumption and find that the advantage of our scheme persists provided that fidelity of the local collective entangling [207] (which creates a GHZ state of N/K qubits) exceeds the threshold fidelity F_{th} , where $1 - F_{\text{th}} \sim 1/(K \log N)$, and the EPR sharing rate is higher than $R_{\text{EPR}} \sim (\log N)^2 \gamma_i$. For the optical clock example presented above, $F_{\text{th}} \sim 0.99$, and $R_{\text{EPR}} \sim 1$ Hz. While local operations with fidelity ~ 0.95 have been realized for $N \sim 5$ ions [153], the errors in such operations increase with N , making this realization more challenging.

7.7 Security

A network with such precise time-keeping capabilities can be subject to both internal and external attacks. Effectively countering them is crucial to establish a reliable ground for cooperation. We consider the network secure if the implemented countermeasures can prevent external parties from benefiting from the network (eavesdropping), as well as effectively detect any malicious activities of any of the members (sabotage).

Sabotage describes the situation where one of the nodes – intended or unintended – operates in a damaging manner. For example, one node could try sending false LO frequencies or wrong measurement bits in the hope of corrupting the collective measurement outcomes. In order to detect such malicious participants, the central node can occasionally perform assessment tests of the different nodes by teleporting an uncorrelated qubit state $[|0\rangle + e^{i\chi}|1\rangle]/\sqrt{2}$, where χ is a randomly chosen phase known only to the center. By checking for statistical discrepancies between the measurement results and the detuning of the LO signal sent by the node under scrutiny, the center

can rapidly and reliably determine whether the particular node is operating properly (See Fig. 7.4a and Appendix F.2), however this strategy breaks down, if multiple sabotage attacks happen within a short time.

Eavesdropping, i.e., the unauthorized attempt to access the stabilized ν_{COM} frequency, can be prevented by encoding the classical channels, over which the center and the nodes exchange feedback signals, using quantum key distribution protocols [96]. Our protocol can keep the stabilized signal hidden from outsiders by mixing the feedback signal with the LO signal at each node only after the non-stabilized LO has been sent to the center (see Fig. 7.4b and Appendix F.2). As a result, even if all LO signals are intercepted, the eavesdropper is able to access only the non-stabilized COM signal. Furthermore, the center exclusively can decode the measurement results sent by the individual nodes using its own measurement outcomes as mentioned above. As a result, the stabilized COM signal remains accessible exclusively to parties involved in the collaboration.

Finally, we note that a distributed operation offers significant security advantages over an alternative approach of having all resources combined in one place from where the signal is distributed. In case of a physical attack of the network, disabling the center or the communication links, the nodes can fall back to an independent clock operation using their local resources.

7.8 Outlook

One of the advantages of the proposed quantum clock network involves its ability to maintain and synchronize the time standards across multiple parties in real-time.

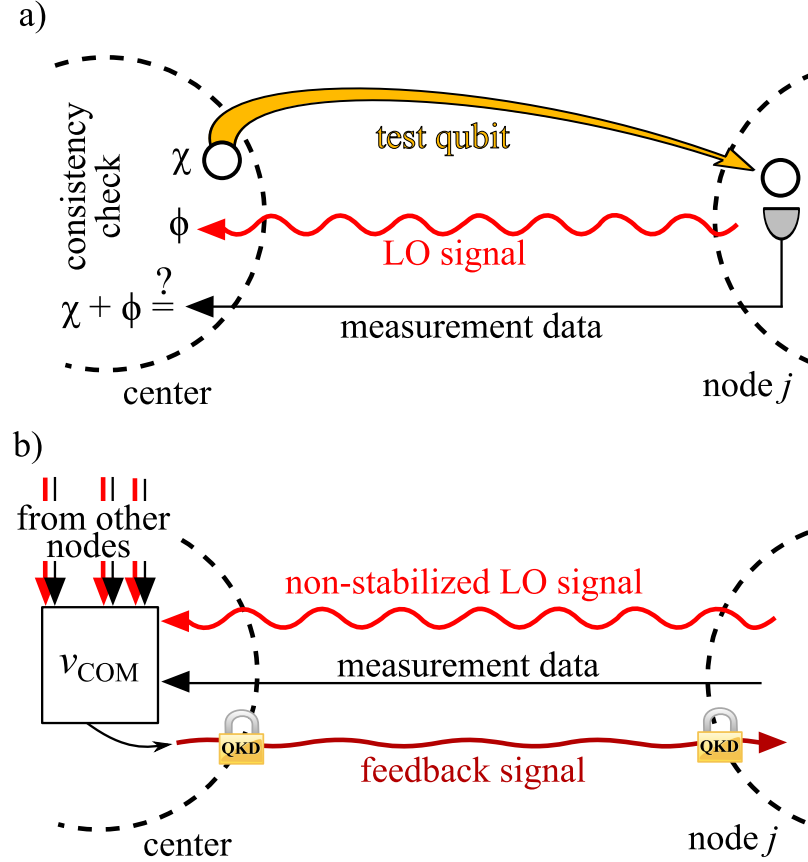


Figure 7.4: Schematics of security countermeasures. a) The center node can choose to test any node j by teleporting a disentangled qubit with a certain phase rotation. A properly operating node creates a local GHZ state $|\langle 0 \rangle + e^{i\chi} |1\rangle\rangle/\sqrt{2}$ from the sent qubit, measures the parity of the GHZ state, and sends it to the center. The measured parity holds information on the phase $\phi' = \chi + \phi$, where ϕ is the accumulated phase of the LO at the node. The center verifies ϕ by comparing it with the classically determined phase of the sent LO signal with respect to the COM signal. b) Eavesdropping can be prevented by prescribing that only the non-stabilized LO signals are sent through classical channels and encoding the radio frequency feedback signal with phase modulation according to a shared secret key.

Unlike the current world time standard, where the individual signals from different clocks are averaged and communicated with a time delay (a so called paper clock), in our quantum clock network, all participants have access to the ultra-stable signal at any time. This makes it possible to measure systematic errors of different clocks in real time, which in turn allows to correct them [23], unlike in the case of the paper clock which has to rely on the retrospectively averaged time signals (see Appendix F.3). The enhanced stability of the network signal hereby allows for longer Ramsey times in the control measurements used to determine the systematics of the single clock. Furthermore, by having full access to their local clocks the different parties keep their full sovereignty and ensure security, as opposed to a joint operation of a single clock.

Realization of the full-scale network of the type described here will require a number of technological advances in both metrology and experimental quantum information science. The remote entanglement can be implemented by using recently demonstrated techniques for individual atom-photon entanglement [163, 53, 221, 20, 180]. Since the teleportation protocol requires quantum links capable of sharing EPR pairs with sufficiently high repetition rate and fidelity, entanglement purification [76] and quantum repeater techniques [70] will likely be required. In practice, qubits used for entanglement distribution may not be ideal for clocks. However, as noted previously remote entanglement does not need to involve coherent qubits at optical frequencies (e.g., polarization entanglement can be used). In such a case, the use of hybrid approaches, combining different systems for entanglement and local clock operations, may be warranted. Similarly, signals from clocks employing different transition fre-

quencies can be coherently connected by frequency combs, allowing clocks with different clock qubits to participate. It might also be interesting to explore if high-fidelity entangled EPR pairs can be used to create remote entangled states of spin-squeezed type [127, 202, 136], or by following the proposed approach for cat state preparation in atomic ensembles [146], or using collective interactions (such as [207]) and repetitive teleportation [5]. In addition, while space-based communication networks will be capable of maintaining optical phase coherence for the links between clocks, we note that establishing ground-space coherent optical links remains a technical challenge and requires an intense research effort which has recently started [64]. Finally, if the entire network is spanned by satellites in space, the on-board local oscillators can further benefit from the much lower noise level compared to ground-based clocks.

If realized, such a quantum network of clocks can have important scientific, technological, and social consequences. Besides creating a world platform for time and frequency metrology, such a network may find important applications to a range of technological advances for earth science [214], precise navigation of autonomous vehicles and space probes (requiring high refresh rate), and to the test and search for the fundamental laws of nature, including relativity and the connection between quantum and gravitational physics [1, 201, 197, 238]. In order to explore these exciting applications one can either use the excellent common frequency reference generated by the clock network, or, alternatively, prepare modified collective states of different nodes that can directly measure the specific signal under study.

Chapter 8

Quantum network of neutral atom clocks

8.1 Introduction

The current record in clock precision is held by ytterbium and strontium clocks [131], capable of reaching $\sim 10^{-18}$ total fractional frequency uncertainty. Apart from the enormous amount of effort and innovation, this unprecedented accuracy was attainable due to the large number of clock atoms ($10^3 - 10^4$) [107, 23, 157]. In our recent work [121], we showed that a quantum network of atomic clocks can result in substantial boost of the overall accuracy if multiple clocks are connected in quantum entanglement. The proposed globally entangled state, Greenberger-Horne-Zeilinger (GHZ) state, is more sensitive to the global phase evolution of the clock atoms, and allows for an improved measurement of the passage of time. If the GHZ state is set up and interrogated in the optimal way [116, 21], frequency measurements can

asymptotically reach the Heisenberg limit [102], associated with the total number of atoms in the entire network.

Imperfections during creation of the GHZ state are the main obstacles for experimental realizations of a quantum clock network. Errors arising during the distribution of entanglement add up, and limit the total number of atoms and clocks with which the fidelity does not drop significantly. Efforts are being made to make both the non-local [192] and local entanglement distribution [206, 190] faster and more reliable. Of particular interest are applications of these ideas to neutral atom clocks.

In this Letter, we show how a non-local GHZ state can be created across multiple, spatially separated neutral atom clocks with high fidelity. Our protocol relies on strong Rydberg blockade for enhancing local atom-atom interaction, collective excitations for enhancing photon-atom interaction, and single photon quantum channels at telecom frequency for reliable non-local connections. We propose and analyze a realization using neutral Yb ensembles, suitable for the current atomic clock technology.

Rydberg blockade is a result of the interaction arising between atoms excited to Rydberg states in an ensemble. If driven resonantly, the first excited atom blocks the transition of a second one, thus at most one atom can get coherently excited to the Rydberg state [73, 74, 77], allowing precise quantum control. Rydberg blockade has been proposed as an efficient tool to realize quantum gates and perform quantum information processing [135, 154, 190, 244, 104, 97]. Different ways of trapping and manipulating Rydberg states are currently under investigation both experimentally [46, 12, 87, 8, 232] and theoretically [223, 22, 224].

8.2 Description of the protocol

We describe our protocol for K identical atomic clocks arranged in a sequence, each connected to its neighbors with optical channels, and each using n identical atoms, trapped in an optical lattice. We use the atomic levels, shown on Fig. 8.1(a) for our protocol: The two levels of the clock transition, g, f , a metastable shelving level s , an excited level e , which spontaneously decays to g , and two strongly interacting Rydberg levels, r_1 and r_2 . We further require transitions between levels, marked with arrows, to be driven independently.

We imagine preparing all atoms in the ground state g , after which our protocol consists of five subsequent steps. First, using blockade, we create two independent collective excitations in each ensemble, using two separate atomic levels (f and s). Second, each ensemble emits single photon pulses that are entangled with one of these collective excitations. Third, the photons are sent towards the neighboring atomic clocks, and measured with a linear optics setup in Bell-basis. Fourth, upon success, each clock performs a local CNOT operation to connect the two collective excitations. The result is a set of K entangled collective excitations, one in each clock, which serve as "seeds" for a global GHZ state. In the fifth, and final, step the clocks locally "grow" a GHZ state out of each seed, and thus a global GHZ state is obtained. In the following, we provide detailed description and analysis of these five steps, discuss the specific realization in Yb atoms and analyze most important sources of imperfections and errors.

8.2.1 Collective excitations

In the first step, we make use of the Rydberg blockade to create a superposition of one and zero excitation in both f and s levels, following the approach of [135, 190, 73]. This is done by performing the following sequence of driving pulses: $[\pi/(2\sqrt{n})]_{g,r1}$, $[\pi]_{f,r1}$, $[\pi]_{f,s}$, $[(\pi/(2\sqrt{n})]_{g,r1}$, $[\pi]_{f,r1}$, shown on Fig. 8.1(a), where $[\phi]_{a,b}$ stands for a pulse with total, single-atom Rabi phase ϕ between level a and b . Starting from the state $|g\rangle^{\otimes n} =: |0\rangle$, this pulse sequence creates the state

$$(1 + f^\dagger)(1 + s^\dagger)|0\rangle =: \left(|0_f\rangle + |1_f\rangle\right)\left(|0_s\rangle + |1_s\rangle\right), \quad (8.1)$$

where f^\dagger and s^\dagger are creation operators of the two (approximately) independent spin wave modes, supported by the two levels f and s .

8.2.2 Non-local connection

In the second step, spin-photon entangled states, using the spin wave modes f and s , are created, using the an extended version of the scheme described in [128]. Each spin-photon entangled state is created by the pulse sequence shown on Fig. 8.1(b), involving $[\pi]_{s,r2}$, $[\pi/\sqrt{n}]_{g,r1}$, $[\pi]_{e,r1}$, $[\pi]_{s,r2}$. With additional pulses applied before and after this sequence flipping the states of f and s waves, and proper timing, this is repeated four times to produce four time-bin separated light pulses, which are entangled with the two spin waves,

$$\left(|0_f\rangle|t_2\rangle + |1_f\rangle|t_4\rangle\right)\left(|0_s\rangle|t_1\rangle + |1_s\rangle|t_3\rangle\right) \quad (8.2)$$

where $|t_j\rangle|t_k\rangle$ is a two photon state with photons emitted at times t_j and t_k .

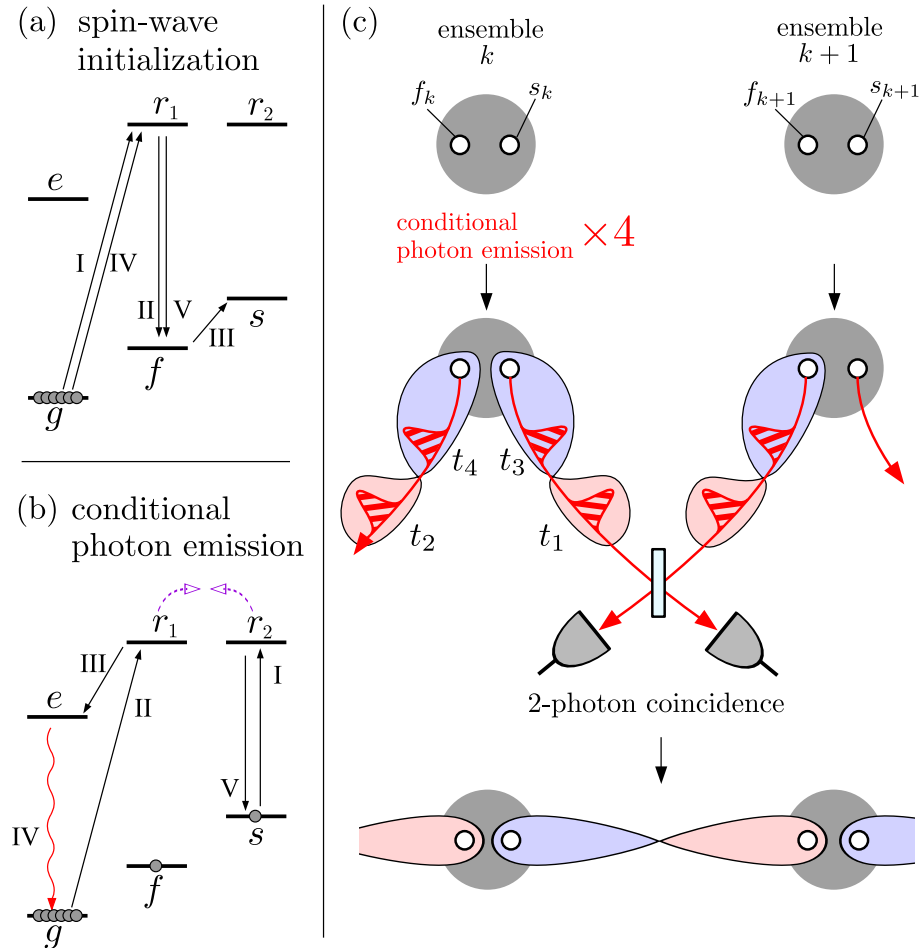


Figure 8.1: Steps to generate pairwise entanglement. (a) Pulse sequence used to initialize the spin-waves f and s in an ensemble. (b) Pulse sequence inducing a conditional photon emission, the emitted photon becomes entangled with the spin state s . (c) In three steps, neighboring ensembles generate pairwise entanglement between their collective excitations. First, they induce $0 + 1$ superpositions of the two independent spin waves, f^\dagger and s^\dagger . Then applying the conditional photon emission sequence four times, they emit four pulses, containing two photons total. Each pair of photons is correlated with a unique spin state. Finally, photons are measured with a linear optics setup, and 2-photon coincidences indicate the creation of entanglement between neighboring ensembles.

In the third step, pairs of time-bin encoded photon pulses from two neighboring ensembles are detected by interfering the two pulses on a beam splitter and measuring two-photon coincidences [70, 108, 185]. As a result, entangled states between neighboring atomic ensembles, k and $k + 1$, are created [134, 205],

$$|0_s\rangle_k|1_f\rangle_{k+1} \pm |1_s\rangle_k|0_f\rangle_{k+1}, \quad (8.3)$$

where the individual kets represent the states of f and s spin waves in the two ensembles, see Fig. 8.1(c).

8.2.3 Local connection

In the fourth step, the ensembles perform a local CNOT operation on the two collective degrees of freedom, f^\dagger and s^\dagger . This is done with the following pulse sequence, $[\pi]_{s,r2}$, $[\pi]_{f,r1}$, $[\pi/\sqrt{n}]_{g,r1}$, $[\pi]_{f,r1}$, $[\pi]_{s,r2}$, shown on Fig. 8.2(a), which promotes any population in s to r_2 , which then blocks the path through r_1 . The result is a conditional flip $|0_f\rangle \leftrightarrow |1_f\rangle$, conditioned on having zero s^\dagger excitations. If we perform $f \leftrightarrow s$ swaps before and after this process, we get a coherent flip between $|0_f, 0_s\rangle \leftrightarrow |0_f, 1_s\rangle$.

To understand the resulting state, let us consider two entangled links, connecting three neighboring ensembles $k - 1, k$ and $k + 1$ as shown on Fig. 8.2(b). The corresponding state, before the fourth step, is

$$(|0, 1\rangle + |1, 0\rangle)_{s_{k-1}, f_k} \otimes (|0, 1\rangle + |1, 0\rangle)_{s_k, f_{k+1}}, \quad (8.4)$$

where $|n_{s_{k-1}}, n_{f_k}\rangle \otimes |n_{s_k}, n_{f_{k+1}}\rangle$ indicate the number of excitations in the modes $s_{k-1}, f_k, s_k, f_{k+1}$ of the three ensembles. After the conditional flip of s_k and measurement of $n_{s_k} \rightarrow m \in \{0, 1\}$, the state becomes $|0, 1, 1-m\rangle + |1, 0, m\rangle$, where the

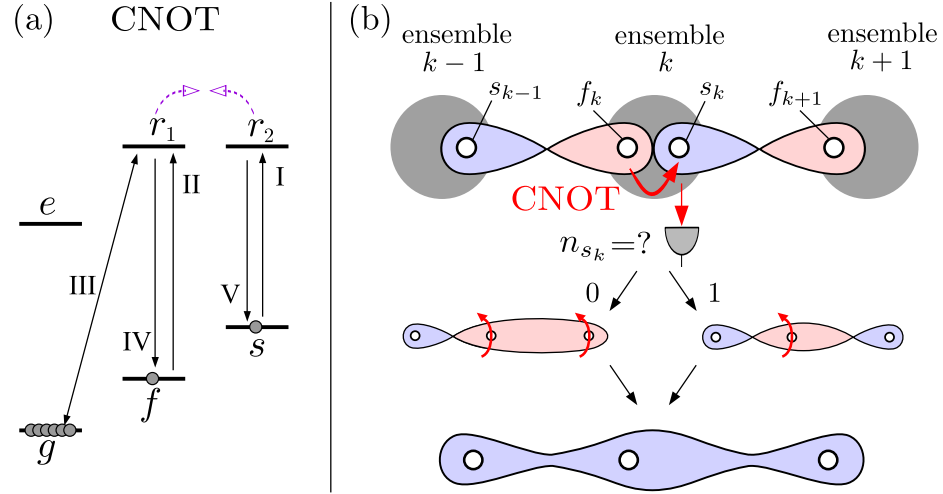


Figure 8.2: Connecting links into non-local GHZ state. (a) CNOT gate between the two excitations f and s : If level s is occupied, then the coherent (de)excitation of the f level is blocked by the Rydberg blockade between the r_1 and r_2 intermediate levels, otherwise it succeeds. (b) Connecting two entanglement links. The local CNOT and measurement operations on ensemble k entangle the two, initially independent, parts of the system: s_{k-1}, f_k and s_k, f_{k+1} . Depending on the outcome of the measurement, either only f_k , or the entire right hand side needs to be flipped, in order to arrive to the proper GHZ state.

remaining kets stand for $|n_{s_{k-1}}, n_{f_k}, n_{f_{k+1}}\rangle$. Depending on the outcome, either only f_k (if $n_{s_k} \rightarrow 1$) or the entire right hand side (if $n_{s_k} \rightarrow 0$) needs to be flipped in order to obtain the desired GHZ state, $\bigotimes_k |0_f\rangle_k + \bigotimes_k |1_f\rangle_k$, of the f excitations of each ensemble, $k = 1, 2, \dots, K$.

8.2.4 Local GHZ growing

In the fifth step, each ensemble locally expands the entanglement from its f degree of freedom to all atoms using a collective Rydberg gate introduced in Refs. [189, 233]. Since the previous steps have already entangled the f excitations across the ensembles, a transition that conditionally excites all local atoms will create a global GHZ state

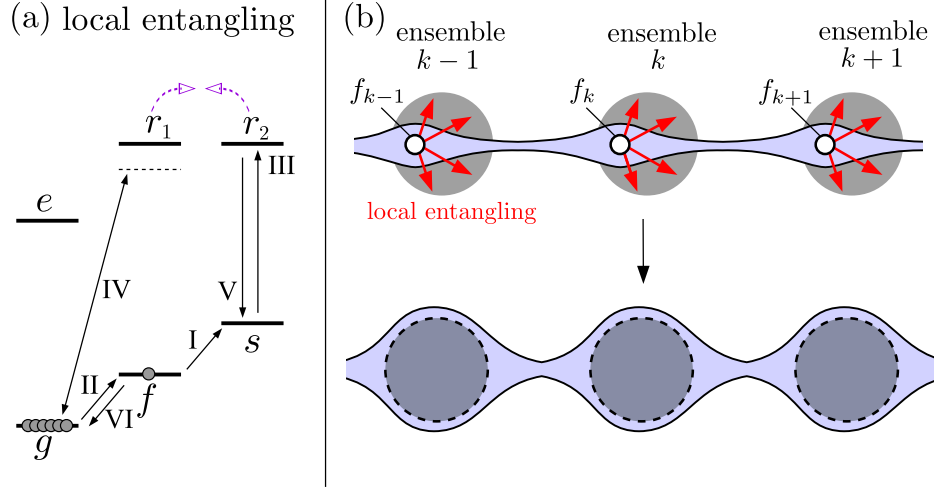


Figure 8.3: Local GHZ creation. (a) Conditional, local GHZ state generation: Any excitation in level s prevents the dressing of g with r_1 , which, otherwise introduces a π phase shift on g . With the conjugation of $\pi/2$ pulses II and VI, this results in a transfer from g to f conditioned on the population of s . (b) The local entangling operation extends the GHZ state from the f spin-wave to all atoms. As a result, every atom in the network gets entangled.

of every atom in the network. The pulse sequence $[\pi]_{f,s}$, $[\pi]_{s,r2}$, $[\pi/2]_{g,f}$, $[\pi(\Delta)]_{g,r1}$, $[\pi/2]_{g,f}$, $[\pi]_{s,r2}$, shown in Fig. 8.3(a), does exactly that, where $[\pi(\Delta)]_{g,r1}$ is an off-resonant dressing pulse, whose Rabi frequency Ω and duration is set properly in order to introduce a conditional π phase shift on level g . This sequence transfers the atoms from g to f only if r_2 is unoccupied, and gets blocked otherwise. The result is

$$\bigotimes_{k=1}^K |0_f\rangle_k + \bigotimes_{k=1}^K |1_f\rangle_k \rightarrow \bigotimes_{k=1}^K |f\rangle^{\otimes n} + \bigotimes_{k=1}^K s^\dagger |g\rangle^{\otimes n}, \quad (8.5)$$

where $|f\rangle$ and $|g\rangle$ denote the state of a single atom. Finally, we get rid of the s excitation with a series of pulses that move it back to g : $[\pi]_{f,s}$, $[\pi]_{f,r1}$, $[\pi]_{f,s}$, $[\pi/\sqrt{n}]_{g,r1}$, and end up with $|f\rangle^{\otimes Kn} + |g\rangle^{\otimes Kn}$, a fully entangled state of all $N = Kn$ atoms in the network.

8.3 Implementation

We next investigate the robustness of our protocol in light of realistic physical imperfections. We assume that all imperfections decrease the coherence between the two components of the GHZ state, and therefore the fidelity can be written as $F = [1 + \exp(-\varepsilon_{\text{tot}})]/2$, where ε_{tot} is the sum of the errors. The errors arising during each non-local connection step $\varepsilon_{\text{non-local}}$ and the errors arising during a local GHZ creation in one clock $\varepsilon_{\text{local}}$ add up to the total error $\varepsilon_{\text{tot}} = (K - 1)\varepsilon_{\text{non-local}} + K\varepsilon_{\text{local}}$, and overall fidelity

$$F \geq \left\{ 1 + \exp \left[-N \left(\frac{\varepsilon_{\text{non-local}}}{n} + \frac{\varepsilon_{\text{local}}}{n} \right) \right] \right\} / 2. \quad (8.6)$$

The error, ε_{tot} , increases linearly with the total number of atoms in the network, N , and the coefficient, $(\varepsilon_{\text{non-local}} + \varepsilon_{\text{local}})/n$, depends on the number of atoms, n , at a single site. For a certain optimal local atom number n_{opt} , the total fidelity is maximal, i.e. decreases with the slowest rate, as N increases. Evenly distributing the atoms into $K_{\text{opt}} = N/n_{\text{opt}}$ groups is therefore optimal.

To be specific, we focus on a possible implementation of our scheme with ensembles of neutral ytterbium atoms whose relevant electronic levels are shown on Fig. 8.4. We identify the following levels of neutral Yb relevant for our protocol: $|g\rangle = |6s6p(^3P_0)\rangle$, $|f\rangle = |6s^2(^1S_0)\rangle$, $|s\rangle = |6s6p(^3P_2)\rangle$ and $|e\rangle = |5d6s(^3D_1)\rangle$, and two Rydberg levels $|r_1\rangle = |6s\tilde{n}s(^1S_0)\rangle$ and $|r_2\rangle = |6s\tilde{n}p_{m=+1}(^1P_1)\rangle$ with the same principle quantum number \tilde{n} . Although the branching ratio for $e \rightarrow g$ decay is not unity, the large population in g collectively enhances this decay channel, and the transition becomes effectively closed. Due to the different symmetries of these states, the co-

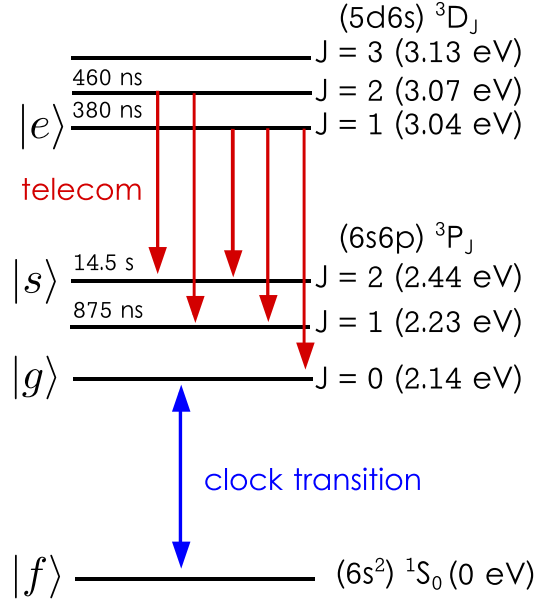


Figure 8.4: Implementation of our protocol in the lower level of neutral Yb. We assign the roles of g and f to the clock levels, the role of s to the metastable $J = 2$ level of $6s6p$, and the role of e to the $J = 1$ level of the excited state $5d6s$, which spontaneously decays to all three levels of $6s6p$ state by emitting a telecom frequency photon.

herent coupling between f, e, s levels and the Rydberg levels r_1, r_2 need to be created via two-photon transitions. We imagine the atoms being held in position by a 2D or 3D optical lattice with period $a = 275.75$ nm, each potential minimum holding a single Yb atom. (The lattice intensity can be modulated during the Rydberg state excitation [220].) (We found that the performance difference between the 2D and 3D lattice is less than a factor of two. See Appendix G.5.)

We consider the following errors in our analysis. During non-local connection, we take into account the finite r_1-r_2 interaction, which allows the creation of an r_1 excitation with some small probability, even if r_2 is populated, the finite lifetime of the s and r_2 levels, the non-zero branching ratio during the decay of e into states other than g , and the dark-count rate of photo-detectors. For the local GHZ creation

step, we account for the same imperfection of the r_1 - r_2 blockade as for the non-local entangling step, the finite lifetimes of the Rydberg levels r_1 and r_2 , and the inhomogeneous broadening of the single excited Rydberg states due to their coupling to double-excited states, induced by the driving field. (See Appendix G.1 and G.2 for details.) We estimate the effect of these errors, and numerically optimize the free parameters: the Rabi frequency Ω and the detuning Δ of the dressing field, and the number of local atoms n , for principle quantum numbers, $50 \leq \tilde{n} \leq 150$ of the Rydberg levels, in order to find the minimal error per atom, $E := \varepsilon_{\text{tot}}/N$.

To illustrate, for $\tilde{n} = 120$, we find the optimum at $n_{\text{opt}} = 298$, $\Delta = 10.9 \times 10^4 \gamma$ and $\Omega = 8.33 \times 10^4 \gamma$, where $\gamma \sim 1 \text{ kHz}$ is the natural linewidth of the Rydberg levels. In this case, the error per atom is $E_{\text{min}} = [\varepsilon_{\text{tot}}/N]_{\text{min}} = 6.7 \times 10^{-5}$ and the fidelity is $F_{\text{max}} = [1 + \exp(-6.7 \times 10^{-5} N)]/2$. Contributions of the different error sources are shown in Table 8.1. (See Appendix G.4 for more details.)

8.4 Clock network optimization

With the optimal ensemble size n_{opt} , determined above, we optimize the remaining parameters of the clock network, namely the total number of entangled atoms N and the number of clocks K . Although having more atoms always results in improved clock precision, entangling all available atoms is not necessarily optimal. To see this, we compare the stability of the entangled clock network and a non-entangled network, and find an optimal entangled atom number N_{opt} by maximizing the precision gain

	error per atom	ratio in total
imperfect blockade	1.41×10^{-5}	21%
r_1 decay	2.89×10^{-5}	43%
r_2 decay	6.62×10^{-7}	1%
inhom. broadening	6.62×10^{-7}	1%
r_2 decay (non-local)	$\sim 10^{-10}$	< 0.1%
photon detection	$\sim 10^{-9}$	< 0.1%
memory error	$\sim 10^{-8}$	< 0.1%
imperfect br. ratios	2.26×10^{-5}	34%
total error per atom	6.70×10^{-5}	100%

Table 8.1: The absolute and relative contribution of the different error sources to the total error per atom E , at $\tilde{n} = 120$, $\Delta = \Delta_{\text{opt}} = 10.9 \times 10^4 \gamma$, $\Omega = \Omega_{\text{opt}} = 8.33 \times 10^4 \gamma$ and $n = n_{\text{opt}} = 298$, for the 3D setup. (See Appendix G.4 for 2D results.)

over the non-entangled scheme,

$$G = \frac{\sigma_{\text{non-ent}}}{\sigma_{\text{ent}}/(2F - 1)} = e^{-EN} \frac{\pi}{8} \sqrt{\frac{N}{\log N}}, \quad (8.7)$$

where $\sigma_{\text{ent}} = \frac{1}{\omega_0 \tau} \frac{8}{\pi} \frac{\sqrt{\log N}}{N}$ (from [121], assuming perfect fidelity, and that τ is smaller than the reduced atomic coherence time $\gamma_{\text{at}}^{-1}/N$) and $\sigma_{\text{non-ent}} = \frac{1}{\omega_0 \tau} \frac{1}{\sqrt{N}}$ (for N independent atoms) are the Allan-deviations of the two schemes, where ω_0 is the central frequency and τ is the total available measurement time. The additional factor of $2F - 1 = e^{-EN}$ is due to the reduced Fisher information of a non-pure GHZ state, where E is the error per atom and F is the fidelity of the initial state. (See supplementary materials for details.) For $E = E_{\min} = 6.7 \times 10^{-5}$, Eq. 8.7 is maximal at $N_{\text{opt}} \approx 1/(2E_{\min}) \approx 7500$, where $G_{\max} = 6.9$, and $F = [1 + e^{-N_{\text{opt}} E_{\min}}]/2 = 0.82$.

Given that the optimal number of atoms at each clock is $n_{\text{opt}} \approx 300$, the optimal number of clocks is $K_{\text{opt}} = N_{\text{opt}}/n_{\text{opt}} \approx 22$. We can entangle 22 clocks, each consisting of ~ 300 atoms, and gain about a factor of ~ 7 in terms of clock precision over the classical scheme. If multiples of 7500 atoms are available, then the best way to utilize them is to create multiple independent GHZ states (either in a single clock or in a network), and combine the measurement results classically. The overall gain of a factor of 7 means that we can use 50 times less atoms to reach the same precision as any non-entangled clock (network).

We note that the same construction can be imagined with distinct atomic ensembles in a single vacuum chamber. The ensembles can be brought into entanglement using either the same method of two-photon emission and detection, or moving a single Rydberg atom close to each ensemble, and sequentially entangling them through blockade. We estimate the errors to be similar (see Appendix G.6), resulting in the

same optimal GHZ size and gain.

8.5 Conclusion

We presented and analyzed a protocol, capable of fully entangling ensembles of neutral atoms located in different atomic clocks. Local interactions are made robust by utilizing the strong interaction between Rydberg excitations, and non-local entanglement creation is made reliable with strong atom-light coupling, suppressed photon propagation errors and long atomic memory lifetimes. We showed that our scheme, in particular a realization with neutral Yb ensembles, is feasible and provides significant gain over non-entangled schemes even in the light of physical imperfections. Our results provide the first detailed proposal for a network that can serve as a first prototype of the global quantum clock network outlined in [121].

Appendix A

Appendices for Chapter 2

A.1 Derivation of reflected mode operator

We obtain the reflected mode operator c_R using input-output relations for a two-sided cavity. By assuming that the two endmirrors have the same transmittivity ($\propto \kappa$), we can write the input-output relation for cavity mode c_a on the driven mirror as

$$c_{a,\text{out}} = \sqrt{\kappa} c_a - c_{a,\text{in}}, \quad (\text{A.1})$$

where $c_{a,\text{in}} = -i\frac{\Omega}{\sqrt{\kappa}}$ is the incoming field operator on the mirror and $c_{a,\text{out}}$ is the output field operator. For direct comparision with c_a we divide by $\sqrt{\kappa}$ and define the reflection mode operator as $c_R \equiv c_{a,\text{out}}/\sqrt{\kappa} = c_a + i\frac{\Omega}{\kappa}$.

A.2 Analytic model

In this appendix we provide the analytic solutions used to calculate one- and two-time correlation functions in steady state. First, one-time correlations are calculated from the steady state solutions of Eqs. (2.13–2.18). We set the time derivatives to zero and solve the equations iteratively, order by order in the weak drive. This procedure yields

$$\bar{A}_{000} \approx 1, \quad (\text{A.2})$$

$$\bar{A}_{100} = -i\alpha \frac{1}{1+4x^2}, \quad (\text{A.3})$$

$$\bar{A}_{011} = -\alpha \frac{2x}{1+4x^2}, \quad (\text{A.4})$$

$$\bar{A}_{200} = -\frac{\alpha^2}{\sqrt{2}} \frac{1+2x^2}{(1+4x^2)(1+6x^2)}, \quad (\text{A.5})$$

$$\bar{A}_{111} = i\alpha^2 \frac{2x}{(1+4x^2)(1+6x^2)}, \quad (\text{A.6})$$

$$\bar{A}_{022} = \alpha^2 \frac{4x^2}{(1+4x^2)(1+6x^2)}, \quad (\text{A.7})$$

where $\alpha = \Omega/\tilde{\kappa}$ ($|\alpha|^2 \ll 1$), $x = g/(4\tilde{\kappa})$ and $\tilde{\kappa} = \kappa - i\Delta$. Using these amplitudes, we can express all equal time averages. The mean photon numbers are

$$\bar{n}_a = |\bar{A}_{100}|^2, \quad (\text{A.8})$$

$$\bar{n}_s = |\bar{A}_{011}|^2, \quad (\text{A.9})$$

$$\bar{n}_R = \left| \bar{A}_{100} + i\frac{\Omega}{\kappa} \right|^2, \quad (\text{A.10})$$

and the photon-photon correlation functions are

$$g_{aa}^{(2)}(0) = \frac{2|\bar{A}_{200}|^2}{|\bar{A}_{100}|^4}, \quad (\text{A.11})$$

$$g_{ss}^{(2)}(0) = \frac{2|\bar{A}_{022}|^2}{|\bar{A}_{011}|^4}, \quad (\text{A.12})$$

$$g_{RR}^{(2)}(0) = \frac{\left| -\left(\frac{\Omega}{\kappa}\right)^2 + 2i\frac{\Omega}{\kappa}\bar{A}_{100} + \sqrt{2}\bar{A}_{200} \right|^2}{\left|i\frac{\Omega}{\kappa} + \bar{A}_{100}\right|^4}. \quad (\text{A.13})$$

To leading order in κ/g these yield Eqs. (2.19–2.24).

At finite temperature we calculate steady state amplitudes within each phonon subspace n similarly in the ansatz of Eq. 2.26. Using the notation $R_\kappa(\omega)$ introduced in Section 2.3.2, the steady state amplitudes within the subspace with n phonons in the optical groundstate are

$$|\bar{A}_{10n}|^2 = \frac{\Omega^2 \sqrt{R_\kappa(0)}}{R_\kappa\left(\frac{g}{2}\sqrt{n+1}\right)}, \quad (\text{A.14})$$

$$|\bar{A}_{01n+1}|^2 = \frac{\Omega^2 g^2 (n+1)}{4R_\kappa\left(\frac{g}{2}\sqrt{n+1}\right)}, \quad (\text{A.15})$$

$$|\bar{A}_{20n}|^2 = \frac{\Omega^4 R_\kappa(g/\sqrt{8})}{R_\kappa\left(g\sqrt{(2n+1)/8}\right) R_\kappa\left(\frac{g}{2}\sqrt{n+1}\right)}, \quad (\text{A.16})$$

$$|\bar{A}_{02n+2}|^2 = \frac{\Omega^4 g^4 (n+1)(n+2)}{32R_\kappa\left(g\sqrt{(2n+1)/8}\right) R_\kappa\left(\frac{g}{2}\sqrt{n+1}\right)}. \quad (\text{A.17})$$

Two-time correlation functions are calculated similarly, using the conditional state after a jump (see Eqs. (2.39) and (2.44)) as the initial condition. For example the unnormalized state after detection of a photon in the c_a mode is $c_a|\psi\rangle = \bar{A}_{100}|000\rangle + \sqrt{2}\bar{A}_{200}|100\rangle + \bar{A}_{111}|011\rangle$. We solve Eqs. (2.13–2.15) for the amplitudes with this state as initial condition. The finite delay correlation of the driven mode is

$$g_{aa}^{(2)}(\tau) = \frac{|A_{100}(\tau)|^2}{|\bar{A}_{100}|^4}. \quad (\text{A.18})$$

in good agreement with the numerics. The correlation of the undriven mode $g_{ss}^{(2)}(\tau)$ is calculated similarly. The unnormalized state after detection in the c_s mode is $c_s|\psi\rangle = \bar{A}_{011}|001\rangle + \bar{A}_{111}|101\rangle + \sqrt{2}\bar{A}_{022}|012\rangle$. Using this as the initial condition we solve Eqs. (2.41–2.43) for the amplitudes in the conditional state. In the limit of $\gamma \ll \kappa$ we obtain

$$g_{ss}^{(2)}(\tau) = \frac{|A_{012}(\tau)|^2}{|\bar{A}_{011}|^4}. \quad (\text{A.19})$$

Appendix B

Appendices for Chapter 3

B.1 Phonon nonlinearities

In Eq. (8) in the main text we have derived an effective master equation (ME) to describe the nonlinear interaction between two phonon modes. In the following we present an alternative, more rigorous, approach, which illustrates the individual approximations made in the derivation of the effective phonon nonlinearity in more detail. We first consider only a single mechanical mode, e.g. $b \equiv b_1$, which also allows us more easily to compare the results with exact numerical calculations of the full model.

B.1.1 Model

We start with the full ME for the two optical modes coupled to a single resonator mode, which in the frame of the driving frequency ω_L can be written as

$$\dot{\rho} = -i[H_0 + H_g + H_\Omega(t), \rho] + \mathcal{L}_{\text{diss}}\rho. \quad (\text{B.1})$$

Here

$$H_0 = \omega_m b^\dagger b - \Delta_s c_s^\dagger c_s - \Delta_a c_a^\dagger c_a, \quad (\text{B.2})$$

and

$$H_g = \frac{g_0}{2} (c_a c_s^\dagger b^\dagger + c_a^\dagger c_s b), \quad (\text{B.3})$$

are the free evolution and the OM coupling, respectively, $H_\Omega(t) = i\Omega_s(t)(c_s^\dagger - c_s)$ is the driving field for the symmetric mode with slowly varying amplitude $\Omega_s(t)$ and

$$\mathcal{L}_{\text{diss}}\rho = \sum_{\eta=s,a} \kappa \mathcal{D}[c_\eta]\rho + \frac{\gamma}{2} \mathcal{D}_{\text{th}}[b]\rho, \quad (\text{B.4})$$

accounts for dissipation. Here we have defined the superoperator $\mathcal{D}_{\text{th}}[b] = (N_{\text{th}} + 1)\mathcal{D}[b] + N_{\text{th}}\mathcal{D}[b^\dagger]$ to describe the coupling to a thermal bath.

B.1.2 Displaced frame

In contrast to the approach outlined in the main text, we now start our analysis with a unitary displacement $U(t)c_s U^\dagger(t) = c_s + \alpha(t)$ where the classical cavity field $\alpha(t)$ obeys

$$\dot{\alpha}(t) = (i\Delta_s - \kappa)\alpha(t) + \Omega_s(t). \quad (\text{B.5})$$

This unitary transformation eliminates the classical driving field and in the new frame the resulting ME can be written as

$$\dot{\rho} = -i[H_{\text{lin}} + H_g, \rho] + \mathcal{L}_{\text{diss}}\rho, \quad (\text{B.6})$$

where $H_\Omega(t)$ has disappeared, but the linear part of the Hamiltonian now contains an additional coupling between the resonator and the anti-symmetric cavity mode,

$$H_{\text{lin}} = H_0 + G(t)c_a b^\dagger + G^*(t)c_a^\dagger b, \quad (\text{B.7})$$

where $G(t) = g_0\alpha(t)/2$. Note that ME (B.6) is still exact and we will use this equation for our exact numerics below.

B.1.3 Hybridized modes

To proceed, we assume that $\alpha(t)$ is constant or slowly varying on the timescale set by the detunings $|\Delta_a + \omega_m^i|$. This allows us to write H_{lin} in its adiabatic eigenbasis

$$H_{\text{lin}} = -\Delta_s c_s^\dagger c_s - \tilde{\Delta}_a C^\dagger C + \tilde{\omega}_m B^\dagger B, \quad (\text{B.8})$$

where the C and B are bosonic operators for the hybridized mechanical and optical modes and $\tilde{\Delta}_a$ and $\tilde{\omega}_m$ are the new eigenfrequencies of H_{lin} for a given $G \equiv G(t)$. We obtain

$$C = \cos(\theta)c_a - \sin(\theta)b, \quad (\text{B.9})$$

$$B = \cos(\theta)b + \sin(\theta)c_a, \quad (\text{B.10})$$

where $\tan(2\theta) = -2|G|/\delta$ and $\delta = -(\Delta_a + \omega_m) = 2J - \omega_m - \Delta_s$. The shifted frequencies are given by

$$-\tilde{\Delta}_a = -\Delta_a - \frac{1}{2} \left(\delta - \sqrt{\delta^2 + 4|G|^2} \right), \quad (\text{B.11})$$

$$\tilde{\omega}_m = \omega_m - \frac{1}{2} \left(\delta + \sqrt{\delta^2 + 4|G|^2} \right). \quad (\text{B.12})$$

We see that by slowly increasing the classical control field $\alpha(t)$, the mechanical mode b is adiabatically converted into a polaronic mode B . For small mixing angles θ the mode still retains its mechanical character, while the finite photonic component is responsible for inducing an effective nonlinearity.

In terms of the hybridized mode operators the dissipative terms can be written as

$$\begin{aligned}\mathcal{L}_{\text{diss}} \simeq & \kappa \mathcal{D}[c_s] + \kappa \cos^2(\theta) \mathcal{D}[C] + \frac{\gamma}{2} \sin^2(\theta) \mathcal{D}_{\text{th}}[C] \\ & + \frac{\gamma}{2} \cos^2(\theta) \mathcal{D}_{\text{th}}[B] + \kappa \sin^2(\theta) \mathcal{D}[B].\end{aligned}\quad (\text{B.13})$$

In particular, we identify an additional optical decay channel with rate $\gamma' = 2\kappa \sin^2(\theta)$ for the B mode. In the following we define as

$$\tilde{\mathcal{L}}_{\gamma} = \frac{\gamma}{2} \cos^2(\theta) \mathcal{D}_{\text{th}}[B] + \frac{\gamma'}{2} \mathcal{D}[B], \quad (\text{B.14})$$

the modified mechanical dissipation Liouvillian. Note that in Eq. (B.13) we have already neglected cross-terms between C and B^\dagger . This is valid in the parameter regime considered below, where κ is small compared to the splitting of these two modes.

Finally, we also express the nonlinear interaction H_g in terms of the hybridized modes and write the result as

$$H_g = H_g^{(1)} + H_g^{(2)} + H_g'. \quad (\text{B.15})$$

Here, the first term is the one of interest

$$H_g^{(1)} = \frac{g_0}{4} \sin(2\theta) (c_s + c_s^\dagger) B^\dagger B, \quad (\text{B.16})$$

and describes the coupling of the c_s mode to the number operator of the B mode. The second term is given by

$$H_g^{(2)} = -\frac{g_0}{2} \sin^2(\theta) (B c_s^\dagger C^\dagger + B^\dagger c_s C), \quad (\text{B.17})$$

and leads to additional corrections. However, for small θ this term is small compared to $H_g^{(1)}$. It can be further reduced if $|\Delta_s - \delta| \gg \Delta_s$. Finally, the last term contains

interactions

$$H'_g = \frac{g_0}{2} \cos^2(\theta) (C c_s^\dagger B^\dagger + C^\dagger c_s B) - \frac{g_0}{4} \sin(2\theta) (c_s + c_s^\dagger) C^\dagger C, \quad (\text{B.18})$$

which can be neglected when either the c_s or the C mode are in the vacuum state.

B.1.4 Adiabatic elimination of the cavity mode

Our goal is now to derive an effective ME for the mechanical degrees of freedom only. To do so, we write the full ME as

$$\dot{\rho} = (\mathcal{L}_0 + \mathcal{L}_1) \rho, \quad (\text{B.19})$$

where

$$\mathcal{L}_0 \rho = -i[H_{\text{lin}} + H'_g, \rho] + \mathcal{L}_{\text{diss}} \rho, \quad (\text{B.20})$$

and

$$\mathcal{L}_1 \rho = -i[H_g^{(1)} + H_g^{(2)}, \rho]. \quad (\text{B.21})$$

The dynamics of \mathcal{L}_0 does not excite the cavity modes, and therefore, in the limit where $\tilde{g} = g_0 \sin(2\theta)/4 \rightarrow 0$ (either g_0 is small or the mixing angle θ is small) the density operator can to a good approximation be written as $\rho(t) = \rho_m(t) \otimes \rho_c^0$, where ρ_c^0 is the vacuum state of the c_s and the C mode. To account for the effects of a small $\mathcal{L}_1 \sim \tilde{g}$ up to second order in perturbation theory we define a projection operator onto this subspace,

$$\mathcal{P} \rho = \text{Tr}_c \{ \rho \} \otimes \rho_c^0, \quad (\text{B.22})$$

and its complement $\mathcal{Q} = \mathbb{1} - \mathcal{P}$. Then

$$\mathcal{P} \dot{\rho} = \mathcal{P} \mathcal{L}_0 \mathcal{P} \rho + \mathcal{P} \mathcal{L}_1 \mathcal{Q} \rho, \quad (\text{B.23})$$

$$\mathcal{Q} \dot{\rho} = \mathcal{Q} (\mathcal{L}_0 + \mathcal{L}_1) \mathcal{Q} \rho + \mathcal{Q} \mathcal{L}_1 \mathcal{P} \rho. \quad (\text{B.24})$$

Up to second order in \tilde{g} we can formally integrate the equation for $\mathcal{P}\rho$ and obtain

$$\mathcal{P}\dot{\rho}(t) \simeq \mathcal{P}\mathcal{L}_0\mathcal{P}\rho(t) + \mathcal{P}\mathcal{L}_1 \int_0^\infty d\tau \mathcal{Q}e^{\mathcal{L}_0\tau} \mathcal{Q}\mathcal{L}_1\mathcal{P}\rho(t). \quad (\text{B.25})$$

We define by $\rho_m(t) = \text{Tr}_c\{\mathcal{P}\rho(t)\}$ the reduced density operator of the mechanical mode and write the final result as

$$\dot{\rho}_m(t) = (\mathcal{L}_m^{(0)} + \mathcal{L}_m^{(1)} + \mathcal{L}_m^{(2)}) \rho_m(t). \quad (\text{B.26})$$

The first term describes the linear part of the dynamics

$$\mathcal{L}_m^{(0)}\rho_m = -i[\tilde{\omega}_m B^\dagger B, \rho_m] + \tilde{\mathcal{L}}_\gamma \rho_m, \quad (\text{B.27})$$

with a modified frequency and modified decay rates for the B mode. The other two terms are given by

$$\mathcal{L}_m^{(1)}\rho_m = - \int_0^\infty d\tau \text{Tr}_c\{[H_g^{(1)}, e^{\mathcal{L}_0\tau} ([H_g^{(1)}, \rho_m \otimes \rho_c^0])]\}, \quad (\text{B.28})$$

and

$$\mathcal{L}_m^{(2)}\rho_m = - \int_0^\infty d\tau \text{Tr}_c\{[H_g^{(2)}, e^{\mathcal{L}_0\tau} ([H_g^{(2)}, \rho_m \otimes \rho_c^0])]\}. \quad (\text{B.29})$$

B.1.5 Simple perturbation theory

In deriving Eq. (B.26) we have so far only assumed that \tilde{g} is small compared to the typical frequency scales of the dynamics of the c_s mode. For now we will also assume that g_0 is small compared to δ and Δ_s . This allows us to neglect the term H'_g in \mathcal{L}_0 and the cavity correlation functions in Eqs. (B.28) and (B.29) can be evaluated in a straight forward manner. For the action of $\mathcal{L}_m^{(1)}$ we obtain

$$\mathcal{L}_m^{(1)}\rho_m = -i[\Lambda(B^\dagger B)^2, \rho_m] + \Gamma_\phi \mathcal{D}[B^\dagger B], \quad (\text{B.30})$$

where $\Lambda = \text{Im}\{S_{gg}^{(1)}(0)\}$, $\Gamma_\phi = \text{Re}\{S_{gg}^{(1)}(0)\}$ and

$$S_{gg}^{(1)}(\omega) = \tilde{g}^2 \int_0^\infty d\tau \text{Tr}_c \{c_s e^{\mathcal{L}_0 \tau} (c_s^\dagger \rho_c^0)\} e^{-i\omega\tau}. \quad (\text{B.31})$$

We find $S_{gg}^{(1)}(\omega) = \tilde{g}^2 / (-i(\Delta_s + \omega) + \kappa)$ and after inserting back the definition of \tilde{g} in the limit $|g_0\alpha/\delta| \ll 1$ we recover the expressions for Λ and Γ_ϕ given in Eq. (9) in the main text. Similarly we obtain

$$\mathcal{L}_m^{(2)} \rho_m = -i[\delta\omega_m^{(2)} B^\dagger B, \rho_m] + \frac{\gamma^{(2)}}{2} \mathcal{D}[B], \quad (\text{B.32})$$

where $\delta\omega_m^{(2)} = \text{Im}\{S_{gg}^{(2)}(\tilde{\omega}_m)\}$, $\gamma^{(2)} = \text{Re}\{S_{gg}^{(2)}(\tilde{\omega}_m)\}$ and

$$S_{gg}^{(2)}(\omega) = \frac{g_0^2 \sin^4(\theta)}{4} \int_0^\infty d\tau \text{Tr}_c \{c_s C e^{\mathcal{L}_0 \tau} (c_s^\dagger C^\dagger \rho_c^0)\} e^{-i\omega\tau}. \quad (\text{B.33})$$

The small frequency shift $\delta\omega_m^{(2)}$ can be absorbed into the definition of $\tilde{\omega}_m$ and, since $\gamma^{(2)} \approx \gamma' \sin^2(\theta) g_0^2 / (4\delta^2)$, for not too large mixing angles θ , $\gamma^{(2)}$ can always be neglected compared to γ' . All together the final effective phonon master equation is

$$\begin{aligned} \dot{\rho}_m = & -i[\tilde{\omega}_m B^\dagger B + \Lambda(B^\dagger B)^2, \rho_m] + \Gamma_\phi \mathcal{D}[B^\dagger B] \rho_m \\ & + \frac{\gamma}{2} \mathcal{D}_{\text{th}}[B] \rho_m + \frac{\gamma'}{2} \mathcal{D}[B] \rho_m, \end{aligned} \quad (\text{B.34})$$

which is the single resonator version of ME (8) given in the main text.

B.1.6 Corrections

Let us now extend the above result to the case where \tilde{g} is small compared to Δ_s and δ , but the bare interaction g_0 is not. In this case the general expressions in Eqs. (B.28) and (B.29) still apply, but the effect of H'_g must be taking into account when evaluating the correlation functions. To illustrate this, let us assume that g_0

is still small compared to δ . Then, by assuming that the C mode is initially in the ground state, we obtain approximately

$$H_{\text{lin}} + H'_g \approx -(\Delta_s - \Delta_B B^\dagger B) c_s^\dagger c_s, \quad (\text{B.35})$$

where the off-resonant frequency shift is

$$\Delta_B = \frac{g_0^2 \cos^4(\theta)}{4(\tilde{\Delta}_a + \tilde{\omega}_m - \Delta_s)}, \quad (\text{B.36})$$

and can be comparable to Δ_s . Therefore, we must evaluate the correlation function for each phonon number state $|n\rangle$ separately and write the resulting non-linear interaction as

$$\mathcal{L}_m^{(1)} \rho_m = \sum_n n^2 (-i [\Lambda(n)|n\rangle\langle n|, \rho_m] + \Gamma_\phi(n)\mathcal{D}[|n\rangle\langle n|]). \quad (\text{B.37})$$

Here $\Lambda(n)$ and $\Gamma_\phi(n)$ are the imaginary and real part of

$$S_{gg}^{(1)}(\omega = -n\Delta_B) = \frac{n^2 \tilde{g}^2}{-i(\Delta_s - n\Delta_B) + \kappa}. \quad (\text{B.38})$$

We see that in this parameter regime more complicated nonlinearities can occur, but the overall magnitude and the ratio between coherent and dephasing interactions remains the same. In principle, this analysis can be extended to the regime, where g_0 is comparable to δ . However, in this case no simple analytic expressions for $\lambda(n)$ and $\Gamma_\phi(n)$ can be derived and need to be evaluated numerically.

B.1.7 Numerical simulation

To assess the validity of the effective phonon ME we now compare our result with the dynamics of the full OMS. Since we are mainly interested in the relation between the phonon non-linearity and the corresponding dephasing and decay rates,

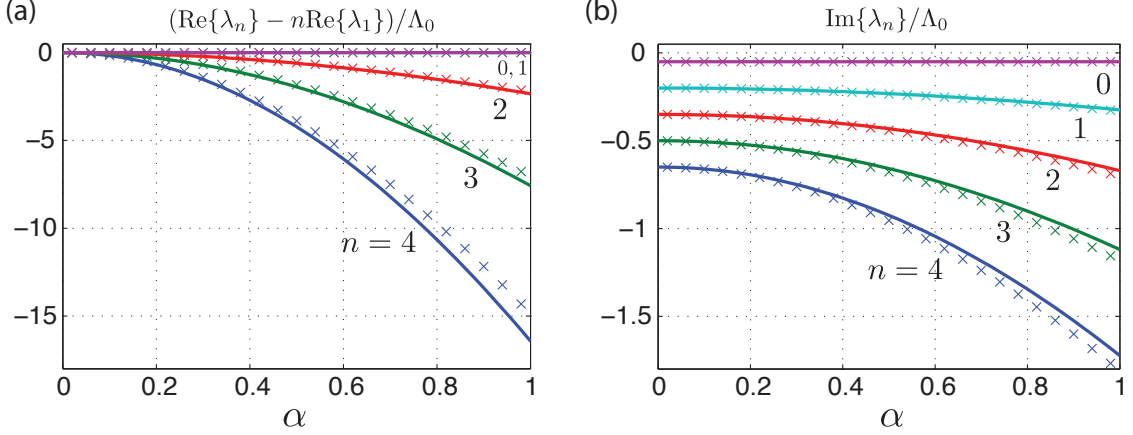


Figure B.1: Comparison of the effective analytic description (Eqs. (B.40), lines) with exact eigenvalues of the Hamiltonian in Eq. (B.39) (crosses) for different cavity field amplitudes α . All results are normalized to the scale $\Lambda_0 = g_0^4 / (16 |\Delta_s| \delta^2)$ of the non-linearity. (a) Deviation of the real parts of the eigenvalues from the result expected for a linear oscillator, such that the splitting of the curves indicates an effective non-linearity. (b) Imaginary parts of the eigenvalues corresponding to decays. In both plots we used the parameters $\Delta_s/g_0 = -1$, $\delta/g_0 = 5$, $\kappa/g_0 = 2.5 \times 10^{-2}$, $\gamma_m/g_0 = 2.5 \times 10^{-4}$ and $N_{\text{th}} = 1$.

it is sufficient to evaluate the spectrum of the non-Hermitian Hamiltonian, which for the full model it is given by

$$\tilde{H}_{\text{full}} = H_{\text{lin}} + H_g - i\kappa c_s^\dagger c_s - i\kappa c_a^\dagger c_a - i\frac{\gamma}{2}(N_{\text{th}} + 1)b^\dagger b - i\frac{\gamma}{2}N_{\text{th}}bb^\dagger. \quad (\text{B.39})$$

In Fig. B.1 we plot the real and imaginary parts of the lowest eigenvalues λ_n of \tilde{H}_{full} , which correspond to the lowest number states $|n\rangle$ of the B mode. From the effective phonon model given in Eq. (B.34) and (B.37) we obtain the approximate analytic results

$$\text{Re}\{\lambda_n\} = n\tilde{\omega}_m + n^2\Lambda(n), \quad (\text{B.40a})$$

and

$$|\text{Im}\{\lambda_n\}| = \frac{\gamma}{2}N_{\text{th}} + n \left(\frac{\gamma}{2}(2N_{\text{th}} + 1) + \frac{\gamma'}{2} \right) + n^2\Gamma_\phi(n). \quad (\text{B.40b})$$

We see a good agreement between these results for the effective model and the exact numerics, both for the real and imaginary parts. Although there are some deviations due to higher-order effects, the effective non-linear splitting (Fig. B.1(a)) is much larger than the induced decoherence (Fig. B.1(b)), as is expected for the chosen parameters. Hence, we conclude that the effective model accurately describes the dynamics of the mechanical resonator, and that the effective phonon non-linearity may serve as a basis for gate operations as discussed in the main text and in the following section.

B.2 Phonon-phonon interactions

The derivation of the effective phonon nonlinearity, as outlined above for a single resonator, can be easily adapted to two resonators as discussed in the main text. In this case we have

$$H_0 = \sum_{i=1,2} \omega_m^i b_i^\dagger b_i - \Delta_s c_s^\dagger c_s - \Delta_a c_a^\dagger c_a, \quad (\text{B.41})$$

and

$$H_g = \frac{g_0}{2} \left[c_a c_s^\dagger (b_1^\dagger - b_2^\dagger) + c_a^\dagger c_s (b_1 - b_2) \right]. \quad (\text{B.42})$$

After changing into the displaced representation to eliminate the driving field we obtain the linearized Hamiltonian

$$H_{\text{lin}} = H_0 + \sqrt{2} (G(t) c_a b_a^\dagger + G^*(t) c_a^\dagger b_a), \quad (\text{B.43})$$

where $b_a = (b_1 - b_2)/\sqrt{2}$ and $G(t) = g_0 \alpha(t)/2$. For similar mechanical frequencies $\omega_m^1 \simeq \omega_m^2 = \omega_m$ the symmetric resonator mode is decoupled and we can simply repeat the analysis from above by identifying $b \equiv b_a$ and replacing g_0 by $\sqrt{2}g_0$.

For arbitrary ω_i , we write the linear part of the Hamiltonian in its diagonal form

$$H_{\text{lin}} = -\Delta_s c_s^\dagger c_s - \tilde{\Delta}_a C^\dagger C + \tilde{\omega}_1 B_1^\dagger B_1 + \tilde{\omega}_2 B_2^\dagger B_2. \quad (\text{B.44})$$

As in the single-resonator case the c_s mode is unaffected, but the c_a mode now couples to both b_1 and b_2 . The resulting hybridized modes C , B_\pm depend on the choice of parameters $\omega_m^{1,2}$, Δ_a and G . For the case of interest, i.e. for a symmetric detuning $\omega_m^{1,2} = -\Delta_a \mp \delta$, we obtain

$$C = \cos(2\Theta)c_a - \sin(2\Theta)(B_1 + B_2)/\sqrt{2}, \quad (\text{B.45})$$

$$B_1 = \cos^2(\Theta)b_1 + \sin(2\Theta)c_a/\sqrt{2} - \sin^2(\Theta)b_2, \quad (\text{B.46})$$

$$B_2 = \cos^2(\Theta)b_2 + \sin(2\Theta)c_a/\sqrt{2} - \sin^2(\Theta)b_1, \quad (\text{B.47})$$

where $\tan(2\Theta) = -\sqrt{2}|G|/\delta$. Therefore, for small Θ the modes $B_{1,2}$ correspond to the original mechanical resonator modes $b_{1,2}$ and $\tilde{\omega}_i \approx \omega_m^i$.

As above, we can now re-express the dissipation and the non-linear coupling H_g in terms of C and B_\pm . The modified mechanical dissipation terms are given

$$\tilde{\mathcal{L}}_\gamma = \sum_{i=1,2} \frac{\gamma}{2} \cos^2(2\Theta) \mathcal{D}_{\text{th}}[B_i] + \frac{\kappa}{2} \sin^2(2\Theta) \mathcal{D}[B_i], \quad (\text{B.48})$$

and for small Θ the optical decay rate $\gamma' = \kappa \sin^2(2\Theta)$ is the same as given above and in the main text. Using the decomposition of the non-linear coupling as done in Eq. (B.15), we obtain

$$H_g^{(1)} = \frac{g_0}{\sqrt{8}} \sin(2\Theta) (c_s + c_s^\dagger) (B_1^\dagger B_1 - B_2^\dagger B_2), \quad (\text{B.49})$$

the contribution $H_g^{(2)}$ vanishes and

$$H'_g = \frac{g_0}{2} \cos(2\Theta) (C c_s^\dagger (B_1^\dagger - B_2^\dagger) + \text{H.c.}) . \quad (\text{B.50})$$

We see that the structure and also the relative frequency scales are identical to the corresponding terms discussed for the single resonator above. Therefore, under the same conditions we can eliminate the cavity mode and obtain the effective phonon master equation

$$\begin{aligned}\dot{\rho}_m = & -i \left[\sum_i \tilde{\omega}_i B_i^\dagger B_i + \Lambda (B_1^\dagger B_1 - B_2^\dagger B_2)^2, \rho_m \right] \\ & + \Gamma_\phi \mathcal{D}[(B_1^\dagger B_1 - B_2^\dagger B_2)] \rho_m + \tilde{\mathcal{L}}_\gamma \rho_m.\end{aligned}\tag{B.51}$$

For small Θ this equation reduces to ME (8) in the main text and higher-order corrections can be included in the same way as discussed for the single resonator case.

Appendix C

Appendices for Chapter 4

This appendix describes the details of the perturbation theory and the derivation of the effective Hamiltonian \hat{H}_{eff} and effective Lindblad operators. We describe the situation both with and without a two-photon drive. Furthermore, we present the results of a numerical simulation of the full dynamics of the gates to verify the results found with perturbation theory and address the question of how strong a drive we can allow for. In the end, this determines the gate time as described in the article. Finally we discuss of the additional errors described in the final part of the article.

C.1 Perturbation theory

We will now give the details of the perturbation theory and the derivation of the effective operators together with the success probabilitites, gate times and gate errors (see Tab. C.1). Our perturbation theory is based on the effective operator formalism described in Ref. [178].

Gate	Origin of error	Error	Probability	Time
CZ-gate	$\gamma_g = 0$	0	$\sim 1 - \frac{6}{\sqrt{C}}$	$\sim \frac{15\pi\sqrt{C}\gamma}{2\Omega^2}$
	$\gamma_g > 0$	$\sim \frac{\gamma_g}{\gamma\sqrt{C}}$		
Toffoli	$\Gamma_i \neq \Gamma_j$	$\lesssim \frac{0.3}{C}$	$\sim 1 - \frac{3}{\sqrt{C}}$	$\sim \frac{4\pi\sqrt{C}\gamma}{\Omega^2}$
	$\gamma_g > 0$	$\sim \frac{\gamma_g}{\gamma\sqrt{C}}$		

Table C.1: The errors, success probabilities and gate times of the N -qubit Toffoli gate and the CZ-gate considered in the article. Note that the branching fraction γ_g/γ can be made arbitrarily small using a far detuned two-photon driving as explained in below. Γ_i is the rate of detectable errors for the qubit state with i qubits in state $|1\rangle$. The success probability of the CZ-gate can be increased at the expense of an error scaling of $1/C$ as explained in the article.

First, we treat the simplest situation where the auxiliary atom is directly driven to an excited state $|E\rangle$ by a weak classical drive Ω as shown in Fig. C.1 (reproduced from Fig. 1 in the article). Note that we allow for some decay from $|E\rangle \rightarrow |g\rangle$ with decay rate γ_g as opposed to the situation in the article. We will later consider the situation where this decay rate is suppressed using a two-photon drive. The level structure of the qubit atoms are also shown in Fig. C.1.

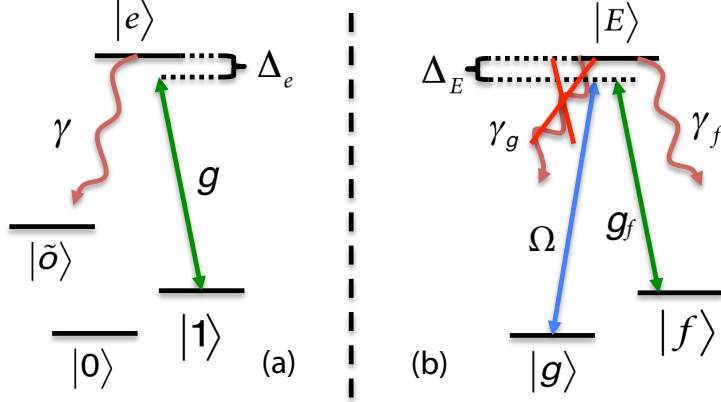


Figure C.1: (a) Level structure of the qubit atoms. Only state $|1\rangle$ couples to the cavity and we assume that the excited level decays to some level $|\tilde{o}\rangle$, possibly identical to $|f\rangle$ or $|0\rangle$. (b) Level structure of the auxiliary atom and the transitions driven by the weak laser (Ω) and the cavity (g_f). We allow for some decay from $|E\rangle \rightarrow |g\rangle$ with decay rate γ_g .

The Hamilton describing the system in a proper rotating frame is given by Eqs. (1)-(3) in the article and is reproduced here

$$\hat{H} = \hat{H}_e + \hat{V} + \hat{V}^\dagger, \quad (\text{C.1})$$

$$\begin{aligned} \hat{H}_e &= \Delta_E |E\rangle\langle E| + g_f (\hat{a}|E\rangle\langle f| + H.c) \\ &\quad + \sum_k \Delta_e |e\rangle_k\langle e| + g (\hat{a}|e\rangle_k\langle 1| + H.c), \end{aligned} \quad (\text{C.2})$$

$$\hat{V} = \frac{\Omega}{2} |E\rangle\langle g|, \quad (\text{C.3})$$

where we have assumed for simplicity that all couplings (g, Ω) are real and k labels the qubit atoms ($\hbar = 1$). We have defined $\Delta_E = \omega_E - \omega_g - \omega_L$, and $\Delta_e = \omega_e - \omega_g - \omega_L + \omega_f - \omega_1$ where ω_L is the laser frequency and otherwise ω_x is the frequency associated with level x . Note that we assume the cavity frequency to be $\omega_c = \omega_L + \omega_g - \omega_f$ such that we are on resonance with the $|g\rangle \rightarrow |E\rangle \rightarrow |f\rangle$ two-photon transition.

The dissipation in the system is assumed to be described by Lindblad operators

such that $\hat{L}_0 = \sqrt{\kappa}\hat{a}$ describes the cavity decay with decay rate κ , $\hat{L}_g = \sqrt{\gamma_g}|g\rangle\langle E|$, and $\hat{L}_f = \sqrt{\gamma_f}|f\rangle\langle E|$ describes the decay of the auxiliary atom and $\hat{L}_k = \sqrt{\gamma}|\tilde{o}\rangle_i\langle e|$ describes the decay of the qubit atoms ($k = 1, 2 \dots N$). As described in the article $|\tilde{o}\rangle$ may or may not coincide with $|0\rangle$ or $|1\rangle$. Assuming that Ω is weak ($\Omega^2/\Delta_E \ll \Delta_E$ and $\Omega \ll g$), we can treat the driving as a perturbation to the system. As shown in Ref. [178], the dynamics of the system is then governed by an effective master equation of the form

$$\dot{\rho} = i \left[\rho, \hat{H}_{\text{eff}} \right] + \sum_x \hat{L}_x^{\text{eff}} \rho (\hat{L}_x^{\text{eff}})^\dagger - \frac{1}{2} \left((\hat{L}_x^{\text{eff}})^\dagger \hat{L}_x^{\text{eff}} \rho + \rho (\hat{L}_x^{\text{eff}})^\dagger \hat{L}_x^{\text{eff}} \right), \quad (\text{C.4})$$

where ρ is the density matrix of the system, \hat{H}_{eff} is an effective Hamiltonian, and L_x^{eff} are effective Lindblad operators with $x = 0, g, f, k$. The effective operators are found from:

$$\hat{H}_{\text{eff}} = -\frac{1}{2} \hat{V}^\dagger \left(\hat{H}_{\text{NH}}^{-1} + (\hat{H}_{\text{NH}}^{-1})^\dagger \right) \hat{V} \quad (\text{C.5})$$

$$\hat{L}_x^{\text{eff}} = \hat{L}_x \hat{H}_{\text{NH}}^{-1} \hat{V}, \quad (\text{C.6})$$

where

$$\hat{H}_{\text{NH}} = \hat{H}_e - \frac{i}{2} \sum_x \hat{L}_x^\dagger \hat{L}_x, \quad (\text{C.7})$$

is the no-jump Hamiltonian. The Hilbert space of the effective operators can be described in the basis of $\{|g\rangle, |f\rangle\}$ of the auxiliary atom and the states $\{|0\rangle, |1\rangle, |\tilde{o}\rangle\}$ of the qubit atoms. To ease the notation, we define the projection operators \hat{P}_n which projects on to the states with n qubits in state $|1\rangle$. From Eq. (C.5) and (C.6) we

then find:

$$\begin{aligned}\hat{H}_{\text{eff}} &= \sum_{n=0}^N \frac{-\Omega^2}{4\gamma} \text{Re} \left\{ \frac{i\tilde{\Delta}_e/2 + nC}{\tilde{\Delta}_e(i\tilde{\Delta}_E/2 + C_f) + \tilde{\Delta}_E nC} \right\} |g\rangle\langle g| \otimes \hat{P}_n \\ &= \sum_{n=0}^N \Delta_n |g\rangle\langle g| \otimes \hat{P}_n\end{aligned}\quad (\text{C.8})$$

$$\begin{aligned}\hat{L}_0^{\text{eff}} &= \sum_{n=0}^N \frac{1}{2\sqrt{\gamma}} \frac{\sqrt{C_f}\tilde{\Delta}_e\Omega}{\tilde{\Delta}_e(i\tilde{\Delta}_E/2 + C_f) + n\tilde{\Delta}_E C} |f\rangle\langle g| \otimes \hat{P}_n \\ &= \sum_{n=0}^N r_{0,n}^{\text{eff}} |f\rangle\langle g| \otimes \hat{P}_n\end{aligned}\quad (\text{C.9})$$

$$\begin{aligned}\hat{L}_g^{\text{eff}} &= \sum_{n=0}^N \frac{1}{2} \frac{(i\tilde{\Delta}_e/2 + nC)\Omega}{\tilde{\Delta}_e(i\tilde{\Delta}_E/2 + C_f) + n\tilde{\Delta}_E C} \frac{\sqrt{\gamma_g}}{\gamma} |g\rangle\langle g| \otimes \hat{P}_n \\ &= \sum_{n=0}^N r_{g,n}^{\text{eff}} |g\rangle\langle g| \otimes \hat{P}_n\end{aligned}\quad (\text{C.10})$$

$$\begin{aligned}\hat{L}_f^{\text{eff}} &= \sum_{n=0}^N \frac{1}{2} \frac{(i\tilde{\Delta}_e/2 + nC)\Omega}{\tilde{\Delta}_e(i\tilde{\Delta}_E/2 + C_f) + n\tilde{\Delta}_E C} \frac{\sqrt{\gamma_f}}{\gamma} |f\rangle\langle g| \otimes \hat{P}_n \\ &= \sum_{n=0}^N r_{f,n}^{\text{eff}} |f\rangle\langle g| \otimes \hat{P}_n\end{aligned}\quad (\text{C.11})$$

$$\begin{aligned}\hat{L}_k^{\text{eff}} &= \sum_{n=1}^N -\frac{1}{2\sqrt{\gamma}} \frac{\sqrt{C_f}\sqrt{C}\Omega}{\tilde{\Delta}_e(i\tilde{\Delta}_E/2 + C_f) + n\tilde{\Delta}_E C} |f\rangle\langle g| \otimes |\tilde{o}\rangle_k \langle 1| \otimes \hat{P}_n \\ &= \sum_{n=1}^N r_n^{\text{eff}} |f\rangle\langle g| \otimes |\tilde{o}\rangle_k \langle 1| \otimes \hat{P}_n,\end{aligned}\quad (\text{C.12})$$

where we have defined the cooperativities $C_{(f)} = g_{(f)}^2/\gamma\kappa$ for the qubit (auxiliary) atoms and the complex detunings $\tilde{\Delta}_E\gamma = \Delta_E - i\gamma_f/2$ and $\tilde{\Delta}_e\gamma = \Delta_e - i\gamma/2$. Note that we have defined the parameters $r_{0,n}^{\text{eff}}$, $r_{g,n}^{\text{eff}}$, $r_{f,n}^{\text{eff}}$ and r_n^{eff} in Eqs. (C.9)-(C.12) to characterize the decays described by the Lindblad operators. Note that $r_0^{\text{eff}} = 0$. In our calculations we parametrize the difference between the auxiliary atom and the qubit atoms by $C_f = \alpha C$ and $\gamma_f = \beta\gamma$ to easier treat the limit of $C \gg 1$ that we are interested in.

C.1.1 Success probability and fidelity

Eqs. (C.9)-(C.12) show that the effect of all Lindblad operators, except \hat{L}_g^{eff} , is that the state of the auxiliary atom is left in state $|f\rangle$. All these errors are thus detectable by measuring the state of the auxiliary atom at the end of the gate. For the heralded gates where we condition on measuring the auxiliary atom in state $|g\rangle$ at the end of the gates, these detectable decays therefore do not effect the fidelity of the gates but only the success probability. The rate Γ_n of the detectable decays for a state with n qubits in state $|1\rangle$ is $\Gamma_n = |r_{0,n}^{\text{eff}}|^2 + |r_{f,n}^{\text{eff}}|^2 + |r_n^{\text{eff}}|^2$ and assuming an initial qubit state described by density matrix ρ_{qubit} the success probability of the gates is

$$P_{\text{success}} = \sum_{n=0}^N \text{Tr} \left\{ e^{-\Gamma_n t_{\text{gate}}} \rho_{\text{qubit}} \hat{P}_n \right\}, \quad (\text{C.13})$$

where t_{gate} is the gate time and Tr denotes the trace.

Having removed the detrimental effect of the detectable errors by heralding on a measurement of the auxiliary atom the fidelity of the gates will be determined by more subtle, undetectable errors (see below). We define the fidelity, F of the gate as

$$F = \frac{1}{P_{\text{success}}} \langle \psi | \langle g | \tilde{\rho}_{\text{qubit}} | g \rangle | \psi \rangle, \quad (\text{C.14})$$

where we have assumed that the ideal qubit state after the gate is a pure state $|\psi\rangle$ and $\tilde{\rho}_{\text{qubit}}$ is the actual density matrix of the qubits and the auxiliary atom after the gate operation.

C.1.2 N -qubit Toffoli gate

As shown in the article, the effective Hamiltonian in Eq. (C.8) is sufficient to make a Toffoli gate by putting the qubit atoms on resonance ($\Delta_e = 0$). We will now

treat the worst case and average fidelities of the general Toffoli gate referred to in the article. The undetectable errors limiting the fidelities are the following.

- As described in the article the energy shifts of the coupled qubit states are all $\Delta_{n>0} \sim \Omega^2/(4\gamma\sqrt{C})$ in the limit $C \gg 1$. However, to higher order in C , we find corrections on the order $\mathcal{O}(\Omega^2/C^{3/2})$ to the energy shifts, which depend on the number of qubits that couples. The gate time of the Toffoli gate is $t_T \sim 4\pi\sqrt{C}\gamma/\Omega^2$ and consequently, the higher order corrections give uneven phase shifts on the order of $\mathcal{O}(C^{-1})$ for the coupled qubit states at the end of the gate. This leads to a phase error in the fidelity of $\mathcal{O}(C^{-2})$.
- The difference between the rates of detectable errors (Γ_n) for different qubit states changes the relative weight of the qubit states during the gate. This error will be $\mathcal{O}(C^{-1})$ as shown below.
- For $\gamma_g > 0$ the undetectable decay from $|E\rangle \rightarrow |g\rangle$ in the auxiliary atom will destroy the coherence between the qubit states. We find that this error will be $\sim \frac{\gamma_g}{\gamma\sqrt{C}}$. For now, we will assume that $\gamma_g = 0$ and thus ignore this error since we will show that we can suppress the branching fraction γ_g/γ arbitrary close to zero by having a two photon driving.

Assuming that $\gamma_g = 0$, the dominating source of error limiting the performance of the Toffoli gate is thus the difference between the rates of the detectable errors for the qubit states. We tune Δ_E such that $\Gamma_0 = \Gamma_1$ and the largest difference between the detectable errors is thus between the completely uncoupled state and the state with all qubit atoms in state $|1\rangle$. As a result, we can find an upper bound on the fidelity

of the N qubit Toffoli gate, considering an initial state $|0\rangle^{\otimes N} + |1\rangle^{\otimes N}$ in the limit $N \rightarrow \infty$ because this state experiences the largest difference between the number of coupled and uncoupled qubits. We find that the upper bound on the fidelity and the corresponding success probability is

$$F_{\text{up}} \sim 1 - \frac{\pi^2 \alpha}{16(\alpha + \beta)} \frac{1}{C} \quad (\text{C.15})$$

$$P_{\text{success,up}} \sim 1 - \frac{(\alpha + 2\beta)\pi}{2\sqrt{\alpha}\sqrt{\alpha + \beta}} \frac{1}{\sqrt{C}}. \quad (\text{C.16})$$

. In general, the fidelity of the gate will, however, be larger than what is suggested above. Considering a generic input state $(|0\rangle + |1\rangle)^{\otimes N}$ with the same parameters as above, we find

$$F_{\text{gen}} \sim 1 - k(N) \frac{\alpha\pi^2}{\alpha + \beta} \frac{1}{C} \quad (\text{C.17})$$

$$P_{\text{success,gen}} \sim 1 - \frac{(d(N)\alpha + 2\beta)\pi}{2\sqrt{\alpha}\sqrt{\alpha + \beta}} \frac{1}{\sqrt{C}}, \quad (\text{C.18})$$

where $k(N), d(N)$ are scaling factors which depend on the number of qubits N . We calculate $k(N)$ and $d(N)$ numerically for $N = 1 - 100$ using the perturbation theory and find that they both decrease with N (see Fig. C.2). The upper bounded and generic fidelities and corresponding success probabilities are shown in Fig. C.2 for different number of qubits, N . As N increases we obtain higher generic fidelity, whereas the success probability is almost independent of N .

C.1.3 CZ-gate

In the special case of only two qubits the Toffoli gate is referred to as a control-phase (CZ) gate. As shown in the article, we can, in this case, completely remove the

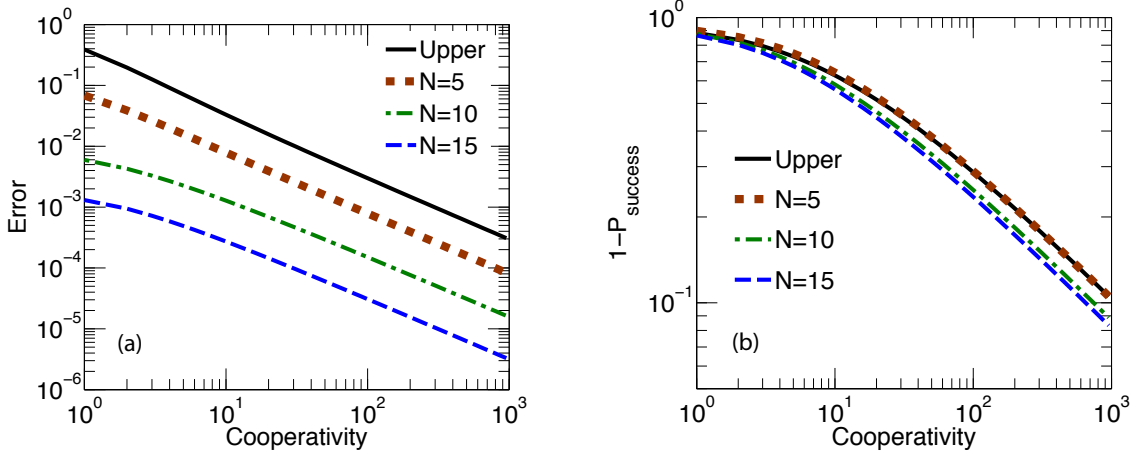


Figure C.2: (a) Gate error of the Toffoli for different initial states as a function of cooperativity. We have plotted the generic error for $N = 5, 10$, and 15 and the upper bound of the error. Note that the generic error decreases as N increases. We have fixed Δ such that $\Gamma_0 = \Gamma_1$ and have assumed that $\alpha = \beta = 1$. (b) The failure probabilities $1 - P_{\text{success,up}}$ and $1 - P_{\text{success,gen}}$ as a function of cooperativity. $1 - P_{\text{success,gen}}$ is plotted for $N = 5, 10, 15$. We have used the same assumptions as in (a). In general, the failure probability only have a weak dependence on N . Note that the line for $1 - P_{\text{success, gen}}, N = 5$ coincides with $1 - P_{\text{success,up}}$.

errors from the gate by choosing the detunings Δ_E and Δ_e such that $\Gamma_0 = \Gamma_1 = \Gamma_2$ and combining it with single qubit rotations we can ensure the right phase evolution. In the general case where $\alpha, \beta \neq 1$, the detunings Δ_e and Δ_E are

$$\Delta_E = \frac{\gamma}{2} \sqrt{\beta} \sqrt{4\alpha C + \beta} \quad (\text{C.19})$$

$$\Delta_e = \frac{\alpha C \gamma^2}{2\Delta_E}. \quad (\text{C.20})$$

The success probability of the gate is then

$$P_{\text{success}} \simeq 1 - \pi \frac{8\beta^2 + 6\beta\alpha + \alpha^2}{8\beta^{3/2}\sqrt{\alpha}} \frac{1}{\sqrt{C}}, \quad (\text{C.21})$$

and we find that the gate time is $t_{\text{CZ}} \simeq \frac{\gamma\pi\sqrt{\alpha}(\alpha+2\beta)(\alpha+4\beta)}{2\beta^{3/2}\Omega^2} \sqrt{C}$ in the limit $C \gg 1$.

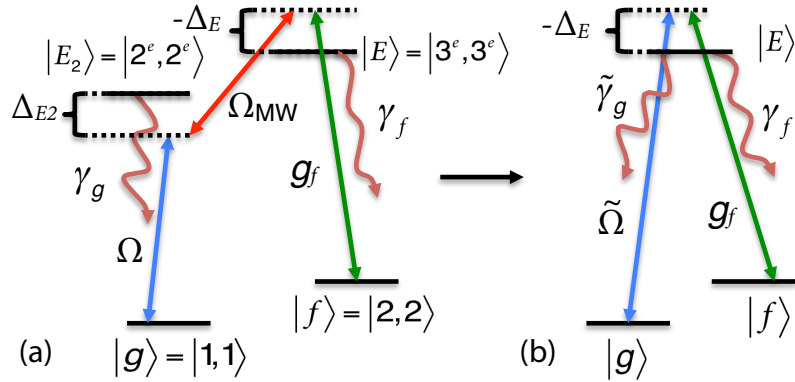


Figure C.3: (a) Level structure of the auxiliary atom and the transitions driven by a weak laser (Ω), a microwave field (Ω_{MW}) and the cavity (g_f). We assume that $|E\rangle \leftrightarrow |f\rangle$ is a closed transition and for simplicity we also assume that $|E_2\rangle \leftrightarrow |g\rangle$ is a closed transition but this is not a necessity. The figure also indicates how the levels could be realized in ^{87}Rb . Here $|r^{(e)}, r^{(e)}\rangle$ with $r = 1, 2, 3$ refers to state $|_{\text{F}}^{(e)} = r, {}_{\text{mF}}^{(e)} = r\rangle$ in ${}^2S_{1/2}$ (${}^2P_{3/2}$). (b) Effective three level atom realized by mapping the two-photon drive to an effective decay rate $\tilde{\gamma}_g$ and an effective drive $\tilde{\Omega}$

C.1.4 Two-photon driving

We now describe the details of the implementation where the auxiliary atoms is driven by a two-photon process as shown in Fig. C.3 (reproduced from Fig. 4(a) in the article) in order to suppress the dominant undetectable error caused by spontaneous decay of the auxilliary atom into the state $|g\rangle$ (\hat{L}_g).

The Hamiltonian in a proper rotating frame is

$$\hat{H} = \hat{H}_e + \hat{V} + \hat{V}^\dagger, \quad (\text{C.22})$$

$$\begin{aligned} \hat{H}_e &= \Delta_E |E\rangle\langle E| + \Delta_{E2} |E_2\rangle\langle E_2| + g_f (\hat{a}|E\rangle\langle f| + H.c.) \\ &\quad + \frac{\Omega_{\text{MW}}}{2} (|E\rangle\langle E_2| + H.c.) \\ &\quad + \sum_k \Delta_e |e\rangle_k\langle e| + g(\hat{a}|e\rangle_k\langle 1| + H.c.), \end{aligned} \quad (\text{C.23})$$

$$\hat{V} = \frac{\Omega}{2} |E_2\rangle\langle g|, \quad (\text{C.24})$$

where we have now defined $\Delta_E = \omega_E - \omega_g - \omega_{laser} - \omega_{\text{MW}}$, $\Delta_{E2} = \omega_{E2} - \omega_g - \omega_{laser}$ and $\Delta_e = \omega_e - \omega_g - \omega_{laser} - \omega_{\text{MW}} + \omega_f - \omega_1$. Here ω_{laser} is the frequency of the laser drive (Ω), ω_{MW} is the frequency of the microwave field (Ω_{MW}) and otherwise ω_x is the frequency associated with level x . We assume that the frequency of the cavity is $\omega_c = \omega_{laser} + \omega_{\text{MW}} + \omega_g - \omega_f$ such that the three photon Raman transition from $|g\rangle \rightarrow |f\rangle$ is resonant. We have assumed that Δ_{E2} is large and positive such that the rotating wave approximation is valid for the microwave field. The Lindblad operators describing the system are the same as described below Eq. (C.1) except that $\hat{L}_g \rightarrow \sqrt{\gamma_g}|g\rangle\langle E_2|$. Assuming a weak drive Ω , we can follow the same recipe as before to find the following effective operators describing the dynamics of the system.

$$\hat{H}_{\text{eff}}^{(2)} = \sum_{n=0}^N \Delta_n^{(2)} |g\rangle\langle g| \otimes \hat{P}_n \quad (\text{C.25})$$

$$\Delta_n^{(2)} = \frac{-\Omega^2}{4\gamma} \text{Re} \left[\frac{\tilde{\Delta}_e(i\tilde{\Delta}_E/2 + C_f) + n\tilde{\Delta}_E C}{\tilde{\Delta}_{E2}\tilde{\Delta}_e(i\tilde{\Delta}_E/2 + C_f) + n\tilde{\Delta}_E\tilde{\Delta}_{E2}C - i\tilde{\Delta}_e\tilde{\Omega}_{\text{MW}}^2/8 - n\tilde{\Omega}_{\text{MW}}^2C/4} \right]$$

$$\hat{L}_0^{\text{eff}(2)} = \sum_{n=0}^N r_{0,n}^{\text{eff}(2)} |f\rangle\langle g| \otimes \hat{P}_n \quad (\text{C.26})$$

$$r_{0,n}^{\text{eff}(2)} = \frac{-1}{4\sqrt{\gamma}} \frac{\sqrt{C_f}\tilde{\Delta}_e\Omega\tilde{\Omega}_{\text{MW}}}{\tilde{\Delta}_{E2}\tilde{\Delta}_e(i\tilde{\Delta}_E/2 + C_f) + n\tilde{\Delta}_{E2}\tilde{\Delta}_E C - i\tilde{\Delta}_e\tilde{\Omega}_{\text{MW}}^2/8 - n\tilde{\Omega}_{\text{MW}}^2C/4}$$

$$\hat{L}_g^{\text{eff}(2)} = \sum_{n=0}^N r_{g,n}^{\text{eff}(2)} |g\rangle\langle g| \otimes \hat{P}_n \quad (\text{C.27})$$

$$r_{g,n}^{\text{eff}(2)} = \frac{\Omega}{2} \frac{\tilde{\Delta}_e(i\tilde{\Delta}_E/2 + C_f) + n\tilde{\Delta}_E C}{\tilde{\Delta}_{E2}\tilde{\Delta}_e(i\tilde{\Delta}_E/2 + C_f) + n\tilde{\Delta}_{E2}\tilde{\Delta}_E C - i\tilde{\Delta}_e\tilde{\Omega}_{\text{MW}}^2/8 - n\tilde{\Omega}_{\text{MW}}^2C/4} \frac{\sqrt{\gamma_g}}{\gamma}$$

$$\hat{L}_f^{\text{eff}(2)} = \sum_{n=0}^N r_{f,n}^{\text{eff}(2)} |f\rangle\langle g| \otimes \hat{P}_n \quad (\text{C.28})$$

$$r_{f,n}^{\text{eff}(2)} = -\frac{\Omega}{4} \frac{(i\tilde{\Delta}_e/2 + nC)\tilde{\Omega}_{\text{MW}}}{\tilde{\Delta}_{E2}\tilde{\Delta}_e(i\tilde{\Delta}_E/2 + C_f) + n\tilde{\Delta}_{E2}\tilde{\Delta}_E C - i\tilde{\Delta}_e\tilde{\Omega}_{\text{MW}}^2/8 - n\tilde{\Omega}_{\text{MW}}^2C/4} \frac{\sqrt{\gamma_f}}{\gamma}$$

$$\hat{L}_k^{\text{eff}(2)} = \sum_{n=0}^{N-1} r_n^{\text{eff}(2)} |f\rangle\langle g| \otimes |\tilde{o}\rangle_k\langle 1| \otimes \hat{P}_n, \quad (\text{C.29})$$

$$r_n^{\text{eff}(2)} = \frac{1}{4\sqrt{\gamma}} \frac{\sqrt{C_f}\sqrt{C}\tilde{\Omega}_{\text{MW}}\Omega}{\tilde{\Delta}_{E2}\tilde{\Delta}_e(i\tilde{\Delta}_E/2 + C_f) + n\tilde{\Delta}_{E2}\tilde{\Delta}_EC - i\tilde{\Delta}_e\tilde{\Omega}_{\text{MW}}^2/8 - n\tilde{\Omega}_{\text{MW}}^2C/4}$$

where we have defined the complex detuning $\tilde{\Delta}_{E2}\gamma = \Delta_{E2} - i\gamma_g/2$ and the parameters $r_{0,n}^{\text{eff}(2)}$, $r_{g,n}^{\text{eff}(2)}$, $r_{f,n}^{\text{eff}(2)}$ and $r_n^{\text{eff}(2)}$ to characterize the decay described by the Lindblad operators.

We are interested in the limit of large detuning Δ_{E2} and large cooperativity C . In this limit, we find that the dynamics of the system can be mapped to a simple three level atom with effective driving $\tilde{\Omega} \sim \Omega\Omega_{\text{MW}}/(2\Delta_{E2})$ and an effective decay $\tilde{\gamma}_g \sim \gamma_g\Omega_{\text{MW}}^2/\Delta_{E2}^2$ as shown in Fig. C.3. In principle, the effective operator $\hat{L}_0^{\text{eff}(2)}$ leads to an effective decay rate of $\tilde{\gamma} = \gamma_g\Omega^2/\Delta_{E2}^2$ to lowest order in C but we find that this first order term do not destroy the coherence between the qubit states since it is independent of n . There is, therefore, no effect of these scattering events and the performance of the gate behaves as if there is an effective decay rate of $\tilde{\gamma}_g \sim \gamma_g\Omega_{\text{MW}}^2/\Delta_{E2}^2$. Note that we also have an AC stark shift imposed on the level $|g\rangle$ by the laser characterized by Ω . This will give an overall phase to the system, $\sim \Omega^2/(4\Delta_{E2})t$, which we can neglect since it does not influence the gates. Since we can do the mapping to the simple three level atom, we find similar results for the performance of the gates for the two-photon scheme as for the simple three level scheme only with effective decay $\tilde{\gamma}_g$ and drive $\tilde{\Omega}$ given by the two-photon process. Note, however, that we now assume $\gamma_g > 0$, which introduces an undetectable error as previously mentioned. We find that this introduces an error in the fidelity of both

gates of roughly

$$\sim \frac{(\alpha^2 - 4\alpha\beta - 6\beta^2)\pi^2}{128\beta^2} \frac{\gamma_g^4}{\gamma^4 \Delta_{E2}^4} + \frac{(\alpha^2 + 4\alpha\beta + 6\beta^2)\pi}{16\sqrt{\alpha\beta}(\alpha + 2\beta)(\alpha + 5\beta)} \frac{\gamma_g \Omega_{MW}^2}{\gamma \Delta_{E2}^2} \frac{1}{\sqrt{C}} \quad (\text{C.30})$$

Nonetheless, this error can be suppressed arbitrarily much by increasing Δ_{E2} , which enable us to have a heralded CZ-gate with arbitrarily small error in a realistic atomic setup using the two-photon drive.

C.2 Gate time

Here we address the question of how strongly we can drive the system and still maintain the validity of perturbation theory. We need to address this question since the gate time depends inversely on the driving strength as shown in the article and hence this limits the achievable gate time. A necessary criterion for our perturbation theory to be valid is that the energy shifts Δ_n (see Eq. (C.8) and Eq. (C.25)) are small compared to the driving, i.e. $\sim \Delta_n^2/\Omega^2 \ll 1$. From Eq. (C.8) we find that $\Delta_n^2/\Omega^2 \sim \Omega^2/(16\Delta_E^2)$ to leading order in the cooperativity C and this criterion is therefore met for $\Omega \ll 4\Delta_E$. Similarly, for the two-photon process, we find from Eq. (C.25) that $(\Delta_n^{(2)})^2/\Omega^2 \sim \Omega^2/(16\Delta_{E2}^2)$, to leading order in C . Here we thus need $\Omega \ll 4\Delta_{E2}$.

Another criterion needs to be met in order for our perturbative theory to be valid. If none of the qubits couple, we are effectively driving the auxiliary atom/cavity system into a dark state of the form $\cos(\theta)|0, g\rangle - \sin(\theta)|1, f\rangle$, where the mixing angle is $\theta \sim \Omega/g$. Here the number refers to the number of cavity photons. To adiabatically eliminate the state $|f, 1\rangle$ from the Hamiltonian as we have done in the

effective Hamiltonian requires that $\Omega/g \ll 1$. Mapping this criterion to the effective three level scheme realized in the two-photon scheme gives $\Omega\Omega_{\text{MW}}/(2\Delta_{E2}g) \ll 1$.

Finally, we need to consider the scattering of photons from the level $|E2\rangle$ in the two-photon scheme. If the number of scattering events, n_{scat} is large compared to $\Omega^2/(16\Delta_{E2}^2)$, the perturbation theory is not valid even though the other criterions are met. We find that $n_{scat} \sim \frac{12\sqrt{C}\gamma^2}{\Omega_{\text{MW}}^2}$ for the CZ-gate and we thus need to have $\frac{3\sqrt{C}\gamma^2\Omega^2}{\Delta_{E2}^2\Omega_{\text{MW}}^2} \ll 1$

The different criterions for the validity of the perturbation theory are summarized in Tab. C.2.

Simple scheme	Two-photon scheme
$\Omega/(4\Delta_E) \ll 1$	$\Omega/(4\Delta_{E2}) \ll 1$
$\Omega/g \ll 1$	$\Omega\Omega_{\text{MW}}/(\Delta_{E2}g) \ll 1$
-	$3\sqrt{C}\gamma^2\Omega^2/(\Delta_{E2}^2\Omega_{\text{MW}}^2) \ll 1$

Table C.2: The criterions for our perturbation theory to be valid.

For all the gate schemes, we have assumed that $\Delta_E \propto \sqrt{C}\gamma$. The first criterion for the simple scheme (see Tab. C.2) can thus be met with a driving of $\Omega = a\gamma\sqrt{C}$ where $a/4 \ll 1$. This driving results in a gate time that decreases as $1/\sqrt{C}$. The value of a will determine the size of the non-adiabatic error. The second criterion is also fulfilled for this driving as long as $\sqrt{\gamma/\kappa} \ll 1$. In realistic systems such as the nanocavity system described in Ref. [218, 220], the ratio κ/γ can be on the order of 100-1000. For the two-photon scheme, we find from Tab. C.2 that we can choose $\Omega = a_2\Delta_{E2}$, $\Omega_{\text{MW}} = b\gamma C^{1/4}$ where the constants a_2, b will determine the size of

the non-adiabatic errors as before. Similar to the situation in the simple scheme we assume that $\sqrt{\gamma/\kappa} \ll 1$.

C.3 Numerical simulation

In order to confirm our results, we numerically integrated the full Master equation, defined by the Hamiltonian \hat{H} and the Lindblad operators, $\hat{L}_j \in \{\hat{L}_0, \hat{L}_g, \hat{L}_f, \hat{L}_1, \hat{L}_2\}$,

$$\frac{d}{dt}\rho(t) = -\frac{i}{\hbar}[\hat{H}, \rho(t)] + \sum_j \frac{1}{2} \left[2\hat{L}_j\rho(t)\hat{L}_j^\dagger - \rho(t)\hat{L}_j^\dagger\hat{L}_j - \hat{L}_j^\dagger\hat{L}_j\rho(t) \right] \quad (\text{C.31})$$

We used the QuTiP 2 package [113], for Python, to set up the problem and used its 12th-order numerical integration algorithm to find the solution $\rho(t)$ as a time series. Then, we used the routines of the same package to analyze the results.

For each time series $\rho(t)$, we determined the gate time t_{gate} , the success probability P_{success} , and the fidelity F . We picked $|\psi_0\rangle_{12} = \frac{1}{\sqrt{2}}(|0\rangle + |1\rangle)_1 \otimes \frac{1}{\sqrt{2}}(|0\rangle + |1\rangle)_2$ as the initial state of the two qubits, $|g\rangle$ for the control atom, and zero photons in the cavity. Starting from here, we let the system evolve under the Master equation Eq. (C.31), and determined $P_g(t)$, the conditional state $\rho_g(t)$ and $F(t)$ as a function of time:

$$P_g(t) = \text{Tr} \left[\rho(t) |g\rangle\langle g| \right], \quad (\text{C.32})$$

$$\rho_g(t) = \frac{|g\rangle\langle g|\rho(t)|g\rangle\langle g|}{P_g(t)}, \quad (\text{C.33})$$

$$F(t) = \max_{\phi_1, \phi_2} \left\langle \psi_t^{\phi_1, \phi_2} \middle| \text{Tr}_{c, c}(\rho_g(t)) \middle| \psi_t^{\phi_1, \phi_2} \right\rangle \quad (\text{C.34})$$

where $\text{Tr}_{c, c}$ is the partial trace operation over the control atom and the cavity, and $|\psi_t^{\phi_1, \phi_2}\rangle$ is the target state transformed with two single qubit z -rotations:

$$|\psi_t^{\phi_1, \phi_2}\rangle = \hat{U}_1(\phi_1)\hat{U}_2(\phi_2)\frac{1}{2}(|00\rangle + |01\rangle + |10\rangle - |11\rangle), \quad (\text{C.35})$$

where $\hat{U}_k(\phi_k) = \exp [i|1\rangle_k\langle 1|_k\phi_k]$ is the z -rotation of qubit k ($= 1, 2$) by the angle ϕ_k . From these time series, we determined the gate time t_{gate} by finding the timepoint where $F(t)$ is maximal,

$$t_{\text{gate}} = \underset{t}{\operatorname{argmax}} F(t) \quad (\text{C.36})$$

The fidelity and the success probability of the gate is then defined as $F = F(t_{\text{gate}})$, $P_{\text{success}} = P_g(t_{\text{gate}})$.

Plots of Fig. C.4 show the gate time (t_{gate}) and the success probability (P_{success}) as a function of a , for $\gamma_g = 0$, $\gamma = 0.01\kappa$, $\Omega = a\gamma\sqrt{C}$ with $C \in \{10, 30, 100, 300, 1000\}$. The detunings, Δ_E and Δ_e were chosen to be close to their optimal value, determined from the adiabatic theory, and numerically optimized to result in identical effective $|g\rangle \rightarrow |f\rangle$ transition rates $\Gamma_0 = \Gamma_1 = \Gamma_2$ for the qubit sectors $|00\rangle, |01\rangle, |11\rangle$. The rates Γ_j were found by numerically diagonalizing the master equation for the qubit sectors separately, and finding the eigenvalue with the smallest (but non-zero) absolute real part. This numerical optimization yielded the maximal fidelity. The symbols correspond to the numerical result, whereas the solid lines show the theoretical values. The agreement of the results confirms the validity of the adiabatic theory for a driving $\Omega = a\gamma\sqrt{C}$ for $C \lesssim 1000$ and $a \lesssim 0.25$. Note, however, that Fig. C.4 shows how the success probability deviates from the adiabatic result for $a \gtrsim 0.25$. A weak increase of this deviation with the cooperativity is seen but from simulations at high C , we believe that this can be removed by gradually ramping Ω up and down to maintain adiabaticity at the beginning and end of the driving pulse. This was not included in the simulations behind Fig. C.4 for simplicity.

Fig. C.5 shows the conditional *infidelity* of the gate as a function of a for the same

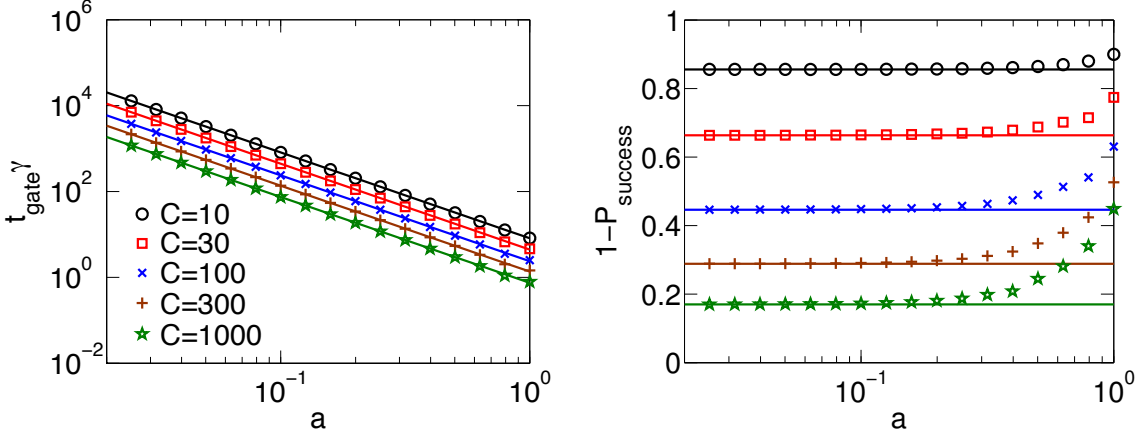


Figure C.4: Gate time (left) and failure probability (right) as a function of driving strength (a) for $\gamma/\kappa = 0.01$, $\gamma_g = 0$, and $C \in \{10, 30, 100, 300, 1000\}$. The driving strength was assumed to be $\Omega = a\gamma\sqrt{C}$.

parameters. The simulation confirms that using $a = 0.25$ is enough to push the (conditional) infidelity of the gate below $4 \cdot 10^{-5}$. The fidelity is limited by non-adiabatic effects, which can be suppressed by decreasing Ω as shown in the figure. Adiabatically ramping up and down at the beginning and end of the gate will also improve the adiabaticity but, for simplicity, we have not included this in the simulations described here. Note, however that for high C ($C > 1000$), we find that this gradual ramping of Ω significantly decreases the non-adiabatic error.

We repeated the above analysis for the two-photon-driving Hamiltonian in Eq. (C.22). We chose $\gamma = \gamma_g = \gamma_f = 0.01 \kappa$, $\Omega = \frac{\Delta_{E2}}{8C^{1/4}}$, and $\Omega_{\text{MW}} = 4\gamma C^{1/4}$, and chose Δ_E and Δ_e detunings again close to their adiabatic optimum, but numerically optimized them with the same procedure as previously. Plots of Fig.C.6 show the gate time and the success probability as a function of Δ_{E2} for $C \in \{10, 20, 50, 100\}$. Symbols indicate the numerical results while solid lines show the theoretical values. Fig. 2b in the article shows the conditional *infidelity* of the two-photon-driven gate as a function of C

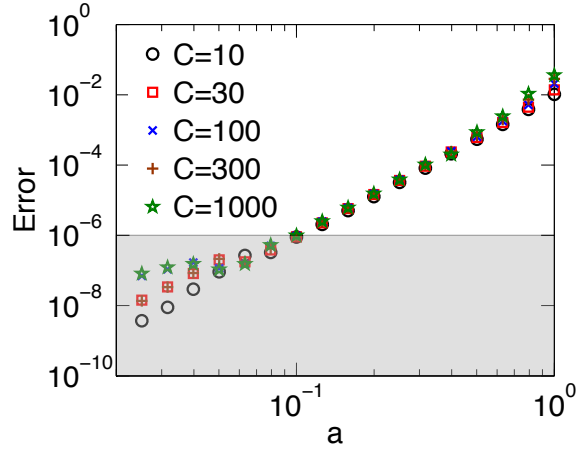


Figure C.5: Conditional infidelity of the gate as a function of the driving strength (a) for $\gamma/\kappa = 0.01$, $\gamma_g = 0$, and $C \in \{10, 30, 100, 300, 1000\}$. The shaded region (at $\sim 10^{-6}$) shows the limit of numerical accuracy. The driving strength was assumed to be $\Omega = a\gamma\sqrt{C}$.

for the same choice of parameters. With these results, we confirm that by increasing Δ_{E2} we can lower the infidelity error to an arbitrary small level. The gate time is a constant of the cooperativity since we have increased Ω_{MW} as $C^{1/4}$ in the simulations. We do see some deviation from the analytical results due to non-adiabatic effects, which could be suppressed by decreasing Ω at the expense of an increase in the gate time. Finally a gradual ramping of Ω could also decrease the non-adiabatic errors but for simplicity, we have not included this in the simulations.

C.4 Additional errors

There are some additional errors in a realistic atomic setup that we have not treated in detail so far. Here we estimate the dominant errors and determine under which conditions, they can be sufficiently suppressed such that they do not limit the performance of the gates. We assume a realistic atomic setup where ^{87}Rb atoms are

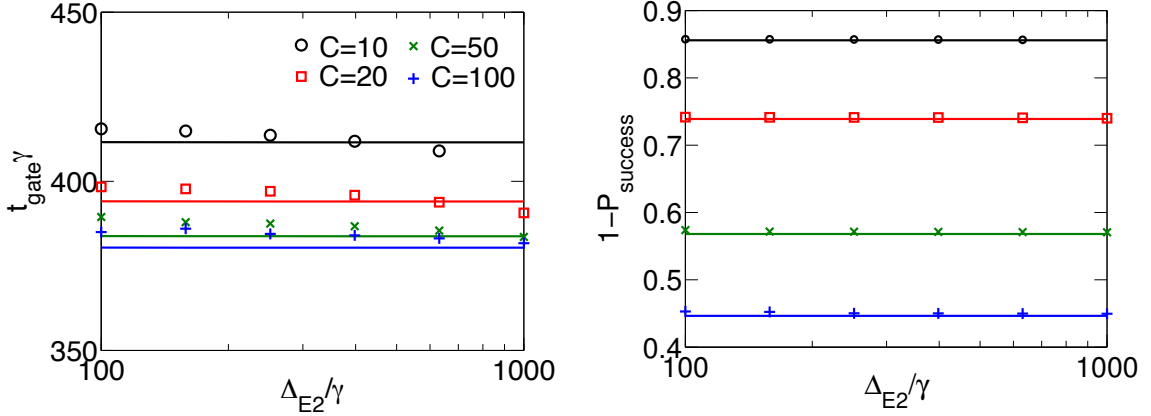


Figure C.6: Gate time (left) and failure probability (right) as a function of Δ_{E2} for $\gamma = \gamma_g = \gamma_f = 0.01\kappa$, $\Omega = \frac{\Delta_{E2}}{8C^{1/4}}$, $\Omega_{\text{MW}} = 4\gamma C^{1/4}$, $C = \{10, 20, 50, 100\}$.

used both for the auxiliary atom and the qubit atoms. In the ^{87}Rb atoms, we assume that $|g\rangle = |1, 1\rangle$, $|f\rangle = |2, 2\rangle$ and $|E_2\rangle = |2^e, 2^e\rangle$, $|E\rangle = |3^e, 3^e\rangle$ where $|r^{(e)}, r^{(e)}\rangle$ with $r = 1, 2, 3$ refers to state $|_{\text{F}}^{(e)} = r, {}_{\text{mF}}^{(e)} = r\rangle$ in $5^2S_{1/2}$ ($5^2P_{3/2}$). In this case, we estimate that the dominant errors are:

- In our perturbative theory, we have assumed that the laser field (Ω) only couple $|g\rangle \rightarrow |E_2\rangle$ in the auxiliary atom. However, for a large detuning Δ_{E2} it may also couple $|f\rangle \rightarrow |E\rangle$, which could lead to an undetectable error where the auxiliary atom is pumped back to $|E_2\rangle$ from, which it decays to $|g\rangle$. This error is, however, suppressed by the large frequency separation, Δ_g of $|g\rangle$ and $|f\rangle$, which is $\Delta_g \sim 1000\gamma$ for ^{87}Rb . We estimate the error using effective operators to find the decay rate back to $|g\rangle$, assuming that the auxiliary atom starts in $|E_2\rangle$ and treating the drive Ω as a perturbation while neglecting the cavity coupling. This is valid as long as $\Delta_g \gg \Delta_E$, which is fulfilled for $C \lesssim 10000$ since $\Delta_E \sim \sqrt{C}$. The error increases with Δ_{E2} but even for $\Delta_{E2} \approx 400\gamma$ we find that for $\Omega_{\text{MW}} = 4\gamma C^{1/4}$, $\Omega = \Delta_{E2}/8$ the error is $\lesssim 10^{-4}$.

- The microwave might also couple the ground states $|0\rangle - |1\rangle$ of the qubit atoms and the ground states $|g\rangle - |f\rangle$ of the auxiliary atom. The coupling of $|0\rangle - |1\rangle$ means that the qubit atoms also couple to the cavity even though they are in state $|0\rangle$. We estimate the error from this to be on the order of $\Omega_{\text{MW}}^2 / (\Delta_g - (\Delta_{E2} - \Delta_E + \Delta_{2 \rightarrow 3}))^2$ where $\Delta_{2 \rightarrow 3}$ is the splitting between $|E_2\rangle$ and $|E\rangle$. For ^{87}Rb , $\Delta_{2 \rightarrow 3} \approx 44\gamma$. Below we argue that we need $\Delta_E < 0$. Since $\Delta_E \approx -\sqrt{C}\gamma$ this error will increase slowly with cooperativity but it is suppressed by Δ_g . For $\Omega_{\text{MW}} = 4\gamma C^{1/4}$, we find that the error is $\lesssim 10^{-4}$ for $C \lesssim 1000$ even for $\Delta_{E2} \approx 400\gamma$. The errors from the coupling of the states $|g\rangle - |f\rangle$ in the auxiliary atom will likewise be suppressed by the large energy splitting Δ_g . These errors can also be further suppressed by decreasing Ω_{MW} at the cost of a larger gate time.

The above errors can be highly suppressed using e.g. ^{88}Sr , $^{138}\text{Ba}^+$ or $^{40}\text{Ca}^+$ instead of ^{87}Rb . For these atoms, the ground states can be encoded in the S_0 and P_0 manifolds for ^{88}Sr and the $S_{1/2}$ and $D_{3/2}$ manifolds for $^{138}\text{Ba}^+$ and $^{40}\text{Ca}^+$, which have separations at optical frequencies between the stable states.

A final error that we will consider is that the transition $|E\rangle \leftrightarrow |f\rangle$ will not be completely closed if the cavity is linearly polarized. This will, e.g. be the case for the system in Ref. [218]. Such a cavity also couples $|f\rangle$ to the states $|1^e, 1^e\rangle$, $|2^e, 1^e\rangle$ and $|3^e, 1^e\rangle$. From $|1^e, 1^e\rangle$ and $|2^e, 1^e\rangle$ there might be an undetectable decay back to $|g\rangle$, which will introduce an error $\propto 1/\sqrt{C}$ in the gates. The probability of an undetectable decay from these states should be compared to the probability of the detectable decays where the cavity photon is scattered off the qubit atoms instead.

For ^{87}Rb , we estimate this error by comparing the strengths of the effective couplings from $|f\rangle$ to $|1^e, 1^e\rangle$ and $|2^e, 1^e\rangle$ with a subsequent decay to $|g\rangle$ with the strength of the effective coupling from $|1\rangle$ to $|e\rangle$ in the qubit atoms with a subsequent decay back to $|1\rangle$. The latter process has a detuning of Δ_E while the first two are additional detuned by the energy gaps between $|3^e, 3^e\rangle$ and $|1^e, 1^e\rangle$ and $|3^e, 3^e\rangle$ and $|2^e, 1^e\rangle$ respectively, assuming that $\Delta_E < 0$. We find that since $|\Delta_E|$ grows as \sqrt{C} the error increases from $\sim 5 \cdot 10^{-5}$ at $C = 1$ to a maximum value of $\sim 2 \cdot 10^{-3}$ for $C \sim 3000$ for which Δ_E is comparable to the extra detunings of the $|1^e, 1^e\rangle$ and $|2^e, 1^e\rangle$ transitions compared to the $|e\rangle$ transition. For $C > 3000$ the error decreases as $1/\sqrt{C}$. Note that this error could be removed by making a 4 photon drive from $|g\rangle$ to $|E\rangle$ by letting $|g\rangle = |1, -1\rangle$. Another approach is to consider other atoms such as $^{40}\text{Ca}^+$, with more favorable levelstructures. The state $|g\rangle$ could be encoded in the $3^2D_{5/2}$ subspace while the state $|f\rangle$ could be encoded in the $4^2S_{1/2}$ subspace and similarly for the qubit states $|0\rangle$ and $|1\rangle$. In such a setup, we will have separations of optical frequencies between the qubit states and we can remove the decay from the excited state back to $|g\rangle$ by, e.g. driving from $3^2D_{5/2}$ to $4^2P_{1/2}$ through $3^2D_{3/2}$.

Appendix D

Appendices for Chapter 5

D.1 Error analysis of the single-photon scheme

The setup of the single-photon scheme is described in Sec. 5.3.1. The single photon detectors are assumed to have a dark count probability of P_{dark} and an efficiency of η_d while the transmission efficiency of the fibers is denoted η_f . As described in Sec. 5.2, the probability of an emitter to go from the excited state, $|e\rangle$ to the ground state $|1\rangle$ is P_{phot} while the excitation probability is ϵ^2 . The scheme is conditioned on a single click at the central station. Depending on which detector gave the click, a single qubit rotation can be employed such that ideally the state $|\Psi^+\rangle$ is created. Going through all the possibilities of obtaining a single click at the central station, we find that the density matrix following a single click, and possible subsequent single qubit rotations, is

$$\begin{aligned}\rho_{1click} = & F_1|\Psi^+\rangle\langle\Psi^+| + \alpha_1|\Phi^+\rangle\langle\Phi^+| + \alpha_1|\Phi^-\rangle\langle\Phi^-| \\ & + \beta_1|\Psi^-\rangle\langle\Psi^-| + \tilde{\alpha}_1|00\rangle\langle00| + \tilde{\beta}_1|11\rangle\langle11|,\end{aligned}\quad (\text{D.1})$$

with coefficients

$$\begin{aligned} F_1 = & \frac{1}{P_{\text{1click}}} \left[2\eta_d\eta_f P_p \epsilon^2 (1 - \epsilon^2) (1 - P_d) + 2\eta_f(1 - \eta_d) P_p \epsilon^2 (1 - \epsilon^2) P_d (1 - P_d) \right. \\ & + \frac{1}{2} \eta_d \eta_f P_p \epsilon^4 (1 - P_p) (1 - P_d) + 2(1 - \eta_f) P_p \epsilon^2 (1 - \epsilon^2) P_d (1 - P_d) \\ & \left. + (1 - \eta_d \eta_f) P_p \epsilon^4 (1 - P_p) P_d (1 - P_d) + (1 - \epsilon^2) \epsilon^2 (1 - P_p) P_d (1 - P_d) \right. \\ & \left. + \frac{1}{2} \epsilon^2 (1 - P_p)^2 P_d (1 - P_d) \right] \end{aligned} \quad (\text{D.2})$$

$$\alpha_1 = \frac{1}{P_{\text{1click}}} \left[\frac{1}{2} \epsilon^2 (1 - P_p)^2 P_d (1 - P_d) \right] \quad (\text{D.3})$$

$$\begin{aligned} \beta_1 = & \frac{1}{P_{\text{1click}}} \left[\frac{1}{2} \eta_d \eta_f P_p \epsilon^4 (1 - P_p) (1 - P_d) + 2(1 - \eta_f) P_p \epsilon^2 (1 - \epsilon^2) P_d (1 - P_d) \right. \\ & \left. + (1 - \eta_d \eta_f) P_p \epsilon^4 (1 - P_p) P_d (1 - P_d) + (1 - \epsilon^2) \epsilon^2 (1 - P_p) P_d (1 - P_d) \right. \\ & \left. + \frac{1}{2} \epsilon^2 (1 - P_p)^2 P_d (1 - P_d) + 2\eta_f(1 - \eta_d) P_p \epsilon^2 (1 - \epsilon^2) P_d (1 - P_d) \right] \end{aligned} \quad (\text{D.4})$$

$$\tilde{\alpha}_1 = \frac{1}{P_{\text{1click}}} \left[2(1 - \epsilon^2)^2 P_d (1 - P_d) + 2(1 - \epsilon^2) \epsilon^2 (1 - P_p) P_d (1 - P_d) \right] \quad (\text{D.5})$$

$$\begin{aligned} \tilde{\beta}_1 = & \frac{1}{P_{\text{1click}}} \left[\eta_d \eta_f P_p \epsilon^4 (1 - P_p) (1 - P_d) + 2(1 - \eta_d \eta_f) P_p \epsilon^4 (1 - P_p) P_d (1 - P_d) \right. \\ & \left. + 2(1 - \eta_d \eta_f)^2 P_p^2 \epsilon^4 P_d (1 - P_d) + 2(1 - \eta_d \eta_f) \eta_d \eta_f P_p^2 \epsilon^4 (1 - P_d)^2 \right], \end{aligned} \quad (\text{D.6})$$

where $P_d = P_{\text{dark}}$ and $P_p = P_{\text{phot}}$. Here we have assumed that with probability $\epsilon^2(1 - P_{\text{phot}})$, an emitter is excited but spontaneously decay to the ground states instead of emitting a cavity photon. Furthermore, we have assumed that the decay rates to the two ground states are equal such that the emitter ends up in $\frac{1}{2}(|0\rangle\langle 0| + |1\rangle\langle 1|)$. Note that the detectors are not assumed to be number resolving. P_{1click} is the total success probability given by

$$\begin{aligned} P_{\text{1click}} = & 2\eta_d\eta_f P_{\text{phot}} \epsilon^2 (1 - P_{\text{phot}} \epsilon^2) (1 - P_{\text{dark}}) + (2\eta_f\eta_d - \eta_f^2\eta_d^2) P_{\text{phot}}^2 \epsilon^4 \\ & + 2(1 - \epsilon^2 P_{\text{phot}})^2 P_{\text{dark}} (1 - P_{\text{dark}}) + 2(1 - \eta_d \eta_f)^2 P_{\text{phot}}^2 \epsilon^4 P_{\text{dark}} (1 - P_{\text{dark}}) \\ & + 4(1 - \eta_d \eta_f) P_{\text{phot}} \epsilon^2 (1 - \epsilon^2 P_{\text{phot}}) P_{\text{dark}} (1 - P_{\text{dark}}). \end{aligned} \quad (\text{D.7})$$

Assuming $P_{\text{dark}} \ll 1$, the dominant error is where both qubits are excited but only a single click is detected at the central station. This leaves the qubits in the state $|11\rangle\langle 11|$ and this error is efficiently detected by the purification scheme described in Ref. [18].

D.2 Error analysis of the two-photon scheme

For the two photon scheme described in Sec. 5.2, we condition on a click in two detectors. Once again we assume that appropriate single qubit rotations are employed depending on which detector combination clicked such that ideally the state $|\Phi^+\rangle$ is created. We find that the density matrix describing the qubit state after a successful event is

$$\rho_{2\text{click}} = F_2|\Phi^+\rangle\langle\Phi^+| + \alpha_2|\Psi^+\rangle\langle\Psi^+| + \alpha_2|\Psi^-\rangle\langle\Psi^-| + \beta_2|\Phi^-\rangle\langle\Phi^-|, \quad (\text{D.8})$$

where we have defined

$$\begin{aligned} F_2 &= \frac{(1 - P_{\text{dark}})^2}{P_{\text{2click}}} \left[\frac{1}{2} \eta_d^2 \eta_f^2 P_{\text{phot}}^2 + \eta_d (1 - \eta_d) \eta_f^2 P_{\text{dark}} P_{\text{phot}}^2 + \eta_f^2 (1 - \eta_d)^2 P_{\text{phot}}^2 P_{\text{dark}}^2 \right. \\ &\quad + P_{\text{dark}}^2 (1 - P_{\text{phot}})^2 + \eta_d (1 - \eta_f) \eta_f P_{\text{dark}} P_{\text{phot}}^2 + \eta_d \eta_f P_{\text{dark}} P_{\text{phot}} (1 - P_{\text{phot}}) \\ &\quad \left. + (1 - \eta_f)^2 P_{\text{phot}}^2 P_{\text{dark}}^2 + 2\eta_f (1 - \eta_d) (1 - \eta_f) P_{\text{phot}}^2 P_{\text{dark}}^2 \right. \\ &\quad \left. + 2(1 - \eta_d \eta_f) P_{\text{phot}} (1 - P_{\text{phot}}) P_{\text{dark}}^2 \right] \end{aligned} \quad (\text{D.9})$$

$$\begin{aligned} \alpha_2 &= \frac{(1 - P_{\text{dark}})^2}{P_{\text{2click}}} \left[\eta_d (1 - \eta_f) \eta_f P_{\text{dark}} P_{\text{phot}}^2 + P_{\text{dark}}^2 (1 - P_{\text{phot}})^2 + \right. \\ &\quad \eta_d \eta_f P_{\text{dark}} P_{\text{phot}} (1 - P_{\text{phot}}) + (1 - \eta_f)^2 P_{\text{phot}}^2 P_{\text{dark}}^2 \\ &\quad + 2\eta_f (1 - \eta_d) (1 - \eta_f) P_{\text{phot}}^2 P_{\text{dark}}^2 + 2(1 - \eta_d \eta_f) P_{\text{phot}} (1 - P_{\text{phot}}) P_{\text{dark}}^2 \\ &\quad \left. + \eta_d (1 - \eta_d) \eta_f^2 P_{\text{dark}} P_{\text{phot}}^2 + \eta_f^2 (1 - \eta_d)^2 P_{\text{phot}}^2 P_{\text{dark}}^2 \right] \end{aligned} \quad (\text{D.10})$$

$$\beta_2 = \alpha_2 + \frac{(1 - P_{\text{dark}})^2}{P_{\text{2click}}} \left[\eta_d (1 - \eta_d) \eta_f^2 P_{\text{dark}} P_{\text{phot}}^2 + \eta_f^2 (1 - \eta_d)^2 P_{\text{phot}}^2 P_{\text{dark}}^2 \right]. \quad (\text{D.11})$$

The success probability P_{2click} is

$$\begin{aligned} P_{\text{2click}} &= (1 - P_{\text{dark}})^2 \left[\frac{1}{2} \eta_d^2 \eta_f^2 P_{\text{phot}}^2 + 4\eta_d \eta_f (1 - \eta_d \eta_f) P_{\text{dark}} P_{\text{phot}}^2 + 4P_{\text{dark}}^2 (1 - P_{\text{dark}})^2 \right. \\ &\quad + 4\eta_d \eta_f P_{\text{dark}} P_{\text{phot}} (1 - P_{\text{phot}}) + 4(1 - \eta_d \eta_f)^2 P_{\text{phot}}^2 P_{\text{dark}}^2 \\ &\quad \left. + 8(1 - \eta_d \eta_f) P_{\text{phot}} (1 - P_{\text{phot}}) P_{\text{dark}}^2 \right] \end{aligned} \quad (\text{D.12})$$

As in the single-photon scheme, we have not assumed number resolving detectors and we have assumed that with probability $(1 - P_{\text{phot}})$, an emitter spontaneously decay to one of the ground states resulting in the state $\frac{1}{2}(|0\rangle\langle 0| + |1\rangle\langle 1|)$.

D.3 Deterministic CNOT gate

Here we describe the local entanglement generation scheme presented in Ref. [209], which can be used to make a deterministic CNOT gate as described in Section 5.3.3.

We assume that weak coherent light is continuously shined onto the cavity such that at most one photon is in the cavity at all times. A single-photon detector continuously monitors if any photons are reflected from the cavity and the coherent light is blocked if a click is recorded before n_{max} photons on average have been sent onto the cavity. If no click was recorded during this time, both atoms are interpreted as being in the g levels. The steps of the entangling scheme are the following.

1. Both atoms are initially prepared in the superposition $|g\rangle + |f\rangle$ by e.g. a $\pi/2$ -pulse.
2. Coherent light is sent onto the cavity. If a click is recorded before on average n_{max} photons have been sent onto the cavity, the levels of the atoms are flipped ($|g\rangle \leftrightarrow |f\rangle$). If no click is recorded, the atoms are interpreted as being in $|gg\rangle$ and the procedure is repeated from step 1.
3. Conditioned on the first click, another coherent light pulse is sent onto the cavity after the levels of the atoms have been flipped. If a click is recorded before $n = n_{max} - n_1$ photons on average have been sent onto the cavity, the entangling scheme is considered to be a success. Here n_1 is the average number of photons that had been sent onto the cavity before the first click. If no click is recorded, the atoms are interpreted as being in $|gg\rangle$ and the procedure is repeated from step 1.

As described above, the entangling scheme is repeated until it is successful leading to a deterministic creation of entanglement in the end. As described in Ref. [208] a series of non-destructive measurements of the atoms together with single qubit rotations

can be used to make a CNOT operation after the entanglement has been created. The non-destructive measurements can be performed using the same technique of monitoring reflected light as in the entangling scheme and we assume that we can effectively tune the couplings to the cavity such that possibly only a single atom couples.

D.4 Rate analysis

Here we analyse the rate of entanglement distribution for the different repeater architectures considered in the main text. The total rate of the repeater is set by the average time of entanglement creation, initial purification and entanglement swapping. Assuming that entanglement generation has a success probability, P_0 , we estimate the average time $\tau_{\text{pair},l;m}$ it takes to generate l entangled pairs in one elementary link using m qubits, which can be operated in parallel, as

$$\tau_{\text{pair},l;m} = \mathcal{Z}_{l;m}(P_0)(L_0/c + \tau_{\text{local}}). \quad (\text{D.13})$$

Here c is the speed of light in the fibers and τ_{local} is the time of local operations such as initialization of the qubits. The factor $\mathcal{Z}_{l;m}(P_0)$ can be thought of as the average number of coin tosses needed to get at least l tails if we have access to m coins, which we can flip simultaneously and the probability of tail is P_0 for each coin [19]. It is furthermore assumed that coins showing tail after a toss are kept and only the coins showing head are tossed again until l tails are obtained. In the repeater context, the coins are entanglement generation attempts and tail is successful entanglement generation. The time it takes per "toss" is $L_0/c + \tau_{\text{local}}$. To calculate the expressions

for $Z_{l;m}(P_0)$, we follow the lines of Ref. [19] where similar factors are derived. The expression for $\mathcal{Z}_{m;m}(p)$ is already derived in Ref. [19] and their result is stated below

$$\mathcal{Z}_{m;m} = \sum_{k=1}^m \binom{m}{k} \frac{(-1)^{k+1}}{1 - (1-p)^k}. \quad (\text{D.14})$$

For $\mathcal{Z}_{l;m}$ where $l \neq m$, we only need to find expressions for $\mathcal{Z}_{1;m}$ with $m = 1, 2, 3, 4$, $\mathcal{Z}_{2;m}$ with $m = 3, 4$ and $\mathcal{Z}_{3;4}$ since we have a maximum of 4 qubits pr. repeater station. For $\mathcal{Z}_{2;3}$, we have that

$$\begin{aligned} \mathcal{Z}_{2;3} = & \binom{3}{3} \sum_{k=1}^{\infty} k(q^3)^{k-1} p^3 + \binom{3}{2} \sum_{k=1}^{\infty} k(q^3)^{k-1} p^2 q \\ & + \binom{3}{1} \binom{2}{1} \sum_{k=1}^{\infty} \sum_{l=1}^{\infty} (k+l)[(q^3)^{k-1} pq^2][(q^2)^{l-1} pq] \\ & + \binom{3}{1} \binom{2}{2} \sum_{k=1}^{\infty} \sum_{l=1}^{\infty} (k+l)[(q^3)^{k-1} pq^2][(q^2)^{l-1} p^2], \end{aligned} \quad (\text{D.15})$$

where $q = 1 - p$. The first term in Eq. (D.15) describes the situations where three tails are obtained in a single toss after a given number of tosses, where all coins showed head. We will refer tosses where all coins show tail as failed tosses. The second term describes the situation where we get two tails in the same toss after a given number of failed tosses. The third and fourth terms are where we get a single tail after a given number of failed tosses. The coin showing tail is then kept and the two remaining coins are tossed until we obtain another tail (third term) or two tails simultaneously (fourth term). The geometric series in Eq. (D.15) can be solved to give

$$\mathcal{Z}_{2;3} = \frac{5 - (7 - 3p)}{(2 - p)p(3 + (p - 3)p)} \approx \frac{5}{6p}, \quad (\text{D.16})$$

where the approximate expression is for $p \ll 1$. Note that the factor of $\frac{5}{6}$ corresponds to a simple picture where it on average takes $\frac{1}{3} \frac{1}{p}$ attempts to get the first 'tail' using

3 coins and $\frac{1}{2} \frac{1}{p}$ attempts to get the second using the remaining 2 coins. In a similar manner, we find that

$$\mathcal{Z}_{1;2} = \frac{1}{2p - p^2} \approx \frac{1}{2p} \quad (\text{D.17})$$

$$\mathcal{Z}_{1;3} = \frac{1}{3p - 3p^2 + p^3} \approx \frac{1}{3p} \quad (\text{D.18})$$

$$\mathcal{Z}_{1;4} = \frac{1}{4p - 6p^2 + 4p^3 - p^4} \approx \frac{1}{4p} \quad (\text{D.19})$$

$$\mathcal{Z}_{2;4} = \frac{-7 + p(15 + p(4p - 13))}{(p - 2)p(3 + (p - 3)p)(2 + (p - 2)p)} \approx \frac{7}{12p} \quad (\text{D.20})$$

$$\mathcal{Z}_{3;4} = \frac{-13 + p(33 + p(22p - 6p^2 - 37))}{(p - 2)p(3 + (p - 3)p)(2 + (p - 2)p)} \approx \frac{13}{12p}. \quad (\text{D.21})$$

Here the approximate expressions are all for $p \ll 1$ and they correspond to the expressions one would get using simple pictures similar to the one described above in the discussion of $\mathcal{Z}_{2;3}$.

After creating a number of entangled pairs in an elementary link of the repeater, they may be combined to create a purified pair of higher fidelity. As previously mentioned, we assume an entanglement pumping scheme since this requires less qubit resources than a cascading scheme. Let $P_{\text{pur}}(F_0, F_0)$ denote the success probability of the purification operation, which depends on the fidelity of the two initial pairs (F_0) and the fidelity of the CNOT gate used in the purification operation. Note that P_{pur} also contains the success probability of the CNOT gate used in the purification for the heralded gate. We estimate the average time $\tau_{\text{pur},1}$, it takes to make one purified pair from two initial pairs of fidelity F_0 , using m qubits in parallel in the entanglement generation step, as

$$\tau_{\text{pur},1} = \frac{\tau_{\text{pair},2;m} + \tau_{\text{pur}}}{P_{\text{pur}}(F_0, F_0)}, \quad (\text{D.22})$$

where $\tau_{\text{pur}} \sim L_0/c + \tau_c$ is the time of the purification operation including the classical

communication time required to compare results. Here τ_c is the time of the CNOT operation and L_0/c is the communication time between the two repeater stations sharing the entangled pairs. To further pump the entanglement of the purified pair, a new entangled pair is subsequently created using $m - 1$ qubits operated in parallel. The average time it takes to make j rounds of purification is thus estimated as

$$\tau_{\text{pur},j} = \frac{\tau_{\text{pur},j-1} + \tau_{\text{pur}} + \tau_{\text{pair},1:m-1}}{P_{\text{pur}}(F_{j-1}, F_0)}, \quad (\text{D.23})$$

with $\tau_{\text{pur},0} = \tau_{\text{pair},2;m} - \tau_{\text{pair},1:m-1}$. Here F_{j-1} is the fidelity of the purified pair after $j-1$ purifications. The total rate of a repeater, consisting both of purification and entanglement swapping, depends on the specific repeater architecture. We will first consider the case of both a parallel and sequential repeater operated with deterministic gates and afterwards the same situations with probabilistic gates.

D.4.1 Deterministic gates

For a parallel repeater with n swap levels and deterministic gates, we first estimate the average time it takes to generate 2^n purified pairs, i.e. a purified pair in each elementary link. We assume that each pair is purified j times such that the time to generate one purified pair is

$$\begin{aligned} \tau_{\text{pur},j} &= \frac{\mathcal{Z}_{2;m}(P_0)(L_0/c + \tau_{\text{local}})}{P_{\text{pur}}(F_0, F_0) \cdots P_{\text{pur}}(F_{j-1}, F_0)} + \sum_{i=0}^{j-1} \frac{\tau_{\text{pur}}}{P_{\text{pur}}(F_i, F_0) \cdots P_{\text{pur}}(F_{j-1}, F_0)} \\ &\quad + \sum_{i=1}^{j-1} \frac{\mathcal{Z}_{1;m-1}(P_0)(L_0/c + \tau_{\text{local}})}{P_{\text{pur}}(F_i, F_0) \cdots P_{\text{pur}}(F_{j-1}, F_0)}, \end{aligned} \quad (\text{D.24})$$

where we have solved the recurrence in Eq. (D.23). We now wish to estimate the total time, $\tau_{\text{link},2^n}$ it takes to make purification in every elementary link, i.e. the time

it takes to make 2^n pairs. A lower limit of $\tau_{\text{link},2^n}$ is simply $\tau_{\text{pur},j}$ but this is a very crude estimate if the purification have a limited success probability since the time is not determined by the average time but by the average time for the last link to succeed. We therefore make another estimate of the average time by treating $\tau_{\text{pur},j}$ as consisting of $2j$ independent binomial events with probabilities

$$P_1 = \frac{P_{\text{pur}}(F_0, F_0) \cdots P_{\text{pur}}(F_{j-1}, F_0)}{\mathcal{Z}_{2;m}(P_0)} \quad (\text{D.25})$$

$$P_2^{(i)} = P_{\text{pur}}(F_i, F_0) \cdots P_{\text{pur}}(F_{j-1}, F_0) \quad (\text{D.26})$$

$$P_3^{(i)} = \frac{P_{\text{pur}}(F_i, F_0) \cdots P_{\text{pur}}(F_{j-1}, F_0)}{\mathcal{Z}_{1;m-1}(P_0)}. \quad (\text{D.27})$$

We then estimate the average time, $\tau_{\text{link},2^n}$ it takes to make 2^n purified pairs as

$$\begin{aligned} \tau_{\text{link},2^n} &= \mathcal{Z}_{2^n;2^n}(P_1)(L_0/c + \tau_{\text{local}}) + \sum_{i=0}^{j-1} \mathcal{Z}_{2^n,2^n}(P_2^{(i)})\tau_{\text{pur}} \\ &\quad + \sum_{i=1}^{j-1} \mathcal{Z}_{2^n,2^n}(P_3^{(i)})(L_0/c + \tau_{\text{local}}). \end{aligned} \quad (\text{D.28})$$

Eq. (D.28) is a better estimate for the average time than $\tau_{\text{pur},j}$ in the limit of small success probabilities since it takes into account that we need success in all links. This is contained in the factors $\mathcal{Z}_{2^n;2^n}$. However, it overestimates the average distribution time when the purification has a large success probability. How much it overestimates depends on n and j . Comparing $\tau_{\text{pur},j}$ to Eq. (D.28) we find numerically that for $n \leq 5$ and $j \leq 2$ there is a factor $\lesssim 2$ between the two estimates, in the limit of large success probability for the purification operation. As discussed in Sec. 5.4 we never consider more than 5 swap levels in our optimization and since we have a limited number of qubits pr. repeater station, we will never have to consider more than 2 rounds of purification. We can therefore use the estimate for $\tau_{\text{link},2^n}$ given in Eq. (D.28).

To get the average time it takes to distribute one entangled pair over the total distance, L_{tot} , of the repeater, we need to add the time of the entanglement swapping, $\tau_{swap,nd}$ to $\tau_{link,2^n}$. We estimate $\tau_{swap,n}$ as

$$\tau_{swap,n} = (2^n - 1)L_0/c + n\tau_c, \quad (\text{D.29})$$

where the first term is the time of the classical communication and τ_c is the time of the CNOT operation involved in the swap procedure. The average distribution rate, of a parallel repeater with deterministic gates, is thus $r = 1/(\tau_{link,2^n} + \tau_{swap,n})$.

For a repeater using sequential entanglement creation with deterministic gates, we estimate the time it takes to generate purified pairs in all 2^n pairs as

$$\tau_{link,2^n}^{(s)} = (\tau_{link,2^{n-1}})|_{m \rightarrow 2m} + (\tau_{link,2^{n-1}})|_{m \rightarrow 2m-1}. \quad (\text{D.30})$$

Here we have indicated that the number of qubits, which can be operated in parallel is $2m$ for the first 2^{n-1} pairs and $2m - 1$ for the next 2^{n-1} pair compared to the parallel repeater, where only m qubits can be used in all 2^n pairs. Note, that we have assumed that first entanglement is established in half of the links and only when this is completed, entanglement is created in the remaining half of the links. This is clearly not the fastest way of operating the repeater but it gives an upper limit of the average distribution time and hence a lower limit on the rate. The entanglement swapping of the sequential repeater is exactly the same as for the parallel repeater and the average total rate, of the sequential repeater with deterministic gates, is thus $r = 1/(\tau_{link,2^n}^{(s)} + t_{swap,n})$.

D.4.2 Probabilistic gates

To estimate the total, average distribution time of a repeater using parallel entanglement creation with n swap levels and probabilistic gates, we will again treat $\tau_{\text{pur},j}$ as consisting of $2j$ independent binomial events, as we did for the deterministic gates. The time it takes to make a single swap can be estimated as

$$\begin{aligned}\tau_{\text{swap},1} &= \frac{\mathcal{Z}_{2;2}(P_1)(L_0/c + \tau_{\text{local}})}{P_{\text{swap}}} + \frac{L_0/c}{P_{\text{swap}}} + \frac{\tau_c}{P_{\text{swap}}} \\ &+ \sum_{i=0}^{j-1} \frac{\mathcal{Z}_{2;2}(P_2^{(i)})\tau_{\text{pur}}}{P_{\text{swap}}} + \sum_{i=1}^j \frac{\mathcal{Z}_{2;2}(P_3^{(i)})(L_0/c + \tau_{\text{local}})}{P_{\text{swap}}},\end{aligned}\quad (\text{D.31})$$

where P_{swap} is the probability of the swap operation, i.e. the probability of the CNOT gate. Eq. (D.31) can be iterated such that the average time it takes to make n swap levels is estimated as

$$\begin{aligned}\tau_{\text{swap},n} &= \frac{\tilde{\mathcal{Z}}_{n;1}(P_{\text{swap}}, P_1)(L_0/c + \tau_{\text{local}})}{P_{\text{swap}}} + \sum_{i=1}^n \frac{\tilde{\mathcal{Z}}_{n;i}(P_{\text{swap}}, P_{\text{swap}})(2^{i-1}L_0/c + \tau_c)}{P_{\text{swap}}} \\ &+ \sum_{i=0}^{j-1} \frac{\tilde{\mathcal{Z}}_{n;1}(P_{\text{swap}}, P_2^{(i)})\tau_{\text{pur}}}{P_{\text{swap}}} + \sum_{i=1}^{j-1} \frac{\tilde{\mathcal{Z}}_{n;1}(P_{\text{swap}}, P_3^{(i)})(L_0/c + \tau_{\text{local}})}{P_{\text{swap}}},\end{aligned}\quad (\text{D.32})$$

where

$$\tilde{\mathcal{Z}}_{n;i}(P_{\text{swap}}, P) = \mathcal{Z}_{2;2} \left(\frac{P_{\text{swap}}}{\tilde{\mathcal{Z}}_{n-1;i}(P_{\text{swap}}, P)} \right), \quad (\text{D.33})$$

$$\tilde{\mathcal{Z}}_{i;i}(P_{\text{swap}}, P) = \mathcal{Z}_{2;2}(P) \quad (\text{D.34})$$

$$\tilde{\mathcal{Z}}_{i;i}(P_{\text{swap}}, P_{\text{swap}}) = 1. \quad (\text{D.35})$$

Here P is either P_1 , $P_2^{(i)}$ or $P_3^{(i)}$. In the limit of $P_0, P_{\text{swap}} \ll 1$ and assuming no initial purification, Eq. (D.32) reduces to the well-known formula [192, 191]

$$\tau_{\text{swap},n} = \frac{(3/2)^n (L_0/c + \tau_{\text{local}})}{P_0 P_{\text{swap}}^n}, \quad (\text{D.36})$$

since $\mathcal{Z}_{2;2}(P \ll 1) \approx 3/(2P)$ and the time of local operations in the swaps can be neglected in this limit. However, for higher success probabilities, Eq. (D.32) more accurately estimates the average distribution time. The average rate of a parallel repeater with probabilistic gates and n swap levels is then $r = 1/\tau_{\text{swap},n}$. From a numerical study, we again find that for $P_{\text{swap}} \approx 1$ and $P_0 \ll 1$, Eq. (D.32) underestimates the average distribution rate with a factor that increases with the number of swap levels, n . However, for $n \leq 5$ and $j \leq 2$, we find that this factor is $\lesssim 2$.

The operation of a sequential repeater with probabilistic gates is not straightforward since it is unclear how the sequential generation of entanglement should take place after a failed swap operation. We therefore choose to assume that initially, entanglement is generated in all 2^n links sequentially. When this is completed the first round of entanglement swapping is performed. If a swap fails, entanglement is restored in a parallel manner in this section, i.e. the sequential operation is only employed in the initial generation of entanglement. Thus if i 'th swaps fail in the first swap level an extra waiting time of

$$\begin{aligned} & \mathcal{Z}_{i;i} \left(\frac{P_{\text{swap}}}{\mathcal{Z}_{2;2}(P_1)} \right) (L_0/c + \tau_{\text{local}}) + \mathcal{Z}_{i;i}(P_{\text{swap}})(L_0/c + \tau_c) \\ & + \sum_{k=0}^{j-1} \mathcal{Z}_{i;i} \left(\frac{P_{\text{swap}}}{\mathcal{Z}_{2;2}(P_2^{(k)})} \right) \tau_{\text{pur}} + \sum_{k=1}^{j-1} \mathcal{Z}_{i;i} \left(\frac{P_{\text{swap}}}{\mathcal{Z}_{2;2}(P_3^{(k)})} \right) (L_0/c + \tau_{\text{local}}) \end{aligned} \quad (\text{D.37})$$

is needed to restore entanglement in the $2i$ 'th links in a parallel manner and swap them successfully. Eq. (D.37) is very similar to Eq. (D.31), which estimates the time needed for a single swap at the first swap level. Nonetheless, the functions $\mathcal{Z}_{i;i}$, which appears in Eq. (D.37) takes into account that we need i successful swaps instead of only a single swap. Furthermore, we assume that the swap operations of a swap level is only initiated when all swap operations in the preceeding level have been successful.

The average time, it takes for all swap operations in the first level to succeed, is then estimated as

$$\begin{aligned} \tau_{\text{swap},1}^{(s)} = & \sum_{i=0}^{2^{n-1}} P_{\text{swap}}^{2^{n-1}-i} (1 - P_{\text{swap}})^i \left[\mathcal{Z}_{i;i} \left(\frac{P_{\text{swap}}}{\mathcal{Z}_{2;2}(P_1)} \right) (L_0/c + \tau_{\text{local}}) \right. \\ & + \mathcal{Z}_{i;i}(P_{\text{swap}})(L_0/c + \tau_c) + \sum_{k=0}^{j-1} \mathcal{Z}_{i;i} \left(\frac{P_{\text{swap}}}{\mathcal{Z}_{2;2}(P_2^{(k)})} \right) \tau_{\text{pur}} \\ & \left. + \sum_{k=1}^{j-1} \mathcal{Z}_{i;i} \left(\frac{P_{\text{swap}}}{\mathcal{Z}_{2;2}(P_3^{(k)})} \right) (L_0/c + \tau_{\text{local}}) + (L_0/c + \tau_c) \delta_{i,0} \right], \quad (\text{D.38}) \end{aligned}$$

where $\delta_{i,0}$ is the Kronecker delta symbol and $\mathcal{Z}_{0;0} = 0$. It is seen that in the limit $P_{\text{swap}} \rightarrow 1$, Eq. (D.38) correctly reduces to $\tau_{\text{swap},1}^{(s)} = L_0/c + \tau_c$, which simply is the time of the classical communication of the results of the bell measurements and the time of the local operations. Eq. (D.38) can be generalized such that the time it takes to perform the l 'th swap level is

$$\begin{aligned} \tau_{\text{swap},l}^{(s)} = & \sum_{i=0}^{2^{n-l}} P_{\text{swap}}^{2^{n-l}-i} (1 - P_{\text{swap}})^i \left[\mathcal{Z}_{i;i} \left(\frac{P_{\text{swap}}}{\tilde{\mathcal{Z}}_{l;1}(P_{\text{swap}}, P_1)} \right) (L_0/c + \tau_{\text{local}}) \right. \\ & + \sum_{k=1}^l \mathcal{Z}_{i;i} \left(\frac{P_{\text{swap}}}{\tilde{\mathcal{Z}}_{l;k}(P_{\text{swap}}, P_{\text{swap}})} \right) (2^{k-1}L_0/c + \tau_c) \\ & + \sum_{k=0}^{j-1} \mathcal{Z}_{i;i} \left(\frac{P_{\text{swap}}}{\tilde{\mathcal{Z}}_{l;1}(P_{\text{swap}}, P_2^{(k)})} \right) \tau_{\text{pur}} \\ & + \sum_{k=1}^{j-1} \mathcal{Z}_{i;i} \left(\frac{P_{\text{swap}}}{\tilde{\mathcal{Z}}_{l;1}(P_{\text{swap}}, P_3^{(k)})} \right) (L_0/c + \tau_{\text{local}}) \\ & \left. + (2^{l-1}L_0/c + \tau_c) \delta_{i,0} \right], \quad (\text{D.39}) \end{aligned}$$

which can be compared to Eq. (D.32) which estimates the time to make a successful swap at the n 'th level (let $n \rightarrow l$ for comparison). Once again the functions $\mathcal{Z}_{i;i}$ takes into account that we need i 'th successful swaps instead of just a single successful swap. The total rate of a sequential repeater with probabilistic gates and n swap

levels can then be estimated as $r = 1/(\tau_{\text{link},2^n}^{(s)} + \tau_{\text{swap},1}^{(s)} + \dots + \tau_{\text{swap},n}^{(s)})$.

Appendix E

Appendices for Chapter 6

E.1 Figure of merit: Allan-variance

Provided N qubits, we aim to devise an efficient interrogation scheme that provides input for the feedback mechanism, using Ramsey spectroscopy. After the k th Ramsey cycle, of length T , an estimate $\Phi_{\text{LO}}^{\text{est}}(t_k)$ is obtained for the accumulated phase of the LO, $\Phi_{\text{LO}}(t_k) = \int_{t_k-T}^{t_k} dt \delta\omega(t)$, ($t_k = kT$, $k = 1, 2, \dots$, and $\delta\omega(t) = \omega(t) - \omega_0$), which differs from the real value by $\Delta\Phi_{\text{LO}}(t_k) = \Phi_{\text{LO}}^{\text{est}}(t_k) - \Phi_{\text{LO}}^{\text{real}}(t_k)$. Using the obtained estimate, the feedback mechanism corrects the phase or frequency of the LO after every cycle, and thus creates a LO signal with better stability. The figure of merit for stability is the Allan-variance, $\sigma_y^2(\tau) = \frac{1}{\omega_0^2} \langle \delta\bar{\omega}^2(t_0) \rangle_{t_0}$ where $\delta\bar{\omega}(t_0)$ denotes the time-average of $\delta\omega(t_0 + t)$ over $t \in [0, \tau]$, where τ is the available averaging time, $\langle \rangle_{t_0}$ stands for time-average over t_0 , which is much longer than τ , ω_0 is the frequency of the chosen clock transition. Consequently, one readily shows that the Allan variance

can be written as,

$$\sigma_y^2(\tau) = \frac{1}{\omega_0^2 \tau^2} \sum_{i=1}^{\tau/T} \sum_{j=1}^{\tau/T} \left\langle \Delta\Phi_{\text{LO}}(t_0 + iT) \Delta\Phi_{\text{LO}}(t_0 + jT) \right\rangle_{t_0}. \quad (\text{E.1})$$

By assuming that $\Delta\Phi_{\text{LO}}$ is a stationary random process, we substitute the average over t_0 with the average over many realizations. With the notation $\Delta\Phi_{\text{LO}}(t_0 + jT) = \Delta\Phi_{\text{LO},j}$, we can write this average as

$$\langle \Delta\Phi_{\text{LO},i} \Delta\Phi_{\text{LO},j} \rangle \approx \langle \Delta\Phi_{\text{LO}}^2 \rangle \delta_{ij}, \quad (\text{E.2})$$

where we further used a white noise assumption, such that phase accumulations in consecutive Ramsey cycle are approximately uncorrelated. Also for realistic $1/f$ laser noise spectra, numerical studies show that this factorization assumption leads to only negligible corrections. Earlier results show that this is the case for initial LO frequency noise spectra, $S_\nu(f)$ that are less divergent than $1/f^2$ at low frequencies [7]. As a result, the Allan-variance simplifies to,

$$\sigma_y^2(\tau) = \frac{1}{\omega_0^2 \tau T} \langle \Delta\Phi_{\text{LO}}^2 \rangle, \quad (\text{E.3})$$

linking the achieving stability directly to the frequency measurement uncertainty during the interrogation. Eq. E.3 serves as our starting point in finding the optimal measurement protocol that minimizes $\sigma_y^2(\tau)$ for fixed N and τ . In the following, we investigate and compare different classical and quantum mechanical strategies for the interrogation of the (from cycle to cycle fluctuating) quantity Φ_{LO} , and we demonstrate that the proposed interrogation protocol using cascaded GHZ states is optimal up to a logarithmic correction.

E.2 Single-step Uncorrelated ensemble

First, we consider the case of naive interrogation using a Ramsey protocol with N uncorrelated atoms.

E.2.1 Sub-ensembles and projection noise

Single ensemble Ramsey spectroscopy is limited to estimating either the real or the imaginary part of $e^{i\Phi_{\text{LO}}}$. However, by dividing the available qubits into two sub-ensembles, X and Y , preparing their individual qubits in different states,

$$X : [|0\rangle + |1\rangle]/\sqrt{2}, \quad (\text{E.4})$$

$$Y : [|0\rangle + i|1\rangle]/\sqrt{2}, \quad (\text{E.5})$$

and performing the same Ramsey measurement on them, we can get estimates on both the real and imaginary parts of $e^{i\Phi_{\text{LO}}}$ and deduce the value of Φ_{LO} up to 2π shifts, instead of π . At the end of the free evolution time, each qubit in ensemble X (Y) is measured in the x -basis ($|\pm\rangle = [|0\rangle \pm |1\rangle]/\sqrt{2}$) and yields the '+' outcome with probability $p_x = [1 - \cos \Phi_{\text{LO}}]/2$ ($p_y = [1 - \sin \Phi_{\text{LO}}]/2$).

After performing the measurement with N total qubits, we obtain $\Phi_{\text{LO}}^{\text{est}}$ from the estimates of p_x and p_y . Since both provide information on $\Phi_{\text{LO}}^{\text{est}}$ equivalent of $N/2$ measurement bits, this results in a total information of N measurement bits, which gives an uncertainty of

$$\langle \Delta\Phi_{\text{LO}}^2 \rangle_{\text{pr}} = \frac{1}{N}, \quad (\text{E.6})$$

up to 2π phase shifts, that are fundamentally undetectable. This method is identical to the one described in [183].

E.2.2 Effects of laser fluctuations: Phase slip errors

Random fluctuations in the laser frequency (characterized by the laser spectrum noise spectrum $S_\nu(f) = 2\gamma_{\text{LO}}/f$) result in the fact that the laser phase itself has to be considered as a random variable after each cycle. Whenever in a given cycle the phase $\Phi_{\text{LO}}(t_k)$ falls outside the interval $[-\pi, \pi]$, the aforementioned technique leads to an estimate deviating from the true value by $\sim 2\pi$. As the variance s^2 of the prior distribution of Φ_{LO} grows with the interrogation time T (one finds $s^2 = \gamma_{\text{LO}}T$ ($s^2 = (\gamma_{\text{LO}}T)^2$) for a white ($1/f$) noise frequency spectrum, where γ_{LO} denotes the laser linewidth of the free-running (non-stabilized) LO) these undetected *phase slips* pose a fundamental limitation on the allowed Ramsey time T , and thus on the overall achievable laser stability.

If we assume a constant rate of phase diffusion, resulting in a Gaussian prior distribution of Φ_{LO} , the probability of a phase slip single cycle of length T can be estimated as

$$\mathcal{P}_{\text{slip}} = 2 \int_{-\pi}^{\pi} d\Phi_{\text{LO}}^{\text{real}} \frac{1}{\sqrt{2\pi s^2}} \exp \left[-\frac{(\Phi_{\text{LO}}^{\text{real}})^2}{2s^2} \right] \quad (\text{E.7})$$

$$= 1 - \text{erf} \left(\frac{\pi}{\sqrt{2}s} \right) = \left(\frac{\sqrt{2}s}{\pi^{3/2}} + \mathcal{O}(s^2) \right) \exp \left[-\frac{\pi^2}{2s^2} \right], \quad (\text{E.8})$$

where erf denotes the error function. As a phase slip in an early Ramsey cycle will remain undetected in the following cycles, its error contribution will accumulate over the total averaging time τ , in the worst case by a factor τ/T . Using this upper bound, and assuming $\mathcal{P}_{\text{slip}} \ll 1$ we write the variance contribution of phase slips as

$$\langle \Delta\Phi_{\text{LO}}^2 \rangle_{\text{slip}} = (2\pi)^2 \frac{\tau}{T} \mathcal{P}_{\text{slip}} \approx (2\pi)^2 \frac{\tau}{T} \frac{\sqrt{2}}{\pi^{3/2}} \sqrt{\gamma_{\text{LO}} T} \exp \left[-\frac{\pi^2}{2\gamma_{\text{LO}} T} \right], \quad (\text{E.9})$$

where the $(2\pi)^2$ prefactor sets the absolute contribution of a manifested slip event to $\pm 2\pi$, and in the second step we approximated $\mathcal{P}_{\text{slip}}$ with the first term of its asymptotic series from Eq. E.8.

E.2.3 Optimal Ramsey time

While (E.3) suggests increasing Ramsey times improve the laser stability, we have seen in the previous section that they also lead to an increased occurrence of phase slips yielding a significant contribution to the measurement uncertainty.

In order to find the optimal Ramsey time we add the contributions from quantum projection noise [Eq. E.6] and phase slip noise [Eq. E.9] under the assumption that the probability of phase slips is small, and obtain an expression for the Allan-variance,

$$\sigma_y^2(\tau) = \frac{1}{\omega_0^2 \tau} \Gamma, \quad (\text{E.10})$$

where

$$\Gamma = \frac{1}{TN} + \sqrt{32\pi} \frac{\tau \gamma_{\text{LO}}^{1/2}}{T^{3/2}} \exp \left[-\frac{\pi^2}{2\gamma_{\text{LO}} T} \right]. \quad (\text{E.11})$$

In order to find the optimal Ramsey time T_{opt} , that minimizes Γ , we introduce the new variable $x = \frac{2}{\pi^2} \gamma_{\text{LO}} T$, and write

$$\Gamma = \frac{2}{\pi^2} \frac{\gamma_{\text{LO}}}{Nx} + \frac{16}{\pi^{5/2}} \frac{\tau \gamma_{\text{LO}}^2}{x^{3/2}} e^{-1/x}. \quad (\text{E.12})$$

Taking the derivative with respect to x results in

$$\frac{d}{dx} \Gamma = -\frac{2}{\pi^2} \frac{\gamma_{\text{LO}}}{Nx^2} + \frac{16}{\pi^{5/2}} \tau \gamma_{\text{LO}}^2 \left(-\frac{3}{2} \frac{1}{x^{3/2}} + \frac{1}{x^{7/2}} \right) e^{-1/x}, \quad (\text{E.13})$$

which, after using the (self-consistent) assumption $x_{\text{opt}} \ll 1$, results in the following transcendental equation for x_{opt} ,

$$x_{\text{opt}}^{3/2} = ((8/\sqrt{\pi}) \gamma_{\text{LO}} \tau N) e^{-1/x_{\text{opt}}}. \quad (\text{E.14})$$

In Section E.4, we provide the derivation of the asymptotic solution,

$$x_{\text{opt}} = [\log((8/\sqrt{\pi})\gamma_{\text{LO}}\tau N)]^{-1} \approx [\log(\gamma_{\text{LO}}\tau N)]^{-1}, \quad (\text{E.15})$$

yielding directly

$$T_{\text{opt}} \approx \gamma_{\text{LO}}^{-1} \frac{\pi^2}{2} [\log(\gamma_{\text{LO}}\tau N)]^{-1}. \quad (\text{E.16})$$

Self-consistently we confirm that already for values $\gamma_{\text{LO}}\tau N \geq 10^4$, the approximation in Eq. E.9 is well justified, so that the above value represents a true local minimum. For larger values of T the phase slip errors grow rapidly, and numerical studies confirm that Eq. E.16 indeed represents a global minimum.

The optimal interrogation time is mainly set by the LO coherence time γ_{LO}^{-1} , and shows a weak dependence on the total number of qubits N , and the averaging time τ (Note, that if we model the LO with a $1/f$ frequency noise spectrum, only the exponent of the log term changes to $-1/2$ in this result). Using this optimized Ramsey time we find for the minimal value of Γ is

$$\Gamma_{\text{min}} = \frac{2}{\pi^2} \frac{\gamma_{\text{LO}}}{N x_{\text{opt}}} + \frac{16}{\pi^{5/2}} \frac{\tau \gamma_{\text{LO}}^2}{x_{\text{opt}}^{3/2}} e^{-1/x_{\text{opt}}} \quad (\text{E.17})$$

$$= \frac{2}{\pi^2} \frac{\gamma_{\text{LO}}}{N} \left(\frac{1}{x_{\text{opt}}} + 1 \right) \quad (\text{E.18})$$

$$\approx \frac{2}{\pi^2} \frac{\gamma_{\text{LO}} \log(\gamma_{\text{LO}}\tau N)}{N}. \quad (\text{E.19})$$

This result is valid as long as the averaging time τ is longer than the proposed T_{opt} from Eq. E.16. If this is not the case, then $T_{\text{opt}} = \tau$, the phase slip noise becomes negligible, and we end up with

$$\Gamma_{\text{min}} = \frac{1}{\tau N}. \quad (\text{E.20})$$

We approximate the crossover region (around $\tau \sim \gamma_{\text{LO}}^{-1}$) by adding leading terms from Eq. E.19 & (E.20) and obtain

$$[\sigma_y(\tau)]_{\min} \approx \frac{1}{\omega_0 \sqrt{N\tau}} \sqrt{\frac{1}{\tau} + \frac{2}{\pi^2} \gamma_{\text{LO}} \log(\gamma_{\text{LO}} \tau N)}. \quad (\text{E.21})$$

In summary, in the region $\tau < T_{\text{opt}}$, the LO noise is negligible leading to a linear scaling of the ADEV with the total averaging time τ . For large averaging times $\tau > T_{\text{opt}}$, phase slips of the laser phase pose a limitation to the maximal possible Ramsey time which results in a $1/\sqrt{\tau}$ scaling of the laser stability. Since we employ uncorrelated atoms, the ADEV displays in both regimes the $1/\sqrt{N}$ scaling of the standard quantum limit (SQL). As modern atomic clocks typically are laser noise limited, $\gamma_{\text{LO}} \gg \gamma_{\text{ind}}$ (where γ_{ind} represents the clock atom linewidth), we neglected the effects of individual atomic dephasing in the above considerations.

E.3 Cascaded interrogation using GHZ states

In this Section, we discuss the possibility of using quantum correlated states, namely GHZ states of the form

$$[|0\rangle + e^{i\chi}|1\rangle]/\sqrt{2}, \quad (\text{E.22})$$

where $|0\rangle$ and $|1\rangle$ are product states of all qubits being in $|0\rangle$ or $|1\rangle$, respectively, and χ will be referred to as the phase of the GHZ state. Such a state, once prepared, is more sensitive to the accumulated phase of the LO, Φ_{LO} , by a factor of N' , the number of qubits entangled:

$$\left(\prod_{j=1}^N \hat{U}_j \right) [|0\rangle + e^{i\chi}|1\rangle] / \sqrt{2} = [|0\rangle + e^{i(\chi+N'\Phi_{\text{LO}})}|1\rangle] / \sqrt{2}, \quad (\text{E.23})$$

where $\hat{U}_j = |0\rangle\langle 0| + e^{i\Phi_{\text{LO}}}|1\rangle\langle 1|$ is the time propagation operator for the interrogation time acting on the j th qubit. This property promises an enhancement in phase resolution, and therefore a better stability for quantum clocks.

E.3.1 Parity measurement

Using the idea with the two sub-ensembles [see Eq. E.4 and (E.5)], we imagine dividing the qubits into two equal groups, and preparing two separate GHZ states:

$$|X\rangle := [|0\rangle + |1\rangle]/\sqrt{2}, \quad (\text{E.24})$$

$$|Y\rangle := [|0\rangle + i|1\rangle]/\sqrt{2}, \quad (\text{E.25})$$

each entangling N' qubits. After the free evolution time, we imagine measuring each qubits in the x -basis ($|\pm\rangle = [|0\rangle \mp |1\rangle]/\sqrt{2}$) separately. In this basis, the above states are written as

$$\left[\left(\frac{|+\rangle - |-\rangle}{\sqrt{2}} \right)^{\otimes N'} + e^{i\phi_\nu} \left(\frac{|+\rangle + |-\rangle}{\sqrt{2}} \right)^{\otimes N'} \right] / \sqrt{2}, \quad (\text{E.26})$$

where $\phi_\nu = \chi_\nu + N'\Phi_{\text{LO}}$, for $\nu \in \{x, y\}$ and $\chi_x = 0$, while $\chi_y = \pi/2$ for the two groups, respectively. The above state can be written as

$$\frac{1}{2^{(N'+1)/2}} \sum_{\mathbf{q} \in \{+, -\}^{N'}} \left[\left(\prod_{j=1}^{N'} q_j \right) + e^{i\phi_\nu} \right] |q_1, q_2, \dots, q_{N'}\rangle. \quad (\text{E.27})$$

Once the qubits are measured one by one, the probability to measure a certain outcome $\mathbf{q} = (q_1, q_2, \dots, q_{N'})$, ($q_j \in \{+, -\}$) is

$$\mathcal{P}(\mathbf{q}) = \frac{1}{2^{N'+1}} |1 + p(\mathbf{q})e^{i\phi_\nu}|^2, \quad (\text{E.28})$$

where $p(\mathbf{q}) = \prod_{j=1}^{N'} q_j$ is the parity of the sum of all measurement bits. This parity is the observable that is sensitive to the accumulated phase, since its distribution is

$$\mathcal{P}(p = \pm 1) = \frac{1 \pm \cos(\phi_\nu)}{2}. \quad (\text{E.29})$$

This is identical to the parity measurement scheme described in [24]. By interrogating $n_0/2$ instances of $|X\rangle$ and $|Y\rangle$, respectively, we can measure the phase of the GHZ state, $N'\Phi_{\text{LO}}$, with uncertainty $1/\sqrt{n_0}$, since each instance provides a single measurement bit, which can be combined the same way as we described in the case of uncorrelated ensembles. The resulting measurement uncertainty, $\Delta\Phi_{\text{LO}}$, is

$$\langle \Delta\Phi_{\text{LO}}^2 \rangle_{\text{pr}} = \frac{1}{(N')^2 n_0} = \frac{n_0}{N^2}, \quad (\text{E.30})$$

which is a factor of N/n_0 smaller than the variance contribution of projection noise for the uncorrelated ensemble protocol, ($N = n_0 N'$).

E.3.2 Failure of the maximally entangled GHZ

Motivated by the increased phase resolution provided by the interrogation of GHZ states, we evaluate the stability of such a protocol. We find that it fails to provide improvement compared to the single-step uncorrelated protocol due to an increased phase slip rate. This is in agreement with earlier results [237, 184].

The probability, that the phase accumulated by $|X\rangle$ ($|Y\rangle$) during the interrogation time T , $N'\Phi_{\text{LO}}$ lies outside the interval $[-\pi, \pi]$, is

$$\mathcal{P}_{\text{slip}} = 2 \int_{\pi/N'}^{\infty} d\Phi_{\text{LO}}^{\text{real}} \frac{1}{\sqrt{2\pi\gamma_{\text{LO}}T}} \exp \left[-\frac{(\Phi_{\text{LO}}^{\text{real}})^2}{2\gamma_{\text{LO}}T} \right], \quad (\text{E.31})$$

which, due to the much lower slipping threshold of π/N' [instead of π in the uncorrelated case, compare Eq. E.7] will become significant for much shorter T cycle times. The resulting variance contribution (following the same argument as before) is

$$\langle \Delta\Phi_{\text{LO}}^2 \rangle_{\text{slip}} = \sqrt{32\pi} \frac{\tau}{T} \sqrt{\gamma_{\text{LO}} T} N' \exp \left[-\frac{\pi^2}{2\gamma_{\text{LO}} T(N')^2} \right]. \quad (\text{E.32})$$

Neglecting the individual qubit noise by the same argument as before, we simply add the contributions from Eq. E.30 and Eq. E.32 to obtain the Allan-variance, $\sigma_y^2(\tau) = \frac{1}{\omega_0^2 \tau} \Gamma$, where

$$\Gamma = \frac{1}{NN'T} + \sqrt{32\pi} \frac{\tau \gamma_{\text{LO}}^{1/2}}{T^{3/2}} N' \exp \left[-\frac{\pi^2}{2\gamma_{\text{LO}} T(N')^2} \right]. \quad (\text{E.33})$$

After optimizing T , we find

$$T_{\text{opt}} \approx \frac{\pi^2}{2} \frac{1}{\gamma_{\text{LO}}(N')^2} \frac{1}{\log[\gamma_{\text{LO}} \tau N(N')^3]}, \quad (\text{E.34})$$

which results in the minimal Allan-variance,

$$[\sigma_y(\tau)]_{\text{min}} \approx \frac{1}{\omega_0} \frac{\sqrt{2}}{\pi} \sqrt{\frac{\gamma_{\text{LO}} N' \log[\gamma_{\text{LO}} \tau N(N')^3]}{\tau N}}, \quad (\text{E.35})$$

which is at least a factor of $\sqrt{N'}$ *bigger* than the smallest obtainable Allan-variance with the single-step uncorrelated protocol [Eq. E.19]. In case of a $1/f$ LO frequency noise spectrum, $T_{\text{opt}} \propto \frac{1}{N}$ (up to logarithmic terms), and the resulting Allan-variance is equal to Eq. E.19, up to logarithmic corrections, yielding effectively no advantage over the uncorrelated scheme.

E.3.3 Cascaded GHZ scheme

As demonstrated in the previous Section, single GHZ states fail to improve clock stability because the increase in sensitivity to the laser detuning, at the same time,

leads to a drastic increase of phase slip errors originating from laser frequency fluctuations. These fluctuations, however, affect all clock qubits in identical manner, and therefore represents a *collective noise*. As such (and unlike, e.g., the individual dephasing of the clock qubits), they do not represent a fundamental limitation for the phase estimation. In the following, we show that this problem can be efficiently addressed using a cascade of GHZ states of varying sizes (and classical states with varying interrogation times) in an incoherent version of the phase estimation algorithm [159]. To this end, we reformulate the problem of estimating Φ_{LO} in a more suitable language.

The laser phase after a given Ramsey cycle can be expressed in a base- D numeral system as

$$(\Phi_{\text{LO}} + \pi)/2\pi = \sum_{j=-\infty}^{\infty} Z_j/D^j, \quad (\text{E.36})$$

with base- D digits $Z_j \in \{0, 1, \dots, D - 1\}$. Let us for the moment assume that the laser phase $\Phi_{\text{LO}} \in [-\pi, \pi]$, such that $(\Phi_{\text{LO}} + \pi)/2\pi = \sum_{j=1}^{\infty} Z_j/D^j \equiv 0.Z_1Z_2Z_3\dots$

Provided with N qubits, we imagine dividing them into M different groups, the j th group ($j = 0, 1, \dots, M - 1$) contains n_0 instances of GHZ states with D^j number of entangled qubits. One readily shows that a GHZ state consisting of D^{M-1} particles picks up the phase

$$\Phi_{M-1} = D^{M-1}\Phi_{\text{LO}} \mod [-\pi, \pi] \quad (\text{E.37})$$

$$= 2\pi(0.Z_MZ_{M+1}Z_{M+2}\dots) - \pi, \quad (\text{E.38})$$

which depend only on digits Z_M and higher of the laser phase to be measured. This insensitivity of the GHZ state with regard to the lower digits Z_1 to Z_{M-1} restates the problems of phase slips. Only if the latter are known, a measurement of the

phase of the GHZ state Φ_{M-1} yields useful information to determine Φ_{LO} . In other words, the natural number $Z_1 Z_2 \dots Z_{M-1}$ represents the number of phase slips of the largest group of GHZ states ($j = M - 1$). These lower digits can be determined one by one from the accumulated phases $\Phi_j = D^j \Phi_{\text{LO}} \bmod [-\pi, \pi]$ of the smaller GHZ ensembles $j = 0, \dots, M - 2$ by using the relation

$$[D(\Phi_{j-1} + \pi) - (\Phi_j + \pi)]/(2\pi) = (Z_j.Z_{j+1}Z_{j+2}\dots) - (0.Z_{j+1}Z_{j+2}\dots) = Z_j. \quad (\text{E.39})$$

Combining all measurement results we find that the best estimate for Φ_{LO} is given by

$$\Phi_{\text{LO}}^{\text{est}} = 2\pi \sum_{j=1}^{M-1} Z_j^{\text{est}} / D^j + \Phi_{M-1}^{\text{est}} / D^{M-1}, \quad (\text{E.40})$$

the precision of which is mostly determined by the uncertainty of the phase of the last group ($j = M - 1$), which contains the GHZ states with the most entangled qubits. Since there are n_0 independent instances of these GHZ states, their phase is known up to the uncertainty, $\langle \Delta \Phi_{M-1}^2 \rangle_{\text{pr}} = \frac{1}{n_0} \approx \frac{\delta D^{M-1}}{N}$, where $\delta = \frac{D}{D-1}$, and therefore we find

$$\langle \Delta \Phi_{\text{LO}}^2 \rangle_{\text{pr}} = \frac{\langle \Delta \Phi_{M-1}^2 \rangle_{\text{pr}}}{D^{2(M-1)}} = \frac{n_0 \delta^2}{N^2}. \quad (\text{E.41})$$

This would be the total uncertainty if we could tell with certainty that all phase slips of the lower levels had been detected correctly. However, the occurrence of an error in the estimation of any Z_j (in the following referred to as *rounding error*) has non-zero probability.

E.3.4 Rounding errors: finding the optimal n_0

If Φ_j is determined with poor precision, the estimate of Z_{j+1} will have a significant uncertainty, causing the final estimate of Φ_{LO} to be uncertain as well. Whenever

$|\Phi_j^{\text{est}} - \Phi_j^{\text{real}}| > \pi/D$, we make a mistake by under- or overestimating the digit Z_{j+1} . To minimize the effect of this error, we need to optimize how the qubits are distributed on various levels of the cascade. In other words, for a given total particle number N and basis D we need to find the optimal value of n_0 , the number of copies of GHZ states in each step ¹.

The probability that a rounding error occurs during the estimation of Z_j is

$$\begin{aligned} \mathcal{P}_{\text{re}} &= 2 \int_{\pi/D}^{\infty} d\phi \rho(\phi - \Phi_j^{\text{real}}) \leq 2 \int_{\pi/D}^{\infty} d\phi n_0^{3/2} \exp\left[-\frac{n_0\phi^2}{2}\right] \\ &\approx \frac{2}{\pi} n_0^{1/2} D \exp\left[-\frac{n_0\pi^2}{2D^2}\right], \end{aligned} \quad (\text{E.42})$$

where $\phi = \Phi_{j-1}^{\text{est}} - \Phi_{j-1}^{\text{real}}$, and ρ is the conditional distribution of Φ_{j-1}^{est} for given Φ_{j-1}^{real} . The employed upper bound is obtained in section E.5, with the assumption $\gamma_{\text{LO}}/\gamma_{\text{ind}} \gg N/n_0$ (γ_{ind} is the individual qubit dephasing rate), so that the projection noise is the dominant noise term. Due to the fixed value of n_0 across different levels of the cascade, this probability is independent of j , however the phase shift imposed on Φ_{LO} by a manifested rounding error of Z_j is $2\pi D^{-j}$ ($j = 1, \dots, M-1$), as rounding errors early in the cascade are more harmful than later ones. This results in the total variance contribution,

$$\langle \Delta\Phi_{\text{LO}}^2 \rangle_{\text{re}} = \mathcal{P}_{\text{re}} \sum_{j=1}^{M-1} (2\pi D^{-j})^2 \approx 8\pi \sqrt{\frac{N}{\delta}} D^{-\frac{M-3}{2}} \exp\left[-\frac{n_0\pi^2}{2D^2}\right] \frac{1}{D^2 - 1}. \quad (\text{E.43})$$

By adding the two error contributions from Eq. F.11 and Eq. F.17, we obtain the total uncertainty, $\langle \Delta\Phi_{\text{LO}}^2 \rangle$ and the corresponding Allan-variance [according to

¹In principle, the clock stability can further be improved by employing different numbers of copies in each step of the Cascade. However, this possibility will not be pursued in this work.

Eq. E.3]

$$\begin{aligned}\sigma_y^2(\tau) &= \frac{1}{\omega_0^2 \tau} \left[\frac{\delta}{NTD^{M-1}} + \frac{8\pi}{T} \sqrt{\frac{N}{\delta}} D^{-\frac{M-3}{2}} \exp \left[-\frac{n_0 \pi^2}{2D^2} \right] \frac{1}{D^2 - 1} \right] \\ &=: \frac{1}{\omega_0^2 \tau} [\Gamma_1 + \Gamma_2]\end{aligned}\quad (\text{E.44})$$

We find the optimal value of n_0 by minimizing this quantity. Introducing the new variable $x \equiv \frac{2D^2}{n_0 \pi^2}$, and using $n_0 \approx N/(\delta D^{M-1})$ we write

$$\Gamma_1 + \Gamma_2 = \frac{2}{\pi^2} \frac{\delta^2 D^2}{N^2 T x} + \frac{\sqrt{128} D^2}{T(D^2 - 1)} \frac{1}{x^{1/2}} \exp \left[-\frac{1}{x} \right] \quad (\text{E.45})$$

Taking the derivative with respect to x and equating it with 0, while using the (self-consistent) assumption $x_{\text{opt}} \ll 1$, results in the condition $\Gamma_2 \approx x_{\text{opt}} \Gamma_1 \ll \Gamma_1$ and the transcendental equation

$$x_{\text{opt}}^{1/2} \approx \frac{\sqrt{32} \pi^2 N^2}{\delta^2 (D^2 - 1)} \exp \left[-\frac{1}{x_{\text{opt}}} \right] \quad (\text{E.46})$$

for x_{opt} . The asymptotic solution in the case of $x_{\text{opt}} \ll 1$ is provided by section E.4:

$$x_{\text{opt}} \approx \left[\log \left(\frac{\sqrt{32} \pi^2 N^2}{\delta^2 (D^2 - 1)} \right) \right]^{-1} \sim [\log(N^2)]^{-1}, \quad (\text{E.47})$$

yielding directly the optimal number of instances of GHZ states per level

$$n_0^{\text{opt}} \sim \frac{2}{\pi^2} D^2 \log(N^2). \quad (\text{E.48})$$

This choice guarantees rounding errors yield a negligible contribution to the total measurement uncertainty, and we find for the corresponding value of $\Gamma_1 + \Gamma_2$

$$[\Gamma_1 + \Gamma_2]_{\min} \approx \Gamma_1(x_{\text{opt}}) = \frac{n_0^{\text{opt}} \delta^2}{N^2 T} \sim \frac{2}{\pi^2} \frac{\delta^2 D^2}{N^2 T} \log(N^2), \quad (\text{E.49})$$

where the factor $\delta = D/(D-1) \in (1, 2]$. Obviously, the use of a binary basis ($D = 2$) is optimal, and the effect of rounding errors lead to a logarithmic correction to the Heisenberg limit.

E.3.5 Phase slip errors: limitations to the Ramsey time T from laser noise

Although the cascade is designed to detect phase slips at levels $j = 1, 2 \dots M - 1$, when we relax the condition $\Phi_{\text{LO}} \in [-\pi, \pi]$, and allow $\Phi_{\text{LO}} \in (-\infty, +\infty)$, the possible phase slips of level $j = 0$ (Z_0) remains undetected. Once this happens, it introduces a 2π phase shift in Φ_{LO} , and therefore contributes to its overall uncertainty with

$$\langle \Delta\Phi_{\text{LO}}^2 \rangle_{\text{slip}} = (2\pi)^2 \frac{\tau}{T} \mathcal{P}_{\text{slip}} = \sqrt{32\pi} \frac{\tau \gamma_{\text{LO}}^{1/2}}{T^{1/2}} \exp \left[-\frac{\pi^2}{2\gamma_{\text{LO}} T} \right], \quad (\text{E.50})$$

where we assumed $\gamma_{\text{LO}} T \ll 1$. This adds an extra noise term $\Gamma_3 := \langle \Delta\Phi_{\text{LO}}^2 \rangle_{\text{slip}} / T$ to the already optimized $[\Gamma_1 + \Gamma_2]_{\min}$ expression, yielding

$$[\Gamma_1 + \Gamma_2]_{\min} + \Gamma_3 = \frac{2}{\pi^2} \frac{\delta^2 n_0^{\text{opt}}}{N^2 y} + \frac{16}{\pi^{5/2}} \tau \gamma_{\text{LO}}^2 \frac{1}{y^{3/2}} \exp \left[-\frac{1}{y} \right], \quad (\text{E.51})$$

where $y = \frac{2}{\pi^2} \gamma_{\text{LO}} T$. After taking the derivative with respect to y and equating it with zero, the assumption $y_{\text{opt}} \ll 1$ results in the condition $\Gamma_3 \approx y_{\text{opt}} [\Gamma_1 + \Gamma_2]_{\min} \ll [\Gamma_1 + \Gamma_2]_{\min}$ and the following transcendental equation,

$$y_{\text{opt}}^{3/2} \approx \frac{8\gamma_{\text{LO}}\tau N^2}{\sqrt{\pi}\delta^2 n_0^{\text{opt}}} \exp \left[-\frac{1}{y_{\text{opt}}} \right], \quad (\text{E.52})$$

for y_{opt} . The asymptotic solution is given again by section E.4:

$$y_{\text{opt}} = \left[\log \left(\frac{8\gamma_{\text{LO}}\tau N^2}{\sqrt{\pi}\delta^2 n_0^{\text{opt}}} \right) \right]^{-1} \sim [\log(\gamma_{\text{LO}}\tau N^2)]^{-1} \quad (\text{E.53})$$

$$T_{\text{opt}} = \frac{\pi^2}{2} \frac{y_{\text{opt}}}{\gamma_{\text{LO}}} \sim \frac{\pi^2}{2} \frac{[\log(\gamma_{\text{LO}}\tau N^2)]^{-1}}{\gamma_{\text{LO}}} \quad (\text{E.54})$$

in the realistic limit of $\gamma_{\text{LO}}\tau N^2 \gg 1$. The corresponding minimal value of $\Gamma_1 + \Gamma_2 + \Gamma_3$ is

$$\left[[\Gamma_1 + \Gamma_2]_{\min} + \Gamma_3 \right]_{\min} \approx \Gamma_1(x_{\text{opt}}, y_{\text{opt}}) = \frac{n_0^{\text{opt}} \delta^2}{N^2 T_{\text{opt}}} \quad (\text{E.55})$$

$$\sim \gamma_{\text{LO}} \frac{4\delta^2 D^2 \log(\gamma_{\text{LO}}\tau N^2) \log(N^2)}{\pi^4 N^2}. \quad (\text{E.56})$$

Since Γ_3 grows exponentially with T , interrogation times exceeding T_{opt} drastically reduce the resulting laser stability. For averaging times $\tau > T_{\text{opt}}$ this limit on the maximal interrogation time imposed by phase slip errors, leads to sub-optimal values of the ADEV $\sigma_y(\tau) \propto 1/\sqrt{\tau}$ according to Eq. E.10 & (E.56). However, this limitation can be overcome as we demonstrate in the following section.

If the averaging time τ is shorter than the interrogation time suggested by Eq. F.31, Γ_3 is negligible compared to Γ_1 , and the corresponding effective linewidth is

$$[\Gamma_1 + \Gamma_2]_{\min} + \Gamma_3 \approx \frac{n_0^{\text{opt}} \delta^2}{N^2 T} = \frac{2}{\pi^2} \frac{\delta^2 D^2}{N^2 T} \log(N^2), \quad (\text{E.57})$$

and the real optimum is at $T = \tau$. The resulting τ^{-1} scaling indicates that this is the noise-free measurement regime, and results in a Heisenberg-limited ADEV (up to the logarithmic correction arising from n_0^{opt}).

E.3.6 Extending the Ramsey time beyond the laser noise limit

As we have seen in the previous Section, for long $\tau > T_{\text{opt}}$, the cascaded GHZ scheme is limited by the LO linewidth γ_{LO} yielding a sub-optimal laser stability [Eq. E.56]. In the following we demonstrate a method to efficiently circumvent this

problem, by employing additional classical interrogations with varying (effective) interrogation times [183, 27]. This allows us to directly assess the digits $Z_0, Z_{-1}, Z_{-2} \dots$, thus effectively countering the problem of phase slips on this level. As such it represents a direct extension of the cascaded GHZ states scheme in the classical domain.

We assume we have additional M^* groups of n_0^* particles at our disposal. Using dynamical decoupling techniques [225], we realize that each ensemble ($j = -1, -2 \dots, -M^*$) during the interrogation picks up a phase $\Phi_j = D^j \Phi_{\text{LO}} \bmod [-\pi, \pi]$ (alternatively, this can be achieved by choosing varying interrogation times for each ensemble according to $T_j = D^j T$, for $j < 0$ [183]). This implies that these ensembles evolve successively slower for decreasing j , and thus, in the spirit of Section E.3.3, directly assess the digits left from the point in the D-numeral representation of Φ_{LO} [compare Eq. E.36] according to Eq. E.39, where we now allow negative values of j .

If all digits are correctly estimated, this accounts for all phase slips up to the last ensemble $j = -M^*$. One readily shows in an analogous calculation to the one in Section E.3.5 that for such a procedure with M^* classical stages the optimal Ramsey time (i.e., the optimized interrogation time of the GHZ states) is exponentially prolonged

$$T_{\text{opt}}^{(M^*)} = D^{M^*} T_{\text{opt}}. \quad (\text{E.58})$$

Note, that here we assumed that the total number of particles employed in the classical part of the scheme is negligible with regard to the total number of particles, $N^* = M^* n_0^* \ll N$. This is a well justified assumption, as in order to prolong the optimal Ramsey time by a factor of k from the original optimum T_{opt} we need a logarithmic number of groups only, $M^* \approx \log_D(k)$, as implied by Eq. E.58. Furthermore, following

the argumentation outlined in Section E.3.4, we find that only

$$n_0^* \geq \frac{2}{\pi^2} D^2 \log(kN^2), \quad (\text{E.59})$$

particles per level are sufficient to ensure that the rounding errors induced by the classical part of the cascade ($j < 0$) are negligible.

As seen in the previous Section, when the optimal Ramsey time exceeds the averaging time, $T_{\text{opt}}^{(M^*)} \geq \tau$ the effective linewidth is given by Eq. E.57 (assuming $N^* \ll N$), as we can neglect the phase slips contribution to the measurement uncertainty (Γ_3). Extending the Ramsey time to its then optimal (i.e., maximal) value $T \sim \tau$ we find the ADEV [compare Eq. E.10]

$$[\sigma_y(\tau)]_{\min} \approx \frac{1}{\omega_0} \frac{\delta \sqrt{n_0^{\text{opt}}}}{N\tau} \approx \frac{\sqrt{2}}{\sqrt{\pi}\omega_0} \frac{D\delta}{N\tau} \sqrt{\log(N^2)}. \quad (\text{E.60})$$

This result illustrates that the presented clock protocol achieves Heisenberg-limited clock stability up to a logarithmic correction arising from the number of atoms necessary to compensate for rounding and phase slip errors. The number of particles needed for the extension of the Ramsey time beyond the laser noise limit $T_{\text{opt}} \approx \gamma_{\text{LO}}^{-1}$ is given as $N^* \approx \frac{2}{\pi^2} D^2 \log(kN^2) \log_D(k)$ and thus negligible compared to the total particle number N . For the optimal choice of basis $D = 2$ the constant factor reduces to $D\delta = 4$.

The above procedure of interrogation with varying Ramsey times (for the groups $j < 0$) can be understood as a classical pre-narrowing of the laser linewidth [183] to a value that eliminates the threat of phase slips, before application of the quantum protocol.

E.3.7 Individual qubit noise and final result

Up to this point we have neglected individual particle dephasing. However, as we increase the Ramsey time beyond the laser noise limit $T > \gamma_{\text{LO}}^{-1}$ we need to consider their effect.

In general, the clock atoms are subject to individual decoherence processes characterized by the atomic linewidth γ_{ind} ($\ll \gamma_{\text{LO}}$). For the group with the largest GHZ states in our scheme this leads to an uncertainty contribution of $\langle \Delta\Phi_{M-1}^2 \rangle_{\text{dephasing}} = D^{M-1} \gamma_{\text{ind}} T / n_0$ which results in the measurement uncertainty

$$\langle \Delta\Phi_{\text{LO}}^2 \rangle_{\text{dephasing}} = \frac{\gamma_{\text{ind}} T}{n_0 D^{M-1}} \approx \frac{\delta \gamma_{\text{ind}} T}{N}, \quad (\text{E.61})$$

which represents a fundamental noise floor in the form of the effective linewidth contribution $\Gamma_4 = \langle \Delta\Phi_{\text{LO}}^2 \rangle_{\text{dephasing}} / T$.

By adding Eq. E.57 and Γ_4 , we obtain an approximation of the total ADEV under single particle noise,

$$[\sigma_y(\tau)]_{\min} \approx \frac{\delta}{\omega_0 \sqrt{\tau N}} \left[\frac{1}{T D^{M-1}} + \gamma_{\text{ind}} \right]^{1/2}, \quad (\text{E.62})$$

where we used $n_0 = N/\delta D^{M-1}$. This equation suggests that the quantum gain in the estimation becomes lost if $T \sim (\gamma_{\text{ind}} D^{M-1})^{-1}$. This is a well known result [110], and in fact represents a fundamental limitation of the maximal Ramsey time allowed in the presence of single particle noise [82]. We approximate the crossover between the regimes $\tau < (\gamma_{\text{ind}} D^{M-1})^{-1}$ ($\tau > (\gamma_{\text{ind}} D^{M-1})^{-1}$), where Eq. E.62 is dominated by the first (second term) by taking $T = \tau$, and rewrite D^{M-1} in terms of the total particle number N to arrive at the final equation characterizing the stability of the cascaded

GHZ scheme

$$[\sigma_y(\tau)]_{\min} \approx \frac{1}{\omega_0 \sqrt{\tau N}} \left[\frac{1}{\tau N} \frac{2\delta^2 D^2}{\pi^2} \log(N^2) + \delta \gamma_{\text{ind}} \right]^{1/2}. \quad (\text{E.63})$$

Again, for the choice of a binary basis $D = 2$ the constant factor is given as $\delta D = 4$.

In summary, we find that the cascaded GHZ scheme enables an optimal, Heisenberg-limited laser stability for short averaging times τ up to a logarithmic correction. This stability reaches the fundamental noise floor given by the single particle dephasing for averaging times $\tau_0 \approx (\gamma_{\text{ind}} D^{M-1})^{-1}$. Note, that in the limit $N \rightarrow \infty$ this crossover value goes to zero, and the clock stability is given by the best possible stability allowed by quantum mechanics for all τ . In comparison, classical protocols reach this fundamental limit in the best case [183] at the fixed time $\tau \approx \gamma_{\text{ind}}^{-1}$. For averaging times larger than this value $\tau \geq \gamma_{\text{ind}}^{-1}$ the quantum protocol does not offer an advantage over an optimal classical protocol due to fundamental quantum metrological bounds [82].

E.4 Analytic solution of $x^n = A \exp[-1/x]$

To carry out direct optimization of the Allan variance, we need to be able to solve transcendental equations of the following form

$$x^n = A \exp \left[-\frac{1}{x} \right]. \quad (\text{E.64})$$

In this Section we obtain an analytic formula for the solution of this equation over the domain $x \in [0, \infty)$, in the limiting case of $A \gg 1$, where n is real. The sign of n determines the number of solutions: In case of $n > 0$, there are three solutions:

$x_{s,0} = 0$, $x_{s,1} \ll 1$ and $x_{s,2} \gg 1$. In case of $n \leq 0$, there is always a single solution, $x_{s,1} \ll 1$. We are going to focus on the $x_{s,1} =: x_s$ solution, and give upper and lower bounds, such that $x_l \leq x_s \leq x_u$, and $x_u/x_l \rightarrow 1$ as $A \rightarrow \infty$.

The general method of Taylor-expanding the right side of Eq. E.64 around $x = 0$ fails due to the non-analytic property of $e^{-1/x}$ function at zero, and forces us to choose an alternate route. Here, we use a recursion formula, and prove its stability around x_s . Rearranging Eq. E.64 and turning it into a recursion f yields

$$x_k = \frac{1}{\log A - n \log x_{k-1}} =: f(x_{k-1}), \quad (\text{E.65})$$

The iteration of f is stable around the fixed point ($f(x_s) = x_s$), if and only if $1 > |f'(x_s)| = x_s|n|$, which is true in the limit $x_s \ll 1$. Stability implies that the fix point can be obtained as the limit

$$x_s = \lim_{k \rightarrow \infty} x_k = \lim_{k \rightarrow \infty} f^{[k]}(x_0), \quad (\text{E.66})$$

if the x_0 starting point is sufficiently close to x_s , where $f^{[k]}$ denotes k iterations of f .

In case of $n \leq 0$, $f'(x_s) = nx_s \leq 0$ therefore $[f^{[k]}(x_0) - f^{[k-1]}(x_0)]$ is an alternating sequence and we can quickly obtain upper (x_u) and lower (x_l) bounds by applying the recursion f twice on $x_0 = 1$:

$$x_l = x_1 = \frac{1}{\log A}, \quad x_u = x_2 = \frac{1}{\log A + n \log \log A}, \quad (\text{E.67})$$

In case of $n > 0$ and $x_0 = 1$, $f^{[k]}(x_s)$ is monotonically decreasing (since $f'(x_s) > 0$), and we can safely choose the upper bound $x_u = x_2$. To obtain a lower bound, we introduce a new variable $\xi = -\log x$, and write Eq. E.65 as

$$\xi_k = \log \log A + \log \left(1 + \frac{n}{\log A} \xi_{k-1} \right) \quad (\text{E.68})$$

$$\leq \log \log A + \frac{n}{\log A} \xi_{k-1} =: g(\xi_{k-1}), \quad (\text{E.69})$$

where we used that $\log(1 + y) \leq y$, $\forall y \in \mathbb{R}^+$ and g is a new recursion. Since g is a monotonically increasing function, the inequality holds for multiple iterations, $\xi_k \leq g^{[k]}(\xi_0)$, and eventually give the upper bound, $-\log x_s = \xi_s \leq \lim_{k \rightarrow \infty} g^{[k]}(\xi_0)$. In the limit of $A \ll 1$, we can assume $\frac{n}{\log A} < 1$, and the sequence of iterations of g becomes convergent. Due to its simple form, we can evaluate its limit in a closed form, which results in the following upper bound for ξ_s and the corresponding lower bound for x_s .

$$\xi_s < \frac{\log \log A}{1 - \frac{n}{\log A}}, \quad \rightarrow \quad x_s > \left(\frac{1}{\log A} \right)^{\frac{1}{1 - \frac{n}{\log A}}}. \quad (\text{E.70})$$

We can obtain an even better (and more conventional) lower bound by applying f once more:

$$x_l = f \left[\left(\frac{1}{\log A} \right)^{\frac{1}{1 - \frac{n}{\log A}}} \right] = \frac{1}{\log A + \frac{1}{1 - \frac{n}{\log A}} n \log \log A} \quad (\text{E.71})$$

For both signs of n , $x_l \log A \rightarrow 1$, $x_u \log A \rightarrow 1$, and $x_u/x_l \rightarrow 1$ as $A \rightarrow \infty$, from which we conclude that

$$\lim_{A \rightarrow \infty} (x_s \log A) = 1. \quad (\text{E.72})$$

For large enough A , we can approximate x_s with $[\log A]^{-1}$, and the relative error is bounded by $|n| \frac{\log \log A}{\log A}$.

E.5 Upper bound on the tail of the distribution of the estimated phase

The probability of rounding errors is given an upper bound in order to obtain a more tractable form for optimization.

E.5.1 Upper bound on the tail of the binomial distribution

Here we derive an upper bound for the binomial distribution

$$\mathcal{P}(k) = \binom{n}{k} p^k (1-p)^{n-k}. \quad (\text{E.73})$$

Central limit theorem implies that for large enough n , $\mathcal{P}(k)$ can be approximated with the normal distribution, $\mathcal{N}(np, np(1-p))$, however, one can be concerned with the fact that this underestimates the tail of $\mathcal{P}(k)$. Here we give $F(k)$ as a strict upper bound on $\mathcal{P}(k)$,

$$\mathcal{P}(k) < F(k) = \exp \left[-2(n-1) \left(\frac{k}{n} - p \right)^2 \right]. \quad (\text{E.74})$$

To see that $F(k)$ is indeed an upper bound of $\mathcal{P}(k)$ for all n, p and k , let us examine the logarithm of the binomial distribution $\mathcal{P}(k = ny)$,

$$L(y) = \log \binom{n}{ny} + ny \log p + n(1-y) \log(1-p), \quad (\text{E.75})$$

where $0 \leq y \leq 1$. The properties, we are interested in, are

- $L(y) < 0$ for all y , since $\mathcal{P}(k) < 1$,
- $\frac{\partial}{\partial y} L(y) \Big|_{y=p} = 0$, and positive for $y < p$ and negative for $y > p$, since $L(y) = \max$ at $y = p$.
- $\frac{\partial^2}{\partial y^2} L(y) = \frac{\partial^2}{\partial y^2} \binom{n}{ny} = -n^2 \left(\psi_1[1 + n(1-y)] + \psi_1[1 + ny] \right)$, where $\psi_1(x) = \frac{d}{dx} \log \Gamma(x)$, the first polygamma function.

By analyzing the series expansion of $\psi_1(1 + \eta)$ for large and small η arguments,

$$\psi_1(1 + \eta) = \frac{1}{\eta} - \frac{1}{2\eta^2} + \mathcal{O}(\eta^{-3}) \quad \eta \gg 1 \quad (\text{E.76})$$

$$\psi_1(1 + \eta) = \frac{\pi^2}{6} - 2.404\eta + \frac{\pi^4}{30}\eta^2 + \mathcal{O}(\eta^3) \quad \eta \ll 1, \quad (\text{E.77})$$

one can show that $\frac{\partial^2}{\partial y^2} L(y)$ is always negative and has a global maximum at $y = 1/2$, where it takes the value

$$\left. \frac{\partial^2}{\partial y^2} L(y) \right|_{y=1/2} = -4(n-1) - \mathcal{O}(n^{-1}). \quad (\text{E.78})$$

Therefore the constant function $f''(y) = -4(n-1)$ is an upper bound of $L'' = \frac{\partial^2}{\partial y^2} L$.

Now, let us integrate both L'' and f'' twice, and choose the integration constants, so that $L(y) < f(y)$. Since $L'(y=p) = 0$,

$$L'(y) < \int_p^y d\zeta f''(\zeta) = -4(n-1)(y-p), \quad (\text{E.79})$$

which is chosen to be $f'(y)$, and since $L(p) < 0$,

$$L(y) < \int_p^y d\zeta L'(\zeta) < \int_p^y d\zeta f'(\zeta) = -2(n-1)(y-p)^2, \quad (\text{E.80})$$

which is chosen to be $f(y)$. Consequently

$$\mathcal{P}(ny) = \exp[L(y)] < \exp[f(y)] = F(ny). \quad (\text{E.81})$$

E.5.2 Upper bound on the distribution of the estimated phase

Here we give an upper bound on the distribution of the Ramsey phase Φ , as determined by estimating $\cos \Phi$ and $\sin \Phi$ from two sub-groups of GHZ states (X, Y) , each providing $n/2$ measurement (parity) bits. Qubits in group X are prepared in $|\mathbf{0}\rangle + |\mathbf{1}\rangle]/\sqrt{2} =: |+\rangle$, and measured in $|+\rangle$ with probability $p_x = [1 + \cos \Phi]/2$ after time T , while qubits in ensemble Y are prepared in $[(\mathbf{0}\rangle + i|\mathbf{1}\rangle]/\sqrt{2}$, and measured in $|+\rangle$ with probability $p_y = [1 + \sin \Phi]/2$ after time T . The number of $|+\rangle$ outcomes k_x and k_y from groups X and Y , respectively are binomial random variables with the

distribution

$$\mathcal{P}(k_\nu) = \binom{n/2}{k_\nu} p_\nu^{k_\nu} (1 - p_\nu)^{n/2 - k_\nu}, \quad (\text{E.82})$$

where $\nu \in \{x, y\}$. Using the upper bound from Eq. E.74, and noting that $n/2 > 1$ we can give the following upper bound on the joint distribution of k_x and k_y ,

$$\mathcal{P}(k_x, k_y) < \exp \left[-\frac{n}{2} \left(\frac{2k_x}{n} - p_x \right)^2 - \frac{n}{2} \left(\frac{2k_y}{n} - p_y \right)^2 \right]. \quad (\text{E.83})$$

Let us introduce the polar coordinates r, φ : $r \cos \varphi = \frac{2k_x}{n} - \frac{1}{2}$ and $r \sin \varphi = \frac{2k_y}{n} - \frac{1}{2}$, and smear the distribution into a continuous density function $\rho(r, \varphi)$, and its upper bound accordingly:

$$\rho(r, \varphi) < \frac{n^2}{4} r \exp \left[-\frac{n}{2} (r^2 - 2r \cos(\varphi - \Phi^{\text{real}}) + 1) \right]. \quad (\text{E.84})$$

The marginal distribution of r is independent of Φ^{real} , which means that r does not hold any information about Φ^{real} . The upper bound on the marginal distribution of φ can be written as

$$\rho(\varphi) < \left(\frac{n}{4} + \frac{n^{3/2} \sqrt{\pi}}{\sqrt{32}} \right) \exp \left[-\frac{n}{2} \sin^2(\varphi - \Phi^{\text{real}}) \right] \quad (\text{E.85})$$

$$\sim n^{3/2} \exp \left[-\frac{n}{2} (\varphi - \Phi^{\text{real}})^2 \right], \quad (\text{E.86})$$

where in the second line we assumed $|\varphi - \Phi^{\text{real}}| \ll 1$, and $n \gg 1$. This result is an upper bound on the distribution of φ , which we are going to use to give an upper bound on the rounding error probability,

$$P_{\text{re}} = 2 \int_{\pi/D}^{\infty} d\varphi \rho(\varphi + \Phi^{\text{real}}). \quad (\text{E.87})$$

The rigorous upper bound on the tail of ρ is provided by Eq. E.86, as long as $\pi/D \ll 1$, and $n \gg 1$.

E.6 Threshold fidelity

In this section we estimate the fidelity of the pairwise entangling operations required to keep the benefit of quantum enhancement. (Following closely the analysis in the supplementary of [121]) In the GHZ state generation step of every cycle, n copies of the cascade are initialized. This requires N/n pairwise entangling operations per copy. Among other unitary operations, this is likely to be the bottleneck. If one entangling operation can be performed with fidelity $F = \exp[-\epsilon]$ ($\epsilon \ll 1$), then N/n repetitions succeed with fidelity $F_{\text{total}} = F^{N/n} = \exp[-N\epsilon/n]$.

Whenever a copy fails on level i of the cascade, its measurement result ϕ_i becomes completely random. This happens with probability $(1 - F_{\text{total}})$. In the meantime, with probability F_{total} , the result is consistent with $\phi_i = \phi_{\text{real}}$, where ϕ_{real} is the actual value of ϕ_i . Out of the n copies nF_{total} contributes to a peak centered at ϕ_{real} , with width of $1/\sqrt{F_{\text{total}}n}$ and weight F_{total} , while the rest contributes to a uniform distribution with weight $(1 - F_{\text{total}})$: The expectation value of ϕ_i is still

$$\langle \phi_i \rangle = \phi_{\text{real}}, \quad (\text{E.88})$$

but the variance is

$$\text{Var}(\phi_i) \approx \frac{1}{n} + \frac{\pi^2}{3}(1 - F_{\text{total}}). \quad (\text{E.89})$$

The threshold fidelity F_{th} is defined by the criteria that if $F \geq F_{\text{th}}$, then $\text{Var}(\phi_i) \approx 1/n$. If this is satisfied, then losing the information from some of the copies does not deteriorate the precision significantly.

This requires $1 - F_{\text{total}} < \frac{3}{\pi^2 n}$, while $F_{\text{total}} = \exp[-\epsilon N/n]$ from above. From these,

we conclude that $F_{\text{th}} = \exp[-\epsilon_{\text{th}}]$, where

$$\epsilon_{\text{th}} \approx \frac{3}{\pi^2 N} \sim \frac{1}{N}. \quad (\text{E.90})$$

In the case $N = 50$ qubits, we require $F_{\text{th}} \approx 0.99$ fidelity level for the pairwise entangling operations. A more feasible approach is entangling multiple qubits at once with a collective gate, such as in [153], currently reaching 0.6 fidelity for up to 14 qubits. However, the resulting infidelities increase with the number of entangled qubits making the creation of large entangled states still challenging.

Appendix F

Appendices for Chapter 7

F.1 GHZ cascade in a network of K clocks

Here, we discuss the details of using quantum correlated states constructed out of $N' = Kn$ qubits, equally distributed among K clocks, namely the GHZ state of the form

$$[|00\dots 0\rangle + e^{i\chi}|11\dots 1\rangle]/\sqrt{2}, \quad (\text{F.1})$$

where $|qq\dots q\rangle = |q\rangle^{\otimes N'}$, $q \in \{0, 1\}$. Entanglement has two effects here: First, it makes the phase of such a GHZ state, χ , sensitive to the accumulated phase of the *center-of-mass* of all the K independent local oscillators, (each located at one of the clocks) $\Phi_{\text{COM}} = \sum_{j=1}^K \Phi^{(j)}/K$, where $\Phi^{(j)} = \int_0^T dt (\omega^{(j)}(t) - \omega_0)$ is the accumulated phase of the LO at clock j , during the interrogation time T , here $\omega^{(j)}(t)$ is the instantaneous frequency of the LO, while ω_0 is the transition frequency of the clock

qubit. Second, it increases the sensitivity, since the relative phase in the state

$$\left(\prod_j^K \prod_i^{N'/K} \hat{U}_{i,j} \right) \left[|\mathbf{0}\rangle + e^{i\chi} |\mathbf{1}\rangle \right] / \sqrt{2} = \left[|\mathbf{0}\rangle + e^{i(\chi+N'\Phi_{\text{COM}})} |\mathbf{1}\rangle \right] / \sqrt{2}, \quad (\text{F.2})$$

grows N' times faster. Here $\hat{U}_{i,j} = |0\rangle\langle 0| + e^{i\Phi^{(j)}}|1\rangle\langle 1|$ is the time evolution operator during the interrogation time, acting on the i th qubit at clock j , and $|\mathbf{0}\rangle$ and $|\mathbf{1}\rangle$ are product states of all qubits being in $|0\rangle$ or $|1\rangle$, respectively.

F.1.1 Parity measurement

By setting the initial phase of the GHZ state, χ , to 0 and $\pi/2$ in two parallel instances, we effectively measure the real and imaginary part of $e^{iN'\Phi_{\text{COM}}}$, and thus get an estimate on the value of $N'\Phi_{\text{COM}}$ up to 2π phase shifts. The most cost-effective way to do this is to measure all qubits in the local x -basis. In this basis, the state from Eq. F.2 can be written as

$$\frac{1}{\sqrt{2}} \left[\left(\frac{|+\rangle - |-\rangle}{\sqrt{2}} \right)^{\otimes N'} + e^{i\phi} \left(\frac{|+\rangle + |-\rangle}{\sqrt{2}} \right)^{\otimes N'} \right], \quad (\text{F.3})$$

where $\phi = \chi + N'\Phi_{\text{COM}}$, and $|\pm\rangle = \frac{|0\rangle \pm |1\rangle}{\sqrt{2}}$. The above state can be expanded in a sum:

$$\frac{1}{2^{(N'+1)/2}} \sum_{\mathbf{q} \in \{+, -\}^{N'}} \left[\left(\prod_{j=1}^{N'} q_j \right) + e^{i\phi} \right] |q_1, q_2, \dots, q_{N'}\rangle, \quad (\text{F.4})$$

where we labeled all qubits with $k \in \{1, 2, \dots, N'\}$, irrespective of which clock they belong to. The probability of a certain outcome $\mathbf{q} = (q_1, q_2, \dots, q_{N'})$, ($q_j \in \{+, -\}$), is

$$\mathcal{P}(\mathbf{q}) = \frac{1}{2^{N'+1}} |1 + p(\mathbf{q})e^{i\phi}|^2, \quad (\text{F.5})$$

where $p(\mathbf{q}) = \prod_{j=1}^{N'} q_j$ is the parity of the sum of all measurement bits. Now, the clocks send their measurement bits to the center node, which evaluates p . This parity is the

global observable that is sensitive to the accumulated phase, since its distribution is

$$\mathcal{P}(p = \pm) = \frac{1 \pm \cos(\phi)}{2}. \quad (\text{F.6})$$

The above procedure is identical to the parity measurement scheme described in [24].

F.1.2 Cascaded GHZ scheme

Here we perform an analysis very similar to the analysis of the scheme in [116], using local GHZ cascade.

Provided with N qubits distributed equally among K clocks, we imagine that each clock separates its qubits into $M + 1$ different groups. The 0th group contains n_1/K uncorrelated qubits, and the i th group ($i = 1, 2 \dots M$) contains n_0 independent instances of 2^{i-1} qubits that are entangled with the other groups of 2^{i-1} qubits in each clock. In other words, there are n_0 independent copies of GHZ states with a total of $2^{i-1}K$ qubits entangled on the i th level of the cascade ($i \geq 1$) (See Fig. F.1).

This way the total number of qubits can be written as

$$N = n_1 + n_0 \sum_{i=1}^M 2^{i-1}K \approx n_0 2^M K \quad (\text{F.7})$$

where we assumed $n_1 \ll N$.

The purpose of this cascaded scheme is to directly assess the digits Y_1 and $\{Z_j : j = 2, 3, \dots\}$ in the binary fraction representation of the phase

$$\Phi_{\text{LO}} \mod [-\pi, \pi] = \frac{2\pi}{K} \left[Y_1 + \sum_{i=1}^{\infty} Z_{i+1}/2^i \right] - \pi, \quad (\text{F.8})$$

where $x \mod [-\pi, \pi] = (x + \pi) \mod 2\pi - \pi$, $Y_1 \in \{0, 1, 2 \dots K-1\}$ and $Z_i \in \{0, 1\}$, and $\Phi_{\text{LO}} = \Phi_{\text{COM}}$. The 0th level of the cascade estimates $\Phi_0 = \sum_{j=1}^K (\Phi^{(j)} \mod [-\pi, \pi]) / K$,

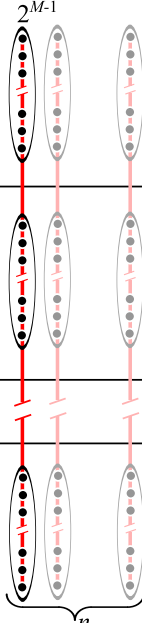
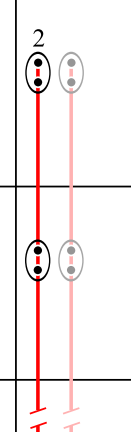
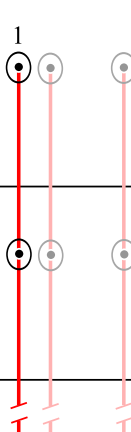
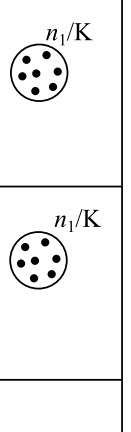
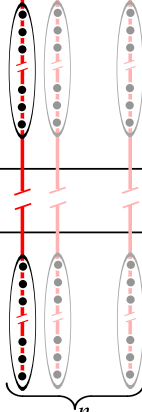
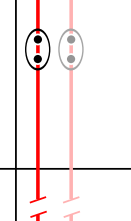
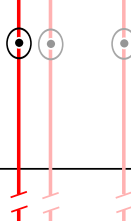
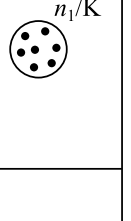
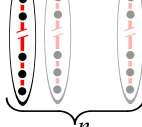
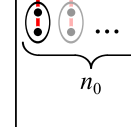
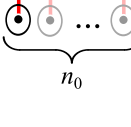
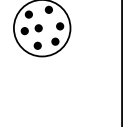
	level M	...	level 2	level 1	level 0
clock 1					
clock 2					
:					
clock K					
# of parallel copies	n_0		n_0	n_0	n_1
degree of entanglement	$2^{M-1}K$		$2K$	K	1
# of qubits	$2^{M-1}Kn_0$		$2Kn_0$	Kn_0	n_1

Figure F.1: GHZ cascade protocol for K clocks. Each allocates qubits for different levels of the protocol: In level 0, n_1/K qubits are put into an uncorrelated ensemble. In level i , ($i = 1, 2 \dots M$), each clock allocates $n_0 2^{i-1}$ qubits for creating n_0 parallel instances of GHZ states with $2^{i-1}K$ entangled qubits. Due to the exponential scaling of the degree of entanglement, most of the total available qubits are used in higher levels of the cascade. This is a necessary condition to achieve Heisenberg scaling, up to logarithmic factors.

and every i th level after that estimates $\Phi_i = K2^{i-1}\Phi_{\text{LO}} \bmod [-\pi, \pi]$. In other words, every level of the cascade is sensitive to a different multiple of the LO phase $\Phi_{\text{LO}} \pmod{2\pi}$. After the separate measurements of the levels, each provide an estimate to Φ_i which can be combined to obtain the best estimate for Φ_{LO} . Here we describe this using the digits Y_1 and Z_i as intermediate quantities, which are calculated from Φ_i the following way,

$$Y_1 = [K(\Phi_0 + \pi) - (\Phi_1 + \pi)] / (2\pi), \quad (\text{F.9})$$

$$Z_i = [2(\Phi_{i-1} + \pi) - (\Phi_i + \pi)] / (2\pi), \quad (\text{F.10})$$

for $i = 2, 3, \dots, M$.

The last group ($i = M$) contains GHZ states with the most entangled qubits. These are the ones with the fastest evolving phase, and therefore they provide the best resolution on Φ_{LO} . Since there are n_0 independent instances, their phase $\Phi_M = 2\pi \sum_{i=1}^{\infty} Z_{M+i}/2^i$ is known up to the uncertainty, $\langle \Delta\Phi_M^2 \rangle_{\text{pr}} = \frac{1}{n_0}$,

Assuming that all lower digits $\{Y_1, Z_j | j = 2 \dots M\}$ have been determined correctly, this results in the total measurement uncertainty for Φ_{LO} :

$$\langle \Delta\Phi_{\text{LO}}^2 \rangle_{\text{pr}} = \frac{\langle \Delta\Phi_M^2 \rangle_{\text{pr}}}{(2^{M-1}K)^2} = \frac{4n_0}{N^2}, \quad (\text{F.11})$$

where, for the moment, we neglected individual qubit noise and assumed $\Phi_{\text{LO}} \in [-\pi, \pi]$. However, in general, the estimation of the lower digits will not be perfect. In the following section we investigate the effect of these *rounding errors* on the final measurement accuracy. From this analysis we find the optimal number of copies n_0 and n_1 .

F.1.3 Rounding errors

Whenever $|\Phi_0^{\text{est}} - \Phi_0| > \pi/K$, or $|\Phi_i^{\text{est}} - \Phi_i| > \pi/2$ (for $i \geq 1$), we make a mistake by under- or overestimating the number of phase slips Y_1 or Z_{i+1} , respectively. To minimize the effect of this error, we need to optimize how the total of N qubits are distributed among the various levels of the cascade. In other words we need to find $n_{0,\text{opt}}$ and $n_{1,\text{opt}}$.

The probability that a rounding error occurs during the estimation of Z_{i+1} is

$$\mathcal{P}_{i,\text{re}} = 2 \int_{\pi/2}^{\infty} d\phi \rho_i(\phi + \Phi_i) \leq 2 \int_{\pi/2}^{\infty} d\phi \frac{1}{s_i^3} \exp\left[-\frac{\phi^2}{2s_i^2}\right] \quad (\text{F.12})$$

where $\phi = \Phi_i^{\text{est}} - \Phi_i$, and ρ_i is the conditional density function of Φ_i^{est} for a given real Φ_i , and $s_i^2 = \text{Var}(\Phi_i^{\text{est}} - \Phi_i) = 1/n_0$ for $i \geq 1$, and $s_0^2 = \langle \Delta\Phi_0^2 \rangle_{\text{pr}} = \frac{1}{K^2} \sum_{j=1}^K \langle (\Delta\Phi^{(j)})^2 \rangle_{\text{pr}} = 1/n_1$, since $\langle (\Delta\Phi^{(j)})^2 \rangle_{\text{pr}} = \frac{K}{n_1}$ for all j . The upper bound for ρ_i is obtained by using the following upper bound for any binomial distribution: $\binom{n}{k} p^k (1-p)^{n-k} \leq \exp\left[-n\left(\frac{k}{n} - p\right)^2\right]$. (For details, see Appendix E.) The resulting probabilities, after dropping the higher order terms in the asymptotic expansions, are

$$\mathcal{P}_{0,\text{re}} \approx \frac{2K}{\pi} n_1^{1/2} \exp\left[-\frac{n_1 \pi^2}{2K^2}\right], \quad (\text{F.13})$$

$$\mathcal{P}_{i,\text{re}} \approx \frac{4}{\pi} n_0^{1/2} \exp\left[-\frac{n_0 \pi^2}{8}\right] \quad (i \geq 1). \quad (\text{F.14})$$

These approximate formulas are valid for $n_0 \geq 5$, as we have checked numerically.

The phase shift imposed on the estimate of Φ_{LO} by a manifested rounding error of Y_1 is $2\pi/K$ and of Z_i is $2\pi/(K2^{i-1})$, for $i = 2, 3, \dots, M$. This results in the total variance contribution,

$$\langle \Delta\Phi_{\text{LO}}^2 \rangle_{\text{re}} = \left(\frac{2\pi}{K}\right)^2 \left[\mathcal{P}_{0,\text{re}} + \sum_{i=2}^M \mathcal{P}_{i-1,\text{re}} (2^{-i+1})^2 \right] \approx \left(\frac{2\pi}{K}\right)^2 \left[\mathcal{P}_{0,\text{re}} + \frac{1}{3} \mathcal{P}_{i-1,\text{re}} \right]. \quad (\text{F.15})$$

We simplify this expression by choosing n_1 so that $\mathcal{P}_{0,\text{re}} \approx \frac{2}{3}\mathcal{P}_{i,\text{re}}$:

$$n_1 = \alpha K^2 n_0, \quad (\text{F.16})$$

where $\alpha \approx \max \left\{ 1, \frac{2}{\pi^2 n_0} \log \left(3K^2 \frac{\sqrt{8}}{\pi n_0^{1/2}} \right) \right\} \ll n_0, K$. With this choice, we can write the rounding error contribution as

$$\langle \Delta\Phi_{\text{LO}}^2 \rangle_{\text{re}} \approx \frac{16\pi}{K^2} n_0^{1/2} \exp \left[-\frac{n_0\pi^2}{8} \right]. \quad (\text{F.17})$$

We note that the amount of extra resources needed for the 0th level is marginally small, since the total qubit number can be expressed as

$$N = n_1 + n_0 K \sum_{i=1}^M 2^{i-1} = n_0 K (\alpha K + 2^M - 2) \approx n_0 K 2^M, \quad (\text{F.18})$$

under the assumption $K \ll 2^M$.

By adding the two error contributions from Eq. F.11 and Eq. F.17, we obtain the corresponding Allan-variance in the stationary noise approximation,

$$\sigma_y^2(\tau) = \frac{1}{\omega_0^2 \tau T} \langle \Delta\Phi_{\text{LO}}^2 \rangle =: \frac{1}{\omega_0^2 \tau} [\Gamma_1 + \Gamma_2] = \quad (\text{F.19})$$

$$= \frac{1}{\omega_0^2 \tau} \left[\frac{4n_0}{N^2 T} + \frac{16\pi}{K^2 T} n_0^{1/2} \exp \left[-\frac{n_0\pi^2}{8} \right] \right] \quad (\text{F.20})$$

Now, let us find the optimal value of n_0 . We write $\Gamma_1 + \Gamma_2$, using the new variable

$$x = \frac{8}{\pi^2} \frac{1}{n_0}, \text{ as}$$

$$\Gamma_1 + \Gamma_2 = \frac{4}{T} \left(\frac{8}{\pi^2 x N^2} + \frac{\sqrt{32}}{K^2} \frac{1}{x^{1/2}} \exp \left[-\frac{1}{x} \right] \right). \quad (\text{F.21})$$

Taking the derivative with respect to x and equating it with 0, while using the assumption $x \ll 1$ results in $\Gamma_2 \approx x_{\text{opt}} \Gamma_1 \ll \Gamma_1$, which can be written as the following transcendental equation for the optimal value, x_{opt} ,

$$x_{\text{opt}}^{1/2} \approx \frac{\pi^2 N^2}{\sqrt{8} K^2} \exp \left[-\frac{1}{x_{\text{opt}}} \right]. \quad (\text{F.22})$$

The general solution of any equation of the form $x^\nu = A \exp[-1/x]$, in the limit of $A \gg 1$ and $x \ll 1$, is $x = [\log(A)]^{-1}$. (For details, see Appendix E.) Using this result we can write

$$x_{\text{opt}} \approx \left[\log \left(\frac{\pi^2 N^2}{\sqrt{8} K^2} \right) \right]^{-1} \sim [2 \log(N/K)]^{-1} \quad (\text{F.23})$$

$$n_{0,\text{opt}} \approx \frac{8}{\pi^2} \frac{1}{x_{\text{opt}}} \sim \left(\frac{4}{\pi} \right)^2 \log(N/K). \quad (\text{F.24})$$

For the realistic case of $N/K \gg 1$, indeed $x_{\text{opt}} \ll 1$, and the corresponding minimal value of $\Gamma_1 + \Gamma_2$ is

$$[\Gamma_1 + \Gamma_2]_{\min} \approx \Gamma_1(x_{\text{opt}}) = \left(\frac{8}{\pi} \right)^2 \frac{\log(N/K)}{N^2 T}. \quad (\text{F.25})$$

This result indicates that, in terms of qubit number, only a logarithmic extra cost is required to achieve the Heisenberg limit.

F.1.4 Phase slip errors

Although the cascade is designed to detect phase slips of all levels $i = 1, 2 \dots M$, a possible phase wrap of level $i = 0$ remains undetected. Since the qubits at different clocks are interrogated independently on the 0th level, each of them estimates the phase of the corresponding LO, $\Phi_0^{(j)}$ ($j = 1, 2, \dots K$), and not Φ_{LO} , the phase accumulated by the local oscillator. The probability of $\Phi_0^{(j)}$ falling outside the interval $[-\pi, \pi]$ at least once during the total measurement time τ is

$$\begin{aligned} \mathcal{P}_{j,\text{slip}} &= 2 \frac{\tau}{T} \int_{-\pi}^{\pi} d\phi \frac{1}{\sqrt{2\pi\gamma_{\text{LO}}T}} \exp \left[-\frac{\phi^2}{2\gamma_{\text{LO}}T} \right] \approx \\ &\approx \frac{\tau}{T} \frac{\sqrt{2}}{\pi^{3/2}} \sqrt{\gamma_{\text{LO}}T} \exp \left[-\frac{\pi^2}{2\gamma_{\text{LO}}T} \right], \end{aligned} \quad (\text{F.26})$$

where γ_{LO} is the linewidth of the local oscillator at clock j , corresponding to a white noise spectrum, resulting in a constant phase diffusion over the interrogation time T , (which is assumed to be approximately equal to the cycle time). The approximate form above is obtained by neglecting the higher order terms in the asymptotic series expansion under the assumption $\gamma_{\text{LO}}T \ll 1$. (The white noise assumption can be relaxed to include more realistic LO noise spectra. However, numerical simulations have shown that, for a LO subject to a feedback loop, the low frequency noise is essentially white even though the LO may have more complicated noise spectrum, such as 1/f noise. Therefore the results derived for white noise applies up to a constant prefactor. [27] We proceed with the white noise assumption for simplicity.) Once such a phase slip happens, it introduces a 2π phase shift in $\Phi_0^{(j)}$, and therefore contributes to its overall uncertainty with $\langle (\Delta\Phi_0^{(j)})^2 \rangle = (2\pi)^2 \mathcal{P}_{j,\text{slip}}$. Physically Φ_0 is the phase of the COM signal, that the center can obtain after averaging the frequencies of all K local oscillators with equal weights, $\Phi_0 = \Phi_{\text{COM}} = \sum_{j=1}^K \Phi_0^{(j)}/K$, therefore $\langle \Delta\Phi_0^2 \rangle = \frac{1}{K^2} \sum_{j=1}^K \langle (\Delta\Phi_0^{(j)})^2 \rangle = \frac{1}{K} \langle (\Delta\Phi_0^{(j)})^2 \rangle$, where we assumed that the LOs are independent but they have the same linewidth, γ_{LO} . Therefore the noise of the COM phase is reduced compared to the individual LOs. Since $\Phi_0 = \Phi_{\text{LO}}$, the above results in the following variance contribution

$$\langle \Delta\Phi_{\text{LO}}^2 \rangle_{\text{slip}} = \sqrt{32\pi} \frac{\tau \gamma_{\text{LO}}^{1/2}}{T^{1/2} K} \exp \left[-\frac{\pi^2}{2\gamma_{\text{LO}} T} \right]. \quad (\text{F.27})$$

After adding this error to the previously minimized projection and rounding error terms (from Eq. F.25), we obtain the corresponding Allan-variance, $\sigma_y^2(\tau) =$

$\frac{1}{\omega_0^2 \tau} ([\Gamma_1 + \Gamma_2]_{\min} + \Gamma_3)$, where

$$[\Gamma_1 + \Gamma_2]_{\min} + \Gamma_3 = \left(\frac{8}{\pi} \right)^2 \frac{\log(N/K)}{N^2} \frac{2\gamma_{\text{LO}}}{\pi^2} \frac{1}{y} + \frac{16}{\pi^{5/2}} \frac{\tau\gamma_{\text{LO}}^2}{K} \frac{1}{y^{3/2}} \exp \left[-\frac{1}{y} \right], \quad (\text{F.28})$$

using the variable $y = \frac{2}{\pi^2} \gamma_{\text{LO}} T$.

Now, let us find the optimal Ramsey time T_{opt} , under the assumption that τ is sufficiently long. After taking the derivative with respect to y and equating it with zero, the assumption $y_{\text{opt}} \ll 1$ results in the $\Gamma_3 \approx y_{\text{opt}} [\Gamma_1 + \Gamma_2]_{\min} \ll [\Gamma_1 + \Gamma_2]_{\min}$ which can be written as the following transcendental equation,

$$y_{\text{opt}}^{3/2} \approx \frac{\pi^{3/2}}{8} \frac{\tau\gamma_{\text{LO}}}{K} \frac{N^2}{\log(N/K)} \exp \left[-\frac{1}{y} \right]. \quad (\text{F.29})$$

The asymptotic solution in case of $y_{\text{opt}} \ll 1$ is (see Appendix E)

$$y_{\text{opt}} \approx \left[\log \left(\frac{\pi^{3/2}}{8} \frac{\tau\gamma_{\text{LO}}}{K} \frac{N^2}{\log(N/K)} \right) \right]^{-1}, \quad (\text{F.30})$$

$$T_{\text{opt}} \approx \frac{\pi^2}{2} \frac{y_{\text{opt}}}{\gamma_{\text{LO}}} \sim \frac{\pi^2}{2\gamma_{\text{LO}}} [\log(\tau\gamma_{\text{LO}} N^2/K)]^{-1} \quad (\text{F.31})$$

in the realistic limit of $\gamma_{\text{LO}}\tau N^2/K \gg 1$. The corresponding minimal Allan-variance is

$$\sigma_y^2(\tau) = \frac{1}{\omega_0^2 \tau} \left[[\Gamma_1 + \Gamma_2]_{\min} + \Gamma_3 \right]_{\min} \approx \frac{1}{\omega_0^2} \frac{L\gamma_{\text{LO}}}{N^2 \tau}, \quad (\text{F.32})$$

where $L = \frac{128}{\pi^4} \log(N/K) \log(\tau\gamma_{\text{LO}} N^2/K)$.

For short τ averaging times, the optimal Ramsey time is $T_{\text{opt}} = \tau$, instead of Eq. F.31. This makes Γ_3 negligible compared to $[\Gamma_1 + \Gamma_2]_{\min}$, resulting in a $1/\tau^2$ scaling:

$$\sigma_y^2(\tau) = \frac{1}{\omega_0^2 \tau} [\Gamma_1 + \Gamma_2]_{\min}^{T=\tau} = \frac{1}{\omega_0^2} \frac{L'}{N^2 \tau^2}. \quad (\text{F.33})$$

where $L' = \left(\frac{8}{\pi} \right)^2 \log(N/K)$. This scaling is more favorable, but it applies to higher τ values up to $\tau \sim \gamma_{\text{LO}}^{-1}$, where it switches to the $1/\tau$ behavior according to Eq. F.32.

F.1.5 Pre-narrowing the linewidth

We can minimize the limiting effect of γ_{LO} by narrowing the effective linewidth of the local oscillators beforehand. We imagine using N^* qubits to locally pre-narrow the linewidth of all LOs down to an effective linewidth $\gamma_{\text{eff}} \sim \gamma_{\text{ind}}N$, before using the remaining $N - N^*$ qubits in the GHZ cascade. This $\gamma_{\text{eff}} \ll \gamma_{\text{LO}}$ allows the optimal Ramsey time going above the previous limit, set by $\sim \gamma_{\text{LO}}^{-1}$ in Eq. F.31. This step-by-step linewidth narrowing procedure, using uncorrelated ensembles in every step, is introduced in [183, 27], and further analyzed in [116]. Working under the small N^* assumption, one can obtain γ_{eff} as

$$\gamma_{\text{eff}} \approx \gamma_{\text{LO}} \left[\frac{2}{\pi^2} \frac{\log(\gamma_{\text{LO}}\tau n)}{n} \right]^{N^*/n}, \quad (\text{F.34})$$

where we imagine using n qubits in each narrowing step. We find the optimal value of n to be

$$n_{\text{opt}} \approx \frac{2e}{\pi^2} \log(\gamma_{\text{LO}}\tau), \quad (\text{F.35})$$

by minimizing γ_{eff} , which yields

$$[\gamma_{\text{eff}}]_{\min} \sim \gamma_{\text{LO}} \exp \left[-\frac{N^* \pi^2}{2e \log(\gamma_{\text{LO}}\tau)} \right]. \quad (\text{F.36})$$

For a given τ , we can always imagine carrying out this pre-narrowing, so that $\gamma_{\text{eff}} < \tau^{-1}$, and therefore Eq. F.33 remains valid with the substitution $N \mapsto N - N^*$ for $\tau > \gamma_{\text{LO}}^{-1}$ as well. The required number of qubits, N^* , is

$$N^* \sim \frac{2e}{\pi^2} \log(\gamma_{\text{LO}}\tau) \log \left(\frac{\gamma_{\text{LO}}}{\gamma_{\text{ind}}N} \right) \ll N. \quad (\text{F.37})$$

due to the exponential dependence in Eq. F.36.

F.1.6 Individual qubit dephasing noise

Our scheme, as well as any scheme, is eventually limited by individual qubit noise. Such a noise dephases GHZ states at an increased rate, compared to uncorrelated qubits, due to the entanglement, giving the corresponding variance contribution for the phase of the GHZ states in the M th group, $\langle \Delta\Phi_M^2 \rangle_{\text{dephasing}} = \frac{2^{M-1}K\gamma_{\text{ind}}T}{n_0}$, after averaging over the n_0 independent copies of the GHZ states, each containing $2^{M-1}K$ entangled qubits. The resulting variance contribution for Φ_{LO} is

$$\langle \Delta\Phi_{\text{LO}}^2 \rangle_{\text{dephasing}} = \frac{\gamma_{\text{ind}}T}{n_0 2^{M-1}K} = \frac{2\gamma_{\text{ind}}T}{N}. \quad (\text{F.38})$$

This term represents a noise floor, which we add to Eq. F.33 and obtain our final result for the minimal achievable Allan-variance,

$$\sigma_y^2(\tau) = \frac{1}{\omega_0^2} \left[\frac{L'}{N^2\tau^2} + \frac{2\gamma_{\text{ind}}}{N\tau} \right]. \quad (\text{F.39})$$

For long τ times, the ultimate limit, set by the standard quantum limit, $\sigma_y^2(\tau) = \frac{1}{\omega_0^2} \frac{\gamma_{\text{ind}}}{N\tau}$, can be reached by changing the base of the cascade. Instead of entangling 2-times as many qubits in each level of the cascade than in the previous level, we imagine changing it to a base number D . Carrying out the same calculation results in our final result for the achievable Allan-variance:

$$\sigma_y^2(\tau) = \frac{1}{\omega_0^2} \left[\left(\frac{D}{2} \right)^2 \frac{L'}{N^2\tau^2} + \frac{D}{D-1} \frac{\gamma_{\text{ind}}}{N\tau} \right], \quad (\text{F.40})$$

where $L' = \left(\frac{8}{\pi}\right)^2 \log(N/K)$. (See Appendix E for details.) The optimal value of D depends on τ . For small τ , $D_{\text{opt}} = 2$, however for large τ one can gain a factor of 2 by choosing $D_{\text{opt}} = D_{\text{max}}$. Due to natural constraints, $D_{\text{max}} \sim \sqrt{N}$, in which regime, the protocol consists of only two cascade levels, an uncorrelated 0th level, with $\sim \sqrt{N}$ qubits and an entangled 1st level with $\sim N$ qubits.

F.2 Security countermeasures

F.2.1 Sabotage

In order to detect sabotage, the center can occasionally perform assessment tests of the different nodes by teleporting an uncorrelated qubit state $[|0\rangle + e^{i\chi}|1\rangle]/\sqrt{2}$, where χ is a randomly chosen phase known only to the center. A properly operating node creates a local GHZ state $[|0\rangle + e^{i\chi}|1\rangle]/\sqrt{2}$ from the sent qubit, measures the parity of the GHZ state, and sends it to the center. The measured parity holds information on the phase $\phi' = \chi + \phi$, where ϕ is the accumulated phase of the LO at the node. Due to the random shift χ , this appears to be random to the node, and therefore indistinguishable from the result of a regular (non-testing) cycle. On the other hand, the center can subtract χ , and recover ϕ from the same measurement results. In the last step, the center verifies ϕ by comparing it with the classically determined phase ϕ_{cl} of the sent LO signal with respect to the COM signal. The expected statistical deviation of ϕ from ϕ_{cl} is $\Delta(\phi - \phi_{\text{cl}}) \sim \sqrt{\frac{K}{N}}$, while the accuracy of the COM phase $\Delta(\phi_{\text{COM}} - T\omega_0) \sim \sqrt{\frac{K}{(K-K_t)N}}$ is much smaller, where K_t is the number of simultaneously tested nodes. In the likely case of $K_t \ll K$, this method is precise enough for the center to discriminate between healthy and unhealthy nodes by setting an acceptance range, $|\phi - \phi_{\text{cl}}| \leq \Lambda \sqrt{\frac{K}{N}}$. E.g. the choice of $\Lambda = 4$ results in a “ 4σ confidence level”, meaning only 0.0063% chance for false positives (healthy node detected as unhealthy), and similarly small chance for false negatives (unhealthy node being undetected) ($\sim \Lambda \frac{\Delta\phi'}{2\pi} \propto 1/\sqrt{N}$) due to the high precision with which ϕ' is measured. The fact, that the teleported qubit can be measured only once, also

prevents the nodes from discovering that it is being tested. In fact the center performs a very simple blind quantum computing task using the resources of the other clocks, see [50, 34, 140].

F.2.2 Eavesdropping

Provided that the threat of sabotage is effectively eliminated, we turn our attention to the problem of eavesdropping. Eavesdroppers would try to intercept the sent LO signals, and synthesize the stabilized ν_{COM} for themselves. Our protocol minimizes the attainable information of this strategy by prescribing that only the *non-stabilized* LO signals are sent through classical channels. This requires the feedback to be applied to the LO signal after some of it has been split off by a beam splitter, and the center to integrate the generated feedback in time. Alternatively, eavesdroppers could try intercepting the LO signals *and* the feedback signals, and gain access to the same information, the center has. This can be prevented by encoding the radio frequency feedback signal with phase modulation according to a shared secret key. Since such a key can be shared securely with quantum key distribution, this protocol keeps the feedback signal hidden from outsiders. As a result, even the hardest-working eavesdropper, who intercepts all LO signals, is able to access only the non-stabilized COM signal, and the stabilized COM signal remains accessible exclusively to parties involved in the collaboration.

F.2.3 Rotating center role

Since the center works as a hub for all information, ensuring its security has the highest priority. In a scenario, where a small number of nodes (without knowing which) cannot be trusted enough to play the permanent role of the center, a rotating stage scheme can be used. By passing the role of the center around, the potential vulnerability of the network due to one untrustworthy site is substantially lowered. This requires a fully connected network and a global scheme for assigning the role of the center.

F.3 Network operation

F.3.1 Different degree of feedback

Apart from the full feedback, described in the main text, alternatively, the center can be operated to provide restricted feedback information to the nodes. If the center sends the averaged error signal $\tilde{\delta}_{\text{COM}}$ only, the LOs at the nodes will not benefit from the enhanced stability and only the center can access the stabilized signal. Of course the LO at each node will have its own local feedback to keep it within a reasonable frequency range around the clock transition. Such a 'safe' operational mode allows the center node to use the resources of other nodes, while keeping the world time signal hidden from them. Such an asymmetric deal can be incentivized by monetary compensation, and allow the inclusion of nodes that cannot be trusted to keep the time signal secret.

As an intermediate possibility, the center can choose to send regionally averaged

feedback signals $\tilde{\delta}_{\text{COM}} + \sum_{j \in R} (\nu_j - \nu_{\text{COM}})/|R|$, uniformly for all $j \in R$ nodes, where R is a set of nodes, ie. a region. Such a feedback scheme creates the incentive of cooperation for the nodes in region R . By properly sharing their LO signals with each other, the nodes can synthesize the regional COM frequency, $\sum_{j \in R} (\nu_j)/|R|$, and steer it with the feedback, received from the center.

F.3.2 Timing

Proper timing of local qubit operations is necessary to ensure that every qubit in the network is subject to the same T free evolution time. The finite propagation time of light signals introduces delays in the quantum links and classical channels. Similarly, during the entangling step, the finite time required to do local entangling operations make the free evolution start at slightly different times for different qubits. Since both the initialization and the measurement are local operations, we can resolve the issue of delay by prescribing that the measurement of qubit i_j (i th qubit at node j) takes place exactly T time after its initialization. Occasional waiting times of known length can be echoed out with a π -pulse at half time.

In extreme cases, this might cause some qubits to be measured before others are initialized. However, this is not a problem, since the portion of the GHZ state that is alive during the time in question is constantly accumulating the ϕ_j phases from the qubits it consists of. This results in the phenomenon that the total time of phase accumulation can be much longer than the length of individual phase accumulations, provided that the said interrogations overlap.

F.3.3 Dick effect

Classical communication between the clocks, separated by large geographical distances, takes considerable time compared to the interrogation time. The requirement to communicate the outcome of the Bell measurement in each teleportation step results in a waiting time in the teleportation protocol. During this waiting time (or dark time) the qubits are not interrogated, and therefore the local oscillator runs uncontrollably. If not countered, this effect (Dick effect) will deteriorate the overall stability of the clock network. Essentially the problem arises from the duty cycle of the clock being less than 100 percent. By employing two parallel realizations of the network scheme (supported by the same clock stations, but using different qubits) whose cycles are offset by half a period in time, we can cover the entire cycle time with at least one copy of the clock network being interrogated at all times. As a result, we can cancel the Dick effect with only a constant factor (~ 2) increase in the required resources, if the required time to prepare and measure the state is not longer than the free evolution.

F.3.4 More general architectures

So far, we focused on the simplest network structure with one center initiating every Ramsey cycle and nodes with equal number of clock qubits.

In a more general setup, node j has N_j clock qubits. If N_j is different for different j , then the nodes will contribute the global GHZ states unequally, resulting in entangled states which consists of different N'_j number of qubits from each site j . Such a state

picks up the phase

$$\Phi = \sum_j N'_j \phi_j, \quad (\text{F.41})$$

where ϕ_j is the phase of the LO at site j relative to the atomic frequency. As a result, the clock network measures the following collective LO frequency

$$\nu_{\text{LO}} = \frac{\sum_j N'_j \nu_j}{\sum_j N'_j}. \quad (\text{F.42})$$

This represents only a different definition of the world time (a weighted average of the times at the locations of the nodes, instead of a uniform average), but it does not affect the overall stability.

The initial laser linewidths of the nodes γ_{LO}^j can also be different. The stability achievable in this case is bounded by the stability obtained for a uniform linewidth $\gamma_{\text{LO}} = \max_j \gamma_{\text{LO}}^j$. If linewidths are known, the center can devise the best estimation method which uses linewidth dependent weights in the LO frequency averaging step.

Although it is simple to demonstrate the important network operational concepts with the architecture with one center, this structure is not a necessary. The quantum channels, connecting different nodes, can form a sparse (but still connected) graph, and the entanglement global entanglement can still be achieved by intermediate nodes acting as repeater stations. This way entanglement can be passed along by these intermediate nodes. Moreover, the center can be eliminated from the entangling procedure by making the nodes generate local GHZ states, and connect them with their neighbors by both measuring their shared EPR qubit with one of the qubits form the local GHZ state in the Bell-basis. After communicating the measurement result via classical channels, and performing the required single qubit operations, a global GHZ state is formed.

F.3.5 Accuracy

We define the accuracy of a time signal as the total uncertainty of its frequency with respect to the fundamental time reference. This includes the precision (characterized by the Allan deviation) and the uncertainty of frequency shifts due to systematic effects. So far we analyzed only the precision.

If two clocks have different levels of uncertainty for the local systematic shifts, then their individual accuracy is different. Our scheme requires the clocks to work together coherently, and thereby it averages out these differences in accuracy sub-optimally. In order to determine the individual accuracies, the clock network has to disentangle one of the clocks from the others. Next, by comparing the time signal from the entangled network with the one from the excluded clock, it can determine if the said clock has higher or lower accuracy than the average. By rotating this scheme, the systematic shifts of the worse clock can be measured more precisely, and, on the long run, this results in an overall improvement of the accuracy.

Apart from the local systematic effects (such as blackbody shift, second order Zeeman shift, etc.), a quantum network of clocks is subject to gravitational redshifts, which affect clocks at different positions differently. In order to ensure precise measurement of this systematic shift, the position of the clocks has to be tracked with high precision. This can be done similarly to the way ground stations track GPS satellites. The time signal generated by the quantum clock network can be used to set up a more precise tracking system, which can measure this systematics at a higher accuracy.

F.3.6 Efficient use of qubits

In the main text, during the generation of the initial global GHZ state, we assumed that the center makes use of $2(K - 1)$ additional ancilla qubits (a_j, b_j) . We chose this to present the idea at its simplest, however the qubits used as ancillae do not have to be sitting uselessly during the interrogation time. The center can use $2(K - 1)$ out of its N/K clock qubits to perform the local generation and teleportation steps. This relabeling goes as follows $\{(b_j = j_1, a_j = (K - 1 + j)_1) : j = 2 \dots K\}$. After it is done, the qubits used as ancillae can be reinitialized, the center can entangle the $2(K - 1)$ qubits (alongside with the others) with 1_1 , and interrogate them without any obstacles. As a result, no clock qubits are wasted in the protocol.

F.3.7 Required EPR generation rate

In the main text, we mainly ignored the time required to generate pairwise entanglement. In this section we investigate the required EPR generation rate to achieve the desired performance. Before every cycle of operation $n[\log(N/K)/\log(2) + 1](K - 1)$ EPR pairs have to be shared between the center and the other clocks, where n is the number of parallel copies, N is the total number of qubits in a single copy and K is the number of clocks. Since $n_{\text{opt}} \sim (4/\pi)^2 \log(N/K)$, and approximately K quantum channels are used, the number of EPR pair per channel is about $(\log(N))^2$. We can assume that entangled qubits can be stored in degenerate memory states until they are used in the beginning of the next cycle. Therefore each channel has T time to initialize the $(\log(N))^2$ number of pairs. The optimal value for T is the available averaging time τ , which we choose to be $\sim 0.1\gamma_i^{-1}$ for order of magnitude estimation.

(Note that $\tau < \gamma_i^{-1}$ is required to benefit from quantum enhancement.) For $N = 10^4$ atoms and $\gamma_i = 2\pi \times 1$ mHz, the EPR generation rate per channel has to be at least $(\log(N))^2 \gamma_i \sim 1$ Hz. Such a rate is within reach of technology currently under intensive research [109].

F.3.8 Threshold fidelity

In this section we estimate the fidelity of the collective entangling operations required to keep the benefit from quantum enhancement. In the GHZ state generation step of every cycle, the n copies of the cascaded network containing K clocks are initialized. This requires K collective entangling operations to be performed per level per copy, one at each clock. Among other unitary operations, this is likely to be the bottleneck. If one collective entangling operation (creating a GHZ state of $N/(Kn)$ qubits) can be performed with fidelity $F = \exp[-\epsilon]$ ($\epsilon \ll 1$), then K repetitions succeed with fidelity $F_{\text{total}} = F^K = \exp[-K\epsilon]$.

Whenever a copy fails on level i , its measurement result ϕ_i becomes completely random. This happens with probability $(1 - F_{\text{total}})$. In the meantime, with probability F_{total} , the result is consistent with $\phi_i = \phi_{\text{real}}$, where ϕ_{real} is the actual value of ϕ_i . Out of the n copies nF_{total} contributes to a peak centered at ϕ_{real} , with width of $1/\sqrt{F_{\text{total}}n}$ and weight F_{total} , while the rest contributes to a uniform distribution with weight $(1 - F_{\text{total}})$: The expectation value of ϕ_i is still

$$\langle \phi_i \rangle = \phi_{\text{real}}, \quad (\text{F.43})$$

but the variance is

$$\text{Var}(\phi_i) \approx \frac{1}{n} + \frac{\pi^2}{3}(1 - F_{\text{total}}). \quad (\text{F.44})$$

The threshold fidelity F_{th} is defined by the criteria that if $F \geq F_{\text{th}}$, then $\text{Var}(\phi_i) \approx 1/n$. If this is satisfied, then losing the information from some of the copies does not deteriorate the precision significantly with which ϕ_i can be determined.

This requires $1 - F_{\text{total}} < \frac{3}{\pi^2 n}$, where the optimal value for n is $n_{\text{opt}} \sim \left(\frac{4}{\pi}\right)^2 \log(N/K)$, while $F_{\text{total}} = \exp[-\epsilon K]$ from above. From these, we conclude that $F_{\text{th}} = \exp[-\epsilon_{\text{th}}]$, where

$$\epsilon_{\text{th}} \approx \frac{3}{16K \log(N/K)} \sim \frac{1}{K \log(N)}. \quad (\text{F.45})$$

Using $N = 10^4$ qubits, distributed in 10 clocks therefore requires $F_{\text{th}} \approx 0.99$ fidelity level for the local entangling operation. Using a multi-qubit entangling gate [207], this operation can be realized with current technology for fidelity ~ 0.95 and for small number of ions (~ 5). [153] The errors in such operations increases with N , making their realization more challenging. Namely, a 2-ion GHZ state was produced with 0.993 fidelity in a trapped ion system [16]. Currently the largest GHZ state of 14 ions was produced with 0.51 fidelity [153].

Appendix G

Appendices for Chapter 8

G.1 Local entangling errors

The initial GHZ state is never perfect due to a series of imperfections in the implementation. Here, we analyze the main errors responsible for lowering the initial fidelity $F_{\text{local}} = [1 + \exp(-\varepsilon_{\text{local}})]/2$ of the GHZ state of n atoms, created via the conditional dressing scheme, described in the main article. We assume the following errors to be independent and small, and we approximate $\varepsilon_{\text{local}}$ with the sum of the individual errors, $\sum_j \varepsilon_j$. We evaluate the errors for a 2D square lattice filled in a circular region and a 3D cubic lattice filled in a spherical region (both of radius R). Where there is a difference between the two cases, we give both results.

G.1.1 Imperfect blockade

If the blockade between the levels r_1 and r_2 , Δ_{12} , is not large enough, the dressing happens even if r_2 is populated by a single atom. Here, we analyze the effect of this

imperfection.

The relevant part of the full Hamiltonian of the system during dressing is

$$H = \frac{\Omega}{2} \sum_k (|r_1\rangle_k \langle g|_k + \text{h.c.}) + \Delta \sum_k |r_1\rangle_k \langle r_1|_k \quad (\text{G.1})$$

$$+ \sum_k \sum_{j \neq k} \Delta_{j,k} |r_1\rangle_k \langle r_1|_k |r_2\rangle_j \langle r_2|_j, \quad (\text{G.2})$$

where Ω and Δ are the Rabi frequency and the detuning of the dressing field, and $\Delta_{j,k} = C_{12}^{(3)} / (\hbar |\mathbf{r}_j - \mathbf{r}_k|^3)$ is the shift due to dipole-dipole interaction. After adiabatically eliminating the level r_1 , we can write the effective Hamiltonian as

$H_{\text{eff}} = \sum_k H_k |g\rangle_k \langle g|_k$, where

$$H_k = -\frac{\Omega^2}{4\Delta} + \sum_{j \neq k} \left(\frac{\Omega^2}{4\Delta} - \frac{\Omega^2}{4(\Delta + \Delta_{j,k})} \right) |r_2\rangle_j \langle r_2|_j, \quad (\text{G.3})$$

where we also restricted the Hilbert space to at most one r_2 excitation.

Ideally, starting from

$$\left(|1_s\rangle + |1_{r2}\rangle \right) \left(|g\rangle + |f\rangle \right)^{\otimes(n-1)}, \quad (\text{G.4})$$

(where $|1_x\rangle = \sum_j |x\rangle_j / \sqrt{n}$ for $x = s, r_2$), after time $t = 4\pi\Delta/\Omega^2$, the part of the wavefunction with no r_2 excitaion picks up a π phase,

$$|1_s\rangle \left(e^{-i\pi} |g\rangle + |f\rangle \right)^{\otimes(n-1)}, \quad (\text{G.5})$$

while the part where r_2 is present is unchanged, or picks up a small and uniform phase ϕ_0 ,

$$|1_{r2}\rangle \left(e^{i\phi_0} |g\rangle + |f\rangle \right)^{\otimes(n-1)}. \quad (\text{G.6})$$

In reality, however, dephasing between the different terms of the superposition occurs. If the system starts from

$$|\Psi_0\rangle = \frac{1}{\sqrt{n}} \sum_j |r_2\rangle_j \bigotimes_{k \neq j} \left(\frac{|g\rangle_k + |f\rangle_k}{\sqrt{2}} \right), \quad (\text{G.7})$$

the effective Hamiltonian evolves it into

$$|\Psi_t\rangle = \frac{1}{\sqrt{n}} \sum_j |r_2\rangle_j \bigotimes_{k \neq j} \left(\frac{e^{i\phi_{j,k}}|g\rangle_k + |f\rangle_k}{\sqrt{2}} \right), \quad (\text{G.8})$$

up to an overall phase, where $\phi_{j,k} = \pi\Delta/(\Delta + \Delta_{j,k})$, while the target state is

$$|\Psi_{\text{target}}\rangle = \frac{1}{\sqrt{n}} \sum_j |r_2\rangle_j \bigotimes_{k \neq j} \left(\frac{e^{i\phi_0}|g\rangle_k + |f\rangle_k}{\sqrt{2}} \right), \quad (\text{G.9})$$

with an appropriately chosen ϕ_0 . The fidelity of Ψ_t with respect to Ψ_{target} is

$$F = |\langle \Psi_{\text{target}} | \Psi_t \rangle|^2 = \left| \frac{1}{n} \sum_j \prod_{k \neq j} \frac{1 + e^{i(\phi_{j,k} - \phi_0)}}{2} \right|^2. \quad (\text{G.10})$$

Assuming $|\phi_{j,k} - \phi_0| \ll 1$, and using

$$\frac{1 + e^{ix}}{2} \approx \exp \left[-\frac{x^2}{4} + i\frac{x}{2} \right], \quad \text{for } x \ll 1 \quad (\text{G.11})$$

we can write

$$F = \left| \frac{1}{n} \sum_j \left(e^{i \sum_k \frac{\phi_{j,k} - \phi_0}{2}} \times e^{-\sum_k \frac{(\phi_{j,k} - \phi_0)^2}{8}} \right) \right|^2. \quad (\text{G.12})$$

We approximate

$$\sum_k (\phi_{j,k} - \phi_0)^2 \approx n \text{Var}(\phi_{j,k}), \quad (\text{G.13})$$

where the variance is taken over all pairs of (j, k) , and we take it out of the summation to get

$$F \approx \left| \frac{1}{n} \sum_j e^{i \sum_k \frac{\phi_{j,k} - \phi_0}{2}} \right|^2 e^{-\frac{n}{4} \text{Var}(\phi_{j,k})}. \quad (\text{G.14})$$

Using the notation, $\psi_j := \sum_{k \neq j} \phi_{j,k}$, we can write and approximate the first term as

$$\left| \frac{1}{n} \sum_j e^{i\psi_j/2} \right|^2 \approx e^{-\frac{1}{4} \text{Var}(\psi_j)}, \quad (\text{G.15})$$

where the variance is taken over all j , and we write the total fidelity as

$$F \approx \exp \left[-\frac{1}{4} \text{Var}(\psi_j) - \frac{n}{4} \text{Var}(\phi_{j,k}) \right] =: e^{-\varepsilon_1}. \quad (\text{G.16})$$

In section G.7 and section G.8, we evaluate the above variances for a circular 2D and spherical 3D cloud of radius R , and average density of a^{-2} and a^{-3} , respectively. Plugging in the results of Eq. G.92, (G.93) yields

$$\begin{aligned}\varepsilon_1 &= \frac{1}{4} [\text{Var}(\psi_j) + n\text{Var}(\phi_{j,k})] \\ &= \left(\frac{\hbar a^3 \Delta}{C_{12}^{(3)}} \right)^2 \times \begin{cases} 0.0209 n^5 + 0.156 n^4 & \text{(2D)} \\ 0.0320 n^4 + 0.273 n^3 & \text{(3D)} \end{cases}\end{aligned}\quad (\text{G.17})$$

G.1.2 Decaying Rydberg states

During dressing, there is an average number of $n(\Omega/(2\Delta))^2$ Rydberg excitations present at level r_1 in the ensemble. Any decay or dephasing of r_1 Rydberg state then results in the loss of fidelity,

$$\varepsilon_2 \approx \gamma_1 t \times n \left(\frac{\Omega}{2\Delta} \right)^2 = \pi n \frac{\gamma_1}{\Delta}, \quad (\text{G.18})$$

where γ_1 is the total rate of loss (environment induced decay and dephasing) from the Rydberg level r_1 , and t is assumed to take the optimal value, $t = 4\pi\Delta/\Omega^2$.

In the same time, in the other part of the wavefunction, there is exactly one r_2 excitation. If this decays and dephases with rate γ_2 , then the fidelity error due to this is

$$\varepsilon_3 \approx \gamma_2 t = 4\pi \frac{\Delta \gamma_2}{\Omega^2}, \quad (\text{G.19})$$

where, again, we used that $t = 4\pi\Delta/\Omega^2$.

G.1.3 Rydberg interaction induced broadening

Although the Rydberg-Rydberg interaction is assumed to be strong, which makes single-to-double excitations off-resonant, the external laser field can easily drive Ra-

man transitions between different single excitations states. Let us define the following states

$$|j\rangle := \sigma_j^\dagger |gg\dots g\rangle, \quad \text{where } \sigma_j^\dagger = |r_1\rangle_j \langle g|_j, \quad (\text{G.20})$$

$$|S\rangle := \frac{1}{\sqrt{n}} \sum_j |j\rangle, \quad (\text{G.21})$$

$$|j, k\rangle := \sigma_j^\dagger \sigma_k^\dagger |gg\dots g\rangle = \sigma_j^\dagger |k\rangle = \sigma_k^\dagger |j\rangle, \quad \text{for } j < k, \quad (\text{G.22})$$

for $j, k \in \{1, 2 \dots n\}$, indexing the atoms in the ensemble.

The full Hamiltonian of the system during the dressing is $H_{\text{full}} = \sum_{j=1}^n H_j$, where

$$\begin{aligned} H_j = & \Delta \sigma_j^\dagger \sigma_j + \frac{\Omega}{2} (|r_1\rangle_j \langle g|_j + \text{h.c.}) \\ & + \sum_{k>j} \Delta_{j,k} \sigma_j^\dagger \sigma_j \sigma_k^\dagger \sigma_k. \end{aligned} \quad (\text{G.23})$$

It contains a Rydberg-Rydberg interaction term, whose strength, $\Delta_{j,k} = \Delta_{rr}(|\mathbf{r}_j - \mathbf{r}_k|)$ depends on the distance between atoms j and k . In the subspace of single and double excitations, $\text{Span}\{|j\rangle, |j, k\rangle\}$, H_j is equivalent to

$$\sum_{k>j} (\Delta + \Delta_{j,k}) |j, k\rangle \langle j, k| + \frac{\Omega}{2} \sum_{k>j} (|j\rangle \langle j, k| + \text{h.c.}), \quad (\text{G.24})$$

which is partially depicted on Fig. G.1.

If all Rydberg shifts are large compared to $\sqrt{n}\Omega$, then the double excitation probability is small, and the dynamics is well described by the following effective Hamiltonian, $H_{\text{eff}} = \sum_j H_{\text{eff},j}$, where

$$H_{\text{eff},j} = \Delta_j |j\rangle \langle j| + \sum_{k>j} \frac{\Omega_{j,k}}{2} (|j\rangle \langle k| + \text{h.c.}), \quad (\text{G.25})$$

where $\Delta_j = -\sum_{k \neq j} \frac{\Omega^2}{4(\Delta_{j,k} + \Delta)}$, and $\Omega_{j,k} = -\frac{\Omega^2}{2(\Delta_{j,k} + \Delta)}$.

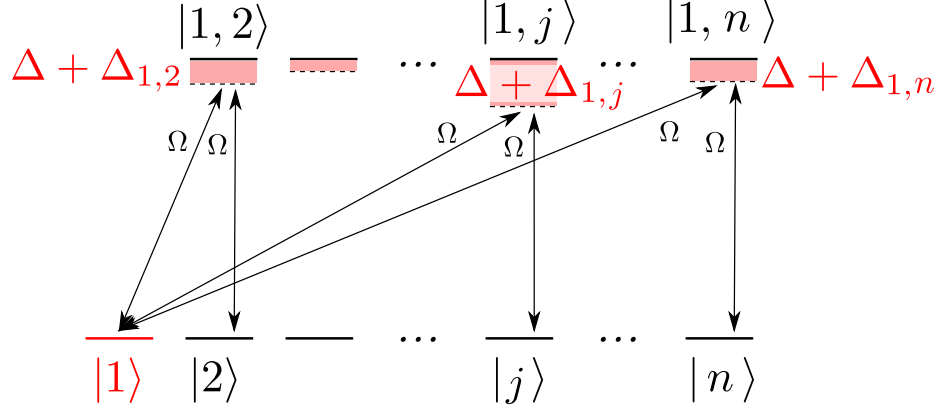


Figure G.1: Different single excitation states ($|j\rangle = \sigma_j^\dagger |gg\dots g\rangle$, $j = 1, 2, \dots, n$) are resonantly coupled to each other through a Raman-transition via double excited states ($|j, k\rangle = \sigma_j^\dagger \sigma_k^\dagger |gg\dots g\rangle$, $j < k$). The effective coupling strengths depend on the detuning of the intermediate level, and results in an inhomogeneous broadening. (The figure shows only the double excited states that couple to $|1\rangle$.)

The two terms in Eq. G.25 have different effects. The first term describes inhomogeneous broadening. Due to this effect, the fidelity of the symmetric state $|S\rangle$ decreases over time, t , as

$$|\langle S | e^{-i \sum_j \Delta_j t} | j \rangle |^2 = \left| \frac{1}{n} \sum_j e^{-i \Delta_j t} \right|^2 \approx e^{-t^2 \text{Var}(\Delta_j)}. \quad (\text{G.26})$$

Since the expected number of excitations during the dressing pulse is small, $\sim n[\Omega/(2\Delta)]^2$, we can write the error as $\varepsilon_{4a} \approx n[\Omega/(2\Delta)]^2 t^2 \text{Var}(\Delta_j)$.

The effect of the second term in Eq. G.25, couples different single-excitation states coherently. We put an upper bound of the effect of this term by analyzing it without the detuning effect of the Δ_j terms. Let us define the following states,

$$|\tilde{j}\rangle := \left(1 - \frac{1}{n}\right)^{-1/2} \left(|j\rangle - \frac{1}{\sqrt{n}} |S\rangle \right), \quad (\text{G.27})$$

for $j = 1, 2, \dots, n$. These states are all orthogonal to $|S\rangle$, normalized, and span an $n - 1$ dimensional space, therefore they are overcomplete by a factor of $n/(n - 1)$,

and they are also almost orthogonal to each other: $|\langle \tilde{j} | \tilde{k} \rangle| = \frac{1}{n} + \frac{1}{n^2} = \mathcal{O}(1/n)$. Let us imagine starting the system in $|S\rangle$, and observing the probability accumulating in all the other states $|\tilde{j}\rangle$. The time evolution of the amplitudes, \tilde{c}_j , dictated by the Heisenberg equations, can be approximated as

$$\begin{aligned} \frac{d}{dt} \tilde{c}_j(t) &= -i \langle \tilde{j} | H_{\text{eff},\Omega} | S \rangle c_s(t) + \mathcal{O}(\tilde{c}_k(t)) \\ &\approx -i \langle \tilde{j} | H_{\text{eff},\Omega} | S \rangle c_s(0), \\ \tilde{c}_j(t) &\approx -it \langle \tilde{j} | H_{\text{eff},\Omega} | S \rangle c_s(0), \end{aligned} \quad (\text{G.28})$$

where, $|c_s(0)|^2 \approx n(\Omega/(2\Delta))^2$, and $H_{\text{eff},\Omega} = \sum_{j,k>j} \Omega_{j,k} (|j\rangle\langle k| + \text{h.c.})$. The conditional probability accumulating in $|\tilde{j}\rangle$ is

$$\begin{aligned} \frac{P_j(t)}{|c_s(0)|^2} &\approx t^2 |\langle \tilde{j} | H_{\text{eff},\Omega} | S \rangle|^2 \\ &\approx t^2 \left| \sum_k \frac{1}{\sqrt{n}} \left(\frac{\Omega_{j,k}}{2} - \frac{1}{n} \sum_l \frac{\Omega_{l,k}}{2} \right) \right|^2 \\ &= t^2 \frac{1}{n} \left| \Delta_j - \frac{1}{n} \sum_l \Delta_l \right|^2, \end{aligned} \quad (\text{G.29})$$

where we used that $\sum_{k \neq j} \Omega_{j,k}/2 = \Delta_j$. The total conditional probability of leaving the symmetric state $|S\rangle$ is

$$\frac{P(t)}{|c_S(0)|^2} \approx t^2 \frac{1}{n} \sum_j \left| \Delta_j - \frac{1}{n} \sum_l \Delta_l \right|^2 = t^2 \text{Var}(\Delta_j), \quad (\text{G.30})$$

and the total error is $\varepsilon_{4b} = P(t) = n[\Omega/(2\Delta)]^2 t^2 \text{Var}(\Delta_j)$. This is identical to the error originating from the Δ_{jk} term of Eq. G.25. We approximate the effect of these two errors by adding them, giving

$$\varepsilon_{4a} + \varepsilon_{4b} = \frac{n}{2} \left(\frac{\Omega}{\Delta} \right)^2 t^2 \text{Var}(\Delta_j). \quad (\text{G.31})$$

We evaluate the variance of Δ_j in section G.9 for both the 2D and the 3D case. The result is given in Eq. G.117 and (G.118). Plugging the result in, and using that $t = 4\pi\Delta/\Omega^2$, we can write the error as

$$\varepsilon_4 \approx \varepsilon_{4a} + \varepsilon_{4b} = \begin{cases} 0.0312 n^9 \left(\frac{\hbar a^6 \Omega}{C_{11}^{(6)}} \right)^2 & \text{(2D)} \\ 0.172 n^7 \left(\frac{\hbar a^6 \Omega}{C_{11}^{(6)}} \right)^2 & \text{(3D)} \end{cases} \quad (\text{G.32})$$

where a is the lattice constant of the 2D (3D) optical lattice holding the atoms, and $C_{11}^{(6)}$ is the coefficient of the van der Waals interaction between two atoms excited to r_1 level.

G.2 Non-local entangling errors

Our protocol requires $K - 1$ links to be set up between K clocks. We denote the fidelity of a single connection by $F_{\text{non-local}} = [1 + \exp(-\varepsilon_{\text{non-local}})]/2$, and we approximate $\varepsilon_{\text{non-local}}$ with the sum of individual errors $\sum_i \varepsilon_i$, detailed below.

G.2.1 Imperfect blockade

When exciting a single collective excitations, imperfect self-blockade can result in leakage into double excited states. The probability of this can be exponentially reduced by applying a smooth driving pulse. E.g., in case of a Gaussian pulse of width τ , and area π , exciting the $g \rightarrow r_1$ transition is expected to be blocked when r_2 is populated, but it succeeds with probability P_{double} ,

$$P_{\text{double}} \approx \frac{\pi^2}{4} \exp \left[-\frac{(\Delta_{12}\tau)^2}{2} \right], \quad (\text{G.33})$$

where $\Delta_{12} = C_{12}^{(3)} / (\hbar(2R)^3)$ is the minimal energy shift in the ensemble due to the interaction of two atoms, one in r_1 and one in r_2 . A detailed analysis of how different pulses affect the transition probability can be found in [55]. $P_{\text{double}} \ll 1$ requires

$$\tau \leq \frac{\sqrt{2}}{\Delta_{12}} = \begin{cases} 2n^{3/2} \frac{\hbar a^3}{C_{12}^{(3)}} & (2D) \\ 2.7 n \frac{\hbar a^3}{C_{12}^{(3)}} & (3D) \end{cases} \quad (\text{G.34})$$

in order to be small compared to the other errors.

G.2.2 Rydberg state decay

The $g \rightarrow r_1$ transition is driven with a pulse of duration τ , during which the r_2 level has a single excitation, which decays with rate γ_2 . The resulting error contribution, after all four photon pulses have been generated, is

$$\varepsilon_5 = 4\gamma_1\tau = \begin{cases} 8n^{3/2} \frac{\hbar a^3 \gamma_1}{C_{12}^{(3)}} & (2D) \\ 10.8 n \frac{\hbar a^3 \gamma_1}{C_{12}^{(3)}} & (3D) \end{cases} \quad (\text{G.35})$$

where we used the expressions for τ from Eq. G.34.

G.2.3 Photon propagation and detection errors

The pairs of photons can get lost in the fiber during propagation and the detection process (which is limited to 50% for time-resolving detectors, and 25% for non-time-resolving ones). The two-photon heralding, however, detects both of these errors. The remaining error comes from dark-counts of the detectors. This affects a single link with the error

$$\varepsilon_6 \approx 4\gamma_{\text{dark}} T_{\text{detect}} = \gamma_{\text{dark}} \frac{20}{n\gamma_e}, \quad (\text{G.36})$$

where γ_{dark} is the dark count rate of the detectors, T_{detect} (chosen such that a properly timed detector would have a chance to catch $1 - e^{-5} > 99\%$ of each photon) is the “open time” of the detector, and γ_e is the spontaneous emission lifetime of the $|e\rangle \rightarrow |f\rangle$ transitions. The factor of n is due to the bosonic enhancement of the said transition, and the factor of 4 is because four pulses are used in each connection.

G.2.4 Memory loss

During the creation step of each link, the state $|s\rangle$ is used as memory. On average, every link relies on one s qubit. The time it takes to attempt the creation of a link is $\sim 2L/c$, the time it takes for a light pulse to do a round-trip between two stations. During this time, quantum information is stored in qubit s , which is subject decoherence happening at a rate γ_s . The infidelity of the link originating from this error is

$$\varepsilon_7 = 4 \frac{2L}{c} \gamma_s. \quad (\text{G.37})$$

State $|f\rangle$ is assumed to be a long-lived clock state, its decoherence rate is negligible.

G.2.5 Imperfect branching ratios

Bosonic enhancement makes the excited atom in state $|e\rangle$ decay preferentially to $|g\rangle$, and emit a photon directly to the spatial mode \mathbf{k}_e , where \mathbf{k}_e is the spatial frequency of the collective mode e . However, in the implementation with Yb atoms (discussed in Section G.3), the decay channel to $|g\rangle$ has a branching ratio of $\zeta = 0.64$.

The total probability of decay through all other channels is

$$\varepsilon_8 = 4 \frac{\gamma_{\text{not } f}}{\gamma_{\text{tot}}} \approx 4 \frac{1 - \zeta}{n\zeta + 1 - \zeta} \sim \frac{2}{n}, \quad (\text{G.38})$$

where n ($\gg 1$) is the number of atoms in a single ensemble.

G.3 Implementation with Yb

We imagine using the lower levels of neutral Yb for our protocol, $|g\rangle = |6s6p(^3P_0)\rangle$, $|f\rangle = |6s^2(^1S_0)\rangle$, $|s\rangle = |6s6p(^3P_2)\rangle$ and $|e\rangle = |5d6s(^3D_1)\rangle$, and two Rydberg levels $|r_1\rangle = |6s\tilde{n}s(^1S_0)\rangle$ and $|r_2\rangle = |6s\tilde{n}p_{m=+1}(^1P_1)\rangle$ with the same principle quantum number \tilde{n} for high-energy state. In the case of the 2D lattice, we set the quantization axis perpendicular to the plane in which the atoms reside, this way the dipole-dipole interaction between two atoms, one in $|r_2\rangle$ and the other in $|r_1\rangle$, depends only on their separation, $|\mathbf{r}_1 - \mathbf{r}_2|$. In the case of the 3D lattice, we rely on the overwhelming strength of the Rydberg interaction to produce reliable blockade even between atoms in different horizontal planes.

G.3.1 Rydberg lifetimes

We use the measured values from [83], and extrapolate the inverse lifetimes of the Rydberg states

$$\gamma_1 \approx \gamma_2 = \gamma = \frac{8.403 \times 10^8 \text{ Hz}}{(\tilde{n} - 4.279)^3} \quad (\text{G.39})$$

where \tilde{n} is the principle quantum number of the Rydberg orbit. Although the measurement was carried out at 300 K, the contribution of the black body radiation is negligible even at this temperature. Furthermore, the photoionization rate in a

trapping field with 10^4 W/cm² intensity is also more than one order of magnitude smaller.

G.3.2 Self-blockade, Δ_{11}

The long-range interaction between two r_1 atoms at a distance R is dominated by the van der Waals potential,

$$\Delta_{11}(R) = \frac{C_{11}^{(6)}}{\hbar R^6}, \quad (\text{G.40})$$

where $C_{11}^{(6)}$ strongly depends on the principle quantum number \tilde{n} . We use results from [222], and extrapolate the $C_{11}^{(6)}$ coefficient to high principle quantum numbers with the following formula,

$$C_{11}^{(6)} = (-0.116 + 0.0339 \tilde{n}) \tilde{n}^{11} \text{ a.u.} \quad (\text{G.41})$$

where the a.u. stands for atomic units, $E_h a_0^6 = 9.573 \times 10^{-80}$ Jm⁶, where E_h is the Hartree energy and a_0 is the Bohr radius.

G.3.3 Cross-blockade, Δ_{12}

The long-range interaction between an r_1 and an r_2 atoms at a distance R is dominated by the dipole-dipole interaction. We assume that the atoms are confined in the xy plane, and because the $6s\tilde{n}p_{m=+1}$ state is polarized in the z direction, the interaction strength is independent of the relative direction of one atom to the other.

$$\Delta_{12}(R) = \frac{C_{12}^{(3)}}{\hbar R^3}, \quad (\text{G.42})$$

where $C_{12}^{(3)}$ depends strongly on the principle quantum number \tilde{n} . We use results from [222], and extrapolate the $C_{12}^{(3)}$ coefficient to high principle quantum numbers with

the following formula,

$$C_{12}^{(3)} = (0.149 + 0.00077 \tilde{n}) \tilde{n}^4 \text{ a.u.} \quad (\text{G.43})$$

where the a.u. stands for atomic units, $E_h a_0^3 = 6.460 \times 10^{-49} \text{ Jm}^3$.

G.3.4 Decay rates of lower levels

The decay rate of $|s\rangle = |6s6p, {}^3P_2\rangle$ is $\gamma_s = [14.5 \text{ s}]^{-1} = 0.069 \text{ Hz}$. The decay rate of the excited state $|e\rangle = |5d6s, {}^3D_1\rangle$ is $\gamma_e = [380 \text{ ns}]^{-1} = 2.63 \times 10^6 \text{ Hz}$.

G.3.5 Photon channels

We assume that neighboring stations are $L < 10 \text{ km}$ apart from each other, we neglect fiber and coupling loss. We further assume that single photon detectors have a low dark count rate, i.e. $\gamma_{\text{dark}} \approx 10 \text{ Hz}$.

G.4 Optimization

The total initial imperfections of a GHZ state with N atoms divided into $K = N/n$ groups, each containing n atoms, is

$$\varepsilon_{\text{tot}} = (K - 1)\varepsilon_{\text{non-local}} + K\varepsilon_{\text{local}} \approx -\frac{N}{n} \sum_i \varepsilon_i, \quad (\text{G.44})$$

where the error contributions are from Eq. (G.17, G.18, G.19, G.32, G.35, G.36, G.37, and G.38). Independently from the total atom number, N , there is an optimal group size, n_{opt} , for which $\sum_i \varepsilon_i/n$ is minimal. If the total number of atoms is increased, it is best to create multiple groups of the same size. Below we find the optimal values of

the parameters Ω , Δ (the Rabi frequency and the detuning of the dressing scheme), and n (the size of the local groups) for fixed values of \tilde{n} (the principle quantum number of the Rydberg state) and $a = 275.75 \text{ nm}$.

Using the following dimensionless variables, $\omega = \Omega/\gamma$, $\delta = \Delta/\gamma$, $\delta_{11} = \frac{C_{11}^{(6)}}{\hbar a^6 \gamma}$ and $\delta_{12} = \frac{C_{12}^{(3)}}{\hbar a^3 \gamma}$, we can write the error per atom as $E := \sum_i \varepsilon_i/n = \sum_i e_i$, where the terms are

$$e_1 = \left(\frac{\delta}{\delta_{12}} \right)^2 \times \begin{cases} 0.021 n^4 + 0.16 n^3 & (2D) \\ 0.032 n^3 + 0.27 n^2 & (3D) \end{cases} \quad (\text{G.45})$$

$$e_2 = \frac{\pi}{\delta} \quad (\text{G.46})$$

$$e_3 = \frac{4\pi}{n} \frac{\delta}{\omega^2} \quad (\text{G.47})$$

$$e_4 = \left(\frac{\omega}{\delta_{11}} \right)^2 \times \begin{cases} 0.031 n^8 & (2D) \\ 0.17 n^6 & (3D) \end{cases} \quad (\text{G.48})$$

$$e_5 = \frac{1}{\delta_{12}} \times \begin{cases} 8n^{1/2} & (2D) \\ 10.8 & (3D) \end{cases} \quad (\text{G.49})$$

$$e_6 = 7.6 \times 10^{-5} \frac{1}{n^2} \quad (\text{G.50})$$

$$e_7 = 1.8 \times 10^{-5} \frac{1}{n} \quad (\text{G.51})$$

$$e_8 = \frac{2}{n^2} \quad (\text{G.52})$$

G.4.1 Optimal parameters

We numerically minimized the sum, $E = \sum_i e_i$, by finding the optimal values of ω, δ and n for every $\tilde{n} \in [50, 150]$. The optimal driving strength ω_{opt} , the optimal detuning for the dressing field δ_{opt} , and the optimal number of atoms at a single clock n_{opt} are shown on Fig. G.2.

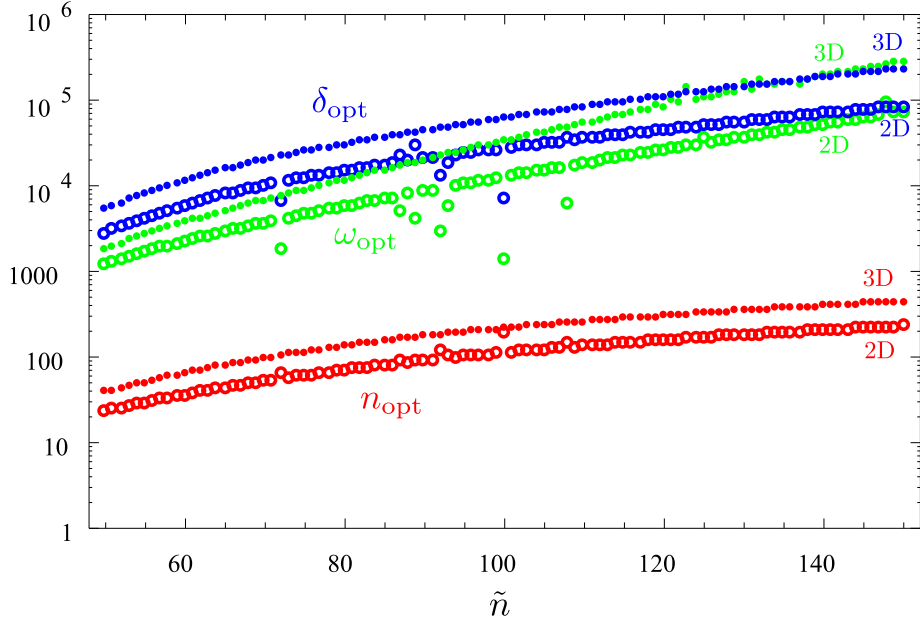


Figure G.2: The dressing fields optimal Rabi frequency $\omega = \Omega/\gamma$, detuning $\delta = \Delta/\gamma$ and the optimal number of atoms in a single clock n is plotted as a function of the principle quantum number of the Rydberg levels \tilde{n} , for the 2D and 3D setup.

The minimal error per atom E_{\min} is shown on Fig. G.3 as a function of \tilde{n} .

G.4.2 Comparison of error sources

We compare the contributions of the different error terms e_i to the total error per atom, $\sum_i e_i$, for $\tilde{n} = 120$. At the optimum (2D: $n_{\text{opt}} = 154$, $\delta_{\text{opt}} = 4.40 \times 10^4$, $\omega_{\text{opt}} = 2.59 \times 10^4$, 3D: $n_{\text{opt}} = 298$, $\delta_{\text{opt}} = 10.9 \times 10^4$, $\omega_{\text{opt}} = 8.33 \times 10^4$), the total error per atom is $E_{\min} = 1.99 \times 10^{-4}$ (2D), and 0.67×10^{-4} (3D). The different error terms contribute to the sum with amounts given in Table G.1 and G.2.

Errors in 2D ensemble	error per atom	ratio in total
imperfect blockade (e_1)	3.30×10^{-5}	17%
r_1 decay (e_2)	7.14×10^{-5}	36%
r_2 decay (e_3)	5.36×10^{-6}	3%
inhom. broadening (e_4)	5.36×10^{-6}	3%
r_2 decay (non-local) (e_5)	$\sim 10^{-9}$	< 0.1%
photon detection (e_6)	$\sim 10^{-9}$	< 0.1%
memory error (e_7)	$\sim 10^{-7}$	< 0.1%
imperfect br. ratios (e_8)	8.40×10^{-5}	42%
total error per atom	1.99×10^{-4}	100%

Table G.1: The absolute and relative contribution of the different error sources to the total error per atom at $\tilde{n} = 120$, $\Delta = \Delta_{\text{opt}} = 4.40 \times 10^4 \gamma$, $\Omega = \Omega_{\text{opt}} = 2.59 \times 10^4 \gamma$ and $n = n_{\text{opt}} = 154$.

Errors in 3D ensemble	error per atom	ratio in total
imperfect blockade (e_1)	1.41×10^{-5}	21%
r_1 decay (e_2)	2.89×10^{-5}	43%
r_2 decay (e_3)	6.62×10^{-7}	1%
inhom. broadening (e_4)	6.62×10^{-7}	1%
r_2 decay (non-local) (e_5)	$\sim 10^{-10}$	< 0.1%
photon detection (e_6)	$\sim 10^{-9}$	< 0.1%
memory error (e_7)	$\sim 10^{-8}$	< 0.1%
imperfect br. ratios (e_8)	2.26×10^{-5}	34%
total error per atom	0.670×10^{-4}	100%

Table G.2: The absolute and relative contribution of the different error sources to the total error per atom at $\tilde{n} = 120$, $\Delta = \Delta_{\text{opt}} = 10.9 \times 10^4 \gamma$, $\Omega = \Omega_{\text{opt}} = 8.33 \times 10^4 \gamma$ and $n = n_{\text{opt}} = 298$.

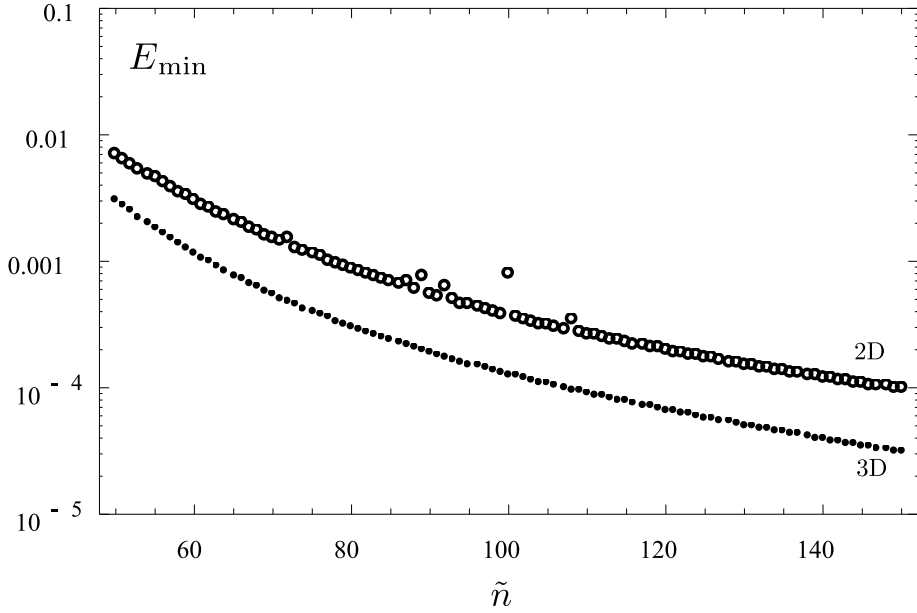


Figure G.3: The minimized error contribution of a single atom as a function of the principle quantum number of the Rydberg levels \tilde{n} , for the 2D and 3D setup.

G.5 Clock precision

G.5.1 Imperfect initialization

The precision of an atomic clock employing a GHZ state of N clock atoms is limited by the initial imperfect creation of the GHZ state described by the fidelity F_N or contrast $c = 2F_N - 1$. We assume that an imperfect creation of the GHZ state result in the density matrix

$$\rho_{\text{non-pure}} = c|\Psi\rangle\langle\Psi| + \frac{1-c}{2}(|0\rangle\langle 0| + |1\rangle\langle 1|), \quad (\text{G.53})$$

where $|\Psi\rangle = \frac{|0\rangle+|1\rangle}{\sqrt{2}}$, $|0\rangle = |0\rangle^{\otimes N}$, $|1\rangle = |1\rangle^{\otimes N}$, and we assumed that only the relative phase between the two components of the GHZ state changes to an unknown value, but no relaxation happens.

G.5.2 Measurement

After the interrogation time, the two components of the GHZ state pick up a relative phase $N\phi$. $|\Psi\rangle \rightarrow |\Psi_\phi\rangle = [|\mathbf{0}\rangle + e^{iN\phi}|\mathbf{1}\rangle]/\sqrt{2}$. Performing a perfect single-atom $-\pi/2$ rotation around the y axis for all atoms transforms this into

$$|\Psi'_\phi\rangle = \frac{1}{\sqrt{2^{N+1}}} \sum_{\{q_j\}} [1 + (-1)^{\sum_j q_j} e^{iN\phi}] |q_1, q_2, \dots, q_N\rangle, \quad (\text{G.54})$$

where $q_j \in \{0, 1\}$ stands for the state of atom j . After this, we measure every atom (in the z -basis). The probability of any resulting sequence, $\mathbf{q} = (q_1, q_2, \dots, q_N) \in \{0, 1\}^{\times N}$, is

$$\mathcal{P}(\mathbf{q}|\Psi'_\phi) = \frac{1}{2^{N+1}} [1 + (-1)^{\sum_j q_j} \cos(N\phi)], \quad (\text{G.55})$$

and the probability of the parity, $p = (\sum_j q_j) \bmod 2$, is

$$\mathcal{P}(p|\Psi'_\phi) = \frac{1 + (-1)^p \cos(N\phi)}{2}, \quad p \in \{0, 1\}. \quad (\text{G.56})$$

On the other hand, these probabilities are different when they are conditioned on being in the mixed part of the density matrix.

$$\mathcal{P}(\mathbf{q}|\rho_{\text{mixed}}) = \frac{1}{2^N}, \quad \mathcal{P}(p|\rho_{\text{mixed}}) = \frac{1}{2} \quad (\text{G.57})$$

$\forall \mathbf{q} \in \{0, 1\}^{\times N}$ and $\forall p \in \{0, 1\}$, where $\rho_{\text{mixed}} = [|\mathbf{0}\rangle\langle\mathbf{0}| + |\mathbf{1}\rangle\langle\mathbf{1}|]/2$.

The resulting total probability is the weighted sum of the two cases,

$$\mathcal{P}(p|\phi) = c\mathcal{P}(p|\Psi'_\phi) + (1 - c)\mathcal{P}(p|\rho_{\text{mixed}}) \quad (\text{G.58})$$

$$= \frac{1 + c(-1)^p \cos(N\phi)}{2}, \quad (\text{G.59})$$

where $c = 2F_N - 1$ is the contrast of the interference fringes.

G.5.3 Fisher information

We rely on inferring the unknown phase ϕ , from a series of parity measurements, as described above. The information content (about ϕ) of a single measured value p is quantified by the Fisher information,

$$\mathcal{F}(\phi) = \sum_{p \in \{0,1\}} \mathcal{P}(p|\phi) \left[\ln \frac{d}{d\phi} \mathcal{P}(p|\phi) \right]^2 \quad (\text{G.60})$$

$$= N^2 \frac{\sin^2(N\phi)}{1/c^2 - \cos^2(N\phi)}, \quad (\text{G.61})$$

where the true value of the phase is ϕ . The average Fisher information is

$$\overline{\mathcal{F}} = \frac{1}{2\pi} \int_{-\pi}^{+\pi} d\phi \mathcal{F}(\phi), \quad (\text{G.62})$$

which we can evaluate in the limit of $c \ll 1$,

$$\overline{\mathcal{F}} \approx \frac{1}{2\pi} \int d\phi c^2 \cos^2(N\phi) = \frac{N^2 c^2}{2}. \quad (\text{G.63})$$

In the other limit, when $1 - c \ll 1$, $F(\phi)$ is approximately c^2 everywhere, except near the points where $\sin(N\phi) = 0$. We approximate the dip at $\phi = 0$ with

$$\frac{\sin^2 x}{1/c^2 - \cos^2 x} \approx \frac{x^2}{\frac{1-c^2}{c^2} + x^2}, \quad \text{where } x = N\phi, \quad (\text{G.64})$$

and the integral with

$$\frac{\overline{\mathcal{F}}}{N^2} \approx c^2 - \frac{2}{2\pi} \int_{-\pi}^{+\pi} dx \left(1 - \frac{x^2}{\frac{1-c^2}{c^2} + x^2} \right) \quad (\text{G.65})$$

$$= c^2 - \frac{\sqrt{1-c^2}}{c} \approx 1 - \sqrt{2(1-c)}, \quad (\text{G.66})$$

where we have used that F is periodic with period $2\pi/N$.

Using these two limits for the average Fisher information, we approximate it with

$$\bar{\mathcal{F}} \approx \begin{cases} N^2 c^2 / 2 & , \text{ if } c \leq 0.7, \\ N^2 \left(1 - \sqrt{2(1-c)}\right) & , \text{ if } 1-c > 0.7. \end{cases} \quad (\text{G.67})$$

The quality of this approximation can be read off from Fig. G.4

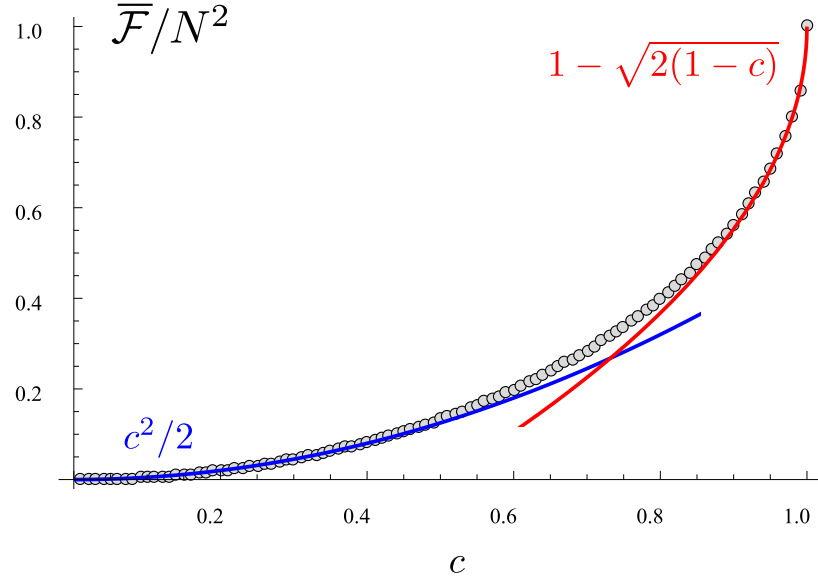


Figure G.4: Average Fisher information as a function of the contrast c (dots). It is well approximation by $c^2/2$ for $c < 0.6$ and by $1 - \sqrt{2(1-c)}$ for $c > 0.8$ (solid curves).

G.5.4 Cramér-Rao bound

The average Fisher information $\bar{\mathcal{F}}$ is a good measure of the posterior uncertainty of the phase ϕ , if the prior distribution of the phase has been previously narrowed down to a small enough interval such that its posterior is single peaked. In case of using the GHZ state, this requires a very narrow prior to start with: $\phi \in [-\pi/N, +\pi/N]$. In our previous work, we showed that this is possible by employing the atoms in a scheme using a series of cascaded GHZ states [116]. The Cramér-Rao bound on the

expected deviation of the estimated ϕ from the true one implies

$$\Delta\phi = \sqrt{\langle(\phi_{\text{estimate}} - \phi_{\text{true}})^2\rangle} \geq [\nu \bar{\mathcal{F}}]^{-1/2}, \quad (\text{G.68})$$

where ν is the number of independent repetitions of the measurement. We are going to assume equality to simplify our analysis.

G.5.5 Allan-deviation

The average fractional frequency uncertainty of an atomic clock (with central frequency ω_0), averaged over a long time period τ , is called Allan-deviation [116],

$$\sigma = \frac{(\Delta\omega)_\tau}{\omega_0} \approx \frac{\Delta\phi_t/t}{\omega_0} \frac{1}{\sqrt{\tau/t}} \approx \frac{1}{\omega_0 \sqrt{\tau}} [\nu t \bar{\mathcal{F}}]^{-1/2} \quad (\text{G.69})$$

where $(\Delta\omega)_\tau = |\frac{1}{\tau} \int d\tau' \omega(\tau') - \omega_0|$ is the deviation of the average frequency over time τ , and $\Delta\phi_t$ is the average deviation of the measured phase (from the true one) in a single interrogation of length t . The $\sqrt{\tau/t}$ factor comes from the number of independent repetitions of the same, t -long, interrogation cycle.

In Ref. [121], we showed that σ can reach

$$\sigma_{\text{ent}} \approx \frac{1}{\omega_0 \tau} \frac{8}{\pi} \frac{\sqrt{\log N}}{N}, \quad (\text{G.70})$$

if $\tau < \gamma_{\text{at}}^{-1}/N$, the reduced atomic coherence time, and if the contrast is perfect, ($c = 1$). Using the approximation for $\bar{\mathcal{F}} \approx N^2 c^2 / 2$, and the fact that $\sigma \propto [\bar{\mathcal{F}}]^{-1/2} \propto c^{-1}$, we can augment this result with a c -dependence, and express the Allan-deviation in the presence of imperfections as

$$\sigma_{\text{ent}}^{(\text{imperfect})} = \sigma_{\text{ent}}/c = \frac{1}{c \omega_0 \tau} \frac{8}{\pi} \frac{\sqrt{\log N}}{N}. \quad (\text{G.71})$$

G.5.6 Comparison to non-entangled interrogation

Using the same number of atoms, N , we can arrange a measurement without using any entanglement. This results in the Allan-deviation of

$$\sigma_{\text{non-ent}}(\tau) \approx \frac{1}{\omega_0 \tau \sqrt{N}}, \quad \text{if } \tau < 1/\gamma_{\text{LO}}, \quad (\text{G.72})$$

where γ_{LO}^{-1} is the laser coherence time. This, representing the standard quantum limit (SQL), is expected to be larger than the Allan-deviation corresponding to the GHZ state scheme, which is almost at the Heisenberg limit. The precision gain of the GHZ scheme over the non-entangled one is

$$G = \frac{\sigma_{\text{non-ent}}}{\sigma_{\text{ent}}/c} = (2F_N - 1) \frac{\pi}{8} \sqrt{\frac{N}{\log N}}. \quad (\text{G.73})$$

Since the fidelity F_N decreases with increasing N , there exist an optimal N_{opt} , for which the gain G is maximal.

G.5.7 Optimal clock network size

If each clock runs with the optimal setup $(\delta_{\text{opt}}, \omega_{\text{opt}}, n_{\text{opt}})$, then the total error per atom, E , is minimal, and the total fidelity can be written as $F_N = [1 + e^{-E_{\min}N}] / 2$.

Plugging this into Eq. G.73 gives

$$G = e^{-E_{\min}N} \frac{\pi}{8} \sqrt{\frac{N}{\log N}}, \quad (\text{G.74})$$

which takes its maximum at $N = N_{\max} \approx \frac{1}{2E_{\min}}$, giving $G_{\max} \approx \frac{\pi}{8} \left[E_{\min} \log \left(\frac{1}{2E_{\min}} \right) \right]^{-1/2}$.

In the meantime the number of atoms at a single clock is given by n_{opt} . As a result the optimal number of clocks becomes

$$K_{\text{opt}} \leq \frac{N_{\max}}{n_{\text{opt}}} \approx \frac{1}{2E_{\min}n_{\text{opt}}}. \quad (\text{G.75})$$

On Fig. G.5, we plot N_{\max} , n_{opt} , and K_{opt} as a function of the principle quantum number of the Rydberg states \tilde{n} . For $\tilde{n} = 120$, we find $N_{\max} \approx 2500$ (2D) and ≈ 7500 (3D).

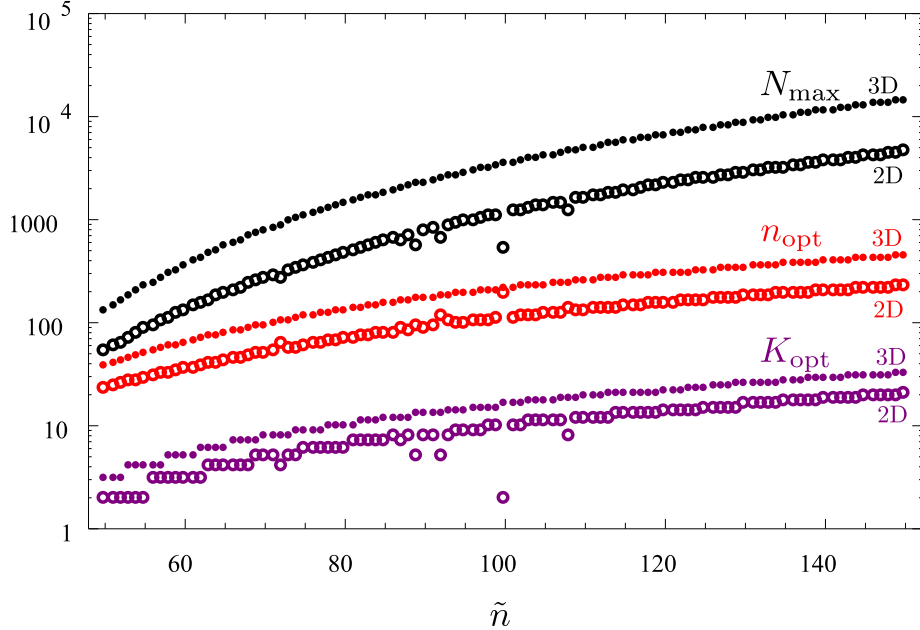


Figure G.5: The optimal total number of entangled atoms in the network N_{\max} and the number of atoms at a single clock n_{opt} as a function of the principle quantum number \tilde{n} . The thin dotted lines show the multiples of n_{opt} . The optimal number of clocks, $K_{\text{opt}} \leq N_{\max}/n_{\text{opt}}$ is written on the corresponding regions of \tilde{n} , for the 2D and 3D setup.

(3D). Using the n_{opt} values from before (≈ 150 and ≈ 300), we find $K_{\text{opt}} = 14$ and 22, for 2D and 3D, respectively.

With the optimal architecture, we can plot the maximal gain G_{\max} (compared to the non-entangled scheme using the same number of atoms) as a function of principle quantum number \tilde{n} . This is shown on Fig. G.6. For $\tilde{n} = 120$, the gain is $G_{\max} = 4.3$ (2D) and 6.9 (3D).

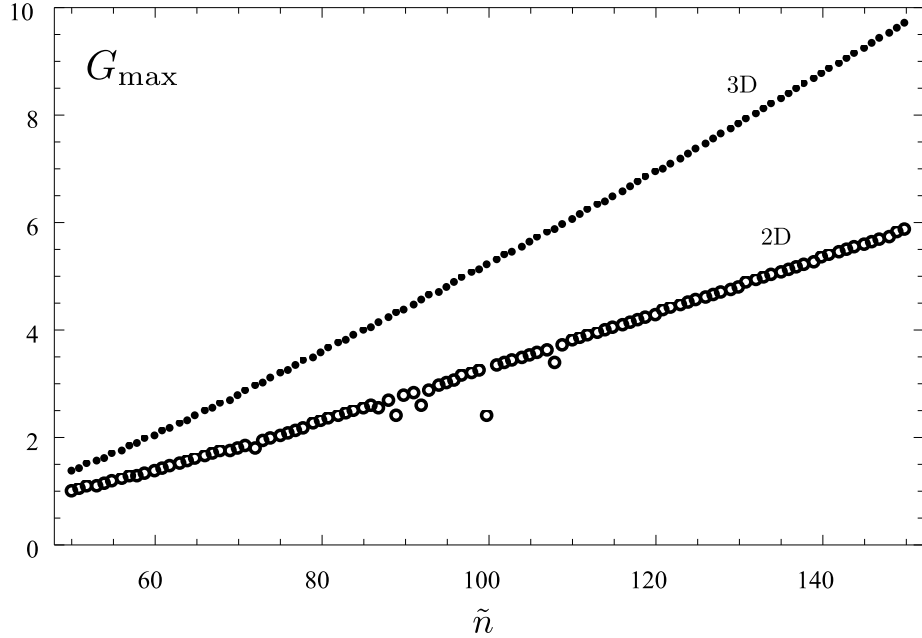


Figure G.6: Maximal gain over the non-entangled scheme provided by the optimal entangled clock network architecture as a function of principle quantum number of the Rydberg states \tilde{n} , for the 2D and 3D setup.

G.6 Multiple local ensembles

Although, in the rest of the paper, we assume that ensembles are separated such that we need to use photons to generate entanglement between them, one can imagine employing multiple atomic ensembles in the same vacuum chamber. With proper optical control, this allows entangling the ensembles by moving a single Rydberg atom to the vicinity of each ensemble sequentially, such that its blockade radius covers one of the clouds entirely.

Disregarding the technical difficulties of trapping multiple atomic ensembles in the same vacuum chamber, this entangling method has a higher fidelity than the previous, photon-based, protocol, since it does not suffer from the errors affecting the photon emission, propagation and detection. We model the imperfections of this

scheme by summing the error terms $\varepsilon_1 + \varepsilon_2 + \varepsilon_3 + \varepsilon_4 + \varepsilon_5$ only (from Eq. (G.17), (G.18), (G.19), (G.32), (G.35)).

In both the 2D and the 3D case the error from the imperfect branching ratio (e_8) makes up $30 - 40\%$ of the total error, and e_6 and e_7 are negligible. This translates to a $\sim 30\%$ decrease in total error per atom (E_{one}), which makes the final gain G about 10% higher.

This means that if the total number of available atoms in a single vacuum chamber is higher than n_{opt} , then the best strategy is to create multiple ensembles of size n_{opt} in the chamber, and entangle them with the above described operation. The gain is still a factor of ~ 8 on top of any classical scheme.

G.7 Calculating $\text{Var}(\phi_{j,k})$

Here, we calculate the variance of

$$\phi_{j,k} = \frac{\pi\Delta}{\Delta + \Delta_{j,k}} \approx \frac{\pi\Delta}{\Delta_{j,k}} = \frac{\pi\hbar\Delta}{C_{12}^{(3)}} |\mathbf{r}_j - \mathbf{r}_k|^3, \quad (\text{G.76})$$

where we assume $\Delta_{j,k} \gg \Delta$ for all (j, k) pairs, over an ensemble of n atoms, trapped in a (square or cubic)lattice with periodicity a , uniformly filling a circular 2D (spherical 3D) region of radius R .

G.7.1 Calculating $\langle \phi_{j,k} \rangle$

Averaging over the cloud of atoms,

$$\langle \phi_{j,k} \rangle = \frac{\pi\hbar\Delta}{C_{12}^{(3)}} \langle |\mathbf{r}_j - \mathbf{r}_k|^3 \rangle, \quad (\text{G.77})$$

can be approximated by the following integral

$$\approx \frac{\pi \hbar \Delta}{C_{12}^{(3)}} \frac{1}{V^2} \int_V d^\eta \mathbf{r}_j \int_V d^\eta \mathbf{r}_k |\mathbf{r}_j - \mathbf{r}_k|^3 = \frac{\hbar R^3 \Delta}{C_{12}^{(3)}} J_1, \quad (\text{G.78})$$

where $\eta = 2, 3$, V is the filled region, of radius R , in a (2D or 3D) lattice, and the integral J_1 is

$$J_1^{(2\text{D})} = \frac{1}{\pi R^7} \int_0^R dr 2\pi r \int_0^{2R} dx S_R(r, x) x^3 \quad (\text{G.79})$$

$$J_1^{(3\text{D})} = \frac{9}{16\pi R^9} \int_0^R dr 4\pi r^2 \int_0^{2R} dx A_R(r, x) x^3 \quad (\text{G.80})$$

where the new variables are: $x = |\mathbf{r}_j - \mathbf{r}_k|$, $r = |\mathbf{r}_j|$, and we used the circular (spherical) symmetry of the cloud and the spherical symmetry of the interaction, to turn the integrals into one dimensional ones. The weighting factor $S_R(r, x)$ is the length of the segment of a circle of radius x , centered at r distance from the origin that lies inside the 2D cloud of radius R . (See Fig. G.7). It can be written as

$$S_R(r, x) = \begin{cases} 2\pi x & , \text{ if } x < R - r \\ 0 & , \text{ if } R + r < x \\ 2x \arccos\left(\frac{x^2 + r^2 - R^2}{2xr}\right) & , \text{ otherwise} \end{cases} \quad (\text{G.81})$$

Similarly, $A_R(r, x)$ is the area of a spherical surface of radius x centered r distance from the center of the 3D cloud located inside the cloud. It can be written as

$$A_R(r, x) = \begin{cases} 4\pi x^2 & , \text{ if } x < R - r \\ 0 & , \text{ if } R + r < x \\ \pi \frac{x}{r} [R^2 - (x - r)^2] & , \text{ otherwise} \end{cases} \quad (\text{G.82})$$

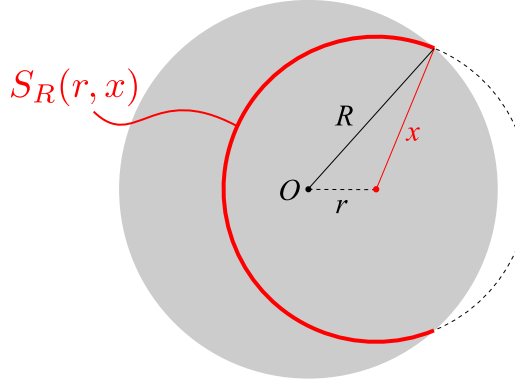


Figure G.7: The length of the circle segment of radius x lying inside the cloud of radius R , $S_R(r, x)$, is between 0 and $2\pi x$ for $R - r < x < R + r$, where r is the separation between the centers.

Using the explicit expressions of Eq. G.81 and (G.82), we can write

$$J_1^{(2D)} = 4 \int_0^1 d\rho \rho \left[\int_0^{1-\rho} d\xi \pi \xi^4 + \int_{1-\rho}^{1+\rho} d\xi \xi^4 \arccos \left(\frac{\xi^2 + \rho^2 - 1}{2\rho\xi} \right) \right] \quad (\text{G.83})$$

$$J_1^{(3D)} = 9\pi \int_0^1 d\rho \rho^2 \left[\int_0^{1-\rho} d\xi \xi^5 + \frac{1}{4} \int_{1-\rho}^{1+\rho} d\xi \frac{\xi^4}{\rho} [1 - (\xi - \rho)^2] \right] \quad (\text{G.84})$$

which we numerically evaluate and find $J_1^{(2D)} = 3.901$, and $J_1^{(3D)} = 4.787$.

G.7.2 Calculating $\langle \phi_{j,k}^2 \rangle$

Similarly, averaging the square is done by evaluating

$$\langle \phi_{j,k}^2 \rangle = \left(\frac{\pi \hbar \Delta}{C_{12}^{(3)}} \right)^2 \langle |\mathbf{r}_j - \mathbf{r}_k|^6 \rangle, \quad (\text{G.85})$$

which can be express with the integral

$$\approx \left(\frac{\hbar R^3 \Delta}{C_{12}^{(3)}} \right)^2 \frac{\pi^2}{R^6 V^2} \int_V d^\eta \mathbf{r}_j \int_V d^\eta \mathbf{r}_k |\mathbf{r}_j - \mathbf{r}_k|^3 = \left(\frac{\hbar R^3 \Delta}{C_{12}^{(3)}} \right)^2 J_2, \quad (\text{G.86})$$

where

$$J_2^{(2D)} = \frac{1}{R^{10}} \int_0^R dr 2\pi r \int_0^{2R} dx S_R(r, x) x^6, \quad (\text{G.87})$$

$$J_2^{(3D)} = \frac{9}{16R^{12}} \int_0^R dr 4\pi r^2 \int_0^{2R} dx A_R(r, x) x^6, \quad (\text{G.88})$$

using the same notation as above. Using the explicit expression of Eq. G.81 and (G.82), we can write

$$J_2^{(2D)} = 4\pi \int_0^1 d\rho \rho \left[\pi \int_0^{1-\rho} d\xi \xi^7 + \int_{1-\rho}^{1+\rho} d\xi \xi^7 \arccos \left(\frac{\xi^2 + \rho^2 - 1}{2\rho\xi} \right) \right] \quad (\text{G.89})$$

$$J_2^{(3D)} = 9\pi^2 \int_0^1 d\rho \rho^2 \left[\int_0^{1-\rho} d\xi \xi^8 + \frac{1}{4} \int_{1-\rho}^{1+\rho} d\xi \frac{\xi^7}{\rho} [1 - (\xi - \rho)^2] \right] \quad (\text{G.90})$$

which we numerically evaluate and find $J_2^{(2D)} = 34.54$, and $J_2^{(3D)} = 42.11$.

G.7.3 Result for $\text{Var}(\phi_{j,k})$

The variance in question is

$$\text{Var}(\phi_{j,k}) = \langle \phi_{j,k}^2 \rangle - \langle \phi_{j,k} \rangle^2 = \left(\frac{\hbar R^3 \Delta}{C_{12}^{(3)}} \right)^2 [J_2 - J_1^2]. \quad (\text{G.91})$$

After plugging in $R = a(n/\pi)^{1/2}$ (for 2D) and $R = a(3n/(4\pi))^{1/3}$ (for 3D), we get

$$\text{Var}(\phi_{j,k})^{(2D)} = 0.6233 n^3 \left(\frac{\hbar a^3 \Delta}{C_{12}^{(3)}} \right)^2 \quad (\text{G.92})$$

$$\text{Var}(\phi_{j,k})^{(3D)} = 1.094 n^2 \left(\frac{\hbar a^3 \Delta}{C_{12}^{(3)}} \right)^2 \quad (\text{G.93})$$

G.8 Calculating $\text{Var}(\psi_j)$

We defined $\psi_j = \sum_{k \neq j} \phi_{j,k}$ in section G.1.1. Here we evaluate its variance.

G.8.1 Calculating $\langle \psi_j \rangle$

The average over the 2D (or 3D) cloud can be written as

$$\langle \psi_j \rangle = \left\langle \sum_k \phi_{j,k} \right\rangle = \frac{1}{n} \sum_j \sum_k \phi_{j,k} = n \langle \phi_{j,i} \rangle, \quad (\text{G.94})$$

which we evaluated in section G.7. Using the notation used there, we can write

$$\langle \psi_j \rangle = n \frac{\hbar R^3 \Delta}{C_{12}^3} J_1. \quad (\text{G.95})$$

G.8.2 Calculating $\langle \psi_j^2 \rangle$

The average of the square can be written as

$$\langle \psi_j^2 \rangle = \frac{1}{n} \sum_j \left(\sum_{k \neq j} \phi_{j,k} \right)^2 = \frac{n^2}{V^3} \int_V d^\eta \mathbf{r}_j \left(\int_V d^\eta \mathbf{r}_k \phi_{j,k} \right)^2, \quad (\text{G.96})$$

where $\eta = 2, 3$, and V is the circular (in 2D) or spherical (in 3D) region filled with n atoms, homogeneously. After plugging in the expression for $\phi_{j,k}$ and using the same notation as in section G.7, we write

$$\langle \psi_j^2 \rangle = n^2 \left(\frac{\hbar R^3 \Delta}{C_{12}^3} \right)^2 J_3, \quad (\text{G.97})$$

where

$$J_3^{(2D)} = \frac{1}{\pi R^{12}} \int_0^R dr 2\pi r \left(\int_0^{2R} dx S_R(r, x) x^3 \right)^2, \quad (\text{G.98})$$

$$J_3^{(3D)} = \frac{27}{64\pi R^{15}} \int_0^R dr 4\pi r^2 \left(\int_0^{2R} dx A_R(r, x) x^3 \right)^2. \quad (\text{G.99})$$

Using the explicit expressions from Eq. G.81 and (G.82) gives

$$\begin{aligned} J_3^{(2D)} &= 8 \int_0^1 d\rho \rho \left[\left(\pi \int_0^{1-\rho} d\xi \xi^4 \right)^2 \right. \\ &\quad + 2 \left(\pi \int_0^{1-\rho} d\xi \xi^4 \right) \left(\int_{1-\rho}^{1+\rho} d\xi \xi^4 \arccos \left(\frac{\xi^2 + \rho^2 - 1}{2\rho\xi} \right) \right) \\ &\quad \left. + \left(\int_{1-\rho}^{1+\rho} d\xi \xi^4 \arccos \left(\frac{\xi^2 + \rho^2 - 1}{2\rho\xi} \right) \right)^2 \right] \end{aligned} \quad (\text{G.100})$$

$$\begin{aligned} J_3^{(3D)} &= 27\pi^2 \int_0^1 d\rho \rho^2 \left[\left(\int_0^{1-\rho} d\xi \xi^5 \right)^2 \right. \\ &\quad + 2 \left(\int_0^{1-\rho} d\xi \xi^5 \right) \left(\int_{1-\rho}^{1+\rho} d\xi \frac{1}{4} \frac{\xi^4}{\rho} [1 - (\xi - \rho)^2] \right) \\ &\quad \left. + \left(\int_{1-\rho}^{1+\rho} d\xi \frac{1}{4} \frac{\xi^4}{\rho} [1 - (\xi - \rho)^2] \right)^2 \right] \end{aligned} \quad (\text{G.101})$$

We evaluate these numerically and find $J_3^{(2D)} = 17.81$, and $J_3^{(3D)} = 25.16$.

G.8.3 Result for $\text{Var}(\psi_j)$

Now, the variance in question can be written as

$$\text{Var}(\psi_j) = \langle \psi_j^2 \rangle - \langle \psi_j \rangle^2 = n^2 \left(\frac{\hbar R^3 \Delta}{C_{12}^{(3)}} \right)^2 [J_3 - J_1^2]. \quad (\text{G.102})$$

After plugging in $R = a(n/\pi)^{1/2}$ (for 2D) and $R = a(3n/(4\pi))^{1/3}$ (for 3D), we get

$$\text{Var}(\psi_j)^{(2D)} = 0.08359 n^5 \left(\frac{\hbar a^3 \Delta}{C_{12}^{(3)}} \right)^2 \quad (\text{G.103})$$

$$\text{Var}(\psi_j)^{(3D)} = 0.1277 n^4 \left(\frac{\hbar a^3 \Delta}{C_{12}^{(3)}} \right)^2 \quad (\text{G.104})$$

G.9 Calculating $\text{Var}(\Delta_j)$

Here, we calculate the variance of $\Delta_j = -\sum_{k \neq j} \frac{\Omega^2}{4(\Delta_{j,k} + \Delta)} \approx -\sum_{k \neq j} \frac{\Omega^2}{4\Delta_{jk}}$ in case of $\Delta \ll \min \Delta_{j,k}$, for an ensemble of n atoms, trapped in a lattice with periodicity a , uniformly filling a circular 2D (spherical 3D) region of radius R . We assume a van der Waals interaction, $\Delta_{j,k} = \frac{C_{11}^{(6)}}{\hbar|\mathbf{r}_j - \mathbf{r}_k|^6}$ between pairs of atoms at \mathbf{r}_j and \mathbf{r}_k .

G.9.1 Calculating $\langle \Delta_j \rangle$

Averaging over the ensemble of atoms,

$$\langle \Delta_j \rangle = \frac{1}{n} \sum_j \Delta_j = \left(-\frac{\hbar\Omega^2}{4C_{11}^{(6)}} \right) \frac{1}{n} \sum_j \sum_{k \neq j} |\mathbf{r}_j - \mathbf{r}_k|^6 \quad (\text{G.105})$$

can be approximated with the following integral

$$\langle \Delta_j \rangle \approx \left(-\frac{\hbar\Omega^2}{4C_{11}^{(6)}} \right) \frac{n}{V^2} \int_V d^\eta \mathbf{r}_j \int_V d^\eta \mathbf{r}_k |\mathbf{r}_j - \mathbf{r}_k|^6 \quad (\text{G.106})$$

$$= -n \frac{\hbar\Omega^2 R^6}{C_{11}^{(6)}} I_1, \quad (\text{G.107})$$

where $\eta = 2$ or 3 , and V is the filled region, of radius R , of the (2D or 3D) lattice, and I_1 is the following integral,

$$I_1^{(2\text{D})} = \frac{1}{(2\pi)^2 R^{10}} \int_0^R dr 2\pi r \int_0^{2R} dx S_R(r, x) x^6, \quad (\text{G.108})$$

$$I_1^{(3\text{D})} = \frac{9}{64\pi^2 R^{12}} \int_0^R dr 4\pi r^2 \int_0^{2R} dx A_R(r, x) x^6, \quad (\text{G.109})$$

where we used the same transformation as in section G.7, and $S_R(r, x)$ and $A_R(r, x)$ are given by Eq. G.81 and (G.82).

Now, we can express I_1 , in terms of the dimensionless variables $\rho = r/R$, $\xi = x/R$, as

$$I_1^{(2D)} = \int_0^1 d\rho \rho \left[\int_0^{1-\rho} d\xi \xi^7 + \frac{1}{\pi} \int_{1-\rho}^{1+\rho} d\xi \xi^7 \arccos \left(\frac{\xi^2 + \rho^2 - 1}{2\xi\rho} \right) \right]$$

$$I_1^{(3D)} = \frac{9}{4} \int_0^1 d\rho \rho^2 \left[\int_0^{1-\rho} d\xi \xi^8 + \int_{1-\rho}^{1+\rho} d\xi \xi^8 \frac{1 - (\xi - \rho)^2}{4\xi\rho} \right]$$

which we evaluate numerically and find $I_1^{(2D)} = 0.875$, and $I_1^{(3D)} = 1.067$.

G.9.2 Calculating $\langle \Delta_j^2 \rangle$

The average of Δ_j^2 can be written as

$$\langle \Delta_j^2 \rangle = \frac{1}{n} \sum_j \Delta_j^2 = \left(\frac{\hbar\Omega^2}{4C_{11}^{(6)}} \right)^2 \frac{1}{n} \sum_j \left(\sum_{k \neq j} |\mathbf{r}_j - \mathbf{r}_k|^6 \right)^2. \quad (\text{G.110})$$

Similarly to the calculation of $\langle \Delta_j \rangle$, we can approximate the sums with integrals and write

$$\langle \Delta_j^2 \rangle = \left(n \frac{\hbar\Omega^2 R^6}{C_{11}^{(6)}} \right)^2 I_2, \quad (\text{G.111})$$

where I_2 takes the following forms

$$I_2^{(2D)} = \frac{1}{16\pi^3 R^{18}} \int_0^R dr 2\pi r \left(\int_0^{2R} dx S_R(r, x) x^6 \right)^2 \quad (\text{G.112})$$

$$I_2^{(3D)} = \frac{27}{256\pi^3 R^{21}} \int_0^R dr 4\pi r^2 \left(\int_0^{2R} dx A_R(r, x) x^6 \right)^2 \quad (\text{G.113})$$

in the two cases.

After plugging in the explicit expressions of $S_R(r, x)$ and $A_R(r, x)$, we can express

I_2 in terms of the dimensionless variables $\rho = r/R$, $\xi = x/R$, as

$$\begin{aligned} I_2^{(2D)} &= \frac{1}{2} \int_0^1 d\rho \rho \left[\left(\int_0^{1-\rho} d\xi \xi^7 \right)^2 \right. \\ &\quad + \frac{2}{\pi} \left(\int_0^{1-\rho} d\xi \xi^7 \right) \left(\int_{1-\rho}^{1+\rho} d\xi \xi^7 \arccos \left(\frac{\xi^2 + \rho^2 - 1}{2\xi\rho} \right) \right) \\ &\quad \left. + \frac{1}{\pi^2} \left(\int_{1-\rho}^{1+\rho} d\xi \xi^7 \arccos \left(\frac{\xi^2 + \rho^2 - 1}{2\xi\rho} \right) \right)^2 \right], \end{aligned} \quad (\text{G.114})$$

$$\begin{aligned} I_2^{(3D)} &= \frac{27}{16} \int_0^1 d\rho \rho^2 \left[\left(\int_0^{1-\rho} d\xi \xi^8 \right)^2 \right. \\ &\quad + \frac{1}{2} \left(\int_0^{1-\rho} d\xi \xi^8 \right) \left(\int_{1-\rho}^{1+\rho} d\xi \frac{\xi^7}{\rho} [1 - (\xi - \rho)^2] \right) \\ &\quad \left. + \frac{1}{16} \left(\int_{1-\rho}^{1+\rho} d\xi \frac{\xi^7}{\rho} [1 - (\xi - \rho)^2] \right)^2 \right] \end{aligned} \quad (\text{G.115})$$

which we evaluate numerically and find $I_2^{(2D)} = 1.146$, and $I_2^{(3D)} = 1.474$

G.9.3 Result for $\text{Var}(\Delta_j)$

Using the results above, we write the variance of Δ_j as

$$\text{Var}(\Delta_j) = \langle \Delta_j^2 \rangle - \langle \Delta_j \rangle^2 = n^2 \left(\frac{\hbar\Omega^2 R^6}{C_{11}^{(6)}} \right) [I_2 - (I_1)^2]. \quad (\text{G.116})$$

Instead of R , we can also write it, in terms of the lattice constant a , and the total number of atoms n , as

$$\text{Var}(\Delta_j)^{(2D)} = \frac{0.380}{\pi^6} n^8 \left(\frac{\hbar\Omega^2 a^6}{C_{11}^{(6)}} \right)^2, \quad (\text{G.117})$$

$$\text{Var}(\Delta_j)^{(3D)} = \frac{81}{128} \frac{0.336}{\pi^4} n^6 \left(\frac{\hbar\Omega^2 a^6}{C_{11}^{(6)}} \right)^2, \quad (\text{G.118})$$

where we used that $R^2\pi = na^2$ (in 2D) and $4\pi R^3/3 = na^3$ (in 3D).

Bibliography

- [1] Alex Abramovici, William E. Althouse, Ronald W. P. Drever, Yekta Gürsel, Seiji Kawamura, Frederick J. Raab, David Shoemaker, Lisa Sievers, Robert E. Spero, Kip S. Thorne, Rochus E. Vogt, Rainer Weiss, Stanley E. Whitcomb, and Michael E. Zucker. Ligo: The laser interferometer gravitational-wave observatory. *Science*, 256:325–333, 1992.
- [2] U Akram, N Kiesel, M Aspelmeyer, and G J Milburn. Single-photon optomechanics in the strong coupling regime. *New Journal of Physics*, 12:083030, 2010.
- [3] Boris Albrecht, Pau Farrera, Xavier Fernandez-Gonzalvo, Matteo Cristiani, and Hugues de Riedmatten. A waveguide frequency converter connecting rubidium-based quantum memories to the telecom c-band. *Nature Communications*, 5:3376, 2013.
- [4] D.W. Allan. Statistics of atomic frequency standards. *Proceedings of the IEEE*, 54:221–230, 1966.
- [5] Ulrik L. Andersen and Timothy C. Ralph. High-fidelity teleportation of continuous-variable quantum states using delocalized single photons. *Phys. Rev. Lett.*, 111:050504, 2013.
- [6] A. André, A. S. Sørensen, and M. D. Lukin. Stability of atomic clocks based on entangled atoms. *Phys. Rev. Lett.*, 92:230801, 2004.
- [7] Axel André. *Nonclassical states of light and atomic ensembles: Generation and New Applications*. PhD thesis, Harvard University, 2005.
- [8] Mauro Antezza, Caterina Braggio, Giovanni Carugno, Antonio Noto, Roberto Passante, Lucia Rizzuto, Giuseppe Ruoso, and Salvatore Spagnolo. Optomechanical Rydberg-atom excitation via dynamic Casimir-Polder coupling. *Phys. Rev. Lett.*, 113:023601, 2014.
- [9] O. Arcizet, P.-F. Cohadon, T. Briant, M. Pinard, and A. Heidmann. Radiation-pressure cooling and optomechanical instability of a micromirror. *Nature*, 444:71–74, 2006.

Bibliography

- [10] Markus Aspelmeyer, Tobias J. Kippenberg, and Florian Marquardt. Cavity optomechanics. *Rev. Mod. Phys.*, 86:1391–1452, 2014.
- [11] Markus Aspelmeyer and Keith Schwab. Focus on mechanical systems at the quantum limit. *New Journal of Physics*, 10:095001, 2008.
- [12] F Bariani, Y O Dudin, T. A B Kennedy, and A Kuzmich. Dephasing of multi-particle Rydberg excitations for fast entanglement generation. *Phys. Rev. Lett.*, 108:030501, 2012.
- [13] J.A. Barnes and D.W. Allan. A statistical model of flicker noise. *Proceedings of the IEEE*, 54:176–178, 1966.
- [14] S Basiri-Esfahani, U Akram, and G J Milburn. Phonon number measurements using single photon opto-mechanics. *New Journal of Physics*, 14:085017, 2012.
- [15] Almut Beige, Daniel Braun, Ben Tregenna, and Peter L. Knight. Quantum computing using dissipation to remain in a decoherence-free subspace. *Phys. Rev. Lett.*, 85:1762–1765, 2000.
- [16] Jan Benhelm, Gerhard Kirchmair, Christian F. Roos, and Rainer Blatt. Towards fault-tolerant quantum computing with trapped ions. *Nature Physics*, 4:463–466, 2008.
- [17] C. H. Bennett and G. Brassard. In *Proceedings IEEE International Conference on Computers, Systems and Signal Processing*. IEEE, 1984.
- [18] Charles H. Bennett, Gilles Brassard, Sandu Popescu, Benjamin Schumacher, John A. Smolin, and William K. Wootters. Purification of noisy entanglement and faithful teleportation via noisy channels. *Phys. Rev. Lett.*, 76:722–725, 1996.
- [19] Nadja K. Bernardes, Ludmiła Praxmeyer, and Peter van Loock. Rate analysis for a hybrid quantum repeater. *Phys. Rev. A*, 83:012323, 2011.
- [20] H. Bernien, B. Hensen, W. Pfaff, G. Koolstra, M. S. Blok, L. Robledo, T. H. Taminiau, M. Markham, D. J. Twitchen, L. Childress, and R. Hanson. Heralded entanglement between solid-state qubits separated by three metres. *Nature*, 497:86–90, 2012.
- [21] D. W. Berry, B. L. Higgins, S. D. Bartlett, M. W. Mitchell, G. J. Pryde, and H. M. Wiseman. How to perform the most accurate possible phase measurements. *Phys. Rev. A*, 80:052114, 2009.

Bibliography

- [22] I. I. Beterov, M. Saffman, E. A. Yakshina, V. P. Zhukov, D. B. Tretyakov, V. M. Entin, I. I. Ryabtsev, C. W. Mansell, C. MacCormick, S. Bergamini, and M. P. Fedoruk. Quantum gates in mesoscopic atomic ensembles based on adiabatic passage and Rydberg blockade. *Phys. Rev. A*, 88(1):010303, July 2013.
- [23] B. J. Bloom, T. L. Nicholson, J. R. Williams, S. L. Campbell, M. Bishop, X. Zhang, W. Zhang, S. L. Bromley, and J. Ye. An optical lattice clock with accuracy and stability at the 10^{-18} level. *Nature*, 506:71–75, 2014.
- [24] J. J . Bollinger, Wayne M. Itano, D. J. Wineland, and D. J. Heinzen. Optimal frequency measurements with maximally correlated states. *Phys. Rev. A*, 54:R4649–R4652, 1996.
- [25] J. Borregaard, P. Kómár, E. M. Kessler, M. D. Lukin, and A. S. Sørensen. Long-distance entanglement distribution using individual atoms in optical cavities. *Phys. Rev. A*, 92:012307, 2015.
- [26] J. Borregaard, P. Kómár, E. M. Kessler, A. S. Sørensen, and M. D. Lukin. Heralded quantum gates with integrated error detection in optical cavities. *Phys. Rev. Lett.*, 114:110502, 2015.
- [27] J. Borregaard and A. S. Sørensen. Efficient atomic clocks operated with several atomic ensembles. *Phys. Rev. Lett.*, 111:090802, 2013.
- [28] J. Borregaard and A. S. Sørensen. Near-heisenberg-limited atomic clocks in the presence of decoherence. *Phys. Rev. Lett.*, 111:090801, 2013.
- [29] J. Borregaard, M. Zugenmaier, J. M. Petersen, H. Shen, G. Vasilakis, K. Jensen, E. S. Polzik, and A. S. Sørensen. Room temperature quantum memory and scalable single photon source based on motional averaging. *arXiv:*, 1501.03916, 2015.
- [30] Samuel L. Braunstein. Quantum limits on precision measurements of phase. *Phys. Rev. Lett.*, 69:3598–3601, 1992.
- [31] R. J. Brecha, P. R. Rice, and M. Xiao. n two-level atoms in a driven optical cavity: Quantum dynamics of forward photon scattering for weak incident fields. *Phys. Rev. A*, 59:2392–2417, 1999.
- [32] Ferdinand Brennecke, Stephan Ritter, Tobias Donner, and Tilman Esslinger. Cavity optomechanics with a bose-einstein condensate. *Science*, 322:235–238, 2008.
- [33] H.-J. Briegel, W. Dür, J. I. Cirac, and P. Zoller. Quantum repeaters: The role of imperfect local operations in quantum communication. *Phys. Rev. Lett.*, 81:5932–5935, 1998.

- [34] A. Broadbent, J. Fitzsimons, and E. Kashefi. Universal blind quantum computation. In *Foundations of Computer Science, 2009. FOCS '09. 50th Annual IEEE Symposium on*, pages 517–526, Oct 2009.
- [35] Daniel E. Browne, Martin B. Plenio, and Susana F. Huelga. Robust creation of entanglement between ions in spatially separate cavities. *Phys. Rev. Lett.*, 91:067901, 2003.
- [36] Dagmar Bruß. Optimal eavesdropping in quantum cryptography with six states. *Phys. Rev. Lett.*, 81:3018–3021, 1998.
- [37] Michael J. Burek, Yiwen Chu, Madelaine S. Z. Liddy, Parth Patel, Jake Rochman, Srujan Meesala, Wooyoung Hong, Qimin Quan, Mikhail D. Lukin, and Marko Lončar. High quality-factor optical nanocavities in bulk single-crystal diamond. *Nature Communications*, 5:5718, 2014.
- [38] V. Bužek, R. Derka, and S. Massar. Optimal quantum clocks. *Phys. Rev. Lett.*, 82:2207–2210, 1999.
- [39] H.J. Carmichael, R.J. Brecha, and P.R. Rice. Quantum interference and collapse of the wavefunction in cavity qed. *Optics Communications*, 82:73 – 79, 1991.
- [40] Tal Carmon and Kerry J. Vahala. Modal spectroscopy of optoexcited vibrations of a micron-scale on-chip resonator at greater than 1 ghz frequency. *Phys. Rev. Lett.*, 98:123901, 2007.
- [41] Carlton M. Caves. Quantum-mechanical radiation-pressure fluctuations in an interferometer. *Phys. Rev. Lett.*, 45:75–79, 1980.
- [42] Jasper Chan, T. P. Mayer Alegre, Amir H. Safavi-Naeini, Jeff T. Hill, Alex Krause, Simon Gröblacher, Markus Aspelmeyer, and Oskar Painter. Laser cooling of a nanomechanical oscillator into its quantum ground state. *Nature*, 478:89–92, 2011.
- [43] Jasper Chan, Amir H. Safavi-Naeini, Jeff T. Hill, Sen Meenehan, and Oskar Painter. Optimized optomechanical crystal cavity with acoustic radiation shield. *Appl. Phys. Lett.*, 101:081115, 2012.
- [44] D E Chang, A H Safavi-Naeini, M Hafezi, and O Painter. Slowing and stopping light using an optomechanical crystal array. *New Journal of Physics*, 13:023003, 2011.
- [45] Darrick E. Chang, Anders S. Sørensen, Eugene A. Demler, and Mikhail D. Lukin. A single-photon transistor using nanoscale surface plasmons. *Nature Physics*, 3:807–812, 2007.

Bibliography

- [46] Yu-Ao Chen, Xiao-Hui Bao, Zhen-Sheng Yuan, Shuai Chen, Bo Zhao, and Jian-Wei Pan. Heralded Generation of an Atomic NOON State. *Phys. Rev. Lett.*, 104(4):043601, January 2010.
- [47] H. K. Cheung and C. K. Law. Nonadiabatic optomechanical hamiltonian of a moving dielectric membrane in a cavity. *Phys. Rev. A*, 84:023812, 2011.
- [48] L. Childress, J. M. Taylor, A. S. Sørensen, and M. D. Lukin. Fault-tolerant quantum communication based on solid-state photon emitters. *Phys. Rev. Lett.*, 96:070504, 2006.
- [49] Lilian Childress, Ronald Walsworth, and Mikhail Lukin. Atom-like crystal defects: From quantum computers to biological sensors. *Physics Today*, 67:38, 2014.
- [50] Andrew M. Childs. Secure assisted quantum computation. *Quantum Info. Comput.*, 5:456–466, 2005.
- [51] Cheng Chin, Rudolf Grimm, Paul Julienne, and Eite Tiesinga. Feshbach resonances in ultracold gases. *Rev. Mod. Phys.*, 82:1225–1286, 2010.
- [52] C. W. Chou, D. B. Hume, J. C. J. Koelemeij, D. J. Wineland, and T. Rosenband. Frequency comparison of two high-accuracy al^+ optical clocks. *Phys. Rev. Lett.*, 104:070802, 2010.
- [53] Chin-Wen Chou, Julien Laurat, Hui Deng, Kyung Soo Choi, Hugues de Riedmatten, Daniel Felinto, and H. Jeff Kimble. Functional quantum nodes for entanglement distribution over scalable quantum networks. *Science*, 316:1316–1320, 2007.
- [54] J. I. Cirac, P. Zoller, H. J. Kimble, and H. Mabuchi. Quantum state transfer and entanglement distribution among distant nodes in a quantum network. *Phys. Rev. Lett.*, 78:3221–3224, 1997.
- [55] C. W S Conover. Effects of pulse shape on strongly driven two-level systems. *Phys. Rev. A*, 84(December):1–15, 2011.
- [56] Thomas Corbitt, Christopher Wipf, Timothy Bodiya, David Ottaway, Daniel Sigg, Nicolas Smith, Stanley Whitcomb, and Nergis Mavalvala. Optical dilution and feedback cooling of a gram-scale oscillator to 6.9 mK. *Phys. Rev. Lett.*, 99:160801, 2007.
- [57] Harald Cramér. *Mathematical Methods of Statistics*. Princeton University Press, Princeton, NJ, 1946.

Bibliography

- [58] Marcelo Davanço, Jasper Chan, Amir H. Safavi-Naeini, Oskar Painter, and Kartik Srinivasan. Slot-mode-coupled optomechanical crystals. *Opt. Express*, 20:24394–24410, 2012.
- [59] Mark de Burgh and Stephen D. Bartlett. Quantum methods for clock synchronization: Beating the standard quantum limit without entanglement. *Phys. Rev. A*, 72:042301, 2005.
- [60] Andrei Derevianko and Hidetoshi Katori. *Colloquium : Physics of optical lattice clocks*. *Rev. Mod. Phys.*, 83:331–347, 2011.
- [61] David Deutsch, Artur Ekert, Richard Jozsa, Chiara Macchiavello, Sandu Popescu, and Anna Sanpera. Quantum privacy amplification and the security of quantum cryptography over noisy channels. *Phys. Rev. Lett.*, 77:2818–2821, 1996.
- [62] S. A. Diddams, J. C. Bergquist, S. R. Jefferts, and C. W. Oates. Standards of time and frequency at the outset of the 21st century. *Science*, 306:1318–1324, 2004.
- [63] L. Ding, C. Baker, P. Senellart, A. Lemaitre, S. Ducci, G. Leo, and I. Favero. Wavelength-sized gaas optomechanical resonators with gigahertz frequency. *Appl. Phys. Lett.*, 98:113108, 2011.
- [64] Khelifa Djerroud, Ouali Acef, André Clairon, Pierre Lemonde, Catherine N. Man, Etienne Samain, and Peter Wolf. Coherent optical link through the turbulent atmosphere. *Opt. Lett.*, 35:1479–1481, 2010.
- [65] J. M. Dobrindt and T. J. Kippenberg. Theoretical analysis of mechanical displacement measurement using a multiple cavity mode transducer. *Phys. Rev. Lett.*, 104:033901, 2010.
- [66] P. Domokos, J. M. Raimond, M. Brune, and S. Haroche. Simple cavity-qed two-bit universal quantum logic gate: The principle and expected performances. *Phys. Rev. A*, 52:3554–3559, 1995.
- [67] S. Droste, F. Ozimek, Th. Udem, K. Predehl, T. W. Hänsch, H. Schnatz, G. Grosche, and R. Holzwarth. Optical-frequency transfer over a single-span 1840 km fiber link. *Phys. Rev. Lett.*, 111:110801, 2013.
- [68] L.-M. Duan and H. J. Kimble. Efficient engineering of multiatom entanglement through single-photon detections. *Phys. Rev. Lett.*, 90:253601, 2003.
- [69] L.-M. Duan and H. J. Kimble. Scalable photonic quantum computation through cavity-assisted interactions. *Phys. Rev. Lett.*, 92:127902, 2004.

Bibliography

- [70] L.-M. Duan, M. D. Lukin, J. I. Cirac, and P. Zoller. Long-distance quantum communication with atomic ensembles and linear optics. *Nature*, 414:413–418, 2001.
- [71] L.-M. Duan, B. Wang, and H. J. Kimble. Robust quantum gates on neutral atoms with cavity-assisted photon scattering. *Phys. Rev. A*, 72:032333, 2005.
- [72] Lu-Ming Duan, G. Giedke, J. I. Cirac, and P. Zoller. Entanglement purification of gaussian continuous variable quantum states. *Phys. Rev. Lett.*, 84:4002–4005, 2000.
- [73] Y O Dudin and A Kuzmich. Strongly interacting Rydberg excitations of a cold atomic gas. *Science*, 336(6083):887–9, May 2012.
- [74] Y O Dudin, A G Radnaev, R Zhao, J Z Blumoff, T A B Kennedy, and A Kuzmich. Entanglement of light-shift compensated atomic spin waves with telecom light. *Phys. Rev. Lett.*, 105:260502, 2010.
- [75] W Dür and H J Briegel. Entanglement purification and quantum error correction. *Reports on Progress in Physics*, 70:1381, 2007.
- [76] W. Dür, H.-J. Briegel, J. I. Cirac, and P. Zoller. Quantum repeaters based on entanglement purification. *Phys. Rev. A*, 59:169–181, 1999.
- [77] M. Ebert, M. Kwon, T. G. Walker, and M. Saffman. Coherence and rydberg blockade of atomic ensemble qubits. *Phys. Rev. Lett.*, 115:093601, Aug 2015.
- [78] J. N. Eckstein, A. I. Ferguson, and T. W. Hänsch. High-resolution two-photon spectroscopy with picosecond light pulses. *Phys. Rev. Lett.*, 40:847–850, 1978.
- [79] Matt Eichenfield, Jasper Chan, Ryan M. Camacho, Kerry J. Vahala, and Oskar Painter. Optomechanical crystals. *Nature*, 462:78–82, 2009.
- [80] Artur K. Ekert. Quantum cryptography based on bell’s theorem. *Phys. Rev. Lett.*, 67:661–663, 1991.
- [81] Dirk Englund, David Fattal, Edo Waks, Glenn Solomon, Bingyang Zhang, Toshihiro Nakaoka, Yasuhiko Arakawa, Yoshihisa Yamamoto, and Jelena Vučković. Controlling the spontaneous emission rate of single quantum dots in a two-dimensional photonic crystal. *Phys. Rev. Lett.*, 95:013904, 2005.
- [82] B. M. Escher, R. L. de Matos Filho, and L. Davidovich. General framework for estimating the ultimate precision limit in noisy quantum-enhanced metrology. *Nature Physics*, 7:406–411, 2011.

Bibliography

- [83] Da-Wei Fang, Wei-Jun Xie, Yi Zhang, Xiao Hu, and Yu-Yan Liu. Radiative lifetimes of rydberg state of ytterbium. *Journal of Quantitative Spectroscopy and Radiative Transfer*, 69:469473, 2001.
- [84] Ivan Favero and Khaled Karrai. Optomechanics of deformable optical cavities. *Nature Photonics*, 3:201–205, 2009.
- [85] Richard P. Feynman. Simulating physics with computers. *International Journal of Theoretical Physics*, 21:467–488, 1982.
- [86] Victor Fiore, Yong Yang, Mark C. Kuzyk, Russell Barbour, Lin Tian, and Hailin Wang. Storing optical information as a mechanical excitation in a silica optomechanical resonator. *Phys. Rev. Lett.*, 107:133601, 2011.
- [87] Ofer Firstenberg, Thibault Peyronel, Qi-Yu Liang, Alexey V Gorshkov, Mikhail D Lukin, and Vladan Vuletić. Attractive photons in a quantum non-linear medium. *Nature*, 502:71–5, 2013.
- [88] J. S. Foresi, P. R. Villeneuve, J. Ferrera, E. R. Thoen, G. Steinmeyer, S. Fan, J. D. Joannopoulos, L. C. Kimerling, Henry I. Smith, and E. P. Ippen. Photonic-bandgap microcavities in optical waveguides. *Nature*, 390:143–145, 1997.
- [89] C. Gardiner and P. Zoller. *Quantum Noise*. Springer, 2004.
- [90] C. Genes, A. Mari, D. Vitali, and P. Tombesi. Chapter 2 quantum effects in optomechanical systems. In *Advances in Atomic Molecular and Optical Physics*, volume 57, pages 33 – 86. Academic Press, 2009.
- [91] G. Giedke, J. M. Taylor, D. D’Alessandro, M. D. Lukin, and A. Imamoğlu. Quantum measurement of a mesoscopic spin ensemble. *Phys. Rev. A*, 74:032316, 2006.
- [92] S. Gigan, H. R. Böhm, M. Paternostro, F. Blaser, G. Langer, J. B. Hertzberg, K. C. Schwab, D. Buerle, M. Aspelmeyer, and A. Zeilinger. Self-cooling of a micromirror by radiation pressure. *Nature*, 444:67–70, 2006.
- [93] V. Giovannetti, D. Vitali, P. Tombesi, and A. Ekert. Scalable quantum computation with cavity qed systems. *Phys. Rev. A*, 62:032306, 2000.
- [94] Vittorio Giovannetti, Seth Lloyd, and Lorenzo Maccone. Quantum metrology. *Phys. Rev. Lett.*, 96:010401, 2006.
- [95] Vittorio Giovannetti, Seth Lloyd, and Lorenzo Maccone. Advances in quantum metrology. *Nature Photonics*, 5:222–229, 2011.

Bibliography

- [96] Nicolas Gisin, Grégoire Ribordy, Wolfgang Tittel, and Hugo Zbinden. Quantum cryptography. *Rev. Mod. Phys.*, 74:145–195, 2002.
- [97] Michael H Goerz, Eli J Halperin, Jon M Aytac, Christiane P Koch, and K Birgitta Whaley. Robustness of high-fidelity Rydberg gates with single-site addressability. *Phys. Rev. A*, 90:032329, 2014.
- [98] M. Grassl, Th. Beth, and T. Pellizzari. Codes for the quantum erasure channel. *Phys. Rev. A*, 56:33–38, 1997.
- [99] Simon Gröblacher, Klemens Hammerer, Michael R. Vanner, and Markus Aspelmeyer. Observation of strong coupling between a micromechanical resonator and an optical cavity field. *Nature*, 460:724–727, 2009.
- [100] Ivan S. Grudinin, Hansuek Lee, O. Painter, and Kerry J. Vahala. Phonon laser action in a tunable two-level system. *Phys. Rev. Lett.*, 104:083901, 2010.
- [101] Subhadeep Gupta, Kevin L. Moore, Kater W. Murch, and Dan M. Stamper-Kurn. Cavity nonlinear optics at low photon numbers from collective atomic motion. *Phys. Rev. Lett.*, 99:213601, 2007.
- [102] Michael J. W. Hall, Dominic W. Berry, Marcin Zwierz, and Howard M. Wiseman. Universality of the Heisenberg limit for estimates of random phase shifts. *Phys. Rev. A*, 85(4):041802, April 2012.
- [103] Klemens Hammerer, Anders S. Sørensen, and Eugene S. Polzik. Quantum interface between light and atomic ensembles. *Rev. Mod. Phys.*, 82:1041–1093, 2010.
- [104] Yang Han, Bing He, Khabat Heshami, Cheng-Zu Li, and Christoph Simon. Quantum repeaters based on Rydberg-blockade-coupled atomic ensembles. *Phys. Rev. A*, 81(5):052311, May 2010.
- [105] B. L. Higgins, D. W. Berry, S. D. Bartlett, H. M. Wiseman, and G. J. Pryde. Entanglement-free heisenberg-limited phase estimation. *Nature*, 450:392–396, 2007.
- [106] Jeff T. Hill, Amir H. Safavi-Naeini, Jasper Chan, and Oskar Painter. Coherent optical wavelength conversion via cavity optomechanics. *Nature Communications*, 3:1196, 2012.
- [107] N. Hinkley, J. A. Sherman, N. B. Phillips, M. Schioppo, N. D. Lemke, K. Beloy, M. Pizzocaro, C. W. Oates, and A. D. Ludlow. An atomic clock with 10^{-18} instability. *Science*, 341:1215–1218, 2013.

Bibliography

- [108] T Honjo, H Takesue, H Kamada, Y Nishida, O Tadanaga, M Asobe, and K Inoue. Long-distance distribution of time-bin entangled photon pairs over 100 km using frequency up-conversion detectors. *Optics Express*, 15(21):13957, 2007.
- [109] D. Hucul, I. V. Inlek, G. Vittorini, C. Crocker, S. Debnath, S. M. Clark, and C. Monroe. Modular entanglement of atomic qubits using photons and phonons. *Nature Physics*, 11:37–42, 2015.
- [110] S. F. Huelga, C. Macchiavello, T. Pellizzari, A. K. Ekert, M. B. Plenio, and J. I. Cirac. Improvement of frequency standards with quantum entanglement. *Phys. Rev. Lett.*, 79:3865–3868, 1997.
- [111] E.T. Jaynes and F.W. Cummings. Comparison of quantum and semiclassical radiation theories with application to the beam maser. *Proceedings of the IEEE*, 51:89–109, 1963.
- [112] Liang Jiang, Jacob M. Taylor, Navin Khaneja, and Mikhail D. Lukin. Optimal approach to quantum communication using dynamic programming. *Proceedings of the National Academy of Sciences*, 104:17291–17296, 2007.
- [113] J.R. Johansson, P.D. Nation, and Franco Nori. Qutip 2: A python framework for the dynamics of open quantum systems. *Computer Physics Communications*, 184:1234 – 1240, 2013.
- [114] David J. Jones, Scott A. Diddams, Jinendra K. Ranka, Andrew Stentz, Robert S. Windeler, John L. Hall, and Steven T. Cundiff. Carrier-envelope phase control of femtosecond mode-locked lasers and direct optical frequency synthesis. *Science*, 288:635–639, 2000.
- [115] M. J. Kastoryano, F. Reiter, and A. S. Sørensen. Dissipative preparation of entanglement in optical cavities. *Phys. Rev. Lett.*, 106:090502, 2011.
- [116] E. M. Kessler, P. Kómár, M. Bishof, L. Jiang, a. S. Sørensen, J. Ye, and M. D. Lukin. Heisenberg-limited atom clocks based on entangled qubits. *Phys. Rev. Lett.*, 112:190403, 2014.
- [117] H. J. Kimble. The quantum internet. *Nature*, 453:1023–1030, 2008.
- [118] T. J. Kippenberg and K. J. Vahala. Cavity optomechanics: Back-action at the mesoscale. *Science*, 321:1172–1176, 2008.
- [119] Dustin Kleckner and Dirk Bouwmeester. Sub-kelvin optical cooling of a micromechanical resonator. *Nature*, 444:75–78, 2006.
- [120] E. Knill, R. Laflamme, and G. J. Milburn. A scheme for efficient quantum computation with linear optics. *Nature*, 409:46–52, 2001.

Bibliography

- [121] P. Kómár, E. M. Kessler, M. Bishof, L. Jiang, a. S. Sørensen, J. Ye, and M. D. Lukin. A quantum network of clocks. *Nature Physics*, 10:582–587, 2014.
- [122] Andreas Kronwald, Max Ludwig, and Florian Marquardt. Full photon statistics of a light beam transmitted through an optomechanical system. *Phys. Rev. A*, 87:013847, 2013.
- [123] Axel Kuhn, Markus Hennrich, and Gerhard Rempe. Deterministic single-photon source for distributed quantum networking. *Phys. Rev. Lett.*, 89:067901, 2002.
- [124] T. D. Ladd, F. Jelezko, R. Laflamme, Y. Nakamura, C. Monroe, and J. L. O'Brien. Quantum computers. *Nature*, 464:45–53, 2010.
- [125] D. Leibfried, M. D. Barrett, T. Schaetz, J. Britton, J. Chiaverini, W. M. Itano, J. D. Jost, C. Langer, and D. J. Wineland. Toward heisenberg-limited spectroscopy with multiparticle entangled states. *Science*, 304:1476–1478, 2004.
- [126] N. D. Lemke, A. D. Ludlow, Z. W. Barber, T. M. Fortier, S. A. Diddams, Y. Jiang, S. R. Jefferts, T. P. Heavner, T. E. Parker, and C. W. Oates. Spin-1/2 optical lattice clock. *Phys. Rev. Lett.*, 103:063001, 2009.
- [127] Ian D. Leroux, Monika H. Schleier-Smith, and Vladan Vuletić. Implementation of cavity squeezing of a collective atomic spin. *Phys. Rev. Lett.*, 104:073602, 2010.
- [128] L. Li, Y. O. Dudin, and A. Kuzmich. Entanglement between light and an optical atomic excitation. *Nature*, 498(7455):466–469, June 2013.
- [129] Jie-Qiao Liao and C. K. Law. Correlated two-photon scattering in cavity optomechanics. *Phys. Rev. A*, 87:043809, 2013.
- [130] Anne Louchet-Chauvet, Jürgen Appel, Jelmer J Renema, Daniel Oblak, Niels Kjaergaard, and Eugene S Polzik. Entanglement-assisted atomic clock beyond the projection noise limit. *New Journal of Physics*, 12:065032, 2010.
- [131] Andrew D. Ludlow and Jun Ye. Progress on the optical lattice clock. *Comptes Rendus Physique*, 16:499 – 505, 2015.
- [132] Max Ludwig, Bjrn Kubala, and Florian Marquardt. The optomechanical instability in the quantum regime. *New Journal of Physics*, 10:095013, 2008.
- [133] Max Ludwig, Amir H. Safavi-Naeini, Oskar Painter, and Florian Marquardt. Enhanced quantum nonlinearities in a two-mode optomechanical system. *Phys. Rev. Lett.*, 109:063601, 2012.

Bibliography

- [134] M. D. Lukin. *Colloquium* : Trapping and manipulating photon states in atomic ensembles. *Rev. Mod. Phys.*, 75:457–472, 2003.
- [135] M. D. Lukin, M. Fleischhauer, R. Cote, L M Duan, D Jaksch, J I Cirac, and P Zoller. Dipole blockade and quantum information processing in mesoscopic atomic ensembles. *Phys. Rev. Lett.*, 87:037901, 2001.
- [136] Xiao-Song Ma, Thomas Herbst, Thomas Scheidl, Daqing Wang, Sebastian Kropatschek, William Naylor, Bernhard Wittmann, Alexandra Mech, Johannes Kofler, Elena Anisimova, Vadim Makarov, Thomas Jennewein, Rupert Ursin, and Anton Zeilinger. Quantum teleportation over 143 kilometres using active feed-forward. *Nature*, 489:269–273, 2012.
- [137] H. Mabuchi and A. C. Doherty. Cavity quantum electrodynamics: Coherence in context. *Science*, 298:1372–1377, 2002.
- [138] J. Majer, J. M. Chow, J. M. Gambetta, Jens Koch, B. R. Johnson, J. A. Schreier, L. Frunzio, D. I. Schuster, A. A. Houck, A. Wallraff, A. Blais, M. H. Devoret, S. M. Girvin, and R. J. Schoelkopf. Coupling superconducting qubits via a cavity bus. *Nature*, 449:443–447, 2007.
- [139] Yuriy Makhlin, Gerd Scöhn, and Alexander Shnirman. Josephson-junction qubits with controlled couplings. *Nature*, 398:305–307, 1999.
- [140] Atul Mantri, Carlos A. Pérez-Delgado, and Joseph F. Fitzsimons. Optimal blind quantum computation. *Phys. Rev. Lett.*, 111:230502, 2013.
- [141] Florian Marquardt, Joe P. Chen, A. A. Clerk, and S. M. Girvin. Quantum theory of cavity-assisted sideband cooling of mechanical motion. *Phys. Rev. Lett.*, 99:093902, 2007.
- [142] Florian Marquardt and Steven M. Girvin. Trend: Optomechanics. *Physics*, 2:40, 2009.
- [143] William Marshall, Christoph Simon, Roger Penrose, and Dik Bouwmeester. Towards quantum superpositions of a mirror. *Phys. Rev. Lett.*, 91:130401, 2003.
- [144] P. Maunz, D. L. Moehring, S. Olmschenk, K. C. Younge, D. N. Matsukevich, and C. Monroe. Quantum interference of photon pairs from two remote trapped atomic ions. *Nature Physics*, 3:538–541, 2007.
- [145] P. C. Maurer, G. Kucsko, C. Latta, L. Jiang, N. Y. Yao, S. D. Bennett, F. Pastawski, D. Hunger, N. Chisholm, M. Markham, D. J. Twitchen, J. I. Cirac, and M. D. Lukin. Room-temperature quantum bit memory exceeding one second. *Science*, 336:1283–1286, 2012.

Bibliography

- [146] Robert McConnell, Hao Zhang, Senka Ćuk, Jiazhong Hu, Monika H. Schleier-Smith, and Vladan Vuletić. Generating entangled spin states for quantum metrology by single-photon detection. *Phys. Rev. A*, 88:063802, 2013.
- [147] D Meiser, Jun Ye, and M J Holland. Spin squeezing in optical lattice clocks via lattice-based qnd measurements. *New Journal of Physics*, 10:073014, 2008.
- [148] Attila Mekis, J. C. Chen, I. Kurland, Shanhui Fan, Pierre R. Villeneuve, and J. D. Joannopoulos. High transmission through sharp bends in photonic crystal waveguides. *Phys. Rev. Lett.*, 77:3787–3790, 1996.
- [149] Constanze Höhberger Metzger and Khaled Karrai. Cavity cooling of a microlever. *Nature*, 432:1002–1005, 2004.
- [150] Pierre Meystre. A short walk through quantum optomechanics. *Annalen der Physik*, 525:215–233, 2013.
- [151] Haixing Miao, Stefan Danilishin, Thomas Corbitt, and Yanbei Chen. Standard quantum limit for probing mechanical energy quantization. *Phys. Rev. Lett.*, 103:100402, 2009.
- [152] M. W. Mitchell. Metrology with entangled states. In *Proc. SPIE 5893, Quantum Communications and Quantum Imaging III*, volume 5893, pages 589310–589310–10, 2005.
- [153] Thomas Monz, Philipp Schindler, Julio T. Barreiro, Michael Chwalla, Daniel Nigg, William A. Coish, Maximilian Harlander, Wolfgang Hänsel, Markus Henrich, and Rainer Blatt. 14-qubit entanglement: Creation and coherence. *Phys. Rev. Lett.*, 106:130506, 2011.
- [154] M. Müller, I. Lesanovsky, H. Weimer, H. P. Büchler, and P. Zoller. Mesoscopic Rydberg Gate Based on Electromagnetically Induced Transparency. *Phys. Rev. Lett.*, 102(17):170502, April 2009.
- [155] Sreraman Muralidharan, Linshu Li, Jungsang Kim, Norbert Lütkenhaus, Mikhail D. Lukin, and Liang Jiang. Efficient long distance quantum communication. *arXiv:*, 1509.08435, 2015.
- [156] T. L. Nicholson, M. J. Martin, J. R. Williams, B. J. Bloom, M. Bishof, M. D. Swallows, S. L. Campbell, and J. Ye. Comparison of two independent sr optical clocks with 1×10^{-17} stability at 10^3 s. *Phys. Rev. Lett.*, 109:230801, 2012.
- [157] T.L. Nicholson, S.L. Campbell, R.B. Hutson, G.E. Marti, B.J. Bloom, R.L. McNally, W. Zhang, M.D. Barrett, M.S. Safronova, G.F. Strouse, W.L. Tew, and J. Ye. Systematic evaluation of an atomic clock at 2×10^{-18} total uncertainty. *Nature Communications*, 6:6896, 2015.

Bibliography

- [158] Naomi H. Nickerson, Joseph F. Fitzsimons, and Simon C. Benjamin. Freely scalable quantum technologies using cells of 5-to-50 qubits with very lossy and noisy photonic links. *Phys. Rev. X*, 4:041041, 2014.
- [159] M. A. Nielsen and I. L. Chuang. *Quantum Computation and Quantum Information*. Cambridge University Press, Cambridge, England,, 2011.
- [160] M. Notomi, E. Kuramochi, and H. Taniyama. Ultrahigh-q nanocavity with 1d photonic gap. *Opt. Express*, 16:11095–11102, 2008.
- [161] A. Nunnenkamp, K. Børkje, and S. M. Girvin. Single-photon optomechanics. *Phys. Rev. Lett.*, 107:063602, 2011.
- [162] A. D. OConnell, M. Hofheinz, M. Ansmann, Radoslaw C. Bialczak, M. Lenander, Erik Lucero, M. Neeley, D. Sank, H. Wang, M. Weides, J. Wenner, John M. Martinis, and A. N. Cleland. Quantum ground state and single-phonon control of a mechanical resonator. *Nature*, 464:697–703, 2010.
- [163] S. Olmschenk, D. N. Matsukevich, P. Maunz, D. Hayes, L.-M. Duan, and C. Monroe. Quantum teleportation between distant matter qubits. *Science*, 323:486–489, 2009.
- [164] Jiannis Pachos and Herbert Walther. Quantum computation with trapped ions in an optical cavity. *Phys. Rev. Lett.*, 89:187903, 2002.
- [165] Oskar Painter, Kartik Srinivasan, John D O’Brien, Axel Scherer, and P Daniel Dapkus. Tailoring of the resonant mode properties of optical nanocavities in two-dimensional photonic crystal slab waveguides. *Journal of Optics A*, 3:S161, 2001.
- [166] Jian-Wei Pan, Christoph Simon, Časlav Brukner, and Anton Zeilinger. Entanglement purification for quantum communication. *Nature*, 410:1067–1070, 2001.
- [167] M Peev, C Pacher, R Alléaume, C Barreiro, J Bouda, W Boxleitner, T Debuisschert, E Diamanti, M Dianati, J F Dynes, S Fasel, S Fossier, M Fürst, J-D Gautier, O Gay, N Gisin, P Grangier, A Happe, Y Hasani, M Hentschel, H Hübel, G Humer, T Länger, M Legré, R Lieger, J Lodewyck, T Lorünser, N Lütkenhaus, A Marhold, T Matyus, O Maurhart, L Monat, S Nauerth, J-B Page, A Poppe, E Querasser, G Ribordy, S Robyr, L Salvail, A W Sharpe, A J Shields, D Stucki, M Suda, C Tamas, T Themel, R T Thew, Y Thoma, A Treiber, P Trinkler, R Tualle-Brouri, F Vannel, N Walenta, H Weier, H Weinfurter, I Wimberger, Z L Yuan, H Zbinden, and A Zeilinger. The secoqc quantum key distribution network in vienna. *New Journal of Physics*, 11:075001, 2009.

Bibliography

- [168] T. Pellizzari, S. A. Gardiner, J. I. Cirac, and P. Zoller. Decoherence, continuous observation, and quantum computing: A cavity qed model. *Phys. Rev. Lett.*, 75:3788–3791, 1995.
- [169] S Perseguers, G J Lapeyre Jr, D Cavalcanti, M Lewenstein, and A Acín. Distribution of entanglement in large-scale quantum networks. *Reports on Progress in Physics*, 76:096001, 2013.
- [170] T. P. Purdy, D. W. C. Brooks, T. Botter, N. Brahms, Z.-Y. Ma, and D. M. Stamper-Kurn. Tunable cavity optomechanics with ultracold atoms. *Phys. Rev. Lett.*, 105:133602, 2010.
- [171] P. Rabl. Photon blockade effect in optomechanical systems. *Phys. Rev. Lett.*, 107:063601, 2011.
- [172] J. M. Raimond, M. Brune, and S. Haroche. Manipulating quantum entanglement with atoms and photons in a cavity. *Rev. Mod. Phys.*, 73:565–582, 2001.
- [173] T. C. Ralph, A. J. F. Hayes, and Alexei Gilchrist. Loss-tolerant optical qubits. *Phys. Rev. Lett.*, 95:100501, 2005.
- [174] Norman F. Ramsey. A molecular beam resonance method with separated oscillating fields. *Phys. Rev.*, 78:695–699, 1950.
- [175] C A Regal and K W Lehnert. From cavity electromechanics to cavity optomechanics. *Journal of Physics: Conference Series*, 264:012025, 2011.
- [176] J. Reichert, M. Niering, R. Holzwarth, M. Weitz, Th. Udem, and T. W. Hänsch. Phase coherent vacuum-ultraviolet to radio frequency comparison with a mode-locked laser. *Phys. Rev. Lett.*, 84:3232–3235, 2000.
- [177] Andreas Reiserer, Norbert Kalb, Gerhard Rempe, and Stephan Ritter. A quantum gate between a flying optical photon and a single trapped atom. *Nature*, 508:237–240, 2014.
- [178] Florentin Reiter and Anders S. Sørensen. Effective operator formalism for open quantum systems. *Phys. Rev. A*, 85:032111, 2012.
- [179] P.R. Rice and H.J. Carmichael. Single-atom cavity-enhanced absorption. i. photon statistics in the bad-cavity limit. *Quantum Electronics, IEEE Journal of*, 24:1351–1366, 1988.
- [180] D. Ristè, M. Dukalski, C. A. Watson, G. de Lange, M. J. Tiggelman, Ya. M. Blanter, K. W. Lehnert, R. N. Schouten, and L. DiCarlo. Deterministic entanglement of superconducting qubits by parity measurement and feedback. *Nature*, 502:350–354, 2013.

Bibliography

- [181] Stephan Ritter, Christian Nölleke, Carolin Hahn, Andreas Reiserer, Andreas Neuzner, Manuel Uphoff, Martin Mücke, Eden Figueroa, Joerg Bochmann, and Gerhard Rempe. An elementary quantum network of single atoms in optical cavities. *Nature*, 484:195–200, 2012.
- [182] Jacob T. Robinson, Christina Manolatou, Long Chen, and Michal Lipson. Ultrasmall mode volumes in dielectric optical microcavities. *Phys. Rev. Lett.*, 95:143901, 2005.
- [183] T. Rosenband and D. R. Leibrandt. Exponential scaling of clock stability with atom number. *arXiv:*, 1303.6357, 2013.
- [184] Till Rosenband. Numerical test of few-qubit clock protocols. *arXiv:*, 1203.0288, 2012.
- [185] A. Rubenok, J. A. Slater, P. Chan, I. Lucio-Martinez, and W. Tittel. Real-World Two-Photon Interference and Proof-of-Principle Quantum Key Distribution Immune to Detector Attacks. *Phys. Rev. Lett.*, 111(13):130501, September 2013.
- [186] J. Rutman. Characterization of phase and frequency instabilities in precision frequency sources: Fifteen years of progress. *Proceedings of the IEEE*, 66:1048–1075, 1978.
- [187] A. H. Safavi-Naeini, T. P. Mayer Alegre, J. Chan, M. Eichenfield, M. Winger, Q. Lin, J. T. Hill, D. E. Chang, and O. Painter. Electromagnetically induced transparency and slow light with optomechanics. *Nature*, 472:69–73, 2011.
- [188] Amir H Safavi-Naeini and Oskar Painter. Proposal for an optomechanical traveling wave phonon-photon translator. *New Journal of Physics*, 13:013017, 2011.
- [189] M. Saffman and K. Mølmer. Efficient multiparticle entanglement via asymmetric rydberg blockade. *Phys. Rev. Lett.*, 102(24):240502, June 2009.
- [190] M. Saffman, T. G. Walker, and K. Mølmer. Quantum information with Rydberg atoms. *Rev. Mod. Phys.*, 82:2313–2363, 2010.
- [191] Nicolas Sangouard, Romain Dubessy, and Christoph Simon. Quantum repeaters based on single trapped ions. *Phys. Rev. A*, 79:042340, 2009.
- [192] Nicolas Sangouard, Christoph Simon, Hugues de Riedmatten, and Nicolas Gisin. Quantum repeaters based on atomic ensembles and linear optics. *Rev. Mod. Phys.*, 83:33–80, 2011.

Bibliography

- [193] Nicolas Sangouard, Christoph Simon, Bo Zhao, Yu-Ao Chen, Hugues de Riedmatten, Jian-Wei Pan, and Nicolas Gisin. Robust and efficient quantum repeaters with atomic ensembles and linear optics. *Phys. Rev. A*, 77:062301, 2008.
- [194] G. Santarelli, Claude Audoin, A. Makdissi, P. Laurent, G.J. Dick, and C. Clairon. Frequency stability degradation of an oscillator slaved to a periodically interrogated atomic resonator. *Ultrasonics, Ferroelectrics, and Frequency Control, IEEE Transactions on*, 45:887–894, 1998.
- [195] Valerio Scarani, Helle Bechmann-Pasquinucci, Nicolas J. Cerf, Miloslav Dušek, Norbert Lütkenhaus, and Momtchil Peev. The security of practical quantum key distribution. *Rev. Mod. Phys.*, 81:1301–1350, 2009.
- [196] S. Schiemann, A. Kuhn, S. Steuerwald, and K. Bergmann. Efficient coherent population transfer in no molecules using pulsed lasers. *Phys. Rev. Lett.*, 71:3637–3640, 1993.
- [197] S. Schiller, G.M. Tino, P. Gill, C. Salomon, U. Sterr, E. Peik, A. Neovsky, A. Görlitz, D. Svehla, G. Ferrari, N. Poli, L. Lusanna, H. Klein, H. Margolis, P. Lemonde, P. Laurent, G. Santarelli, A. Clairon, W. Ertmer, E. Rasel, J. Müller, L. Iorio, C. Lmmerzahl, H. Dittus, E. Gill, M. Rothacher, F. Flechner, U. Schreiber, V. Flambaum, Wei-Tou Ni, Liang Liu, Xuzong Chen, Jingbiao Chen, Kelin Gao, L. Cacciapuoti, R. Holzwarth, M.P. He, and W. Schfer. Einstein gravity explorera medium-class fundamental physics mission. *Experimental Astronomy*, 23:573–610, 2009.
- [198] A. Schliesser, R. Rivière, G. Anetsberger, O. Arcizet, and T. J. Kippenberg. Resolved-sideband cooling of a micromechanical oscillator. *Nature Physics*, 4:415–419, 2008.
- [199] Michael Schmidt, Max Ludwig, and Florian Marquardt. Optomechanical circuits for nanomechanical continuous variable quantum state processing. *New Journal of Physics*, 14:125005, 2012.
- [200] R. J. Schoelkopf and S. M. Girvin. Wiring up quantum systems. *Nature*, 451:664–669, 2008.
- [201] A. Seidel, M.P. Hess, J. Kehrer, W. Schafer, M. Kufner, M. Siccardi, L. Cacciapuoti, I.A. Sanches, and S. Feltham. The aces microwave link: Instrument design and test results. In *2007 IEEE International Frequency Control Symposium Joint with the 21st European Frequency and Time Forum*, pages 1295–1298. IEEE, 2007.

Bibliography

- [202] Jacob F. Sherson, Hanna Krauter, Rasmus K. Olsson, Brian Julsgaard, Clemens Hammerer, Ignacio Cirac, and Eugene S. Polzik. Quantum teleportation between light and matter. *Nature*, 443:557–560, 2006.
- [203] Peter W. Shor. Polynomial-time algorithms for prime factorization and discrete logarithms on a quantum computer. *SIAM Journal on Computing*, 26:1484–1509, 1997.
- [204] Bruce W. Shore and Peter L. Knight. The jaynes-cummings model. *Journal of Modern Optics*, 40:1195–1238, 1993.
- [205] David Shwa, Raphael D. Cohen, Alex Retzker, and Nadav Katz. Heralded generation of Bell states using atomic ensembles. *Phys. Rev. A*, 88(6):063844, December 2013.
- [206] Anders Sørensen and Klaus Mølmer. Quantum computation with ions in thermal motion. *Phys. Rev. Lett.*, 82(9):1971–1974, 1999.
- [207] Anders Sørensen and Klaus Mølmer. Entanglement and quantum computation with ions in thermal motion. *Phys. Rev. A*, 62:022311, 2000.
- [208] Anders S. Sørensen and Klaus Mølmer. Measurement induced entanglement and quantum computation with atoms in optical cavities. *Phys. Rev. Lett.*, 91:097905, 2003.
- [209] Anders S. Sørensen and Klaus Mølmer. Probabilistic generation of entanglement in optical cavities. *Phys. Rev. Lett.*, 90:127903, 2003.
- [210] Dan M. Stamper-Kurn. Cavity optomechanics with cold atoms. *arXiv:*, 1204.4351, 2012.
- [211] K. Stannigel, P. Komar, S. J. M. Habraken, S. D. Bennett, M. D. Lukin, P. Zoller, and P. Rabl. Optomechanical quantum information processing with photons and phonons. *Phys. Rev. Lett.*, 109:013603, 2012.
- [212] K. Stannigel, P. Rabl, A. S. Sørensen, P. Zoller, and M. D. Lukin. Optomechanical transducers for long-distance quantum communication. *Phys. Rev. Lett.*, 105:220501, 2010.
- [213] Y. Tanaka, T. Asano, and S. Noda. Design of photonic crystal nanocavity with q -factor of $\sim 10^9$. *Lightwave Technology, Journal of*, 26:1532–1539, 2008.
- [214] B. Tapley, J. Ries, S. Bettadpur, D. Chambers, M. Cheng, F. Condi, B. Gunter, Z. Kang, P. Nagel, R. Pastor, T. Pekker, S. Poole, and F. Wang. Ggm02 an improved earth gravity field model from grace. *Journal of Geodesy*, 79:467–478, 2005.

Bibliography

- [215] J. M. Taylor, A. S. Sørensen, C. M. Marcus, and E. S. Polzik. Laser cooling and optical detection of excitations in a *lc* electrical circuit. *Phys. Rev. Lett.*, 107:273601, 2011.
- [216] J. D. Teufel, T. Donner, Dale Li, J. W. Harlow, M. S. Allman, K. Cicak, A. J. Sirois, J. D. Whittaker, K. W. Lehnert, and R. W. Simmonds. Sideband cooling of micromechanical motion to the quantum ground state. *Nature*, 475:359–363, 2011.
- [217] J. D. Teufel, Dale Li, M. S. Allman, K. Cicak, A. J. Sirois, J. D. Whittaker, and R. W. Simmonds. Circuit cavity electromechanics in the strong-coupling regime. *Nature*, 471:204–208, 2011.
- [218] J. D. Thompson, T. G. Tiecke, N. P. de Leon, J. Feist, A. V. Akimov, M. Gullans, A. S. Zibrov, V. Vuletić, and M. D. Lukin. Coupling a single trapped atom to a nanoscale optical cavity. *Science*, 340:1202–1205, 2013.
- [219] J. D. Thompson, B. M. Zwickl, A. M. Jayich, Florian Marquardt, S. M. Girvin, and J. G. E. Harris. Strong dispersive coupling of a high-finesse cavity to a micromechanical membrane. *Nature*, 452:72–75, 2007.
- [220] T. G. Tiecke, J. D. Thompson, N. P. de Leon, L. R. Liu, V. Vuletić, and M. D. Lukin. Nanophotonic quantum phase switch with a single atom. *Nature*, 508:241–244, 2014.
- [221] E. Togan, Y. Chu, A. S. Trifonov, L. Jiang, J. Maze, L. Childress, M. V. G. Dutt, A. S. Sørensen, P. R. Hemmer, A. S. Zibrov, and M. D. Lukin. Quantum entanglement between an optical photon and a solid-state spin qubit. *Nature*, 466:730–734, 2010.
- [222] Turker Topcu. *in preparation*.
- [223] Turker Topcu and Andrei Derevianko. Intensity landscape and the possibility of magic trapping of alkali-metal Rydberg atoms in infrared optical lattices. *Phys. Rev. A*, 88(4):043407, October 2013.
- [224] Turker Topcu and Andrei Derevianko. Divalent Rydberg atoms in optical lattices: Intensity landscape and magic trapping. *Phys. Rev. A*, 89(2):023411, February 2014.
- [225] Götz S. Uhrig. Keeping a quantum bit alive by optimized π -pulse sequences. *Phys. Rev. Lett.*, 98:100504, 2007.
- [226] E. Urban, T. A. Johnson, T. Henage, L. Isenhower, D. D. Yavuz, T. G. Walker, and M. Saffman. Observation of rydberg blockade between two atoms. *Nature Physics*, 5:110–114, 2009.

Bibliography

- [227] S. J. van Enk, J. I. Cirac, and P. Zoller. Ideal quantum communication over noisy channels: A quantum optical implementation. *Phys. Rev. Lett.*, 78:4293–4296, 1997.
- [228] S. J. van Enk, J. I. Cirac, and P. Zoller. Purifying two-bit quantum gates and joint measurements in cavity qed. *Phys. Rev. Lett.*, 79:5178–5181, 1997.
- [229] Michael Varnava, Daniel E. Browne, and Terry Rudolph. Loss tolerance in one-way quantum computation via counterfactual error correction. *Phys. Rev. Lett.*, 97:120501, 2006.
- [230] E. Verhagen, S. Deléglise, S. Weis, A. Schliesser, and T. J. Kippenberg. Quantum-coherent coupling of a mechanical oscillator to an optical cavity mode. *Nature*, 482:63–67, 2012.
- [231] Herbert Walther, Benjamin T H Varcoe, Berthold-Georg Englert, and Thomas Becker. Cavity quantum electrodynamics. *Reports on Progress in Physics*, 69:1325, 2006.
- [232] T. M. Weber, M. Höning, T. Niederprüm, T. Manthey, O. Thomas, V. Guarnera, M. Fleischhauer, G. Barontini, and H. Ott. Mesoscopic Rydberg-blockaded ensembles in the superatom regime and beyond. *Nature Physics*, 11(January):157–161, January 2015.
- [233] Hendrik Weimer, Markus Müller, Igor Lesanovsky, Peter Zoller, and Hans Peter Büchler. A rydberg quantum simulator. *Nature Physics*, 6:382–388, 2010.
- [234] Stefan Weis, Rémi Rivière, Samuel Deléglise, Emanuel Gavartin, Olivier Arcizet, Albert Schliesser, and Tobias J. Kippenberg. Optomechanically induced transparency. *Science*, 330:1520–1523, 2010.
- [235] D. J. Wilson, C. A. Regal, S. B. Papp, and H. J. Kimble. Cavity optomechanics with stoichiometric sin films. *Phys. Rev. Lett.*, 103:207204, 2009.
- [236] I. Wilson-Rae, N. Nooshi, W. Zwerger, and T. J. Kippenberg. Theory of ground state cooling of a mechanical oscillator using dynamical backaction. *Phys. Rev. Lett.*, 99:093901, 2007.
- [237] D. J. Wineland, W. M C. Monroe, Itano, D. Leibfried, B. E. King, and D. M. Meekhof. Experimental issues in coherent quantum-state manipulation of trapped atomic ions. *J. Res. Natl. Inst. Stand. Technol.*, 103:259, 1998.
- [238] P. Wolf, Ch.J. Bordé, A. Clairon, L. Duchayne, A. Landragin, P. Lemonde, G. Santarelli, W. Ertmer, E. Rasel, F.S. Cataliotti, M. Inguscio, G.M. Tino, P. Gill, H. Klein, S. Reynaud, C. Salomon, E. Peik, O. Bertolami, P. Gil,

Bibliography

- J. Pramos, C. Jentsch, U. Johann, A. Rathke, P. Bouyer, L. Cacciapuoti, D. Izzo, P. De Natale, B. Christophe, P. Touboul, S.G. Turyshev, J. Anderson, M.E. Tobar, F. Schmidt-Kaler, J. Vigué, A.A. Madej, L. Marmet, M.-C. Angonin, P. Delva, P. Tourrenc, G. Metris, H. Müller, R. Walsworth, Z.H. Lu, L.J. Wang, K. Bongs, A. Toncelli, M. Tonelli, H. Dittus, C. Lmmerzahl, G. Galzerano, P. Laporta, J. Laskar, A. Fienga, F. Roques, and K. Sengstock. Quantum physics exploring gravity in the outer solar system: the sagas project. *Experimental Astronomy*, 23:651–687, 2009.
- [239] Chi Xiong, Wolfram H P Pernice, Xiankai Sun, Carsten Schuck, King Y Fong, and Hong X Tang. Aluminum nitride as a new material for chip-scale optomechanics and nonlinear optics. *New Journal of Physics*, 14:095014, 2012.
- [240] Jun Ye, Jin-Long Peng, R. Jason Jones, Kevin W. Holman, John L. Hall, David J. Jones, Scott A. Diddams, John Kitching, Sébastien Bize, James C. Bergquist, Leo W. Hollberg, Lennart Robertsson, and Long-Sheng Ma. Delivery of high-stability optical and microwave frequency standards over an optical fiber network. *J. Opt. Soc. Am. B*, 20:1459–1467, 2003.
- [241] Nanfang Yu and Federico Capasso. Flat optics with designer metasurfaces. *Nature Materials*, 13:139–150, 2014.
- [242] Jing Zhang, Kunchi Peng, and Samuel L. Braunstein. Quantum-state transfer from light to macroscopic oscillators. *Phys. Rev. A*, 68:013808, 2003.
- [243] Mian Zhang, Gustavo S. Wiederhecker, Sasikanth Manipatruni, Arthur Barnard, Paul McEuen, and Michal Lipson. Synchronization of micromechanical oscillators using light. *Phys. Rev. Lett.*, 109:233906, 2012.
- [244] Bo Zhao, Markus Müller, Klemens Hammerer, and Peter Zoller. Efficient quantum repeater based on deterministic Rydberg gates. *Phys. Rev. A*, 81(5):052329, May 2010.
- [245] Shi-Biao Zheng. Implementation of toffoli gates with a single asymmetric heisenberg xy interaction. *Phys. Rev. A*, 87:042318, 2013.